Alma Mater Studiorum · Università di Bologna

DOTTORATO DI RICERCA IN FISICA

XXXIII Ciclo

Settore Concorsuale: 02/A1 - Fisica sperimentale delle interazioni fondamentali

Settore Scientifico Disciplinare: FIS/01 - Fisica sperimentale

Measurement of the ^{235}U(n,f) cross section relative to the neutron-proton elastic scattering up to 500 MeV at n_TOF

Presentata da: Alice Manna

Coordinatore Dottorato:
Prof. Michele Cicoli

Supervisore:
Dott. Cristian Massimi

Co-supervisore:
Prof. Gianni Vannini

Esame finale anno 2021

"Se non siete curiosi, lasciate perdere."

Achille Castiglioni

Abstract

Neutron cross section standards are fundamental ingredients for both measurements and evaluations of neutron-induced reaction cross sections. This is the case of ^{235}U(n,f) cross section: one of the most important standard cross sections at thermal neutron energy and between 0.15 MeV and 200 MeV. Above 200 MeV this reaction plays an important role for several applications, ranging from biological effectiveness, via nuclear astrophysics, to nuclear technology, as well as for fundamental nuclear physics. However, no measurement exists for neutron energies above 200 MeV. This led to a request for new absolute measurements of ^{235}U(n,f) cross section, in order to extend the precision and possibly to establish it as a standard up to 1 GeV. The n_TOF facility at CERN offers the possibility to study such reaction thanks to the wide neutron energy spectrum available in its experimental area, from thermal to 1 GeV. A dedicated measurement campaign was carried out to provide accurate and precise cross-section data of the ^{235}U(n,f) reaction in the energy region from 10 MeV to 500 MeV. The experimental setup consisted of two chambers to detect the ^{235}U fission events, while the number of neutrons impinging on the ^{235}U samples was simultaneously measured by exploiting the neutron-proton scattering process. To this end, three Proton Recoil Telescopes were used to detect the protons emitted from two polyethylene samples placed along the neutron beam, downstream of the fission chambers. In this PhD thesis the development, implementation and characterisation of the two telescopes under the responsibility of the INFN are discussed, as well as the analysis of the data acquired during the 5 weeks of beam period at CERN. In this measurement campaign, the n_TOF neutron flux in the energy interval between 10 and 500 MeV was measured for the first time. In addition, the analysis of one of the two chambers dedicated to the measurement of fission events is presented in detail. From these data, the ^{235}U(n,f) cross section was determined and represents, at this time, the unique measure of this kind.

Contents

Introduction

The ^{235}U(n,f) cross section is well known because of the significant amount of accurate experimental data, resulting from developments in the experimental methodology and analysis procedures. As a consequence, from the cooperation of an international panel of experts, these data were combined and evaluated in order to propose a reference cross section with corresponding uncertainties below 1%. The ^{235}U(n,f) cross section is not the only one, but certainly within the most important neutron cross-section standards, and it is recognised as a convenient reference for other reaction cross-section measurements at thermal energy and between 0.15 MeV and 200 MeV. However, outside these energy ranges the cross section is either not so well known - for instance, the n_TOF collaboration recently highlighted some inconsistency in the region between 10 and 30 keV - or was never measured, as for example above 200 MeV, where evaluations can only rely on theoretical calculations. Within the continuous effort for the improvement of the standards by the International Atomic Energy Agency (IAEA) together with ENDF/B, the longstanding quest for ^{235}U(n,f) cross section data turns out to be still pending above 20 MeV (only 2 data sets are present in the 20-200 MeV energy region). In particular, the request is for fission measurements relative to the neutron-proton elastic scattering, which is considered the primary reference for neutron cross section measurements.

Moreover, the neutron-induced fission cross section on ^{235}U is relevant for the study of fission at intermediate energies (above 20 MeV). While at low energy the fission is considered a well-established nuclear process that statistical models can reproduce with increasing level of complexity, at higher energy, where the nuclear fission can be described as a two-step process (pre-equilibrium followed by nuclear evaporation) the study is hindered by the lack of firm experimental data. In fact, above 20 MeV a few neutron-induced fission cross-section data in other nuclides are available, and they are measured relative to ^{235}U(n,f). It is worth mentioning that in this regime the fission dynamic depends also on nuclear structure effects. In addition, multiple-chance fission can take place, as attested by the step-like structure of fission cross section above the threshold. This phenomenon is thought to be attributable to the superposition of different (n,xnf) reactions. At energies above 200 MeV, the projectile sees the target nucleus as a collection of individuals nucleons. Therefore, the collision process can be described as a succession of binary collisions with the target nucleons, which can

be ejected from the nucleus or can eject other nucleons in turn, thus giving rise to a fast intra-nuclear cascade. Clearly, by increasing the kinetic energy of the projectile, a more complex regime is reached, including multifragmentation, and production of barionic and mesonic resonances. In a macroscopic picture of the nucleus, fission can be considered as a diffusive process over the potential barrier, and governed by nuclear viscosity, whose nature represents one of the major open questions in fission dynamics. Therefore, the study of the fission of highly excited nuclei remains a topic of great interest.

As mentioned above, the data on neutron induced fission cross-sections at intermediate energy are relevant to basic nuclear physics, in particular to understand the connection between collective and single particle degrees of freedom in nuclei, which reflects the dynamic effects of the nuclear fission process. Moreover, the same fission data are key ingredients in several nuclear physics applications, for instance the energy production with accelerator driven systems, radioactive waste transmutation, as well as in nuclear astrophysics and radiation shield design for accelerators and to evaluate the dose received by aircrew.

All these motivations clearly called for a measurement of the ^{235}U(n,f) cross section as a function of the energy, above 20 MeV and possibly up to 1 GeV. However, it is difficult to carry out measurements at a sufficiently large number of energies to resolve fine structures in the ^{235}U(n,f) cross section. Thanks to its very wide neutron energy spectrum, which extends from thermal energy up to more than 1 GeV, the n_TOF facility offered the opportunity to perform such a measurement with a good accuracy. The n_TOF facility, operational since 2001 at CERN, is based on a very intense spallation neutron source produced by the high energy (20 GeV/c), high peak current and low duty cycle proton beam from the Proton-Synchrotron accelerator. Bunches of 7×10^{12} protons are accelerated and sent towards on a massive lead target, where some 10^{15} neutrons per bunch are produced. The facility features two experimental area, respectively located at 18.5 and 185 meters from the neutron source. The experiment described in this document was performed at the longest flight path station in order to exploit the high energy resolution and low intrinsic background.

The idea of measuring ^{235}U(n,f) relative to the neutron-proton elastic scattering at energies above 20 MeV dates back to 2014, it independently arose within the Istituto Nazionale di Fisica Nucleare and Physikalisch-Technische Bundesanstalt groups participating to the n_TOF collaboration. By merging the two proposals, the final setup was designed to measure simultaneously the ^{235}U fission by means of two fission fragment detectors (respectively a Parallel Plate Avalance and Ionization Chamber, PPAC and PPFC) and the neutron flux using three different Recoil-Proton Telescopes (RPTs). This latter measurement is based on the knowledge of the neutron-proton elastic scattering cross-section, and it exploits the detection of the recoil proton from the n-p reaction in a polyethylene target. A detailed preparative study and several test beams were required before the experimental campaign could start in September

2018. In fact, while PPAC were already been successfully used at n_TOF to measure the fission cross section (relative to ^{235}U) of a large number of actinides up to 1 GeV neutron energy, no neutron flux measurement was performed at n_TOF using RPTs before this experimental campaign. Therefore, the prerequisite for the ^{235}U(n,f) study was the availability of such a flux detector, suitable for the special conditions at a spallation source, i.e. the presence of an intense γ-flash and a continuous neutron energy distribution extending from thermal energies to the GeV energy range.

In the first part of my PhD project, I have participated to the development and characterization of two RPTs, especially realized by INFN for this experiment. I took part to the construction processes and afterwards I followed and analysed the data of two tests under proton and neutron beam, respectively. From the acquired information, it was possible to improve the RPT design for the final measurement. I worked on the preparation of the experiment at CERN and I followed it during the 5 weeks of the required beam time. During the measurement, I continuously monitored the performances of the detectors by analyzing the daily data output. In addition, I was responsible for the experimental schedule, which included several measurement configurations. After the measurement, the second part of the PhD project was devoted to the analysis of the data obtained by the PPAC and by the two RPTs developed by INFN. In particular, a large effort was dedicated to the characterization of the RPT detectors and the extraction of the neutron flux, which includes the production of Monte Carlo simulations to correct for experimental complications. In parallel, I contributed to the analysis of the PPAC data, from the data reduction to the extraction of the detector efficiency and the application of correction factors. The combination of the results obtained with the PPAC and RPTs made it possible to extract the ^{235}U(n,f) cross section from 12 to 500 MeV with an uncertainty of 5.5% on average. I maintained a continuous discussion with the PTB group, allowing us to properly assess difficulties originating from the experiment and in addition to ease the reduction of systematic uncertainties.

The present PhD thesis is divided into 6 Chapters. The scientific motivations related to the measurement of ^{235}U(n,f) are described in in Chapter 1. They span from basic nuclear physics (the study of fission at intermediate energy) to nuclear physics applications (energy production via ADS of fast reactors and radiation protection) and to Nuclear Astrophysics (nucleosynthesis in neutron star mergers). In Chapter 2 the neutron time-of-flight facility at CERN is described, providing details on the CERN neutron source as well as on the experimental complications related to its combination with the time-of-flight method. An overview of the available equipment, including the data acquisition system is also reported. Chapter 3 is dedicated to the instrumentation especially developed for the ^{235}U(n,f) experimental campaign. It consists of two complementary (in terms of energy interval of operation) fission chambers, used to detect fission events induced by neutron on ^{235}U, and three recoil-proton telescopes, used to estimate the neutron flux impinging on the uranium samples. In Chapter 4 the analysis

of the data collected with the PPAC detector is described in detail: from the data reduction to the determination of the efficiency. Here particular care is given to correction factors, as for example the one attributable to anisotropy of fission events. Chapter 5 describes the analysis of the RPT data, including the large effort in producing correct Monte Carlo simulations required to include in the data analysis experimental effects such as multiple scattering, sample-edge effects, beam absorption as well as energy loss of charged particles in the sample itself. The last Chapter reports the preliminary neutron flux and ^{235}U(n,f) cross section I obtained so far. The result includes a comprehensive evaluation of the uncertainties which are of the order of 8% up to 35 MeV and 5.3% above. After a comparison between my results and the ones obtained by the PTB group, who was responsible of the analysis of the PPFC and PTB-telescope data, the present ^{235}U(n,f) cross section is compared to the two existing data sets in the region between 20 and 200 MeV and to theoretical calculation above 200 MeV. The present results, although preliminary show that between 20 and 100 MeV a better agreement is found with the data reported by Lisowski and collaborators from a time-of-flight experiment performed at on the WNR facility at Los Alamos National Laboratory in the 80s. In addition, from 100 to 200 MeV neutron energy the obtained cross section agrees both with IAEA evaluation and the Lisowski measurement within 5%.

Chapter 1

Nuclear fission and its applications

Nuclear fission is an extremely complex collective process in which a highly-deformed heavy nucleus undergoes a deep rearrangement, eventually breaking into two fragments of comparable masses and releasing a large amount of energy. This phenomenon is nowadays well-established and one knows that it can be induced by a vast combination of projectile-target systems and that it can also occur spontaneously in some elements. Neutron-induced fission reactions play a crucial role in a variety of fields of fundamental and applied nuclear science. In basic nuclear physics they provide important information on properties of nuclear matter, while in nuclear technology they are at the basis of present and future reactor designs. Finally, there is a renewed interest in fission reactions in nuclear astrophysics due to the multi-messenger observation of neutron star mergers and the important role played by fission recycling in r-process nucleosynthesis. In the past, the most extensive studies were performed for neutron-induced fission at low energies, especially for nuclides that are relevant for nuclear power engineering. Consequently, evaluated neutron data libraries have been produced, in the energy region up to 20 MeV. During the last decades, such studies have largely shifted to higher energies where the experimental data are scarce, sometimes discrepant or absent. In addition to the theoretical interest, the quest for fission data above 20 MeV is motivated by new applications of the fission reaction.

1.1 Introduction to the fission process

In 1934 Fermi and his collaborators irradiated many elements to study the induced radioactivity following a neutron capture. In particular, they exposed natural uranium and thorium, to neutrons, using radon-beryllium sources with maximum 800 mCi (30 GBq) and moderating the projectiles in paraffin to obtain thermal-energy neutrons [1]. Several β activities were identified in the irradiated probe and interpreted as decay chains following neutron absorption in uranium. Only in 1939 Otto Hahn and Fritz Strassmann, after a careful radiochemical study, identified barium after bom-

barding uranium with neutrons [2], and pointed out that the observed activities were due to several elements with roughly half the mass of uranium. This led Lise Meitner and Otto Robert Frisch to give the first interpretation of the new phenomenon named nuclear disintegration. In their explanation the heavy nucleus is considered as a volume-charged, uncompressible liquid-drop, in which the decrease of surface tension, following the absorption of a neutron, causes its break-up into two parts [3]. Meitner and Frisch called this process fission, a term employed in biology to describe a cellular division.The basic theoretical concepts on which our understanding of nuclear fission is still based today were also developed very quickly after Meitner and Frisch's paper. Feenberg [4], Frenkel [5] and v. Weizsäcker [6] showed independently that a classical, spherical, homogeneously charged drop looses its stability against spontaneous deformation based on the calculation of the potential energy of the nucleus as a function of its shape. This first description of the fission process was, shortly after, improved by N. Bohr and J. A. Wheeler [7].

The liquid drop model (LDM) [7, 8] treats the fission as a collective phenomenon. The binding energy B of the nucleus, using a semiempirical mass formula, is given by the sum of five terms:

$$B \;=\; a_v\, A - a_s\, A^{2/3} - a_c\, Z(Z-1)A^{-1/3} - a_{sym}\,\frac{(A-2Z^2)}{A} + \delta \qquad (1.1)$$

where $a_v\, A$ is the contribution given by the volume, $a_s\, A^{2/3}$ is the surface contribution, $a_c\, Z(Z-1)A^{-1/3}$ is the term that takes into account the Coulomb repulsion of the protons, $a_{sym}\,\frac{(A-2Z^2)}{A}$ is the symmetry term between the number of protons and neutrons in the nucleus, and finally δ is the pairing term and takes into account the empirical fact that an even number of neutrons or protons is more strongly bound than an odd number of them. In each terms A is the mass number and Z is the proton number of the element [9].

The LDM considers the effect on the binding energy of an initially spherical nucleus that is beginning to stretch. Since the nucleus is assumed to be uncompressible, only the surface and Coulomb terms are relevant to the deformation energy. When the initial sphere is distorted into an ellipsoid, with an eccentricity ε, its surface area increases as $S = 4\pi R^2(1 + \frac{2}{5}\varepsilon^2 + \dots)$. On the other hand, the Coulomb repulsion decreases and the related term can be shown to be modified by the factor $(1 - \frac{1}{5}\varepsilon^2 + \dots)$. Therefore, qualitatively, the Coulomb force acts to elongate the nucleus to its transition state, the surface tension component acts to maintain the cohesion of the nucleus in contrast to the elongation. Thus the difference in energy between a spherical nucleus and ellipsoid of the same volume is:

$$\Delta E \;=\; B(\varepsilon) - B(\varepsilon = 0) \;=\; \left(-\frac{2}{5}\, a_s\, A^{2/3} + \frac{1}{5}\, a_c\, Z^2 A^{-1/3}\right)\, \varepsilon^2. \qquad (1.2)$$

If the second term is larger than the first, the energy difference is positive, it means that the nucleus gains energy through the stretching, and the more the nucleus is stretched,

the more energy is gained. Therefore the condition for fission process, is

$$\frac{1}{5}\, a_c\, Z^2 A^{-1/3} > \frac{2}{5}\, a_s\, A^{2/3} \tag{1.3}$$

By calculation, in an ellipsoidal nucleus, the surface area varies twice as fast as the Coulomb energy as the nucleus is deformed. This means that, simplifying, the fission occurs when the ratio of its electrostatic energy to twice the surface energy becomes larger than 1, which is equivalent to say:

$$x \approx \frac{1}{50} \cdot \frac{Z^2}{A} > 1. \tag{1.4}$$

This quantity has a relevant role in estimating the probability of a nuclear spontaneous fission and this is called the *fissility parameter*. Therefore the nuclei with $\mathrm{Z}^2/\mathrm{A} > 50$, or values of x greater than unity, are unstable against spontaneous fission. Therefore if the energy conditions are favourable, the parent nucleus reaches the scission point at which it essentially comprises two highly-charged nuclei in contact with one another. From the scission point the fragments accelerate away from each other due to the Coulomb repulsion of the constituent groups of protons, to 90% of their final kinetic energy in 10^{-20} s; they reach a speed of 5% speed of light. The fission fragments at this stage are usually neutron-rich and radioactive and, therefore, they are susceptible of disintegration via β decay and to the emission of neutrons and γ-rays.

In other words, the liquid drop model predicts spherical shapes for the ground states of stable nuclei and a potential barrier, called the *fission barrier*, that must be crossed in order for the process to occur. E_A is the *activation energy*, and it is the difference between the maximum of the barrier and the energy of the initial nucleus in the ground state. The Coulomb barrier is roughly equal to the energy released in fission of heavy nuclei. The fission process can take place in two ways:

a) the first possibility is to give the nucleus an excitation energy greater than E_A; for some nuclei the absorption of a relatively small amount of energy, such as from a low-energy neutron or photon may be enough, to form a intermediate state that is at or above the barrier; in such situation the induced fission competes successfully with other modes of decay of the compound nucleus.

b) The second possibility is spontaneous fission which, inside this model, can occur via quantum mechanical tunneling through the fission barrier. Figure 1.1 shows the sketch of all the fission process steps: the initial nucleus in the ground state, the increase of the deformation up to the saddle point, after which the Coulomb repulsion prevails over the surface energy and fission takes place.
In this process also the viscosity plays a role, which is related to the time-scale of the process and, therefore, to the competition between the fission process and the other decay channels, we shall go into more detail in the section 1.1.4.

In spite of the first successes in the fission process description, the LDM cannot explain some basic properties of the actinides: their non-spherical ground states and their asymmetric mass division. It is necessary to introduce the shell effect in the fission

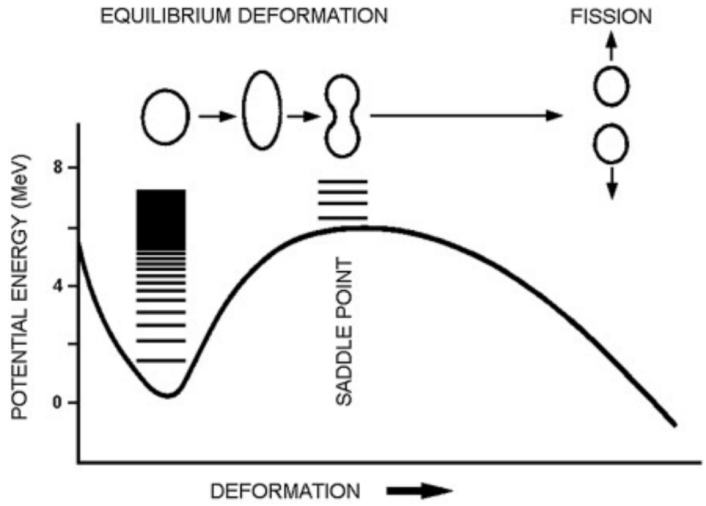

Figure 1.1: Variation of the energy of a deformed nucleus as a function of the distortion as sketched. When the two fragments are separated, the energy falls with increasing separation because of the decreasing Coulomb energy. An energy barrier must be crossed for fission to occur. Picture from ref. [10].

process explanation.

The overhaul of the fission model was necessary following the 1962 discovery of *fission isomers* by Polikanov and his colleagues [11]. It was postulated that nuclear isomers are a metastable nuclear excited state, in an intermediate potential well, with unusually short half-life for spontaneous fission. A complete understanding of the mechanism came in the mid-1960s, in the work by V. M. Strutinsky [12, 13] about the shell effects in the determination of nuclear masses and deformation energy. The LDM described well the nuclear properties that depend smoothly on the number of nucleons while, the shell model explained the nuclear properties that depend strongly on the arrangement of the outermost nucleons. This last effect is treated as a correction to the liquid drop model energy which contains the dominant surface and Coulomb effects. The total energy in this model is the sum of the energy given by the liquid drop model and the shell corrections δU, that takes into account the quantum-mechanical structure of the nucleus:

$$B = B_{LDM} + \delta U. \tag{1.5}$$

Although these effects are larger in the vicinity of *magic nuclei*, microscopic corrections to the LDM occur to some extent in all nuclei.

1.1.1 The fission barrier

The most drastic effect of shell structure occurs in the fission barrier itself. The Strutinsky approach leads to the conclusion that the potential energy as a function of the nuclear deformation has two minima, as it is shown in figure 1.2, giving the so-called double-humped barrier. The deformation variable should be understood as a measure of progress along the energetically most favorable path to fission. The first minimum contains the ground state and several excited levels, whereas the second one

explains the existence of spontaneously fissioning shape isomers. Following this model,

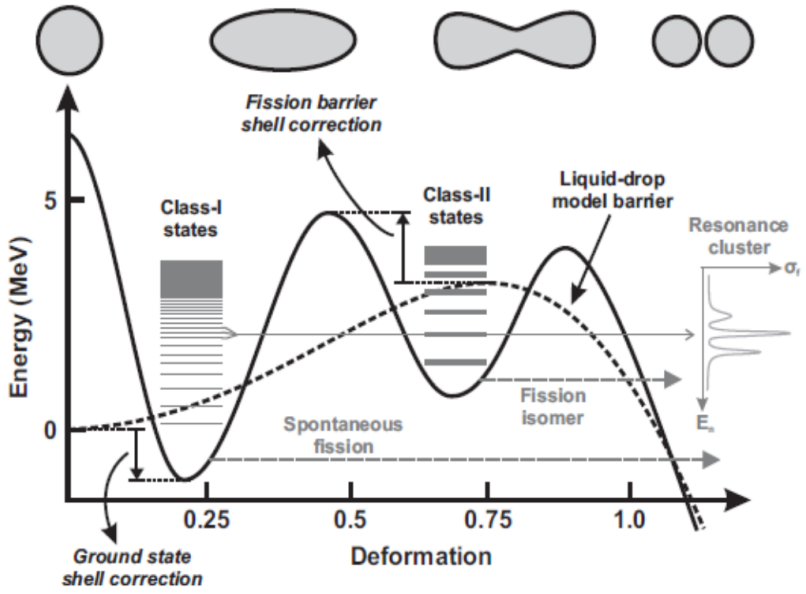

Figure 1.2: Schematic picture of the nuclear energy as a function of the deformation of a typical actinide nucleus. The dashed line shows the single barrier predicted by the LDM, while the solid line includes the corrections due to shell structure. The double-humped fission barrier can explain the existence of short-live fission isomers. They have a higher probability of fissioning compared with the ordinary ground state because they must penetrate a much thinner potential barrier.

when an actinide absorbs a nucleon and it is excited above its fission barrier, the most common result is prompt fission, but one cannot discard the possibility of radiative capture, that is, capture of the nucleon followed by γ-ray emission, leading the nucleus to a state in the first well. However, a third possibility is that the excited nucleus remains trapped in the second well in an excited isomeric state, which can either decay to the first minimum or fission spontaneously. The fission barrier in this case is much narrower than the barrier that the nucleus feels in the first well and this explains the much shorter fission half-life than the half-life of the ground state.

Another influence of the second potential well is on the structure of the resonances in fission cross section. The fission resonances, produced by an excited compound nucleus following neutron capture, are not always clustered in well-separated groups. This effect occurs because the second well is not quite as deep as the first. The density of the states of any nucleus depends on the excitation energy above the ground state: the higher we go above the ground state, the closer together are the states. States in the second well at the same energy as those in the first well are, on the average, further apart. This means that if the excitation energy is over the height of the barrier, the fissioning states are selected through the overlap in energy between the narrow closely spaced states in the first well, and the broader more widely spaced states in the second well. Therefore, effect is translated to the cross section and gives rise to resonance spacing of the order of eV.

1.1.2 Mass distribution of the fission fragments

Nuclear fission consists in the nucleus division into two fragments of comparable mass (primary fission fragments - FFs) together with one or more neutrons (prompt neutrons). More rarely, a light cluster, usually an α particle, is emitted together with the two heavy fragments in a direction perpendicular to the fission axis (ternary fission). The fission fragments as well as the neutrons evaporated from the fissioning nucleus are not uniquely determined: there is a distribution of masses of the two fragments to which the number of prompt neutrons emitted is linked. An example of the distribution of the probability for each fission product to occur is shown in figure 1.3(a). The distribution must be symmetric about the center: for every heavy fragment, there must corresponding light fragment; symmetrical fission corresponds to a minimum of the curve and it is less probable by a factor about 600 relative to the maximum yield. The mass asymmetry in fission fragment yield is observed to be qualitatively similar for most cases of fission, but some differences are observed with changes in mass of the fissionable isotope and excitation energy. The mass asymmetry is generally most

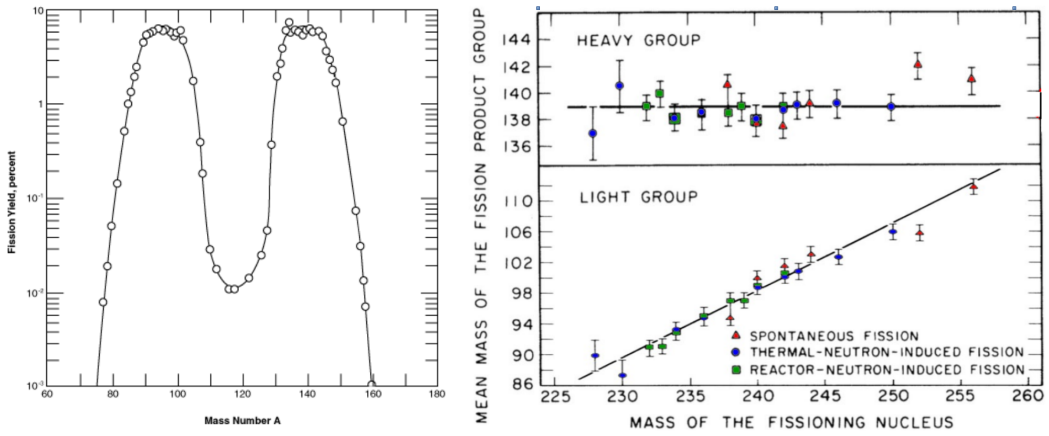

(a) (b)

Figure 1.3: Left: Mass distribution of fission fragments from thermal fission of ^{235}U [9]. Right: Dependence of average masses of heavy and light groups of fission fragments on mass of fissioning nucleus [14].

pronounced at low energies and the yield of symmetric products increases with the energy of the stimulating particle (mainly neutrons, protons, α, photons).
The variation of the mass of fragments with increasing mass of the fissioning nucleus is more enhanced for the lighter fragment than for the heavier one. This behavior is illustrated in figure 1.3(b), which shows the average masses of the light and heavy fragments versus the mass of fissioning nucleus: the average mass of the heavy fragment stays nearly constant, while the average mass of the lighter fragment increase linearly as A increases. The explanation for these observed effects in the mass distribution of the FFs lies in the shell model, in particular it is related to the *magic numbers*. The heavy fragment (in the A$\sim$139 region) is bounded in terms of nuclear structure by closed nucleon shells at 82 and 50 for neutrons and protons, respectively. Just at the lower

edge of the heavy fragment mass distribution there is a double magic nucleus. This exceptionally stable configuration determines the low edge of the mass distribution of the heavier fragment. Consequently, a variation in mass of the parent isotope is often observed more significantly as a change in mass of the light fragment.

Another interesting behavior of the mass distribution is that asymmetric fission tends to symmetric fission when the projectile energy increases, therefore, when the nucleus has a large excitation energy. This is due to the fact that the high level density has to include an average over a large number of states and not just a few isolated ones. This behavior is typical of the highly fissionable nuclei, such as those of a very large mass; figure 1.4 is shows an example for the case of ^{238}U bombarded with protons from 10 to 150 MeV. At 150 MeV the minimum in the symmetric fission disappears, giving place to a plateau where the production of A=100-130 fragments are equally probable.

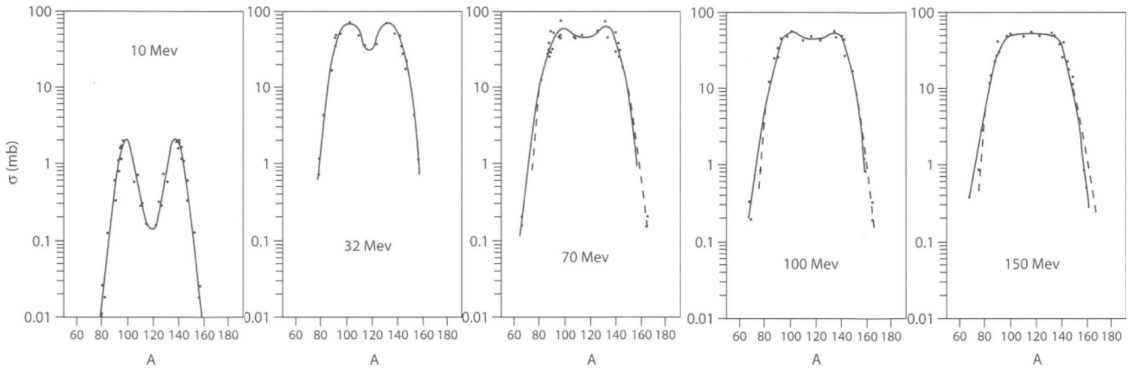

Figure 1.4: Cross section for the production of a mass number A fragment in the ^{238}U fission induced by protons with several different energies [15].

Although a large amount of experimental data on the mass distribution has been available for a long time [16, 17], no comprehensive theory yet exists that can account for all the observations.

1.1.3 Fission fragment angular distribution

Non isotropic angular distribution of fission fragments was observed for the first time in in the early 1950s in photofission of ^{232}Th [18, 19], where fission fragments emitted preferentially at 90° with respect to the γ beam direction were found. Later experiments found similar results in neutron-induced fission reactions [20, 21]. It is now known from Bohr's 1956 theory [22] that, due to the population of only a few discrete energy levels of the fissioning nucleus at the saddle point, fission fragment emission at intermediate energies is anisotropic. Bohr first suggested that for excitation energies near the barrier the nucleus is thermodynamically cold as most energy is stored in deformation energy. The concept of near-barrier fission through discrete low-lying transition states provides the framework in which the angular distributions depend on the quantum numbers of the discrete transition states involved. Halpern and Strutinsky introduced a statistical treatment that generalizes the energy dependence of fragment angular distributions to moderate and high excitation energies above the fission barrier [23].

One of the characteristic properties of the transition nucleus in the statistical saddle point model is its thermodynamical temperature, related to the energy available to populate different level states. In a simplified picture the fissioning nucleus exhibits anisotropic emission when it is thermodynamically cold and only very few energy levels are populated. If the available energy increases, more states are populated and the emission becomes more isotropic.

The standard theory (more details can be found in ref. [24]) is based on the model of transition states at the saddle point of the axially symmetric fissioning nucleus. When a nucleus is deformed with an axial symmetry it can be demonstrated that its total spin $\vec{J}$ is characterized by three good quantum number, namely J for its modulus, its projection M along an arbitrary fixed axis (that is usually taking in the beam direction), but also its projection K along the moving symmetry axis; so that the spin is defined by the triplet (J,M ,K). M and J are constants of the motion and are conserved in the entire fission process, because of the conservation of the total angular momentum. In the process to fission, the nucleus can suffer vibrations and changes in shape, redistributing its energy and angular momentum so that the K value of the transition nucleus is unrelated to the initial K values of the compound nucleus. The directional dependence of fission fragments resulting from a transition state with quantum numbers J, K and M is uniquely determined; therefore, K is a good quantum number after reaching the transition state deformation. Based on these assumptions the probability of emitting fission fragments from a transition state with quantum number J, M and K at an angle ϑ is:

$$P^{J}_{M,K}(\vartheta) = \left[\frac{(2J+1)}{4\pi R^2}\right] \mid d^{J}_{M,K}(\vartheta) \mid^2 2\pi R^2 \, sin\vartheta \, d\vartheta \tag{1.6}$$

where the angle ϑ represents the angle between the symmetry axis of the fissioning nucleus and the space-fixed axis, which is usually taken as the beam direction for induced fission.
The rotation matrix $d^{J}_{M,K}(\vartheta)$, introduced by Wigner [25], is given by:

$$\begin{aligned} d^{J}_{M,K}(\vartheta) = {} & [(J+M)!(J-M)!(J+K)!(J-K)!]^{1/2} \times \\ & \times \sum_{X} (-1)^X \frac{[sin(\vartheta/2)]^{K-M+2X} [cos(\vartheta/2)]^{2J-K+M-2X}}{(J-K-X)!\,(J+M-X)!\,(X+K-M)!\,X!} \end{aligned} \tag{1.7}$$

where the sum is over X = 0,1,2,3..., and contains all terms in which no negative value appears in the denominator for any of the quantities in parentheses. The angular distribution for the fission fragments is uniquely defined by the rotational wave function and it is obtained by dividing the probability of emitting fission fragments at an angle ϑ (equation 1.6) by $sin\vartheta$:

$$W^{J}_{M,K}(\vartheta) = \left[\frac{(2J+1)}{2}\right] |d^{J}_{M,K}(\vartheta)|^2. \tag{1.8}$$

Several angular momenta are involved in a nucleon induced-fission reaction. The quantities $\vec{I_0}$, $\vec{s}$ and $\vec{S}$ are the target spin, projectile spin (= 1/2 for a neutron or proton) and channel spin (total spin of the compound nucleus) respectively. The channel spin $\vec{S}$ is defined by the relation:

$$\vec{S} = \vec{I_0} + \vec{s} \tag{1.9}$$

and the total angular momentum $\vec{J}$ is given by the sum of the channel spin $\vec{S}$ and the nucleus orbital angular momentum $\vec{l}$:

$$\vec{J} = \vec{S} + \vec{l}. \tag{1.10}$$

The density of levels in a transition nucleus with spin $\vec{J}$ and projection K on the nuclear symmetry axis can be approximated by a Gaussian distribution, centered around K=0, which is characterized by the variance K_0^2. The variance K_0^2 is given by $K_0^2 = \Im_{eff} T/\hbar$, $\Im_{eff}$ being the effective momentum of inertia and T the thermodynamic temperature of the fissioning nucleus.

The angular anisotropy of fission fragments is typically defined as the ratio of counts parallel to the beam to counts perpendicular to the beam, as a function of incident neutron energies, and it is expressed as:

$$A = \frac{W(0^\circ_{c.m.})}{W(90^\circ_{c.m.})} \approx 1 + \frac{\langle I^2 \rangle}{4K_0^2} \tag{1.11}$$

where $\langle I^2 \rangle$ is the mean square angular momentum of the compound nucleus. Angular distributions have been studied in the excitation region up to several tens of MeV for many targets and for a variety of projectiles, including neutrons, protons, deuterons, α particles and heavy ions; experimental observations show common features. Angular distributions are more peaked along the beam direction as the beam energy or the projectile mass is increased. The anisotropy increases by increasing the weight of high J states. On the other hand, the K distribution is characterized by K_0^2, which increases with the excitation energy (directly related to the thermodynamic temperature). Therefore, the anisotropy decreases as the value K_0^2 increases. The anisotropy decreases as the Z^2/A value of the target increases.

1.1.4 The fission process at intermediate energy

Nuclear reactions at intermediate or high energy of the projectile are well described as a two step process. In the first step, the incident particle interacts with one nucleon or a cluster of nucleons inside the nucleus, and then the energy transferred to these particles is redistributed to other nucleons by an intranuclear cascade process. During this step of the nuclear reaction, some particles and/or light clusters (such as deuterons, tritons and alphas) may escape from the nucleus, through a pre-equilibrium process, thus reducing the total energy of the compound system. In the second step, the nuclear evaporation, the excitation energy is distributed among all the remaining nucleons, i.e., the residual nucleus reaches a thermodynamical equilibrium. At this step the nucleus

may undergo fission: it is the competition between particle evaporation and fission processes that determines the particle multiplicities and the fissility of the nuclear remnant.

During the last decade, great interest has been paid to dynamic effects in the fission process, i.e., effects which are not taken into account in the statistical description of the process. An appropriate way to account for fission dynamics is to consider fission as a diffusion process over the fission barrier. In the framework of such an approach, suggested long ago by Kramers [26], the fission width [1], which measure the fission probability, depends on a dissipation coefficient, which characterizes the viscosity of nuclear matter. In addition, the formation of such a large-amplitude collective motion as the fission process requires a finite time, and during that time fission will be suppressed, while competing decay channels are active. Calculations of Grange and Weidenmüller [27] show that these effects grow rapidly with increasing excitation energy of the fissioning nucleus. Therefore these effects have to be necessarily taken into account for the description of nucleon-induced fission at intermediate and high energies.

The upper limit to the incident neutron energy in evaluated nuclear data libraries is traditionally set to 20 MeV, therefore the energy range from 20 MeV to 1 GeV is the interval in which neutron-induced fission deserves further investigation. From the theoretical point of view, it is useful to divide this wide range in two sub-intervals: from few to 200 MeV, named intermediate-low energy region; and from 200 MeV to 1 GeV is the intermediate-high energy region. In the first subgroup it is possible to perform fission calculations using quantum models; instead above 200 MeV calculations are performed only with semi-classical models that use mainly Monte Carlo methods to simulate the fission reaction.

Intermediate-low energy fission

In the energy range up to 200 MeV nuclear structure effects are prominent, hence their description requires more detailed consideration of competitive reaction mechanisms.

The pre-equilibrium phase is commonly described by a semi-classical exciton model (e.g., reference [28]) or by a quantum-mechanical multi-step compound (e.g., reference [29, 30]) plus direct model, while the compound nucleus decay of the remnant is treated within the framework of the statistical Hauser-Feshbach formalism [31].

For heavy nuclei, the neutron emission is a dominant reaction that competes with nuclear fission. The multiple-chance fission (i.e. fission preceded by neutron evaporation) becomes possible as the excitation energy of the compound nucleus exceeds

[1] The fission width, Γ_f, is related to the probability to decay via fission given by:

$$P_f = P_{CN}\frac{\Gamma_f}{\Gamma} \tag{1.12}$$

where P_{CN} corresponds to the probability of formation of the compound nucleus and Γ is the sum of the reaction widths of all the possible decay modes. The total width Γ is correlated to its lifetime τ by the Heisenberg uncertainty principle $\Gamma\tau \sim \hbar$.

the sum of the fission barrier plus the neutron binding energy. So, the reaction (n,nf) is called *second-chance fission*; as the neutron energy increases, the thresholds of the *third-chance fission* (n,2nf) and *fourth-chance fission* (n,3nf) reactions are opened. In general, the fission cross section above the threshold presents a step-like structure, due to the superposition of the different (n,xnf) reactions, as shown in figure 1.5. From the same figure one can see that there is a strong correlation between the opening of the thresholds of different fission chances and the angular distribution of the emitted fragments: the angular anisotropy coefficient exhibits also a multiple chance structure similar to the one exhibited by the fission cross section.

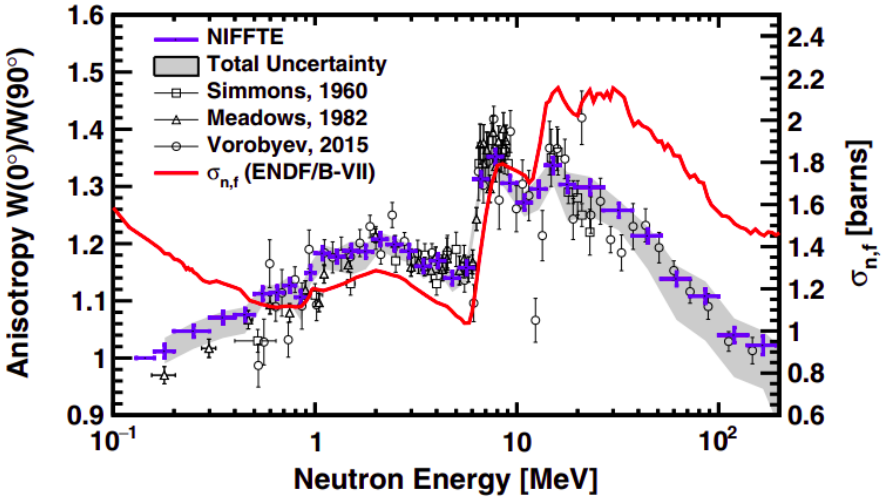

Figure 1.5: The fission fragment anisotropy as a function of neutron energy for the neutron-induced fission of ^{235}U from 0.18 to 200 MeV, in light-blue, compared to the most comprehensive data sets available in the literature [32, 33, 34] and the neutron-induced fission cross section of ^{235}U, from ENDF/B-VII [35]. The multiple-chance structure is observed both in fission cross section and in the anisotropy parameter. Figure from [36].

Intermediate-high energy fission

At incident energies above 200 MeV, the projectile sees the target as a collection of individual nucleons. When the de Broglie wavelength of relative motion of projectile and target nucleons, $\lambda = \hbar/p$, satisfies the inequalities

$$\lambda \ll r < d \tag{1.13}$$

with r the range of the nuclear forces and d the average distance of neighbouring nucleons, it is reasonable to describe the propagation of the particle as a succession of binary collisions with the target nucleons, which can be ejected from the nucleus or can eject other nucleons in turn, thus giving rise to a fast intranuclear cascade. The secondary fast particles, usually carry the major part of the incident energy away from the target. The remaining part of the incident energy is left in the residual nuclei in the form of the holes in the Fermi-sea and is rapidly thermalized, the particle-hole configuration is the starting point for the preequilibrium stage of the reaction. Thus

by the end of the initial fast stage we have a number of excited nuclides, which cool down at the next evaporation stage by the competing processes of fission or particle evaporation. When the excitation energy per nucleon increases beyond about 3 MeV, the multifragmentation process begins to be a competitive process, with evaporation and fission still present. Let us, mention that, above 300 MeV, the incident neutron has energy enough to produce barionic and mesonic resonances in the target nucleus. The first of such a process is the creation of Δ barions, giving rise to new de-excitation channels including π emission and subsequent charge interchange.
As long as the participating nucleons are fast enough, their motion lends itself to a classical description, characteristic of the cascade stage, described, for instance, by the Cascade-Exciton Model (CEM), originally formulated at Dubna [37].

The role of viscosity

The evolution from low-energy (evaporation and fission) towards high-energy decay processes (fragmentation and vaporization) suggests that such a transition has indeed been observed in nuclear collisions in the nucleonic regime. However, the obvious question here is whether one can relate such phenomena with the thermodynamical properties of nuclear matter. Therefore, the measurement of the relevant variables turning the transition from a liquid-like state to a gas-like state such as the nuclear temperature, the excitation energy and the volume in which the system decays represents a formidable challenge.

Nuclear fission is a dynamical process, which needs time to develop, in fact it is a highly dissipative and a slow process. The reason is that such processes lead to a large deformation of the system during which friction has time to act and possibly to play a crucial role. In a macroscopic picture of the nucleus, Grangé and Weidenmüller [38], following the pioneering work of Kramers, treated fission as a diffusive process over the potential barrier, which is governed by nuclear viscosity. The clearest evidence of the effects is that the light particles emitted during the time needed by the nucleus to reach the scission configuration, and in particular the pre-scission ones. According to this approach, in case of large values for the viscosity of nuclear matter, the motion of the fission degree of freedom would be slowed down and the resulting stochastic force could bring nuclei back inside the saddle point with a non-negligible probability. Grangé and Weidenmüller solved the time-dependent diffusion problem introducing the transient time or time required by the fissioning system to attain a quasi-stationary fission decay rate. During this time, fission is suppressed, while other decay channels, mostly neutron emission, are open. These ideas were used to interpret the large pre-scission neutron emission observed in fusion-fission reactions [39, 40]. Therefore, the increased particle emission probability at the earliest times with the increasing of the projectile energy, slows down the collective motion by cooling down the system and modifies the fission barrier of the fissioning nucleus influencing the further evolution of the nucleus

and, in particular, reducing its fission probability in a considerable way.
The absolute value of the friction parameter β describing the viscosity of nuclear matter, and its possible dependencies on temperature and deformation, are being investigated since the 80's using different observables and reaction mechanisms (for a review see [41] and [42]). Experimental evidences on how nuclear viscosity affects the compound fission process, as well as the competition with the fusion-evaporation process, has come from the observation of the evolution of many observables, in addition to cross-sections, such as pre-scission multiplicities of neutrons, charged particles and γ-rays with the excitation energy and time distribution of the fission events, which typically extends over 3 orders of magnitude (from 10^{-16} to 10^{-19} s) [43].
The nature of viscosity represents one of the major open questions in fission dynamics. The energy dissipation, i.e. the conversion from the collective to intrinsic motion, is a phenomenon related to the motion of nucleons inside the system in route towards fission.

Neutron and proton induced fission

During the last decades, a new generation of intermediate energy neutron sources has become available, thus making it possible to start systematic measurements of (n,f) cross sections in the energy region above 20 MeV and to compare them with (p,f) cross sections. Only in 1994 the first comparison of the (p,f) and (n,f) cross sections (as well as for the (γ, f) cross section) of the nuclei from ^{232}Th to ^{239}Pu was carried out for the incident particle energy up to 100 MeV [44]. In following works (for instance ref. [45, 46, 47]) the range of the comparison of the experimental data of the neutron- and proton-induced fission has been widened to lighter nuclei, down to ^{197}Au. It has been observed that the σ_{pf}/σ_{nf} ratio depends strongly on the incident nucleon energy and increases with the decrease of the fissility parameter Z^2/A of the target nuclei.
At very low energy, the reaction cross section for incident protons is decreased by the Coulomb repulsion, which leads to a global sharp decrease below the Coulomb barrier. Increasing the projectile energy well above the proton Coulomb barrier, where the Coulomb factor, $1 - V/E$ (where V is the potential energy), is close to unity, the difference between the two cross section becomes smaller. It is experimentally known [48] that at the lower extreme of the intermediate energy range ($\sim$100 - 150 MeV) the (n,f) cross section is systematically lower than the (p,f) cross section for a given target nucleus. The difference tends to decrease with increasing incident energy, so that at 1 GeV the behavior of protons and neutrons is expected to be quite similar and the corresponding fission cross sections of the same order.
The differences between the proton- and neutron-induced fission cross section are probably determined by the differences in the inelastic nucleon-nucleus interactions for incident nucleons and target nuclei with different isospins. Therefore, measurements for different isotopes allow the investigation of the role of the isospin both for the incident particle and the target nuclei (so-called *double isospin effect*). But, until now, it is a difficult effect to evaluate because fission induced by intermediate-energy neutrons has

been studied much less extensively than proton induced fission, and the available (n,f) cross section data sets are often discrepant.

Nevertheless a large number of measurements have been performed for fission fragment detection since the discovery of fission, yet, neither experimental nor theoretical studies of fission are conclusive enough to fully understand the process and the dynamics involved. In particular, the (n,f) cross section at intermediate energies is, for most nuclei, unmeasured and cannot be predicted with satisfying accuracy. Thereby, the study of the fission of highly excited nuclei remains a topic of great interest. There are several open questions as how the mass-yield, neutron emission, γ-ray emission, isomeric yields and independent mass-chain yields change depending on the kind of the incoming particle. Moreover, there is lively interest also in the study of the energy dependence, the viscosity of hot nuclear matter and the overall properties of hot systems with thermal excitation energies larger than several tens of MeV.

1.2 Applications of fission reaction data

Data on neutron induced fission cross sections at intermediate energy are extremely important for nuclear theory: to understand the connection between collective and single particle degrees of freedom in nuclei, which reflects the dynamic effects of the nuclear fission process (see, e.g., [49]). In addition, these fission reaction data sets are used in important applications such as energy production with accelerator driven systems, radioactive waste transmutation, in nuclear astrophysics, radiation shield design for accelerators and the dose received by aircrew. All these applications require proton and neutron fission cross sections to be determined with high accuracy in a wide energy range, which are nowadays scarce, mainly because of the lack of suitable neutron sources.

1.2.1 Reactor technology

On the basis of stated plans and policies around the world, the International Energy Agency (IEA) [50] forecasts that the global energy needs will continue to rise by 1% per year until 2040, adding a demand equivalent to China's current total [51]. This growth is driven by a rising population, which, according to UN projections [52], will reach 9 billion people by 2040, and an expanding economy, with global GDP[2] increasing by 3.4% a year. At present, over 80% of the world's energy is produced by combustion of fossil fuels (oil, coal and natural gas), which are responsible for the release of CO_2, inevitable in any combustion of fossil fuels, and other pollutant gases in the atmosphere. Moreover, they are considered the main causes of the greenhouse effect, global warming, climate change and biodiversity harm.
The potential effects of this increase are controversial, and depending on the atmospheric models; the various scenarios, for a period until 2100, foresee an increase in

[2]GDP is the Gross Domestic Product

global temperature from (1.0 ± 0.4)°C to (3.7 ± 0.7)°C compared to today's temperature [53].
Several energy mix scenarios have been studied to improve the sustainability of energy production, which has three important and often conflicting goals:

Energy Security: includes the effective management of primary energy supply from domestic and external sources, the reliability of energy infrastructure and the ability of energy providers to meet current and future demand.

Energy Equity: means accessibility and affordability of energy supply across the population.

Energy Sustainability: deals with the achievement of supply and demand with an improvement in energy efficiencies, and with the development of energy supply from renewable and other low-carbon sources.

Renewable power generation, which benefits from a strong community support, certainly plays a key role in reducing CO_2 emissions. With the present technological development, the contribution of renewable energy production is expected to increase rapidly in the future, however it seems unlike that it will be able to cover the entire energy demand. The main problems are the fact that renewable energy sources have a relatively low efficiency [54] and needs to store the energy produced [56, 57, 58]. Indeed, the link between the production possibilities and the base load electricity demand, as sun, wind, tides and waves cannot be controlled to directly provide continuous base load power, or peak load power when it is needed, this requiring the use of other controllable sources and leading to an increase in the cost of energy production. Therefore, renewable energy sources (including hydropower) do not represent an extensive replacement, capable of substituting fossil fuels in the medium term.
Nuclear energy is one of the possible options to mitigate the above mentioned issue in the forthcoming decades, it features a strongly reduced CO_2 emission and it can be developed on a large scale. There are, however, three major concerns regarding the use of nuclear energy: the safety of the operation of nuclear power plants; the efficient management of nuclear waste accumulated over the past sixty years of power plant operation; the proliferation of nuclear material and its potential use in military or terrorist related activities. However, all these three issues could be effectively addressed with the development of low operation risk nuclear systems with reduced safety margins and nuclear fuel recycling capabilities.

Both the Generation-IV reactors and the transmutation of nuclear waste are part of this framework.
The concept of the new reactors is based on a more efficient burn-up capability and on the use of actinides, including those which may be recovered from ordinary reactor used fuel [59]. The nuclear waste, that is planned to be used, consists mainly of minor actinides such as plutonium, neptunium, americium and curium isotopes, which constitute a considerable fraction of the high-radiotoxicity component of nuclear waste. These elements require a fast neutron spectrum to match the fission cross-sections and transmute them into nuclides with lower half-life. The fast neutron environment mini-

mizes neutron capture reactions and maximizes fissions in actinides, which means less production of long-lived nuclides in radioactive waste.

On the other side Partitioning and Transmutations (P&T) technologies have a great impact on a significant reduction of risk and simplification of the final storage conditions. In fact, the successful implementation of these methods, would eliminate the need for nuclear waste storage on a geologic time scale. [60]. The transmutation is possible using a chemical process, isolating the different elements (partitioning) and designing a nuclear device capable of burning a minor actinide enriched fuel (transmutation) in such a way that the volume and radiotoxicity of the high-activity, long-lived waste is reduced. Transmutation can change the nuclear properties drastically. For transuranic elements, key processes of waste transmutation are fission reactions, as:

$$n + {}^{239}\mathrm{Pu}\,(2.44 \times 10^4\ \mathrm{y}) \xrightarrow{\text{fission}} {}^{134}\mathrm{Cs}\,(2\ \mathrm{y}) + {}^{104}\mathrm{Ru}\,(\text{stable}) + 2n + 200\ \mathrm{MeV} \tag{1.14}$$

and for fission fragments are capture processes, as:

$$n + {}^{99}\mathrm{Tc}\,(2.11 \times 10^5\ \mathrm{y}) \xrightarrow{\text{capture}} {}^{100}\mathrm{Tc} \xrightarrow{\beta\ (16\ \mathrm{s})} {}^{100}\mathrm{Ru}\,(\text{stable}) \tag{1.15}$$

where the half-life of each isotope is given in parenthesis. These reactions require a nuclear source with a fast or thermal neutron spectrum depending on the reaction that should be exploited: fast neutron for actinides for which the most effective process is fission, while a thermal spectrum is necessary for fission fragments for which the transmutation proceeds through capture reaction.
An alternative solution, particularly suitable for actinides, is to use an Accelerator Driven System (ADS) [61, 62]. The ADS concepts have been proposed and pushed by several scientists in the mid-1990's including Rubbia and collaborators, for the design of a nuclear reactor based on the Th-U fuel cycle, the so-called Energy Amplifier [63], and Venneri [64] and collaborators, who studied a more general use of fast and thermal neutrons as burners of fission products. The basic idea of ADS is to feed a subcritical reactor core driven by extra neutrons coming from a spallation target irradiated by an energetic high-intensity ion beam. A beam of high energy (∼1 - 2 GeV) and intensity (20 - 100 mA) is required to produce the amount of required neutrons, which could have a flux a few orders of magnitude larger than in conventional power reactors. In such a system the neutron spectrum is stretched from thermal energy up to the energy of the incident charged particles, with a peak at an energy of a few MeV. The advantage of accelerator-driven transmutation systems over other related concepts is that it allows the incineration of long-lived minor actinides that are difficult to use as fuel in facilities based on self-supporting chain reactions. Another advantage of ADS is that the associated reactor can be operated in a subcritical mode, which improves the inherent safety of the system. The fission channel contributes to the radioactivity produced in the target, as well as to the chemical and radiological toxicity of the reaction products. The Belgian Nuclear Research Centre (SCK.CEN) is working on the construction of the first prototype of multi-purpose hybrid nuclear research reactor designed as an

ADS, MYRRHA (Hybrid Multipurpose Research Reactor for High Technology Applications) [65]. It is conceived as a flexible fast spectrum irradiation facility able to work in both sub-critical and critical mode. The final design consists of a proton accelerator delivering a 600 MeV proton beam to a liquid lead-bismuth spallation target that in turn couples to a Pb-Bi cooled fast nuclear core. The maximum output of the reactor will be of 100 MW_{th}. MYRRHA is expected to become gradually operational as of 2027 and it will demonstrate the ADS concept intended for the efficient treatment of the high level nuclear waste through partitioning & transmutation.

One of the prerequisites for computational modeling of Generation-IV nuclear power plants and of ADS is the availability of evaluated nuclear data for the most important neutron-induced reactions involved within a wide range of incident energy. In addition, the design of the new reactors relies strongly on the knowledge of the formation cross sections of residual nuclei produced in such reactions. The experimental nuclear data and the predictive power of available nuclear reaction models and codes available with respect to the description of the fission process are not good enough at present for new applications in the field of emerging nuclear technologies. Sensitivity studies performed by means of Monte Carlo simulations indicate that for most long-lived fission fragments and minor actinides, the present uncertainties are much larger than needed for the reliable design and safe operation of advanced nuclear reactors [66]. Therefore it is necessary to improve the current knowledge of capture and fission cross-sections data for a long list of fertile and fissile isotopes.

1.2.2 Nuclear Astrophysics

The dominant mechanisms, that could potentially give rise to the formation of the A>60 stable nuclei observed in nature, are the so-called rapid neutron-capture process, or r-process [67], and the slow neutron-capture process, s-process [68]. The s-process occurs inside massive stars at relatively low neutron densities, where neutron capture times are much longer than typical β-decay half-lives. Thereby, the s-process reaction path follows the stability valley and involves mostly stable isotopes. On the contrary, the r-process occurs with very high temperature and neutron density; with these physical conditions it becomes possible that a nucleus absorbs a neutron before it can decay. The r-process reaction path starts into the neutron-rich region of the nuclide chart and then it is gradually shifted towards the valley of stability. The sites of the r-process have not been completely identified yet; the explosive scenarios such as the stellar collapses are potential conditions where the production of neutrons is large enough to give rise to a successful r-process. The core-collapse supernovae (SNe) [69], the neutron stars (SN) environments, with their high-temperatures, and the decompression of cold neutronized matter from violent collisions of binary NSs or NSs with companion black holes [70, 71] are all good candidates, which satisfy the extreme conditions required for stronger r-processing. Therefore, the recent multi-messenger observation, by means of gravitational waves, γ-ray burst and other electromagnetic radiation, of the neutron

star merger event GW170817 [72] has triggered a renewed interest in the r-process nucleosynthesis.

In a r-process scenario the number of free neutrons per seed nucleus reach a few hundreds, leading to the production of heavy or even super-heavy nuclei. With such a neutron richness (typically $N_n \simeq 10^{33-35}$ cm^{-3} at the drip density), the heaviest and neutron-rich nuclei, which are far from the valley of stability are produced in terms of milliseconds. At this point, for nuclei with $Z \geq 103$, neutron-induced as well as spontaneous fission becomes efficient prohibiting the formation of super-heavy nuclei and recycling the heavy material into lighter fragments which will restart capturing the free neutrons. This process, referred to as *fission recycling* [73, 74], can take place two to three times before the neutrons are exhausted. Indeed after several hundred of ms, the density has dropped by a few orders of magnitude and the neutron density experiences a dramatic fall-off. When neutrons get exhausted by captures, the nuclear flow is dominated by β-decays back to the beta stability valley.

The fission recycling plays a fundamental role by shaping the final r-abundance distribution at the end of the neutron irradiation: it is found that the $A \sim 278$ fissioning nuclei, are main progenitors of the $110 \leq A \leq 170$ nuclei. The effect is illustrated in figure 1.6, that shows the final abundances resulting from an expanding material that experiences r-process nucleosynthesis. The calculations have been performed with the SKYNET code [75], with a reasonable value of the electron fraction Y_e of 0.1 (such value is representative of neutron-rich matter, as the one dynamically ejected from a neutron star mergers event, NSM). Compared with the observed solar system r-process

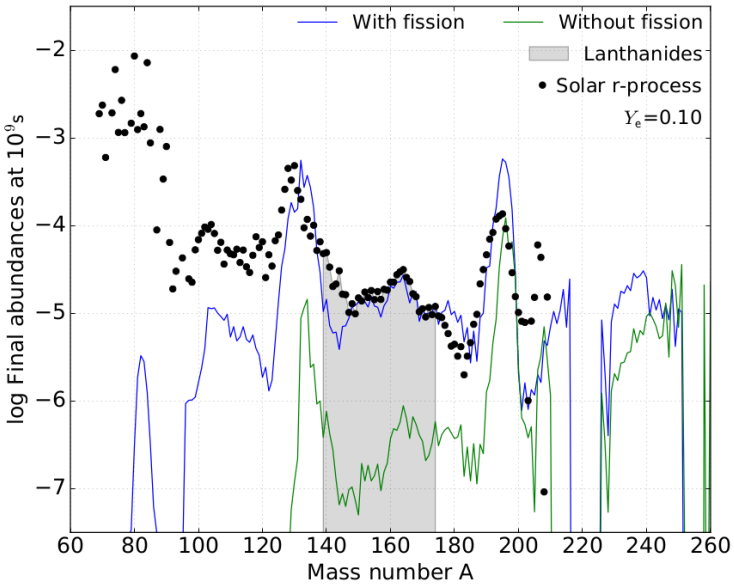

Figure 1.6: The r-process abundance in the solar system (solid symbols) are compared with SKYNET calculations performed with and without fission recycling. Fission processes are fundamental to reproduce the observed abundance distribution, in particular in the peak at A∼130 and in the lanthanides region (shaded area). Figure from [76].

abundances [77], the calculation clearly demonstrate the fundamental role of fission recycling, generally believed to be responsible for an important component of the ob-

served r-process heavy element abundances.

Neutron-induced, β-delayed and spontaneous fission reaction play a key role in the nucleosynthesis of heavy elements that takes place in the universe following explosive events like supernovae or neutron star mergers [78]. New data on fission on a variety of actinides are therefore essential, as the predictive power of current models can only be improved by comparison with a large set of experimental results.

1.2.3 Dosimetry applications

Another important application to be mentioned is the evaluation of the high energy neutron effect on the biological tissues and on the electronic devices. To study these effects, due to the absence of electric charge in neutrons, it is necessary to know the absolute value of a neutron-induced cross section with extreme precision to be taken as reference. About ten cross sections are considered as reference and the ^{235}U(n,f) is one of them, as we will see in the section 1.3. At energies higher than 200 MeV, the lack of experimental data implies that there are no well known cross sections, therefore, so to be able to evaluate the effects caused by high energy neutrons it is first necessary to overcome the absence of data sets.

Since the human activities involving the exposure to cosmic ray radiation have been increasing in the last years, mainly due to high altitude commercial flights, shuttle flights, medical and biological research on spatial stations, an accurate neutron dosimetry is required.

NASA and other space agencies have started since several years the study of the risk assessment for astronauts in view of long duration space missions like a travel to Mars. Experimental data about nuclear interactions between different kinds of space radiation and human tissues are of paramount importance in order to study the most suitable spacecraft shielding. There are three main sources of energetic particles in space: Solar Particle Events (SPE), Galactic Cosmic Rays (GCR) and the geomagnetically trapped particles. SPE are mainly due to protons emitted from the Sun during coronal mass ejections and solar flares: their energy spectrum can reach the GeV region. GCR consist of high energy nuclei (from hydrogen to iron) produced by supernovae in the Milky Way galaxy: protons and alpha particles account for $\approx 98\%$ and the overall energy spectrum of radioprotection interest ranges from MeV to TeV. The geomagnetically trapped particles consist of protons and electrons confined by the Earth magnetic field in two regions, called Van Allen belts. Trapped radiation originates from the interaction of GCR and solar particles with the Earth's magnetic field and the atmosphere. In this scenario the secondary neutrons make a significant contribution to the total absorbed dose received by space crews. The neutrons are produced by charged-particle interactions with materials e.g., spacecraft, planetary surface, Mars (or other planet) atmosphere, base structures, and even the astronauts themselves. The produced neutrons extend

in a very wide energy spectrum from thermal energy to more than 1 GeV [79]. There have been significant advances in experimental techniques to provide reasonably good measurements of the neutron flux below few MeV [80]; however, measurements above this energy remain an issue. Measurements of higher energy neutrons are essential to determine the crew radiation risk.

A similar reasoning can be done for aircraft crews which are exposed to elevated levels of cosmic radiation of galactic and solar origin and secondary radiation produced in the atmosphere, the aircraft structure and its contents. Following recommendations of the International Commission on Radiological Protection [81, 82], the European Union (EU) introduced a revised Basic Safety Standards Directive [83] which included exposure to natural sources of ionizing radiation, including cosmic radiation, as occupational exposure. The radiation field in aircraft at altitude is complex, it is composed by many types of ionizing radiation with energies ranging from thermal up to many GeV. The intensity of the different particles making up atmospheric cosmic radiation, their energy distribution, and their potential biological effect on aircraft occupants vary with altitude, the geomagnetic coordinates and time in the Sun's magnetic activity cycle. Here, at aviation altitudes, the neutron component of the secondary cosmic radiation contributes about half of the dose equivalent, but until recently it has been difficult to accurately calculate or measure the cosmic-ray neutron spectrum in the atmosphere to determine accurate dosimetry.

Summing up, knowledge on the neutron reaction mechanism as a function of incident energy is of great importance to design the spacecraft and to evaluate the damage and the biological effect in the human tissue. But not only, in fact this information is also needed to calculate the short-term and long-term radioactivity, building up radioactive ion-beam facilities, in the accelerator-driven systems and in general for the new generation of accelerators at high intensities, both for designing the shielding and estimating the residual activation of such devices.
The knowledge of the radiation damage and ionization due to neutron interaction is crucial also for electronics exposed to ionizing radiation: for istance satellites, nuclear reactors in power plants for sensors and control circuits, particle accelerators for control electronics particularly particle detector devices.

1.3 Standard cross sections

An essential point for the analysis of any high precision measurement of reaction cross-sections, is the point-wise knowledge is of the incident neutron flux as a function of energy. Since it is impossible to determine the beam neutron intensity by measuring the beam current as for the protons, the neutron flux detectors rely on detecting the secondary events produced by neutron-induced nuclear reactions for which the cross sections are very well known. These particular reactions have gained the status of *neutron standards cross section* [84] over the years, each within the specific energy

ranges over which they are well known. The evaluations were accepted internationally to ensure that the same standards are used worldwide in all major evaluation projects.

An idealized standard should have some characteristics [85] in particular, the ease of obtaining a high-purity sample; the reaction of interest should have few (or no) other open channels that could cause interference; in the standard energy region, the cross section should be large with a minimal amount of structure and finally the reaction should have an high Q-value. In addition, a reaction to be defined as standard, must have a huge available database to improve the accuracy and provide an uncertainty as small as possible. The reactions, to date, defined as standard are H(n,n), ^{6}Li(n,t), ^{10}B(n,$\alpha_1\gamma$), ^{10}B(n,α), C(n,n), Au(n,γ), ^{235}U(n,f) and ^{238}U(n,f). The database of each of these neutron cross-section standards contains more than 10000 experimental data points, which include different types of measurements, for instance the absolute cross sections, non-normalized cross sections (shape), the ratio between two standard cross sections.
There are several reasons to have many standard reactions; in particular the possibility of choosing the reaction which best suits the one to be measured. For instance, for neutron capture experiments it is appropriate to perform the measurement of the sample of interest and the standard one, without additional detectors or electronics; in this way only a simple beam monitor is required to relate the neutron beam intensity for the two runs. The situation is somewhat similar for fission measurements, a fission standard can be used in ratio measurements with convenient detectors such as double fission chambers. Then all detectors are essentially identical and require similar electronics.
There is also a need for many standards because none satisfies all the requirements for a standard for all neutron energies of interest. Indeed a neutron cross section is a strong function of the energy, and therefore each standard reaction can be defined as such only in a specific energy range.

As mentioned above, the standards have an important role in the definition of a data library. Not many cross-sections can be defined as absolute and almost all the cross sections, in a given data library, depend on the standard cross sections because they are measured relative to the cross-section standards, for the sake of normalization to absolute values. There is very large space for improvements to the standards since an improvement in a standard causes an improvement in every cross section relative to that standard.
The evaluation of the standard cross section is a process in constant evolution. Thus an IAEA Data Development Project, *Maintenance of the Neutron Cross Section Standards* has been initiated to maintain and guide the evaluation procedure both in terms of management and requests for new experimental measures that in the improvements in evaluation procedure to be used. Measurement programmes have continuously improved the database of the standards, and therefore it is important to re-evaluate these cross-sections taking into account new experimental data and improved evaluation techniques. This continuous updating occurs through close interactions with parallel or-

ganizations around the world, most notably with Europe (JEFF) [86], United States (ENDF/B) [87], Japan (JENDL) [88], Russia (BROND) [89], China (CENDL) [90] and with South Korea.
Organizations such as the International Atomic Energy Agency (IAEA) and the Organization for Economic Cooperation and Development (OECD)'s Nuclear Energy Agency (NEA) [91] provide valuable forums for exchanging developments in evaluation, measurement, and theory from laboratories across the world. The last evaluation of the neutron cross section standard reactions and their energy ranges, included in the Nuclear Energy Agency Nuclear Data Committee/International Nuclear Data Committee (NEANDC/INDC) Nuclear Standards File, are shown in table 1.1.

Table 1.1: Neutron cross section standards and their energy range, release 2017 [84].

Cross section	Energy range standard
H(n,n)	1 keV to 20 MeV
^{3}He(n,p)	0.0253 eV to 50 keV
^{6}Li(n,t)	0.0253 eV to 1 MeV
^{10}B(n,α_1 γ)	0.0253 eV to 1 MeV
^{10}B(n,α)	0.0253 eV to 1 MeV
C(n,n)	10 eV to 1.8 MeV
^{197}Au(n,γ)	0.0253 eV and 200 keV to 2.5 MeV
^{235}U(n,f)	0.0253 eV, 7.8 eV to 11 eV and 150 keV to 200 MeV
^{238}U(n,f)	2 MeV to 20 MeV

The database for the standards still needs improvement. For example, from the table it is evident that no cross section standard exists for incident energy region above 200 MeV, which is the present upper limit where absolute cross-sections exists. This led the IAEA to issue a request for the new measurements of the neutron induced fission cross sections, e.g. relative to n-p scattering, on uranium, bismuth, lead and plutonium, which have the highest priority in establishing neutron induced fission reaction standards above 200 MeV [92].

1.3.1 n-p scattering cross section

The n-p elastic scattering is considered the main reference reaction for fast neutrons and its cross section was evaluated first and independently of the other neutron standards, therefore this cross section was treated as absolute in the evaluation process [93]. This is to say that this well known reaction is considered the standard reference for many nuclear measurements [94].

The increasing quality of neutron-induced nuclear reaction measurements has required, over the years, a high-quality evaluation of the n-p cross section and its uncertainty.
From the quantum mechanical point of view, the differential cross section for elastic scattering is given in terms of the scattering amplitude (for a detailed treatment see [10]). Nucleon-nucleon scattering is the simplest two-body reaction and there are different nuclear interaction methods to solve this problem. Among them the most used is the method of partial waves in which the scattering amplitude is written as a sum of contributions from different angular momenta, given in term of phase shifts. A description of this interaction relies on semiphenomenological N-N potentials, for example the Bonn [95], Paris [96] and Nijmegen [97], which are based on meson exchange theory: long-range nuclear forces in the N-N system are generated primarily by the exchange of a virtual pion [98], short-range nuclear forces are reproduced by the exchange of heavier mesons, such as sigma, omega and rho.
The first independent evaluation for the hydrogen cross-section obtained from a charge independent R-matrix analysis of n-p and p-p experimental data below 30 MeV by Dodder and Hale [100], was included in the ENDF/B-VI library [99]. In the high energy region, in the 1991 the differential H(n,p) cross section was accepted by the NEANDC/INDC [101] as a primary standard cross section in the energy range from 20 MeV to 350 MeV; at higher energies the opening of the inelastic channel is no longer negligible. To that end the VL40 phase-shift energy-dependent solution obtained by Arndt and collaborators [102, 103] was adopted. This charge-independent evaluation has been carried out mainly on the basis of experimental information below 400 MeV, by fitting a number of parameters to the existing database, with the aid of the generalized least-squares method and the phase-shift data. A fit to the n-p database is impossible without the inclusion of polarization measurements and the p-p data to define the isovector component of the N-N interaction. VL40 provides an evaluation of the following quantities: total cross section, elastic scattering cross section (including angular distributions), inelastic (pion production) cross section (including angular distributions), capture cross section, covariance matrix of evaluated total cross section and photon production cross section. However, some measurements, performed in the late 1900s and early 2000s, of the hydrogen angular distribution turned out not to be consistent with the evaluation. Larger cross sections (of about 10%), measured at Uppsala University [104], of the differential cross section H(n,p) at 96 MeV and 162 MeV have a steeper angular shape in the backward direction, i.e. from 150° to 180°, compared with the evaluated shape given by the Arndt VL40 phase-shift solution. A similar disagreement was observed at the Paul Scherrer Institute (PSI) [105], in the energy range from 280 MeV to 580 MeV. In view of these and other new data sets, Arndt et al. [106, 107] updated the analysis of NN scattering evaluation, in which the energy range was extended up to 1.6 GeV and later on to 2.5 GeV.
Currently an extensive database exists for nucleon-nucleon scattering, with measurements from several laboratories worldwide. The full database includes all the available

unpolarized and polarized measurements which are accessible through the online Scattering Analysis Interactive Dial-in (SAID) facility [108]. The latest evolution of the SAID database is summarized in [109], at present it contains 12,693 points of n-p scattering and 24,916 for p-p scattering. These data sets make it possible a direct scattering amplitude reconstruction at a number of energies and angles. The latest phase shift solutions [109, 110] were generated using a new fit to the full database of the p-p and n-p elastic scattering data: up to 3 GeV for p-p data, and 1.3 GeV for n-p data. These new evaluations extend up to 3 GeV, in the laboratory reference frame, with an uncertainty of the order of 5% thanks to the systematic studies performed at Argonne National Laboratory (ANL), Cooler Synchrotron (COSY), Indiana University Cyclotron Facility (IUCF), Los Alamos Meson Physics Facility (LAMPF), Paul Scherrer Institute (PSI), Saclay Proton Synchrotron (SATURN), TRI University Meson Facility (TRIUMF), Triangle Universities Nuclear Laboratory (TUNL), and other facilities.

At present, there are several evaluations of the n-p cross sections below 20 MeV (the largest difference is only $\sim$0.5%); the most widely known are the ENDF/B and JENDL nuclear data files. The latest JENDL database, JENDL-4.0 [111], in the low energy range, below 20 MeV, accepted the evaluation from ENDF/B-VII.0 [35]. While in the JENDL/High Energy file [112] includes the n-p scattering cross section in the high energy region, up to 3 GeV, taken from the Arndt phase-shift evaluation.
In conclusion, σ_{np} is a standard cross section from 1 keV to 20 MeV; however, thanks to its extensive database and the accurate evaluations, it is considered a valid reference up to 3 GeV.

1.3.2 Fission reaction of ^{235}U at neutron energy above 20 MeV

The neutron induced fission of ^{235}U is one of the most important standard cross sections, with the largest amount of experimental data. The wide energy range in which the reaction is defined as reference together with the ease of use of the ^{235}U(n,f) cross-section makes this standard popular.
In the energy range between 20 MeV and 200 MeV the ^{235}U(n,f) reaction is extensively used as a reference for neutron flux evaluation in most of the fission cross sections measurements performed for various applications, already illustrated in the previous section 1.2 and ranging from the investigation of the biological effectiveness to the measurement of high-energy neutron cross sections of relevance for accelerator-driven nuclear systems or nuclear astrophysics. Despite its widespread use, however, the recommended ^{235}U(n,f) cross section data at energies above 20 MeV are based on a small set of measurements performed relative to the differential n-p scattering cross section, which is the primary standard for neutron measurements. The reliable data available, in that energy range, are from Nolte et al. [113] and Lisowski et al. [114] which are in mutual agreement within the error bars, as shown in figure 1.7. On the basis of the data of Lisowski et al. it was proposed by Carlson [115] to extend to 200 MeV the energy

range where the fission cross section on ^{235}U can be considered as a fission standard. Nonetheless, in the high-energy region, the uncertainties in all the data sets are rather large.

Above 200 MeV, the situation is even worse, because no data exist, and evaluations rely on theoretical estimates using the ^{235}U(p,f) reaction above 200 MeV as guidance. Until a few years ago, JENDL/HE [116] evaluations were thought to be the most reliable ones. But, recently, the International Atomic Energy Agency (Nuclear Data Section), released a new evaluation [92] which is, at high energy, inconsistent with JENDL/HE. Figure 1.7 shows a comparison of the JENDL/HE evaluation of the ^{235}U(n,f) cross section, the new IAEA evaluation [92] and the predictions based on intranuclear cascade model INCL++ [118] coupled to the de-excitation model GEMINI++ [119] from [117].

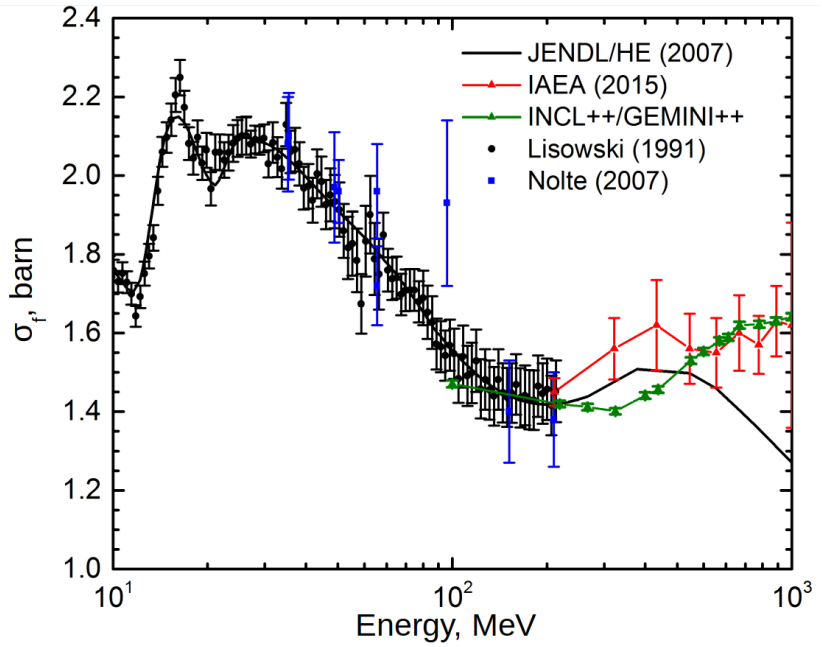

Figure 1.7: The ^{235}U(n,f) cross section from the JENDL/HE [116] and IAEA [92] evaluations, the experimental data [113, 114] measured relative to the n-p cross section and a new theoretical calculation [117] based on the intranuclear cascade model INCL++ [118] coupled to the de-excitation model GEMINI++ [119].

Hence, there is a clear and long-standing demand from the International Atomic Energy Agency (IAEA) to improve this situation of the neutron-induced fission reaction on ^{235}U for neutron energy between 20 MeV and 1 GeV.

Chapter 2

The n_TOF facility at CERN

Neutron-induced fission reactions play a crucial role in a variety of fields of fundamental and applied nuclear science. Contributions to nuclear data come from a plethora of experimental facilities based on different nuclear reactions capable of producing neutron beams. An exploitable method is the spallation mechanism, which is a remarkably powerful source of neutrons: in an infinite lead spallation target, one 20 GeV/c proton may produce as many as 600 neutrons. This method, being characterized by a white pulsed neutron source, requires to be flanked to the time-of-flight technique. Due to their different constructions and operation modes, pulsed neutron sources have different characteristics: the flight path length and the pulse width are related to the neutron energy resolution of a facility. In this chapter the focus is on the neutron time-of-flight facility n_TOF at CERN, whose characteristics make it particularly suited for high accuracy and precision measurements.

2.1 Neutron beam production

As already highlighted in chapter 1, nuclear data and, in particular, neutron-induced reactions are important for a number of research fields. In nuclear astrophysics, a related topic is the understanding of the formation of the nuclei present in the universe and the origin of the chemical elements. Most nuclei heavier than iron are produced by neutron capture in stellar nucleosynthesis [120, 121, 122, 123]. Neutron-induced reaction cross sections reveal also the nuclear level structure in the vicinity of the neutron binding energy of nuclei [124, 125]. In addition, neutron-induced reactions cross section are a key ingredient for the safety and criticality assessment of nuclear technology, including research on medical applications [126], radiation dosimetry, the transmutation of nuclear waste, accelerator-driven systems, future Generation IV reactor systems and nuclear fuel investigations [127, 128, 129].

Figure 2.1 shows the reaction cross sections for a typical heavy nucleus as a function of the energy and in the lower panel several neutron energy spectra relevant for stellar environments and applications (for instance fission and fusion) on the same energy scale. Cross sections can be measured either at specific energies using mono-energetic

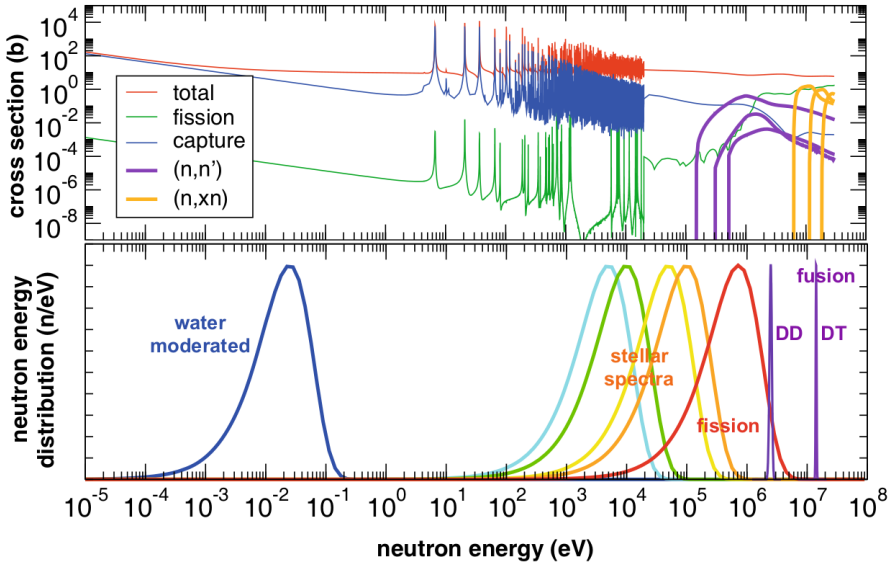

Figure 2.1: Neutron-induced reaction cross sections for a typical heavy nucleus as a function of the neutron kinetic energy (upper panel), together with characteristic neutron energy distributions present in stellar environments and in technological applications (lower panel). All distributions have been normalized to their maximum value. Figure from ref. [131].

neutron beams, or in the form of point-wise cross sections exploiting pulsed beams, or as average values on a particular neutron spectrum. Clearly, energy dependent cross-section measurements on a wide energy range, represent the most valuable option for nuclear data. These measurements can be performed only by means of a pulsed white neutron source that is optimised for the time-of-flight (TOF) method.
Pulsed neutron sources can be realized using electron- or proton-based accelerators. In particular, electron-based accelerators provide high-energy electrons, which produce Bremsstrahlung in a target made out of material with a high mass number (e.g. Ta, Hg, or U). As a consequence, neutrons are produced via photonuclear reaction. On the other hand, high-energy proton accelerators produce neutrons via spallation reactions induced on massive targets. In this case the advantage is the very high yield of neutrons per proton. In table 2.1 the most significative TOF facilities in the world are listed together with their main characteristics. It is worth noticing that some facilities have several measurement stations at different flight paths so that several experiments can be performed in parallel.

2.1.1 The spallation mechanism

The spallation reaction is a process in which a light projectile with energy from a few hundreds MeV to few GeV, interacts with a heavy nucleus causing the emission of a large number of hadrons or fragments. The spallation can be thought of as a two-stage process. In the first fast stage, which occurs in the first $\sim 10^{-22}$ s, the primary particle reacts with individual nucleons inside the nucleus. The reaction creates an intranu-

Table 2.1: Characteristics of the time-of-flight facilities used for cross-section measurements.

Facility	Type	Particle Energy, MeV	Target	Pulse width, ns	Frequency, Hz	Flight Path length, m
GELINA [132] (EC-JRC-IRMM, Belgium)	e^-	80 - 140	U	1	40 - 800	10 - 400
nELBE [133] (HZDR, Germany)	e^-	40	Pb	0.01	5×10^5	4
ORELA [134] (ORNL, USA)	e^-	140	Ta	2 - 30	1 - 1000	10 - 200
RPI [135] (Troy, NY, USA)	e^-	60	Ta	7 - 5000	500	10 - 250
J-PARC/MLF-ANNRI [136] (Tokai, Japan)	p	3×10^3	Hg	100	25	21, 28
LANSCE - MLNSC [137] (LANL, USA)	p	800	W	135	20	7 - 60
LANSCE - WNR [137] (LANL, USA)	p	800	W	0.2	13.9×10^3	8 - 90
CSNS [138] (Dongguan, China)	p	1.6×10^3	W	<400	25	2 - 19.5 - 30
n_TOF [130, 139] (CERN, Switzerland)	p	20×10^3	Pb	7	0.4	20 - 185

clear cascade of neutrons, protons, pions with the energy of a few hundreds MeV, while barionic and mesonic resonances are produced at energy of few GeV; all the particles generated are confined within the nucleus. Some particles, the ones with enough energy, escape from the nucleus, and are emitted mainly in the direction of the incident particle. The energy of the trapped particles is redistributed equally inside the nucleus, which is left in a highly excited state. In the second stage, about $\sim 10^{-16}$ s after the primary reaction, the nuclear de-excitation takes place and the excited nucleus relaxes by emitting light particles with energy less than 20 MeV. These particles (including neutrons) are emitted isotropically during the evaporation process.

The key ingredients for a spallation neutron source, such as n_TOF, are the projectile beam, the target and the moderator. All these elements play a basic role in the neutron yield, energy distribution spectrum and energy resolution:

- As a consequence of the neutron escape during the intranuclear cascade, the overall neutron spectrum extends to energies up to that of the incident particles. The energy and also the number of neutrons produced increase with increasing energy of the projectile.
- The choice of a specific geometry and material of the spallation target used as neutron source is a compromise among several parameters. First of all the number of the neutrons outgoing in a spallation process. In addition, the energy dependence of the neutron spectrum depends on the dimension and the material of the spallation target. In fact spallation can occur in every nucleus, and the neutron yield increases with the nuclear mass. The number of produced low-energy neutrons increase with the target dimension and reaches an asymptotic value. On

the other hand, the requirements on the dimension of the neutron beam and its halo at the detector station imply also strong constraints on the lateral size of the target.

- The energy spectrum of neutrons released in a spallation neutron sources can extend up to GeV; with 90% of the neutrons concentrated in the MeV region. Therefore, because of the importance of reactions induced by thermal and low-energy neutrons, a shift of several orders of magnitude is necessary. The neutron slowing down is accomplished by elastic collisions with the atoms of a *moderator* substance.

2.2 Time-of-flight method

The choice of spallation as production mechanism is natural when high energy proton or deuteron beam is available, considering the large number of neutrons produced for each incident primary particle [140]. In the spallation process the initially fast neutrons can be moderated and a white spectrum of neutrons, covering an energy range from meV to GeV. Therefore it is desirable to determine the energy of the neutrons arriving in the experimental area, and eventually interacting with the target.
The time-of-flight technique is based on the determination of the velocity v of a neutron from the time t it needs to travel a distance L. This time is derived from the difference between the instant T_s, in which the neutron reaches and interact with the sample, and the instant T_0 in witch the neutron is generated in the spallation target. At the n_TOF facility, for instance, the stop signal is obtained from the detection of the reaction products which are emitted in the neutron-induced reaction, while the T_0 represents the time the proton beam passes through a monitor placed just in front of the entrance of the spallation target. The observed TOF t_m becomes:

$$t_m = (T_s - T_0) + t_0, \tag{2.1}$$

where t_0 is a time offset. This time offset, which is mostly due to a difference in cable lengths, can be deduced from a measurement of the so-called γ-flash. Indeed when the protons hit the spallation target, γ-rays and ultrarelativistic particles are produced and, travelling along the beam line, reach the experimental area, eventually generating a very large signal in all detectors.
The time of flight t_m, defined in equation 2.1 is related to the velocity v of the neutron at the moment it leaves the target and enters the beam pipe by:

$$v = \frac{L}{t} = \frac{L}{t_m + (t_t + t_d)} \tag{2.2}$$

where L is the distance between the outer surface of the neutron-producing target and the sample placed in the experimental area or the front of the detector, t_t is the time difference between the moment that the neutron leaves the target and the moment of creation and t_d is the time difference between the time of the detection of the reaction

products and the moment the neutron enters the detector or the sample.
The neutron kinetic energy E_n can be expressed relativistically as:

$$E_n = E_{tot} - mc^2 \;=\; mc^2(\gamma - 1). \tag{2.3}$$

In this equation m is the rest mass of the neutron and γ represents the Lorentz factor:

$$\gamma = \frac{1}{\sqrt{1-(v/c)^2}}, \tag{2.4}$$

with c the speed of the light.

The energy resolution ΔE of a TOF spectrometer is related to the velocity resolution Δv:

$$\frac{\Delta E}{E} = (\gamma + 1)\gamma\frac{\Delta v}{v}. \tag{2.5}$$

It is worth noticing that at low velocities ($\gamma \approx 1$) the relative energy resolution is twice the relative velocity resolution. The velocity resolution is a combination of the resolution broadening due to the TOF t and distance L represented by Δt and ΔL respectively:

$$\frac{\Delta v}{v} = \sqrt{\left(\frac{\Delta t}{t}\right)^2 + \left(\frac{\Delta L}{L}\right)^2}. \tag{2.6}$$

The distance L can be determined by metric measurement with an uncertainty of less than 1 mm. The TOF corresponding to a distance L, its uncertainty, depends on t_m, t_t and t_d. As can be seen from equation 2.6 the longer the flight-path, the better is the accuracy on the measured velocity, and therefore the energy resolution of the spectrometer. A long flight-path, however, leads to a decrease in the neutron flux that goes as L^2. For this reason the length of baselines of the facilities are a compromise between a energy resolution and neutron flux.

2.2.1 Resolution function of a Time-of-Flight spectrometer

A common feature of neutron time-of-flight facilities is the fact that neutrons of a given energy do not leave the target-moderator assembly at the same time, thus making the time-to-energy relation non univocal. Several independent experimental components contribute to the fact that the time of flight t and the flight-path length L for a neutron energy E_n are not fixed values but merely distributions:

- the finite duration, in time, of the accelerator burst of primary beam (which affects T_0);
- the moderation time in the target-moderator assembly (t_t)
- the neutron transport in the sample (t_d)
- the time resolution of the detector and electronics (which affects T_s).

The convolution of these distribution is known as the resolution function $R_t(t_m, t_i)$. The first and the last contributions, listed above, can be represented by a simple analytical function, like a normal distribution with a width independent of neutron energy. The t_d component is typically negligible thanks to the small thickness of the samples. Therefore the broadening in time is dominated by the neutron transport in the target-moderator assembly, which is non-Gaussian and in addition highly asymmetric. Consequently, resolution functions strongly depends on the physics properties of the target-moderator assembly (dimensions and materials). The distribution of this component cannot be experimentally measured, however, it can be deduced from Monte Carlo simulations or approximated by analytical expressions.
The effect of this spread in time is twofold: first of all, it broadens together with the Doppler effect the observed widths of the resonances. Secondly, experimental data result with an energy shift, due to the additional time spent by neutrons within the target. Therefore the resolution function needs to be used for a precise time-to-energy conversion. As schematically shown in figure 2.2, a neutron with real energy E_n cor-

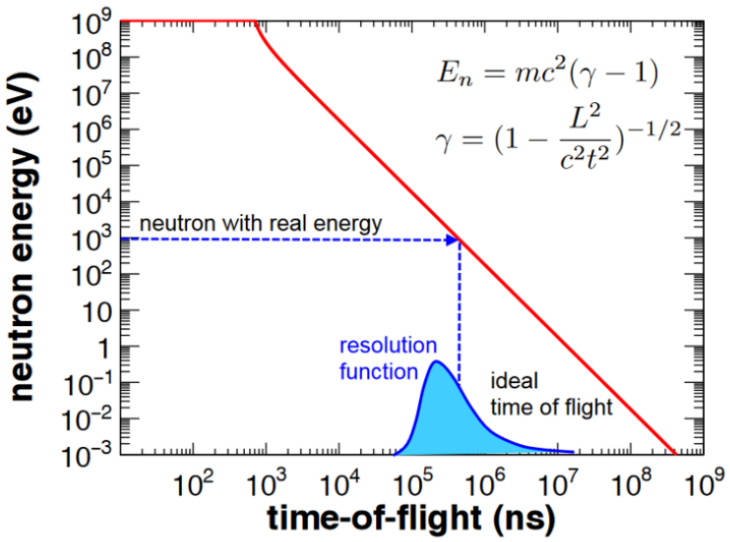

Figure 2.2: In red, the ideal relation between the energy and the time of flight of a neutron related to a fix flight path. In blue, the resolution function relates the ideal time-of-flight to the measured one.

responds to an ideal time of flight t_i for a fixed flight path L. The resolution function $R_t(t_m, t_i)$ relates the ideal time of flight to the measured one t_m and transforms an ideal time-of-flight spectrum $S_i(t_i)$ into measured time-of-flight spectrum $S_m(t_m)$:

$$S_m(t_m) = \int S_i(t_i) R_t(t_m, t_i) dt_i. \tag{2.7}$$

2.3 The n_TOF facility

The n_TOF facility is a pulsed neutron source based on the 20 GeV/c proton beam from the CERN Proton Synchrotron accelerator (PS). Protons are accelerated towards a

lead spallation target, yielding about 350 neutrons per incident proton [130]. Figure 2.3 shows schematically the CERN accelerator complex, responsible for the protons used at n_TOF.

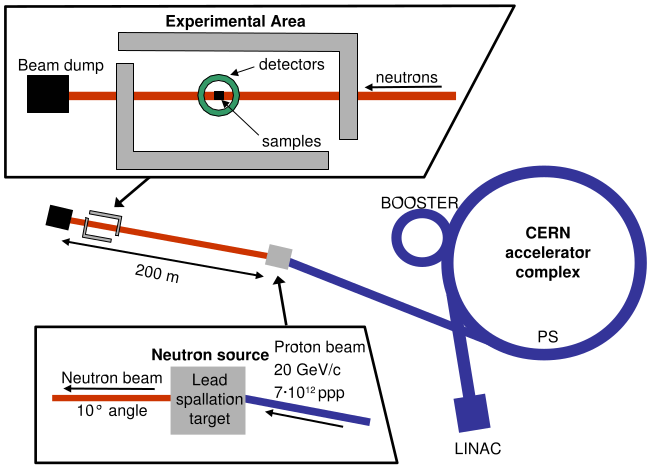

Figure 2.3: Layout of the n_TOF facility within the CERN accelerator complex. The LINAC feeds the PS-Booster, which accelerates the PS protons of 1.4 GeV/c up to 20 GeV/c. The beam is extracted and sent to the n_TOF spallation target in bunches of 7×10^{12} protons.

The n_TOF experimental program [131, 142] is focused on measurements of neutron cross-sections for three main categories of reactions: a) fission reactions, which are important for development of advanced nuclear systems [143]; b) radiative capture reactions, which are relevant to nuclear astrophysics and for the design and operation of nuclear reactors [144]; c) charged particle emission reactions which are relevant to applications [145], such as Boron Neutron Capture Therapy, fusion and nuclear astrophysics [146].

The history of n_TOF has started in the years between 1995 and 1997 from an idea proposed by Carlo Rubbia [141]. The facility became fully operational in 2001. Two different target-moderator assemblies have been used until now. During Phase-1 (2001-2004) a first spallation target consisted of lead block with a total volume of $80\times80\times60$ cm^3. After the first four years of operation, in which data were taken for 36 nuclides in capture and fission experiments,the target had to be replaced due to corrosion problems caused by insufficient cooling. At the end of a four-year halt and a complete upgrade of the neutron production target, the facility resumed operation at the end of 2008 till the end of 2012 (n_TOF-Phase-2). At the beginning of the second experimental campaign (n_TOF Phase-2), the experimental area was upgraded to a Work Sector Type A, with a series of safety and monitoring systems, in order to make measurements of high-activity samples without certified sealing possible. This key modification was essential to exploit the full potential of the facility. 18 reactions were studied during Phase-2, in addition to capture and fission measures, the research activity was extended to (n,α) measurements. During the so called CERN long shutdown 1, a second experimental area has been constructed in the period from May 2013 to July 2014. Afterwards the n_TOF Phase-3 started and finished the end of the 2018. Neutron-induced fission,

radiative capture and charged particle emission of 38 nuclides were measured in the two experimental areas in Phase-3.

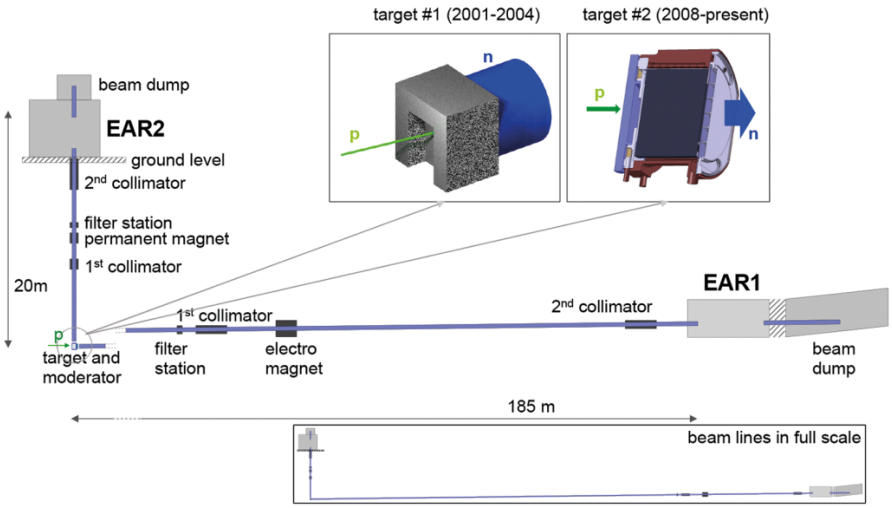

Figure 2.4: Schematic view of the two beam lines of the n_TOF facility. The first experimental area (EAR-1) is located horizontally at the nominal distance of 185 m from the neutron source, while the experimental area (EAR-2) is located at 90° with respect to the proton beam direction with a flight path of about 20 m. The two different spallation targets are shown in the top inset. Picture from reference [131].

Thanks to the high-energy and high peak current of PS, in combination with the massive Pb target, a very high instantaneous neutron flux is available in EAR-1 and EAR-2. In addition the energy range spans over eleven orders of magnitude from thermal energy to GeV. A scheme of the facility is given in figure 2.4.

2.3.1 The n_TOF spallation source

As already mentioned above, the first key ingredient is the proton accelerator, which allows n_TOF to play a major role in the field of neutron cross-section measurements. The main characteristics of the PS are the high proton energy, the high current and the small repetition rate. The PS can accelerate high intensities up to 7×10^{12} ppp (protons per pulse) in form of short pulses. The machine operates in the so-called *supercycle* mode, during which various bunches can be delivered to several users/experiments. The duration of the supercycle is limited by the spallation-target temperature and radioactivity. At maximum 4 proton bunches in a supercycle can be delivered to the n_TOF spallation target, reducing the repetition rate down to 0.25 - 0.40 Hz; anyhow it never exceed 0.8 Hz, corresponding to bunches separated by 1.2 s. The PS beam is optimized for the n_TOF facility, in particular by reducing the bunch time width from the original 13 ns down to 7 ns (rms), with the aim of increasing the time resolution of the neutron beam.

The small time width and repetition rate of the proton bunch allow measurements to be made over long times of flight, and therefore low energies, without any overlap into

the next neutron cycle. The large energy range that can be measured at once is one of the key characteristics of the facility.

The proton beam is extracted from the PS and sent onto the spallation target by using a fast extraction system. The proton beam can be delivered on target in two different operational modes:

- Dedicated mode: a 7×10^{12} proton bunch at 20 GeV/c is sent to the target during a 1.2 s PS cycle fully dedicated to n_TOF. The bunch time distribution has a gaussian shape and a width of 7 ns.
- Parasitic mode: during the ramping of a slow ejection cycle for the East Hall, before reaching 24 GeV, at the 19 GeV energy a $\sim3.5\times10^{12}$ proton bunch is extracted from the PS and sent to n_TOF.

The proton intensity sent onto the target is measured pulse by pulse through a Beam Current Transformer (BCT) located about 6 meters upstream with respect to the spallation target in the proton beam line. The digitized value of the beam intensity is available to the users in the PS control system. As for all the other transformers in the PS complex, the value of the proton intensity is checked by performing periodical calibration procedures. In order to detect any drift of BCT, the signal given by a resistive Wall Current Monitor (WCM) also named PKUP, is recorded [130]. This latter monitor, mounted immediately after the BCT, provides a pulse proportional to the instantaneous proton beam intensity. In conclusion, the WCM signal is used both for normalization purpose and for calibration of the time of flight.

The n_TOF spallation target installed in 2008 consists of a 1.3 ton monolithic cylindrical block of lead, with length of 40 cm and diameter of 60 cm. The spallation target is surrounded by a separate cooling circuit resulting in a 1 cm water layer in the beam direction, followed by an exchangeable moderator with a thickness of 4 cm. The cooling system is a pressurized circuit ensuring a water flow sufficient to keep the temperature at the lead surface at a value sufficiently lower than the water boiling point. Demineralized water is used as a moderator, as well as water with a saturated ^{10}B-solution (H_2O + 1.28% H_3BO_3) in order to reduce the number of 2.2 MeV γ rays from H(n,γ)^{2}H, which would otherwise form an important contribution to the background.

In summary, the high momentum and the high peak current of the proton bunches are responsible for the very high number of neutrons per protons burst, also referred to as instantaneous neutron flux.

2.4 The first experimental area (EAR-1)

The first experimental area [147] begins at 182.3 m from the spallation target and is designed to clean as much as possible the neutron beam from the secondary particles largely produced in the spallation reactions. Firstly, the beam line is shifted by an angle

of 10° with respect to the incident proton beam direction. This solution minimizes the number of undesired secondary particles towards EAR-1. In particular, γ rays and light charged particles are mainly produced in the forward direction. The neutron beam line is kept under vacuum with a pressure in the tube is less than 1 mbar. Along the neutron flight path, sketched in figure 2.5, several elements are placed in order to minimize the background and to shape the neutron beam. It is worth mentioning the

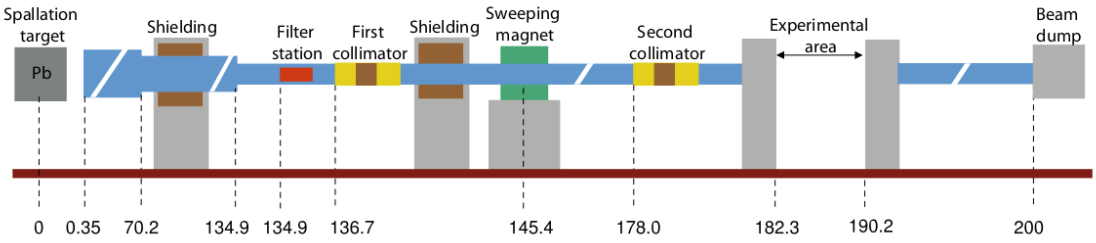

Figure 2.5: Schematic view of the n TOF neutron beam line from the spallation target to the beam dump of EAR-1 (distances are given in meters).

sweeping magnet (200 cm long, 44 cm gap and 3.6 Tm field), placed at 145 m from the spallation target, which deflects the charged particles remaining in the beam with a momentum up to 10 GeV/c, and a iron and concrete shielding that stop particles travelling around the beam. Two collimators are also present to shape the neutron beam: the diameter of the beam tube is progressively reduced from 800 mm at the exit of the spallation target to 400 mm before the first collimator. From the entrance of the second collimator (175 m from the exit from the target) to the experimental area the diameter of the tube is reduced to 200 mm. The diameter of the second collimator can be chosen between 18 mm (with 235 cm of steel plus 50 cm of borated polyethylene) and 80 mm (with 50 cm of borated polyethylene plus 125 cm of steel plus 75 cm of borated polyethylene) to meet the requirements of each measurement.

The beam line extends 10 m beyond the end of the experimental area and ends in a beam dump consisting of a 49×49×47 cm^3 polyethylene block containing three radiation monitors. More details can be found in Ref. [148, 149].

Resolution Function

The experimental campaign of measurement of ^{235}U(n,f) is focused on the high energy region, from few MeV to 1 GeV, where no resolved resonances are present, therefore the only effect to take into account, due to the moderation time, t_t, (introduced in the section 2.2.1) is the energy shift. Therefore the TOF expressed in equation 2.1 should be corrected to:

$$TOF_m = t_m + t_t \tag{2.8}$$

where t_t, as mentioned above, is the time difference between the time when the proton enters the spallation target and the time the neutron escapes from the target and the moderator system. The moderation time was simulated combining two different

Monte Carlo codes, FLUKA [150] and MCNP [151]. Figure 2.6 shows the resolution functions due to the neutron transport in the target-moderator assembly obtained from simulations. These distributions clearly show a strong dependence on the neutron energy. The response functions of a TOF spectrometer can be expressed in terms of time or equivalent distance $\lambda(E_n)$, which is the effective distance travelled by the neutron in the target-moderator system before entering the beam line. With this piece of information, the flight path travelled by a neutron detected at a given time can be expressed as the sum of a fixed geometrical length L and an additional small length $\lambda(E_n)$ that is a function of neutron energy and accounts for the distribution of neutron energies for a given time of flight. The equivalent distance is defined as $\lambda(E_n) = vt_t$, where v is the velocity of the neutron at the moment it escapes from the target-moderator assembly. This transformation of variables results in probability distributions of $\lambda(E_n)$ which are less dependent on the neutron energy and they are confined into a narrow range, as shown in the right panel of figure 2.6.

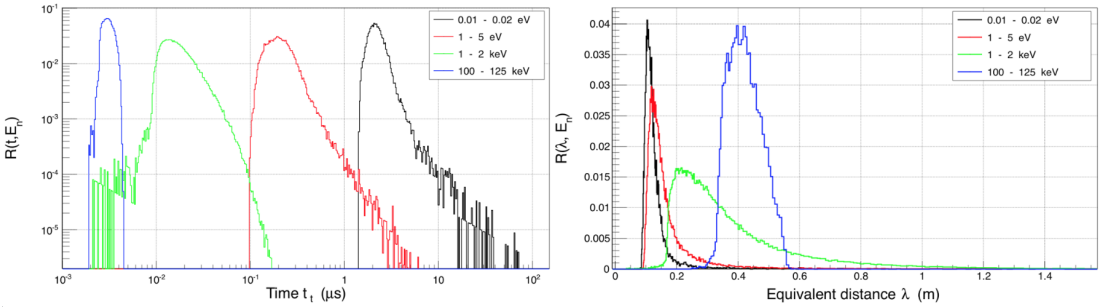

Figure 2.6: Left panel: Probability distribution of the time t_t that a neutron spends travelling in the target-moderator system of n_TOF. Right panel: Probability distribution of the equivalent distance λ that a neutron travels in the target-moderator assembly of n_TOF.

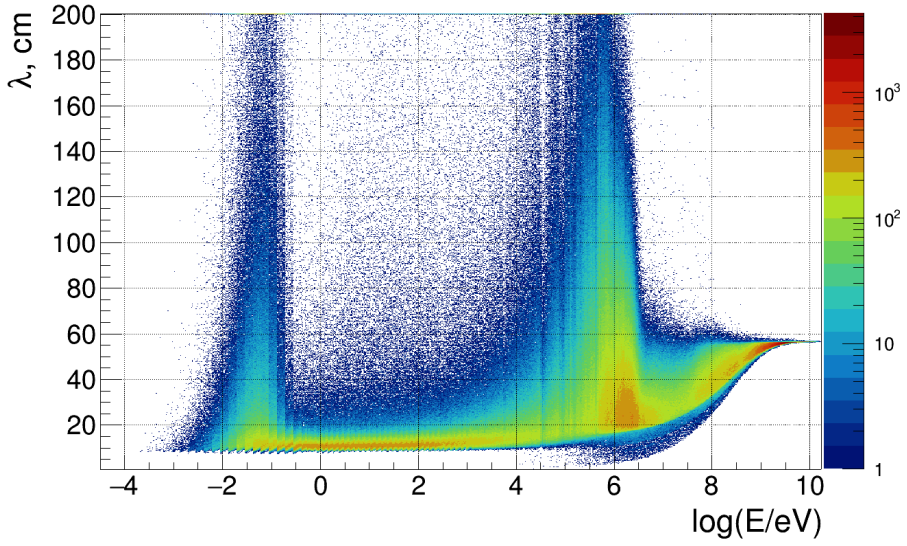

Figure 2.7: Resolution function at the EAR-1 sample position (185 m) obtained from FLUKA simulations. It is expressed as a distribution of the equivalent distance as a function of the neutron energy, in the energy range from thermal to 10 GeV.

Therefore the resolution function for a given incident neutron energy can be easily transformed into equivalent distributions in either energy, time, or distance by using the conservation of probability

$$R_E\,(E_n)\,dE_n \;=\; R_t\,(t)\,dt \;=\; R_L\,(L)\,dL \tag{2.9}$$

where E_n, L and t are mutually related.
The resolution function obtained from FLUKA is shown in figure 2.7. At high energies the spectrum of the moderation distance is squeezed to a constant value of 56 cm. At this energy no moderation occurs, all particles travel at about the speed of light and the so-called moderation time just represents the travelling time between the entrance side of the target and the exit side from the moderator.

2.4.1 Uncertainties on the neutron energy

Because the moderation is a stochastic process, there is an intrinsic uncertainty associated with the moderation time (Δt), or, equivalently, an uncertainty in the flight path ($\Delta\lambda$), defined as:

$$\Delta\lambda \;=\; v \times \Delta t. \tag{2.10}$$

This leads to an uncertainty in the reconstructed energy. The main contributions to the uncertainty in the distance ΔL are related to the determination of the total flight-path, i.e. the geometrical term plus $\lambda(E)$. For each energy a distribution of the moderation length is obtained from simulations, so that, in order to evaluate this last contribution we can use the peak and the RMS of the λ distribution. Although the difference between the two in terms of $\Delta\lambda$ may not be negligible, the difference in energy resolution is small. In addition, the time uncertainty Δt is due to the 7-ns proton bunch-width of the proton pulse. Figure 2.8 shows $\Delta\lambda$, and the relative ΔE as a function of neutron energy. As can be seen, the moderation time is dominant in the low energy region, while above few MeV the finite duration of the primary burst gives the greatest uncertainty. As a consequence of the long flight-path, EAR-1 allows an excellent relative energy resolution ranging from 10^{-4} to 10^{-2} at a neutron energy of 1 eV and 1 GeV respectively.

2.4.2 Background conditions

The spallation process as well as the absorption of neutrons in the moderators are responsible for a sizable production of γ-rays and charged particles, and a fraction reaches the experimental hall. While charged particles are removed from the beam by placing a magnet along the beam line, neutrons and γ-rays can be only minimized by geometrical consideration. Produced photons can be separated into two groups: a prompt component resulting from the spallation process with times $t < 1$ μs, and a delayed component arriving at time $t \geq 1$ μs up to a few 100 μs. The latter is due to thermal neutron capture by elements present in the moderator and the lead target.

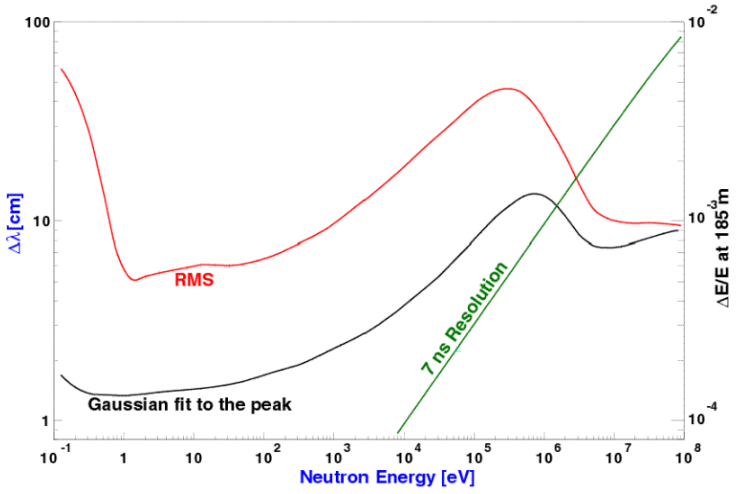

Figure 2.8: Monte Carlo simulation of the two main contributions of the neutron resolution at 185 m from the target: the moderation time (taking into account the peak of the distribution, in black, or the RMS, in red) and the duration of the primary pulse. The 7 ns resolution due to the proton beam dominates the resolution above neutron energy of few MeV (figure from [148]).

The corresponding time-of-flight distributions of the photons arriving in the first experimental hall are displayed in figure 2.9.
The prompt component is the so called γ-flash, arriving in the detector area about 617 ns ($= L/c$) after the proton beam hit the spallation target. However, the term γ-flash is somewhat misleading because it refers to ultrarelativistic particles, photons and a halo of photons and charged particles produced by the interaction of the high energy neutrons and photons with the second collimator. All these components affect each of the detectors used at n_TOF, therefore, the γ-flash provides a mean of accurately measuring the t_0 of each pulse (see Section 2.2). Its presence has also a drawback: detectors are blinded to high energy neutrons. The paralyzing effect due to this first signal is different in each detector and depends on the detector type i.e. the sensitivity to γ rays and its position with respect to the beam.

2.5 The second experimental area (EAR-2)

The second experimental area, EAR-2 [152, 153, 139], is a complementary and independent area with respect to EAR-1. EAR-2 has been just built perpendicularly to the spallation target, at much shorter distance of 20 m than the first measuring station, i.e. 20 m from the target. A schematic view of the new beam line is presented in figure 2.10.
Following the same idea of the first beam line, also along the second one a permanent magnet is placed to deviate all the undesirable charged particles. Two collimators are present to shape the neutron beam. In details, a first 1 m cylindrical collimator made of iron is located about 10 m from the spallation target. A second 3 m long collimator

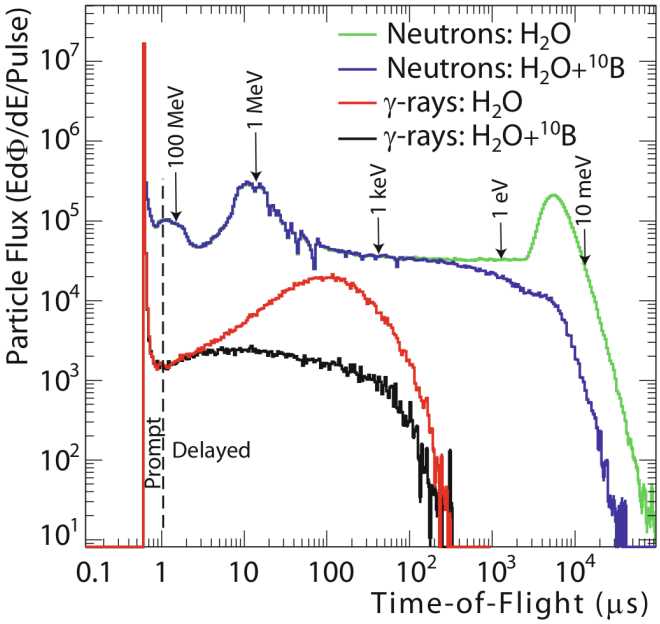

Figure 2.9: Time of arrival of photons and neutrons in EAR-1, when the capture collimation is used with either water or borated water as moderator. The role of borated water in the reduction of in-beam γ-rays in the keV region is cleary visible. Picture from reference [149].

is placed immediately below the floor of EAR-2 and contains a Pb shielding for in-beam γ rays. After crossing the experimental area, the neutron beam is *dumped* in a heavy structure on top of the EAR-2 building. This beam dump consists of an iron core which slows down fast neutrons, surrounded by borated polyethylene that thermalizes and finally captures most of the neutrons in the vertical beam.

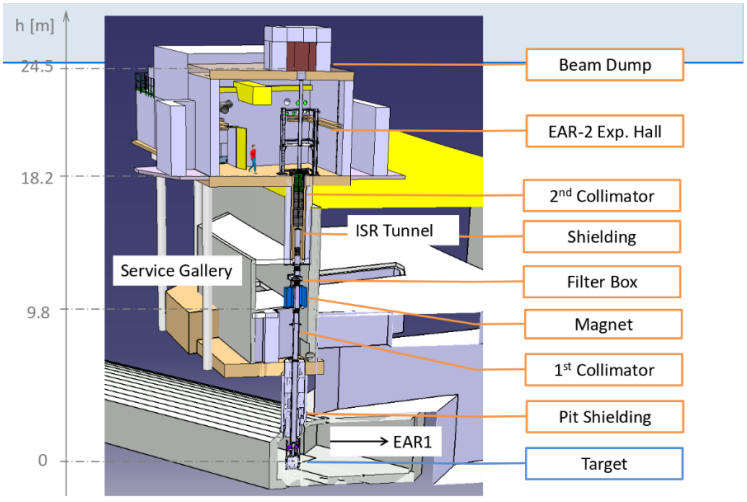

Figure 2.10: Layout of the second experimental area and the vertical beam line (distances are given in meters).

The extremely high neutron flux in EAR-2, approximately a factor of 25 higher than in EAR-1, allows us to perform challenging measurements that cannot be carried out anywhere else. In particular, it makes it possible to perform experiments with samples of very small mass (< 1 mg) and to measure the neutron cross-section of unstable iso-

topes with very high specific activity, i.e. with half-life as short as a few years, thanks to a drastic improvement of the signal-to-background ratio. The possibility of using samples with a mass smaller than 1 mg is essential for reducing the activity of isotopes with short half-life, or in case of rare materials.

Like EAR-1, the second experimental area is classified as Class A Laboratory, adequate for handling unsealed radioactive material.

2.6 Neutron beam characteristics

Accurate measurements of neutron-induced reaction cross-sections require a very good knowledge of the various features of the neutron beam in the experimental area, in particular its resolution function and its energy spectrum: the total number of neutrons entering the area as a function of energy, the spatial beam profile and the neutron and γ-ray background in and outside the beam. For this reason, a measurement campaign specifically devoted to the neutron beam characterisation has been performed for each spallation target installed so far at n_TOF. In particular, a large effort is dedicated to neutron flux measurements in both experimental areas.

The neutron flux has been determined by means of reference reactions, in particular the ^{6}Li(n,α), ^{10}B(n,α) and ^{235}U(n,f) ones, using different detection systems for different energy ranges. More details on the measurements and on the neutron flux characterisation for the second spallation target (2008 - 2018) can be found in ref. [154] for EAR-1 and in ref. [155] for EAR-2.
The experimental data were flanked by Monte Carlo simulations with the FLUKA, MCNP radiation transport codes and with GEANT4 [156, 157]. The good agreement between data and simulations, provides the validation of the latter, thus allowing one to extract further information that is not experimentally accessible, as is the case, e.g., for the neutron moderation in the target-moderator assembly. In fact, the neutron flux is the main experimental quantity that can be used to benchmark the simulations.

The evaluated neutron fluxes of the two experimental areas are reported in figure 2.11 per unit of lethargy (dn/dlnE).

A comparison of the neutron beam characteristics in the two experimental areas is reported in table 2.2.

Table 2.2: Comparison of the main features of the two experimental areas operation at n_TOF.

	EAR-1	EAR-2
Neutron flux	10^{6} n/bunch	10^{7} n/bunch
Energy range	25 meV - 1 GeV	10 meV - 100 MeV
Energy resolution	10^{-4}-10^{-2}	10^{-3}-10^{-2}
Beam size (FWHM)	3 or 8 cm	3 cm

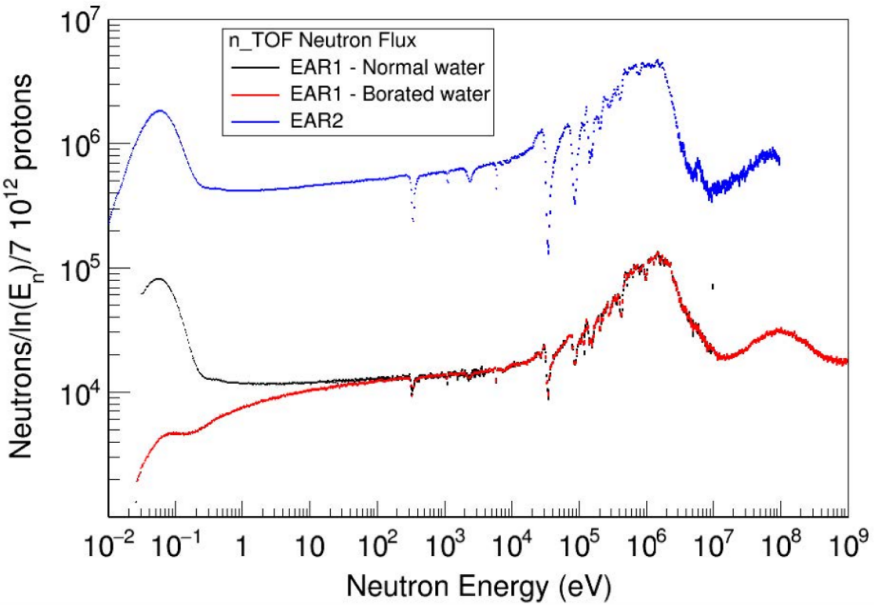

Figure 2.11: The number of neutrons per equidistant logarithmic energy bin., i.e. per unit of lethargy, $(dn/dlnE)$ per 7×10^{12} protons on target. The reported value is integrated over the full Gaussian beam profile with a nominal FWHM of 18 mm in EAR-1 and 21 mm in EAR-2, as seen at the sample position at nominal distances of 185 m (EAR-1) and 20 m (EAR-2).

Together with the high instantaneous neutron flux and the wide energy range, the high energy resolution represents the main advantages of the n_TOF neutron beams for measurements of neutron-induced fission cross-sections. In particular, the high resolution of EAR-1 allows us to perform measurements with high accuracy, while the high flux of EAR-2 is fundamental for measurements with high-activity and/or low mass samples, as it minimises the background related to the natural radioactivity of the sample, and allows one to collect high-quality data.
In summary, the two experimental areas can be considered complementary to each other, and a combination of data collected in both areas can provide, in some cases for the first time, high-accuracy and high-resolution data in a wide energy range.

2.7 The data acquisition system (DAQ)

The n_TOF data acquisition system must meet some key requirements related to the main features of the facility. First of all the acquisition time window for each PS pulse corresponds to the whole neutron energy range, i.e. from a few μs before the γ-flash for approximately 100 ms (corresponding to the TOF of a 0.01 eV neutrons in EAR-1). This also corresponds to the longest time window since the travel path to the EAR-2 is only of 20 m, which gives an acquisition time window of about 10 ms. The acquisition is triggered by the PS timing signal and the data samples have be transferred to the memory of the host controller before the next acquisition starts again 1.2 s later. The Data Acquisition System (DAQ) of the n_TOF facility, presented in detail in Ref. [158], is fully digital, flexible and almost dead-time free. The main advantage

of such a system is that it allows the offline analysis of the digitized pulses. By using dedicated pulse shape analysis (more details can be found in the next section), the pile-up and background events can be identified. Indeed this DAQ architecture has the exclusive capability to sample and store the full analogue waveform of the detector signals for each neutron pulse.
Each DAQ unit hosts several high sampling Data Acquisition Cards (DAC) as well as the high speed writing local storage able to sustain the raw data bandwidth related to a maximum acquisition window. It guarantees a data buffer for 3 days of acquisition in nominal operation conditions, to overcome network traffic issues in the data transfer to the CERN Advanced STORage manager (CASTOR) [159] . A scalable and versatile data acquisition system has been designed based on SPDevices ADQ412DC and ADQ14DC-4C modules, which has been developed with special attention to the neutron beam repetition rates.
The main characteristics of the two models are similar and are summarized in the table 2.3.

Table 2.3: n_TOF DAQ Cards characteristics, expressed using: Programming Power Voltage (VPP) and GigaSamples (GS) and MegaSamples (MS).

	ADQ412DC	DQ14DC-4C
Resolution	12 bit	14 bit
Full Scale Input Range (FSR)	0.1 - 5 Vpp	0.05 - 5 Vpp
Sampling frequency & N. of channels	1.8 GS/s 4-ch 3.6 GS/s 2-ch	1.0 GS/s 4-ch
On board Memory Size	175 MS/ch	256 MS/ch

The data acquired are in the form of raw data files, consisting mainly of the digitized detector signals. These files are sent to a temporary disk pool close to the measurement station and, once closed, they are transferred to CASTOR tape system for final storage and further processing.

For the ^{235}U(n,f) reaction cross-section measurement 41 channels of DQ14DC-4C digitizers working at 1 GSamples/s were used. In addition a fast zero-suppression algorithm selects only those data with an amplitude above an user-defined threshold for each channel, reducing in this way the amount of data to be stored.

2.8 Pulse Shape Analysis

Once stored in digital form, the electronic signals are accessible for offline analysis in order to obtain the time-of-flight and pulse height information. A general purpose Pulse Shape Analysis (PSA) framework [160] was developed and adopted at n_TOF for this purpose. The routine is characterized by a minimal number of explicit assumptions

about the nature of the signals and is based on a pulse template adjustment, thus aiming at being applicable to a wide range of detectors.
By independently setting and editing the 23 parameters used by the PSA routine it is possible to: a) define the baseline trend, b) suppress the noise, c) identify signals and their shape and d) extract the physical information (amplitude, area, polarity, width, time of arrival etc.) from the pulses (including the one produced by γ-flash).
The pulse recognition is based on the signal derivative. The first derivative is calculated as the difference between a set of user-defined N points taken for integration, using the signal (s) integration of both sides of each i point:

$$d_i = \sum_{j=1}^{min[N,i,P-1-i]} (s_{i+j} - s_{i-j}) \tag{2.11}$$

where P is the total number of point composing the recorded signal. To obtain a straightforward implementation of this algorithm a recursive relationship is necessary, implementing this calculation a number of times proportional to N×P. After derivation, the signals have a bipolar shape and the peak discrimination is carried out by applying some conditions to the signal polarity. Pulses are recognized in the signal when their derivative crosses a certain predefined threshold value. A signal candidate is identified when a consecutive four threshold crossing occurs, the first two occurring at negative values and the last two at positive ones (in case of negative polarity, otherwise it is requires the opposite). This principle was implemented in order to facilitate the recognition of signals in case of the low pulses or very high pileup. The final step is to reconstruct a clean signal by subtracting the baseline, also reconstructed through calculation, and applying the eliminating conditions. The final waveform reconstruction takes also into account a user defined amplitude threshold as an eliminating condition to discriminate real events from noise.
Figure 2.12 shows an example of each step used in the pulse shape analysis routine. In the top panel there is the raw movie; in the one the middle panel shows the derivative and the two green lines represent the thresholds set for the signal recognition. Finally, the bottom panel, shows the *clean* signals after the baseline subtraction.

After baseline subtraction, the amplitude, area, status of the pileup and timing properties such as the time of arrival are determined for each pulse. The n_TOF pulse recognition framework provides the possibility of performing numerical pulse shape fitting in each identified signal given a user specified pulse shape. By pulse shape we refer to the template pulse of a fixed form, given by the tabulated set of points (t_i, p_i), where t_i is the time coordinate of the i-th point and p_i is its height. The quality of the fit is evaluated at each alignment point by means of a reduced χ^2. This procedure is mandatory for high counting rates, where the signal overlapping is frequent, since the amplitude and timing information can be extracted much more reliably. In fact, when the time difference between two signals is short enough to cause pile-up, the second pulse lies in the tail of the first one and it is evident that the amplitude of each signal would be overestimated unless a pulse shape fitting is used.

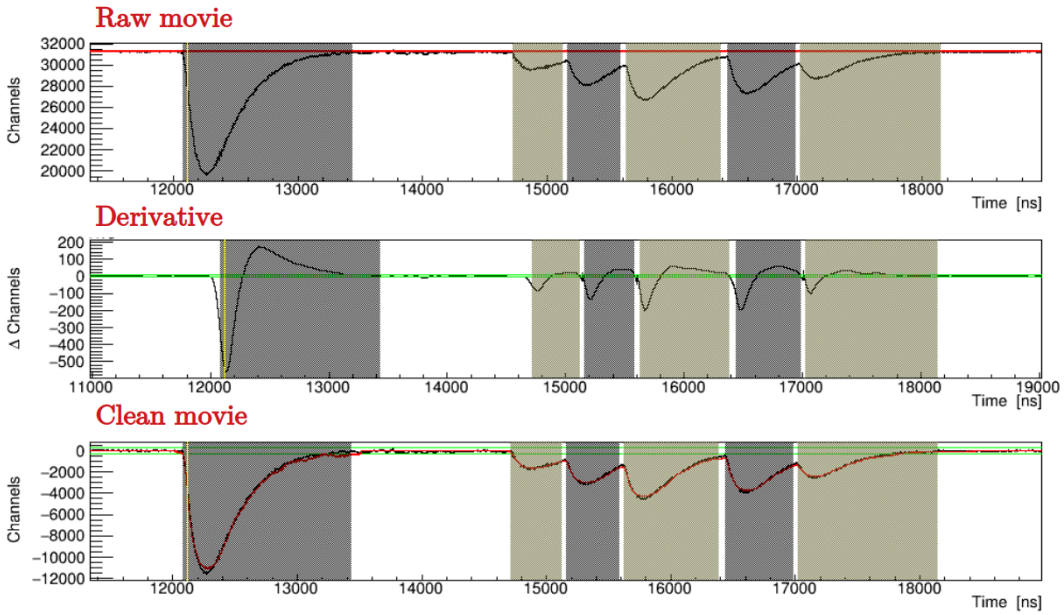

Figure 2.12: The signal recognition from the raw input (top panel) is based on the calculation of the first derivative (middle panel). The *clean* signal (bottom panel) is then calculated after the subtraction of the baseline.

Therefore, for instance, in case of pileup of two signals, the number of different signals present is initially identified using the derived spectrum and the set parameters. Subsequently both the amplitude and the area under the pulse are determined from the best fitted result; therefore the optimal fitted Pulse Shape is subtracted from the signal before proceeding to the next pulse in line, thus correcting for pileup.

In general the area under the pulse may be calculated by simple signal integration or from a pulse shape fit while the extraction of the timing properties relies on the digital implementation of the constant fraction discrimination, with a constant fraction factor of 30%.

Chapter 3

The measurement of ^{235}U(n,f) cross section at the n_TOF facility

A precise and accurate measurement of the ^{235}U(n,f) cross-section relative to n-p elastic scattering was performed in September 2018 at the CERN n_TOF facility. The energy distribution of the n_TOF neutron beam is one of the features that finally allow the determination of the absolute cross section of the fission reaction at high energy, for the first time. The setup was designed to measure simultaneously the fission reaction by means of two fission detectors and the neutron flux using three different recoil proton telescopes. The measurement is rather challenging in particular as regards the neutron flux detection; therefore, the three telescopes were designed and developed for this measurement by the n_TOF collaboration. The method used to measure neutron-induced the fission cross sections and the complete experimental setup used in the experimental campaign are described here in detail.

3.1 Neutron cross section measurement

The probability that a nuclear reaction takes place can be expressed in term of the cross section. Considering a neutron travelling a distance dx in a material with N nuclei per unit volume, and dP the probability of a reaction, the σ can be expressed by:

$$\sigma = \frac{dP}{Ndx} = \frac{R}{\Phi N} \tag{3.1}$$

R representing the reaction rate produced by the neutron flux per unit time Φ crossing the sample. The cross section varies according to the type of the target nucleus, to the type of the reaction involved and to the kinetic energy of the projectile.
Neutron-induced reactions that compete with each other are mainly: elastic scattering, inelastic scattering, neutron capture and fission. The total cross-section (σ_{TOT}) for a

nucleus can be expressed as a sum of the above mentioned contributions:

$$\sigma_{TOT} = \sigma_{el} + \sigma_{in} + \sigma_{\gamma} + \sigma_{f}. \tag{3.2}$$

In the first stage of many nuclear reactions, the neutron combines with the target nucleus to form an excited compound nucleus (CN). The decay mode and the decay probabilities of CN are independent of the formation of the compound nucleus itself. For example, the fission cross section, σ_f, is a measure of the probability that a compound nucleus decays through fission. In a fission reaction the CN splits into two fission fragments (FFs) together with an average number of neutrons which is typically 2 or 3. In such reaction the atomic number (Z) and the atomic mass (A) are always preserved. The experimental value of a fission cross section in equation 3.1 depends on the number of counts recorded by the detector for the isotope under investigation $C(E_n)$, for a given neutron energy, and the total efficiency ε of the detection system:

$$\sigma_f(E_n) = \frac{C(E_n)}{N\ \Phi(E_n)\ \varepsilon}. \tag{3.3}$$

For the analysis of absolute measurements of neutron-induced reaction cross sections, the simultaneous measurement of the instantaneous flux is essential, as shown in equation 3.3.
The fission cross section is obtained from the ratio between the number of detected fission events and the events coming from the reaction used to measure the flux, according to the following expression:

$$\sigma_f(E_n) = \frac{C_f(E_n)}{C_{st}(E_n)} \frac{\varepsilon_{st}\, N_{st}}{\varepsilon_f\, N_f}\ \sigma_{st} \tag{3.4}$$

where subscript f refers to the fission detector and subscript st refers to the neutron flux detector based on a cross section standard.

3.2 Neutron flux detection

In the case of the n_TOF beam, the neutron flux is defined as the number of neutrons per incident proton pulse (neutrons per bunch) and integrated over the full spatial beam-profile arriving at the experimental area with a given energy. In other words, a flux measurement based on standard cross sections is essentially reaction cross section measurement using a converter target irradiated by a neutron beam. As a consequence the reaction yield is obtained by counting the number of the events due to the charged particles produced. In particular, the experimental yield, $Y_{\varphi}(E_n)$, can be expressed as:

$$Y_{\varphi}(E_n) = \frac{C_{\varphi}(E_n)}{\Omega\, A\, \varepsilon\, \Phi(E_n)}, \tag{3.5}$$

where $C_{\varphi}(E_n)$ is the counting rate corrected for dead time and background, A is the effective area of the sample seen by the incident neutron beam, Ω is the solid angle

subtended by the detection system, ε is the efficiency of the detector and $\Phi(E_n)$ is the incident neutron flux. The theoretical yield for the reaction under investigation is:

$$Y_\varphi(E_n) = (1 - e^{-n\sigma_{tot}}) \frac{\sigma_{st}}{\sigma_{tot}}, \tag{3.6}$$

which reduces to $n\sigma_{st}$ when $n\sigma_{tot}$ is small. In equation 3.6 n is the areal number density of the sample and σ_{st} and σ_{tot} are, respectively, the standard cross section of the reaction of interest and the total cross section for the isotope used as neutron converter.

Combining equation 3.5 and equation 3.6 one obtains that the energy dependence of the neutron flux turns out to be:

$$\Phi(E_n) = N_\varphi \frac{C_\varphi(E_n)}{\sigma_{st}(E_n)}, \tag{3.7}$$

where N_φ is a normalization factor which groups together the quantities independent of energy.

Several factors have to be considered in searching for the most appropriate reaction to be used for flux monitoring. First, the cross section for the reaction must be as large as possible, so that efficient detectors can be built with small dimensions. Second, since gamma-rays are often present with neutrons beams, the higher is the Q-value, the greater is the energy carried by the reaction products, and the discrimination between them and the background becomes more effective.
The cross section of a neutron reaction, is regulated by strong interaction and, in most materials, is a strong function of neutron energy, it is therefore appropriate to choose different reference reactions based on the energy range of interest. In first approximation, it is possible to classify neutrons according to their kinetic energy:

1. slow neutrons, when the kinetic energy ranges from thermal to about a few keV;
2. fast neutrons, above.

For slow neutrons, the detectors used to measure the neutron flux are based on the detection of the secondary events produced by a nuclear reaction, such as (n,p), (n,α), (n,γ), (n,f) or on the nuclear scattering from light charged particles, which are detected.

Figure 3.1 shows the neutron energy dependence of the cross section of the most popular reactions for the conversion of slow neutrons into directly detectable particles: ^{3}He(n,p), ^{10}B(n,α), ^{6}Li(n,α). These large and structureless cross sections are proportional to $1/v$ over a large energy range; since they are considered as a standard, see table 1.1, they are widely used in neutron flux detectors.

The ^{10}B(n,α) reaction can may be written:

$$^{10}B + n \longrightarrow \begin{cases} ^7Li + \alpha & 2.792 \text{ MeV (ground state)} \\ ^7Li^* + \alpha & 2.310 \text{ MeV (excited state)} \end{cases} \tag{3.8}$$

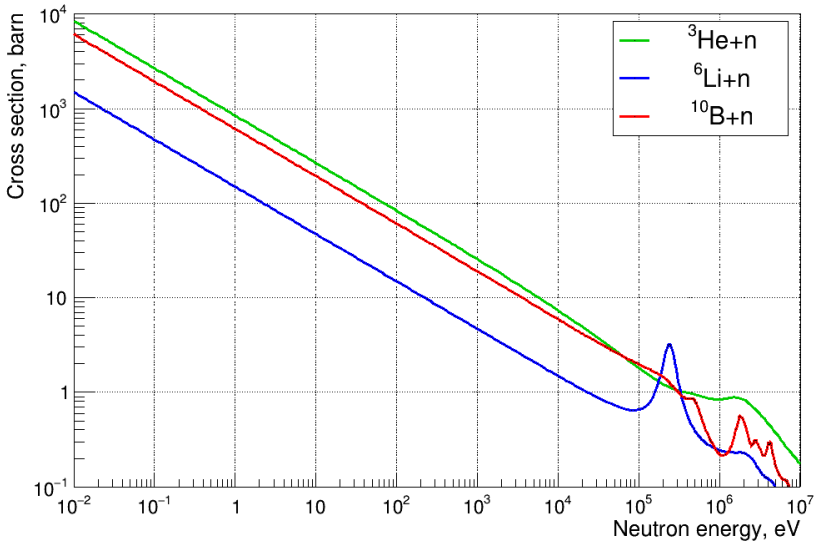

Figure 3.1: Cross section versus neutron energy for some reactions of interest in neutron detection. Data from ENDF/B-VIII.0 [161].

where the right-hand side indicates that the reaction product ^{7}Li may be left either in its ground state or in its first excited state. When thermal neutrons are used to induce the reaction, about 94% of all interactions lead to the excited state and only 6% directly to the ground state.

Another popular reaction for the detection of slow neutrons is the (n, α) reaction on ^{6}Li. The reaction proceeds only to the ground state of the product and the Q-value is 4.78 MeV:

$$^{6}Li + n \longrightarrow^{3} H + \alpha. \tag{3.9}$$

The last widely isotope used is ^{3}He:

$$^{3}He + n \longrightarrow^{3} H + p. \tag{3.10}$$

The thermal neutron cross section for this reaction is 5330 barns, significantly higher than that for boron and lithium reactions, with a Q-value of 764 keV. Although ^{3}He is commercially available, its cost is relatively high.

The fission cross sections of ^{233}U, ^{235}U, ^{239}Pu are relatively large at low neutron energies, for instance the cross section of ^{235}U(n,f) at the thermal point is 584 barns, and thus these materials can be used for slow neutron detectors. One characteristic of the fission reaction is its extremely large Q-value ($\sim$200 MeV), which enables a very clear discrimination between the fission fragments and background particles.

In principle, the reactions used to detect slow neutrons, could be applied to detect the fast neutrons as well; however, as for example shown in figure 3.1, the probability that a neutron induces one of these reactions decreases rapidly with increasing neutron energy.

Therefore, fast neutron detectors must use a modified or completely different detec-

tion scheme to provide a significant detection efficiency. A common conversion process useful to measure the number of fast neutrons while preserving the information about their kinetic energy is the elastic scattering with light nuclei. In this interaction an incident neutron transfers a portion of its kinetic energy to the target nucleus, thus giving rise to a recoil nucleus. The energy that can be transferred from a slow neutron is therefore very small, and the resulting recoil nuclei are too low in energy to generate a significant detector signal. Once the neutron energy reaches the keV range, however, recoil nuclei can be detected directly and assume a large importance for fast neutron detection. Hydrogen, deuterium and helium can be used as target nuclei, though hydrogen is the effective. The cross section for neutron elastic scattering with hydrogen is quite large and its energy dependence is accurately known. More important, however, is the fact that an incident neutron can transfer up to its entire energy in a single collision (see equation 3.13, below). Recoil nuclei that result from neutron elastic scattering from ordinary hydrogen are called recoil protons [162]. For incoming neutrons with non-relativistic kinetic energy conservation of momentum and energy in the center-of-mass system gives the following relation for the energy of the recoil nucleus:

$$E_R = \frac{2A}{(1+A)^2}\,(1 - cos\,\Theta)\,E_n \tag{3.11}$$

where A is the the mass of the target nucleus, E_n and E_R are the incoming neutron kinetic energy and the recoil nucleus kinetic energy respectively, expressed in the laboratory system, Θ is the scattering angle of the neutron in the center of mass system and ϑ is the scattering angle of the recoil nucleus in the laboratory system. To convert the equation 3.11 to the laboratory coordinate system, we can use the following transformation:

$$cos\,\vartheta = \sqrt{\frac{1 - cos\,\Theta}{2}} \tag{3.12}$$

which, when combined with equation 3.11, gives the following relation for the recoil nucleus energy in terms of its own angle of recoil:

$$E_R = \frac{4A}{(1+A)^2}\,(cos^2\vartheta)\,E_n. \tag{3.13}$$

From equation 3.13 one can deduce that the energy given to the recoil nucleus is uniquely determined by the scattering angle. When the recoil is emitted almost perpendicular to the incoming neutron direction, equation 3.13 predicts that the recoil energy is near zero. At the other extreme, in a head-on collision of the incoming neutron with the target nucleus, the target will transfer the maximum possible recoil energy; in the case of hydrogen (A=1) the maximum energy is all the energy of the incident neutron. Devices based on the proton detection, from the neutron-hydrogen interaction, and on the narrow selection of recoil directions are generally known as Proton Recoil Telescopes (RPTs) [163, 164, 165].

From equation 3.13, the energy of recoil protons observed at an angle ϑ with respect

to the incoming neutron direction is given by:

$$E_p = E_n \, cos^2\vartheta. \tag{3.14}$$

Equations 3.11 - 3.14 can be extended in the relativistic regime, as required in the present measurement, however, here for the sake of clarity they are discussed in the non relativistic case.

3.3 Proton Recoil Telescope

As discussed in the first chapter, the energy range of interest for the fission measurement under investigation is from 10 MeV to 1 GeV, therefore the reaction to be exploited for neutron flux measurement is n-p elastic scattering. The experimental setup was composed by 3 RPTs in order to cover the total energy range of interest and reduce the systematic uncertainties.
A telescope for proton recoil in its simplest form is composed by a radiator of a hydrogenous material such as polyethylene and a proton detector. In this configuration, neutrons impinge on the radiator, whose thickness is kept small compared to the range of the lowest energy recoil proton to be measured. The angle ϑ at which recoil protons are observed is defined by positioning a detector at a given distance from the radiator. Because of the $cos^2\vartheta$ fall-off of recoil proton energy, the detector is usually positioned at a small angle with respect to the neutron direction but large enough to avoid neutron-induced background events from the primary beam in the detector. In figure 3.2 there

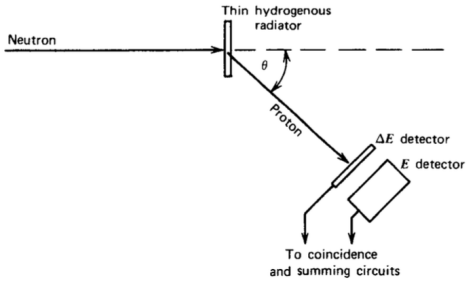

Figure 3.2: A proton recoil telescope, as sketched in [9].

is a scheme of a common proton recoil telescope, in which a very thin ΔE detector is placed in front of a thicker E detector, which fully stops the recoil protons. A proton recoil telescope could, in principle, use a single detector. However, the use of multiple detectors in coincidence allows one to reduce the background of secondary particles, i.e. γ-rays and charge particles, produced by the neutrons either in the target or in the detectors. Two signals, in the ΔE and E detector, are considered to be in coincidence if the time difference between the two, Δt, falls inside a selected window. In order to reduce the probability of random coincidences, the Δt window must be set as small as possible. By operating the two detectors in coincidence, only particles coming from the radiator are recorded. The sum of the two signals is proportional to the total

proton energy. This type of detector is often used as particle identifier exploiting the information on energy deposition in each detector. The stopping power for a particle with charge z in a material characterized by atomic number Z and mass number A, is described by the Bethe-Bloch formula (for more details see reference [166]):

$$-\frac{dE}{dx} = 2\pi N_a r_e^2 m_e c^2 \rho \frac{Z}{A}\frac{z^2}{\beta^2}\left[ln\left(\frac{2m_e\gamma^2 v^2 W_{max}}{I^2}\right) - 2\beta^2 - \delta - 2\frac{C}{Z}\right] \tag{3.15}$$

where $v = \beta c$ is the particle velocity. In the non-relativistic approximation ($\beta << 1$), ΔE is proportional to v^{-2} and the equation 3.15, for a particle with energy E and mass M, can be simplified as:

$$-\frac{dE}{dx} = K_1\frac{Mz^2}{E}\,ln\left(K_2\frac{E}{M}\right) \tag{3.16}$$

where K_1 and K_2 are constant. Since the logarithmic term is not very sensitive to the energy variation it can be incorporated in the constant obtaining:

$$\Delta E \cdot E = kz^2 M \tag{3.17}$$

where k is a constant that depends on the absorption capacity of the material. From the equation 3.17 it is clear that plotting the energy loss from the particle in the first thin detector (ΔE) versus the total energy of the particle (E) it is possible to distinguish the different families of particles which correspond to different values of z^2M (ΔE-E method). The particle identification is the key feature of this detector because it allows one to discriminate the protons from other charged particles, produced by the reactions of neutrons with the carbon, present in the polyethylene target.

The main disadvantage of the proton recoil telescope is its extremely low detection efficiency, typically one count per 10^5 neutrons. This low efficiency stems from two factors, neither of which can be improved without sacrificing the energy resolution of the device. First, the radiator thickness must be kept small to avoid appreciable energy loss of the recoil protons before they leave the radiator, but this implies a low value of areal number density in the sample. Second, the solid angle subtended by the telescope must be kept relatively small to avoid including too large a spread in recoil angles, and consequently smearing the peaked response function. One of the attractive features of the RPT is the fact that its detection efficiency can be calculated quite accurately. The probabilities of neutron scattering and subsequent proton recoil detection are quite easily calculated from the accurately known hydrogen scattering cross section and geometric evaluation of the detector solid angle.

Since the cross section to be investigated is completely unknown, it was decided to pursue a redundant approach. Three new compact designs were implemented on the basis of similar but different principles, thus allowing a cross check of the results and a consequent better estimate of the systematic uncertainty in the determination

of the neutron fluence. As already mentioned, one of the key issues in the absolute measurement of the ^{235}U(n,f) cross section at n_TOF is the presence of an intense γ-flash, a prompt signal with a tail extending to large times. This huge signal blinds all the detectors for some time after its arrival, thus preventing one from reaching high neutron energies. At the same time, a good time resolution is needed to mimimise the probability of signal pile-up. Therefore, the measurement requires a RPT concept based on detectors excellent timing properties: the detector signal must be characterised by very fast rise and decay times. To this end, the RPTs developed for this experiment, were mainly constituted by low Z detector materials, i.e. fast plastic scintillator detectors. The drawback in the use of low density materials is the limitation in the kinetic neutron energy up to which recoil protons can be stopped (with a reasonable detector thickness), which enable the clear identification of an isolated recoil peak.

3.3.1 RPT developed by PTB

One of the three telescopes used in the ^{235}U(n,f) fission campaign at n_TOF, was developed by Physikalisch-Technische Bundesanstalt (PTB, Germany), the national metrology institute of the Federal Republic of Germany. This detector (called RPT-PTB), is shown in figure 3.3 and consists of three detectors. This triple-stage RPT has two transmission detectors that consist of a square EJ204 plastic scintillators [167], 45×45 mm^2 (ΔE1) and 38×38 mm^2 (ΔE2) in size, respectively. The first detector is positioned at a distance of 200 mm from the sample. The thickness of the detectors are optimised for the neutron energy range to be covered and varies from 0.5 mm to 5 mm. Moreover, the dimension of the ΔE2 detector, which has the smallest transverse dimensions of all the three detectors, defines the solid angle of the RPT-PTB. The stop detector (E) is a cylindric EJ204 scintillator of 80 mm diameter. In addition, the thickness of this detector is optimized with respect to the energy range: 50 mm for neutron energy from 25 MeV to 100 MeV, 100 mm from 50 MeV to 150 MeV. The ΔE scintillator detectors are inserted in a rooflike structure with 0.1 mm aluminium walls covered with a diffuse white reflector on the interior and coupled to a XP2020Q PMTs [168] (figure 3.3(b)). Due to the diffuse reflector the inhomogeneity of the light collection is less than 10%. The envelope and the front side of the cylindrical E detectors are also covered with a white diffuse reflector and coupled to XP2020 PMTs.

In the RPT-PTB data analysis a triple coincidence is required. The ΔE1 and the E detector are larger, than ΔE2, to ensure that all charged particle originating from the sample and passing through the middle detector also produce signals in the first and the last detector. The diameter of the E detectors is also sufficiently large to limit incomplete energy deposition to a tolerable level, thus avoiding “tails” in the shape of the recoil peak. The elongated design of this RPT results in a directional sensitivity of the telescope to events originating from the sample, suppressing background events originating elsewhere. The main design goal for this instrument is to achieve directional

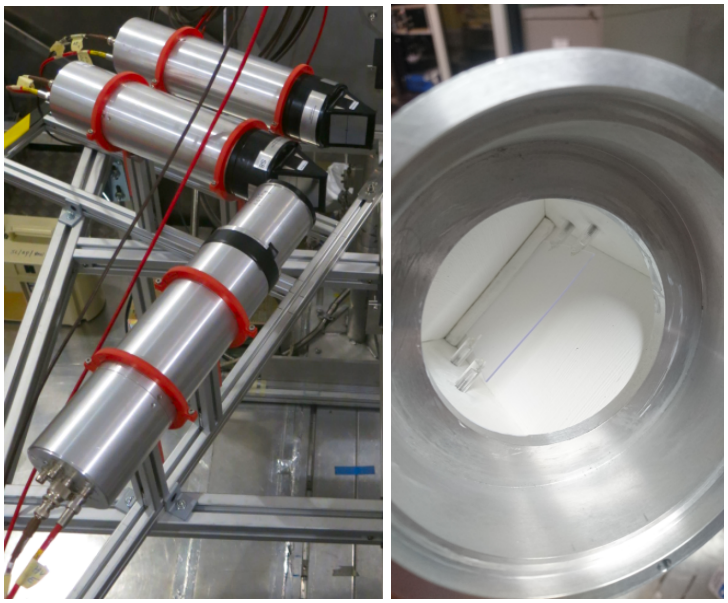

(a) (b)

Figure 3.3: In the left (figure 3.3(a)) picture of the triple stage RPT-PTB: three plastic scintillators, two ΔE and the stop detector, E. In the right (figure 3.3(b)) the detail of the interior of the cover for the ΔE detectors with a diffuse white reflector to reduce the inhomogeneity of the light collection.

sensitivity for background suppression and reduced influence of angular straggling for an accurate definition of the solid angle, required during the data analysis.
Events produced by light charged particles other than protons can be identified and discarded by the ΔE-E method. After the triple coincidences the second pivot, on which the analysis is based, is the energy deposited in the E detector. For a given neutron energy, recoil protons stopped in the RPT give rise to a well defined peak in the pulse height distribution of the last detector, for the kinematics of the reaction. The protons produced by reactions between neutrons and carbon, are produced following the absorption of the neutron and the formation of the compound nucleus. The absorption deletes all information on the incident direction of the neutron and the subsequent decay emits particles isotropically into space. For these reasons, as shown in figure 3.4, protons from n-p scattering reactions and those produced by background reactions are easily identifiable: the first are concentrated on the peak of the distribution; the second are placed before the peak.

In order to exploit the peak generated by n-p elastic scattering, it is necessary that the protons stop inside the telescope, i.e. before the so-called punch-through. In fact, when protons do not stop inside the detector the two contributions, that is the recoil protons and the protons from the C reactions, overlap and the identification and separation of the two is no longer easily applicable. Therefore with the PTB telescope it is possible to extract the flux in the energy region from 30 MeV to 150 MeV.

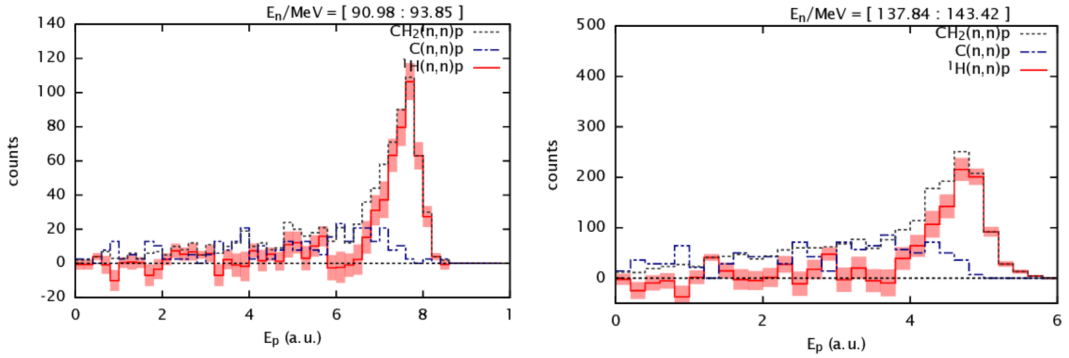

(a) (b)

Figure 3.4: Two examples in two different neutron energy regions, of the E spectra obtained with the RPT-PTB. The black dotted line is the spectrum obtained with the polyethylene sample in the beam, the blue line the spectrum with the carbon target and the red line the difference between the two, corresponding to the events of n-p elastic scattering.

3.3.2 RPTs developed by INFN

The two RPTs developed by Istituto Nazionale di Fisica Nucleare (INFN, Italy) were designed in order to be as compact as possible: a sketch of the structure and a picture of one RPT are shown in figure 3.5. The two telescopes work in two different energy ranges with an overlapping zone: the low energy detector, hereafter referred to as RPTL-INFN, has been optimized for neutron energy reactions from 10 to 150 MeV; the high energy telescope, named RPTH-INFN, works above 100 MeV. Both telescopes consist of a

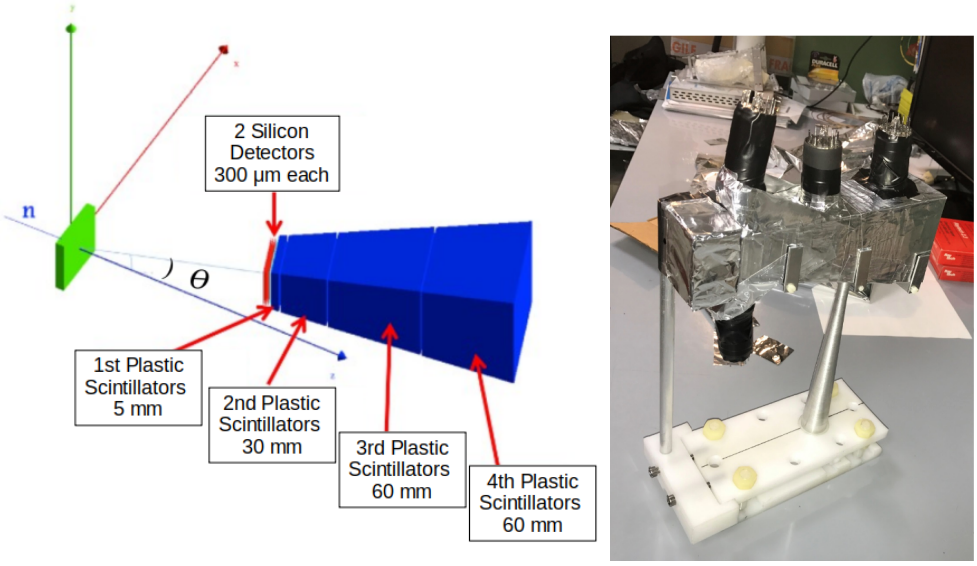

(a) (b)

Figure 3.5: In figure 3.5(a) a geometrical drawing of the multi-stage telescope: the two silicon detectors followed by the four plastic scintillators. in figure 3.5(b) the final detector assembled in the mechanical support.

trapezoidal structure pointing to the radiator sample and they are composed by four independent BC408 plastic scintillators [169], hence the name multi-stage detectors,

with a increasing thickness: 0.5, 3.0, 6.0 and 6.0 cm. The total length of the two detectors is 16 cm with an increasing transverse size, from 3×3 cm^2 to 7.2×7.2 cm^2, in order to cover a fixed solid angle, relative to the target centre. The last three slabs are read out independently through the coupling, at the center of a side face, with a 1" Hamamatsu R1924A Photomultiplier tube (PMT) [170], by means of optical glue. The light collection of the first scintillator has a strong dependence on the impact point of the particle, due to its reduced thickness, therefore it was decided to couple it with two light-guides each with a PMT on opposite sides of the scintillator (the detail of the first scintillator is shown in figure 3.7(a)). The digitalized value of the collected light, to be used for the data analysis, is the geometrical average between the two recorded values, technique already successfully exploited in other applications [171, 172]. All

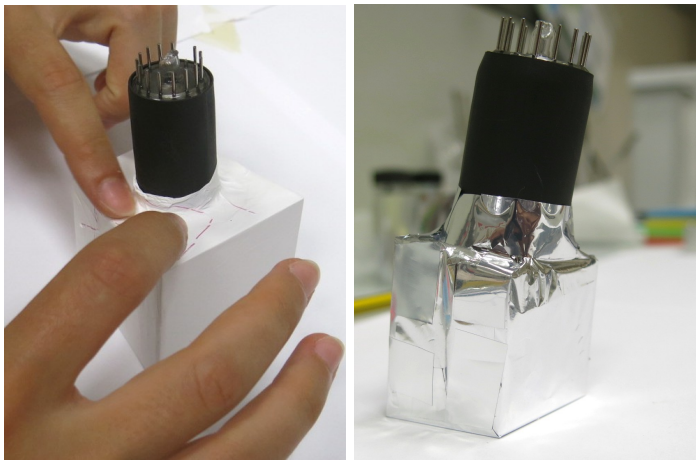

(a) (b)

Figure 3.6: Plastic scintillator with a PMT glued on a lateral face, wrapped with teflon, on the left (figure 3.6(a)) and then aluminized mylar, on the right (figure 3.6(b)).

the scintillators were first wrapped with teflon and then with aluminized mylar, see for instance figure 3.6, in order to maximize the efficiency of collection of scintillation light while preventing cross talk between adjacent detectors. Then they were put together by means of adhesive aluminum tape and finally installed onto the very light mechanical support made of aluminum, to keep the background produced by scattered neutrons as low as possible, and fixed on a PET (polyethylene terephthalate) base. The RPTL-INFN has two silicon detectors placed in front of the first thin scintillator. The silicon detectors MSX09-300 [173], 300 μm thick, were installed in a dedicated holder (figure 3.7(b)), 7 mm apart from each other with a 4 μm thick aluminum foil placed on the entrance and exit windows. An additional 10 μm aluminum cap was later installed for redundant protection and light shielding. The silicon detectors allow one to reduce the minimum detectable neutron energy from 40 MeV to 10 MeV.

As said before, the main problem to be solved was to minimize the effect of the γ-flash. Using fast detectors with a fast recovery time can shorten the time interval between the start of the γ-flash and the first useful signal, thus allowing one to extend upwards the measurable neutron energy range. BC408 is a very fast plastic scintillator characterized

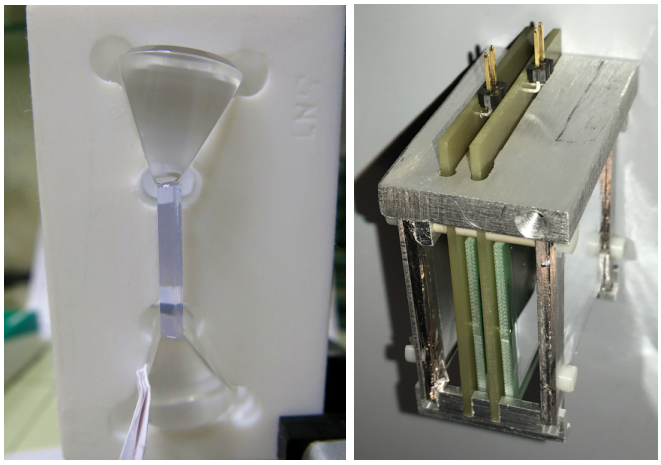

(a) (b)

Figure 3.7: Two details of the RPT-INFN. In figure 3.7(a) the lightguides being glued with the first plastic scintillator. In the picture 3.7(b) The two silicon detectors assembled in their case.

by a decay time of 2.1 ns, feature which makes it possible to detect useful signals even below 100 ns after the γ-flash corresponding to neutrons of about 1 GeV. An example of detector behavior observed online during the measurement is shown in figure 3.8, where the data from the two silicon detectors are reported in red and blue, and the data recorded by the first plastic scintillator in green. Case *a* in figure 3.8 shows a useful signal produced by a plastic scintillator 80 ns after the start of the γ-flash.

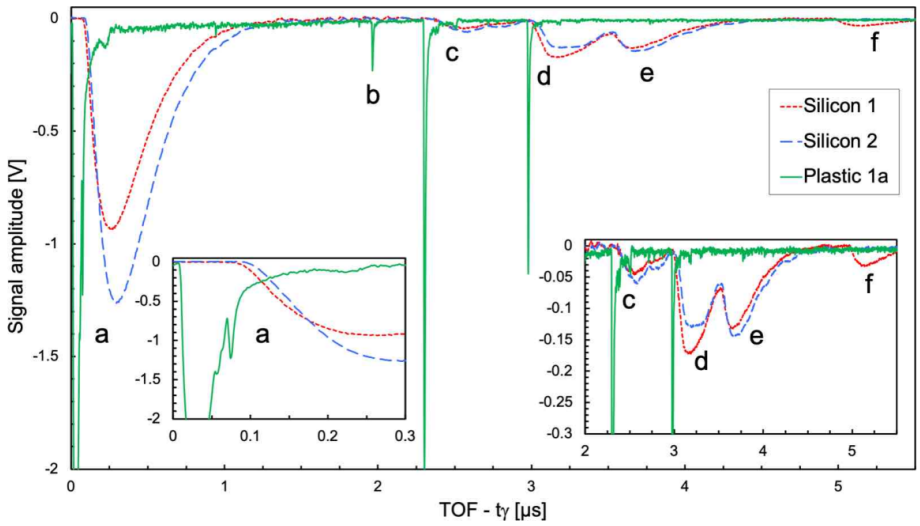

Figure 3.8: Sample signals produced by the two silicon detectors, in blue and red, and the first plastic scintillator, in green, in the first 5.5 μs of data acquisition.

The analysis of the events in coincidence among the different detectors is the fundamental principle at the base of the analysis of the telescopes, as the coincidence contributes to the suppression of the γ background and of the events that do not originate in the C_2H_4 target. Moreover, thanks to the multi-stage structure it is possible to select, for each neutron energy, the best configuration in terms of number of detectors

in coincidence. In figure 3.8 there are few examples concerning the different regions of competence of the detectors. For example, region c, at 2.296 μs after the γ-flash, i.e. 22 MeV, is a case where valid signals are detected in the two silicon detectors and in the first plastic scintillator. Region e, 11 MeV of neutron energy, represents a case where the proton is so slow that it crosses the first silicon detector and stops in the second one, therefore no signal is produced in the scintillators. Finally, region f, 6 MeV, shows the case of a very low energy proton that is stopped in the first silicon. In table 3.1 the main background reactions, originating from the interaction of neutrons with carbon, are listed. The table shows that in the final state there can be light particles which would reach the telescope: protons, deuterons, tritium, α particles, and more. Thanks to the negative Q-value of the reactions and the different energy deposited by the different particles, coherently with the equation 3.15, using the best configuration of coincidence between the detectors, it is possible to select only events with protons.

Table 3.1: Main background reactions produced by the interaction of neutrons with carbon.

Reaction	Q-value (MeV)
n + ^{12}C $\longrightarrow$ ^{9}Be + α	- 5.7
n + ^{12}C $\longrightarrow$ n + 3 α	- 7.9
n + ^{12}C $\longrightarrow$ ^{12}B + p	- 13.6
n + ^{12}C $\longrightarrow$ ^{11}B + n + p	- 17.3
n + ^{12}C $\longrightarrow$ ^{11}B + d	- 14.9
n + ^{12}C $\longrightarrow$ ^{10}B + t	- 20.5

Figure 3.9 shows that by choosing the right detectors it is possible to identify the background events coming from ^{12}C: there are two ΔE-E matrices produced by simulated data of a 56 MeV neutron energy beam impinging on a polyethylene target. In figure 3.9(a) ΔE and E are the energy deposited in the first and the second silicon detector, respectively. In this configuration it is possible to identify four hyperbolas produced by four different families of particles: protons, deuterons, tritons and α particles (listed above in table). From the matrix it is possible to deduce that the particles with z=1 are not stopped in the second silicon detector, indeed E increases up to a maximum value and then starts to decrease, and the majority of events are concentrated near zero. On the contrary, taking into account the energy deposited in the first (ΔE) and in the second (E) plastic scintillators, only protons and deuterons remain, since the range of produced α particles, at that energy, are stopped in the second silicon detector and the tritons in the first scintillator. In this last configuration the selection of events generated only by protons is straightforward: to eliminate the signals of heavier particles it is enough to apply a proper analysis condition around the trend of the hyperbola generated by protons.

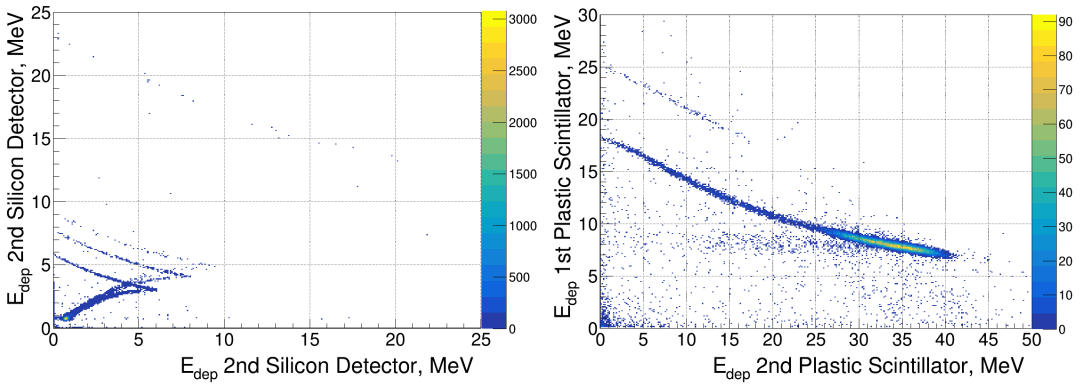

(a) (b)

Figure 3.9: Monte Carlo simulation of a 56 MeV neutron energy beam impinging a polyethylene target. Figure 3.9(a) shows the energy deposited in the first silicon detector, ΔE, as a function of the energy deposited in the second silicon detector, E. The ΔE-E matrix 3.9(b) shows the energy deposited in the first scintillator as a function of the energy deposited in the second one.

Description of the targets

Polyethylene samples were chosen to maximize the hydrogen density in the solid target. Although this material presents a favorable stoichiometric ratio between hydrogen and carbon, the latter is a source of background and therefore it requires dedicated measurements with a graphite sample of equivalent thickness. Indeed, charged-particle discrimination based on the ΔE-E technique is used to identify and suppress deuterons and α particles. On the contrary, the background related to the ^{12}C(n,px) reactions cannot be completely discriminated from recoil protons, and must therefore be measured and subtracted using pure carbon samples.
Three different C_2H_4 sample thicknesses were used in order to cover the entire energy range of interest. The samples were used in dedicated runs optimized for different neutron energy ranges in order to maximize the counting statistics while keeping the proton energy straggling at a reasonable level. In a specular way, in order to have a background evaluation as realistic as possible, three graphite samples were used with corresponding areal density of carbon atoms.
The different samples, and their main features, used during the experimental campaign are presented in table 3.2.

3.4 Fission detection setup

The measurement of energy deposited in gas by fission fragments (FFs) produced in thin deposits of fissile material is one of the standard techniques for measurement of neutron-induced fission cross-sections. Due to the peculiarity (multiplicity and kinematics) of the fission process, the number of detected FFs is therefore equal to the

Table 3.2: Characteristics of the samples.

Sample	Thickness mm	Mass g	Atomic density 10^{-3} atoms/barn	Atoms of H 10^{-3} atoms/barn	Atoms of C 10^{-3} atoms/barn
C_2H_4	1.025 ± 0.004	9.761 ± 0.005	2.102 ± 0.009	8.41 ± 0.04	4.20 ± 0.02
	1.834 ± 0.011	17.240 ± 0.005	3.77 ± 0.02	15.08 ± 0.10	7.54 ± 0.05
	4.917 ± 0.004	47.193 ± 0.005	10.15 ± 0.02	40.60 ± 0.09	20.30 ± 0.05
C	0.500 ± 0.005	9.066 ± 0.005	4.45 ± 0.06	-	4.45 ± 0.06
	1.00 ± 0.01	17.480 ± 0.005	8.70 ± 0.06	-	8.70 ± 0.06
	2.50 ± 0.01	44.103 ± 0.005	21.97 ± 0.12	-	21.97 ± 0.12

number of fission reactions. The fragments produced are energetic charged heavy particles which start out stripped of many electrons; their very large effective charges produce a specific energy loss greater than any other radiation. The energy loss at the beginning of the track is at its maximum, and the rate of energy loss continues to decrease as the fragment slows down and additional charges are picked up. The pickup of electrons, begins immediately at the start of the track, and therefore the effective charge of the particle, z, continuously drops. The resulting decrease of the energy loss due to the reduction of the z is large enough to overcome the increase that normally accompanies a reduction in velocity.

The fission cross section was measured with two different detectors. It was necessary to use two chambers in combination due to the challenging energy range of interest, up to 1 GeV, which, translating energy in time of flight means 100 ns after the γ-flash. Along the neutron beam line ten fissile deposits were placed, in total, 59.771 mg of ^{235}U and they were stacked in a parallel plate avalanche counters (PPACs) and a parallel plate ionization chamber (PPFC).
The main advantages of the PPAC setup is their fast time response and the very low thickness of material present in the neutron beam. This last feature combined with the low gas pressure, makes the detector essentially insensitive to the γ-flash. However, it detects only fission fragments emitted into a forward cone with an opening angle of about 60° and its fragment detection efficiency is not easy to evaluate. On the other hand, the efficiency of detection of fission fragments of a PPFC is very well known but, due to the background events, it is impossible to detect events produced by neutrons with energy above 150 MeV. Therefore, the idea is to use both the detectors and evaluate through the PPFC the efficiency of the PPAC in the overlapping energy range of the chambers. This allows the measurement of fission fragments with the PPACs up to an incident neutron energy of 1 GeV.

3.4.1 Parallel Plate Ionization Chamber

Fission ionization chambers operate in the ionization regime, in which the signal is strictly related to the charge produced by ionization in the gas, for more details see [174]. This happens when the electric field between electrodes is high enough to collect all the charges produced by ionization and low enough to prevent the production of secondary pairs. In first approximation, the charge collected is independent of the

applied voltage. Provided that an appropriate distance between electrodes is chosen and that the ionization chamber operates at a suitable gas pressure it is possible to discriminate heavy fragments from light particles (because light particles are not stopped in the gas). Infact, the main source of background are the α particles from the target, but neutron-induced fission fragments produce much more ionization per interaction in the chamber; therefore, in the optimized working condition of the chamber, the signals produced by FFs are larger that those produced by any other competing reaction.
The basic features for a fission chamber are:

- the minimum amount of material in and around the neutron beam and in particular the thickness of the electrodes, the windows and the sample backing;
- a fast charge collection time in order to allow reliable operation at the very high instantaneous counting rates available at the n_TOF facility.

The fission chamber [175] used in the measurement, has been developed by Physikalisch-Technische Bundesanstalt (PTB). The PPFC is constituted by a stack of cells which contains the parallel plate electrode assembly, mounted one after the other along the direction of the neutron beam, as shown in figure 3.10. To minimize the effect of neutron scattering the construction is light-weight: all electrodes are in aluminium with a thickness of 10 μm, the windows are made of 2 μm thick kapton. A basic cell is made by three electrodes: the central one is plated on both sides with a fissile isotope, while the external ones are used to define the electric field in the gas-filled region. The chamber is operated at atmospheric pressure with a continuous gas flow

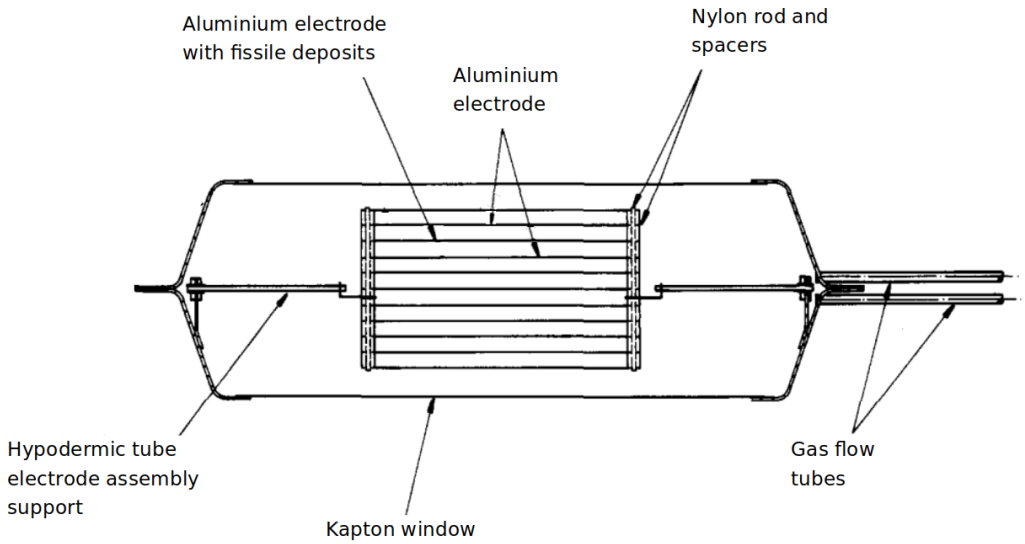

Figure 3.10: Schematic view of the multi-plate fission chamber developed from Physikalisch-Technische Bundesanstalt [175].

of mixture 90% argon and 10% methane. Eleven 86 mm diameter circular plates form the electrode assembly of the four aluminium supports where the fissile element is deposited. The separation between the electrodes is 5 mm and the overall length of

the chamber in the direction of the incident beam is 100 mm. These dimensions result from the usual compromise between the need for fast timing resolution and the need for a good discrimination pulses between fission fragments and α particles.

(a) (b)

Figure 3.11: Figure 3.11(a) shows in detail the placement of the uranium targets inside the chamber: in each plate two samples are arranged back to back. Photo 3.11(b) exhibits the mounting of the camera.

Description of the targets

8 UF_4 targets, 42.00 mm diameter, were arranged in pairs back to back, as shown in figure 3.11. The total amount of ^{235}U material is 32.660 mg.
The uranium thin film targets, one of them in figure 3.12(a), were prepared by molecular plating [176] by the Joint Research Centre in Geel (JRC-Geel). This technique consists in cathodic deposition of compounds from an organic solvent. It is generally performed in a cell containing two electrodes, where the cations are electrodeposited onto the working electrode.
The deposition of the ^{235}U material, on the Al substrate, 0.3 mm thick, was carried out using a constant voltage of 360 V in isopropanol. The anode is a platinum grid rotating at a speed of about 5 to 10 turns per minute. The cathode is connected to a holder including the Al substrate that determines the spot diameter of the ^{235}U deposit [177].
The available starting material for the production of thin uranium deposits is triuranium octoxide (U_3O_8). The U_3O_8 was dissolved in HNO_3 , evaporated to near dryness and thereafter re-dissolved in HNO_3 at a concentration related to the required amount to be deposited on the substrate and, at least, isopropanol was added. The molecular plating was stopped after 2 hours. The Al substrate with deposit was taken out of the cell and heated up on a hotplate for 5 minutes at 100° to evaporate the remaining isopropanol [178].
The uranium deposits were characterised by their morphology and elemental composition. The concentration of ^{235}U in the samples is 99.93%, the other isotopes present are: ^{234}U with a percentage of 0.035973(75)%, ^{236}U at 0.009629(53)% and ^{238}U at 0.02073(14)%. In addition, the uniformity of the deposits was studied by autoradiography. The targets were placed on a film with a x-ray sensitive thin layer; the resulting

image is proportional to the uranium distribution in the sample. One of the 8 image obtained is shown in figure 3.12(b). The convolution between the spatial distribution of the neutron beam and the point of impact of the neutron beam in the target results, in a total, density that is 8% higher than the nominal density (2.3574 mg/cm^2).

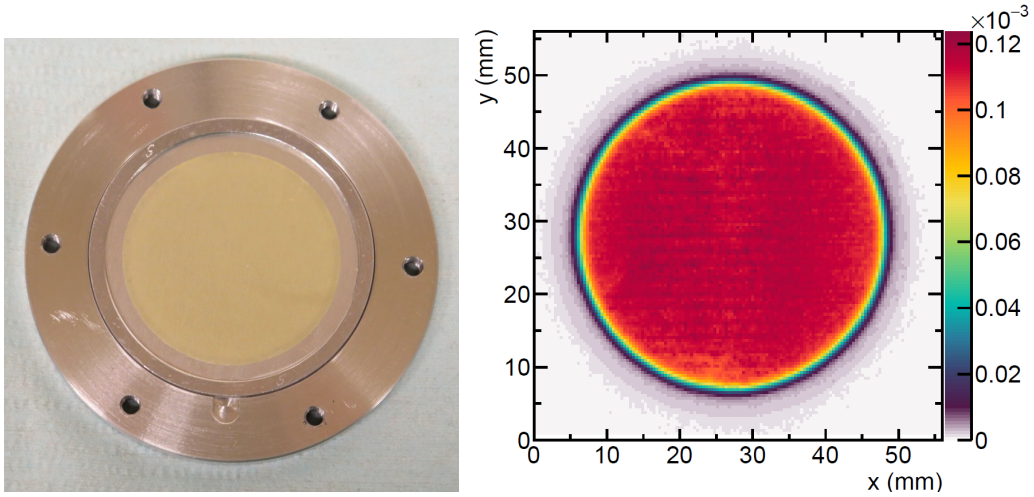

(a) (b)

Figure 3.12: 3.12(a) shows one of the 8 uranium targets placed inside the fission ionization chamber. The color histogram, in figure 3.12(b), is one of the autoradiographies of the sample, proportional to the mass distribution of the sample itself.

3.4.2 Parallel Plate Avalanche Counters

The Parallel Plate Avalanche Counter (PPAC) is a type of gas detector that operates in avalanche regime, which is defined by a combination of gas pressure and electric field. The counter consists of 3 parallel plate electrodes, a central anode surrounded by two cathodes, separated by a gap that is normally kept as small as possible in order to maintain a high electric field and to reduce the time spread, leading to a good time resolution. The electrodes are enclosed in a container in which a gas is introduced, and a constant electric field is produced between the plates.

The basic operating principle involves a charged particle that crosses the gap between the plates leaving a track of primary ions and electrons which drift to their respective collecting electrodes. During their drift the electrons are multiplied through the usual gas multiplication process creating a swarm of electrons that drift to the anode (for a thorough discussion see [174]). The shape of the output signal consists of a fast component, typically of the order of nanoseconds, generated by the electron collection, and a much slower component produced by the motion of the positive ions. Only the fast component is used for timing purposes, while the slow component is suppressed by the short time constant of the collection circuit. PPACs present great improvements over other types of detectors with regard to their time resolution, which is typically less than 1 ns, but can reach values below 200 ps. PPACs are widely used to detect fission fragments [180, 181]; in facts even in the environments with high levels of background they

are transparent to long-range particles as neutrons, photons and electrons. Although the detectors are sensitive to α particles, which are a common source of background when the targets are actinide nuclei, they provide good pulse-height discrimination between the α particles and the fission fragments.

The detectors used for fission at n_TOF were designed and built at the Institut de Physique Nucléaire d'Orsay, France (IPN) [182]. The space between the anode and each cathode is 3.2 mm, filled with forced flow of octofluoropropane (C_3F_8) maintained at low-pressure (4 mbar). The electrodes, with an area of 20×20 cm^2, are made of 1.7 μm

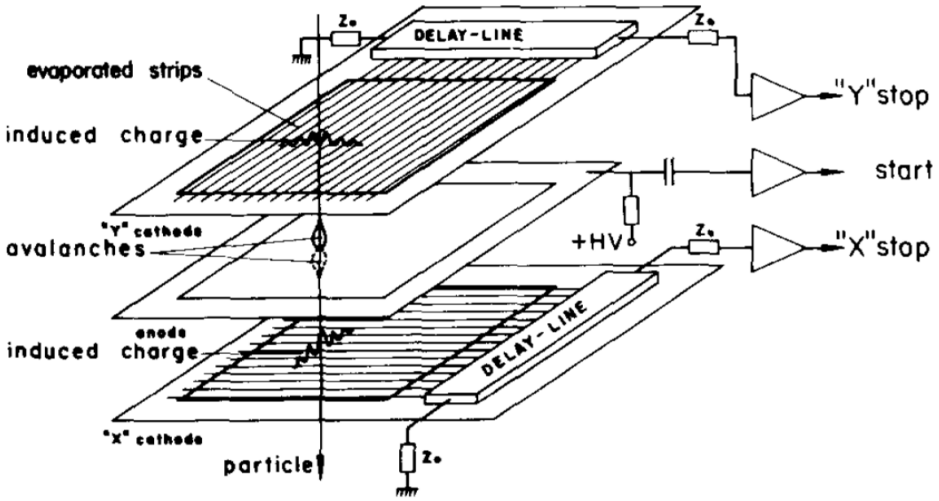

Figure 3.13: Schematic view of a position-sensitive PPAC with a common anode and two stripped cathodes [183].

thick mylar foils, coated with gold, 700 nm thick, to make them conductive. For the anode the coating is uniform and double sided, whereas for the cathodes the coating is divided into 2 mm wide strips. The golden strips have a width of 1.9 mm and with a distance of 0.1 mm between two adjacent strips. The gold deposition was performed by evaporation, under vacuum, using 0.1 mm thread masks. The strips allow a localisation of the avalanche by using a delay line; the time difference between delay line outputs provides a one-dimensional position. By combining the signals from the two stripped orthogonal cathodes, the fission fragment trajectory can be reconstructed. The active area of the detector and a detailed view of the delay line are shown in figure 3.15. The detector design of a PPAC consists of a common anode and two stripped cathodes in orthogonal directions, as illustrated in figure 3.13. The avalanche produced induces a positive pulse in the cathode strips closer to the avalanche position. Each strip acquires part of the induced charge and the centroid of the charge distribution provides accurate information about the position of the avalanche thanks to the measurement of the delay time between the pulse on the anode and the pulses propagating along the delay lines. The delay line consists of a 20 cm of plastic rod with a coiled copper wire and an intermediate space of 6 mm at each side connects the delay line to the preamplifiers.

The frame is made of a kind of epoxy resin, which is coated with a thin metallized layer of copper, gold plated to prevent copper oxidation, in order to shield the detector against electromagnetic noise.

The design of this PPAC allows us to detect in coincidence the two fission frag-

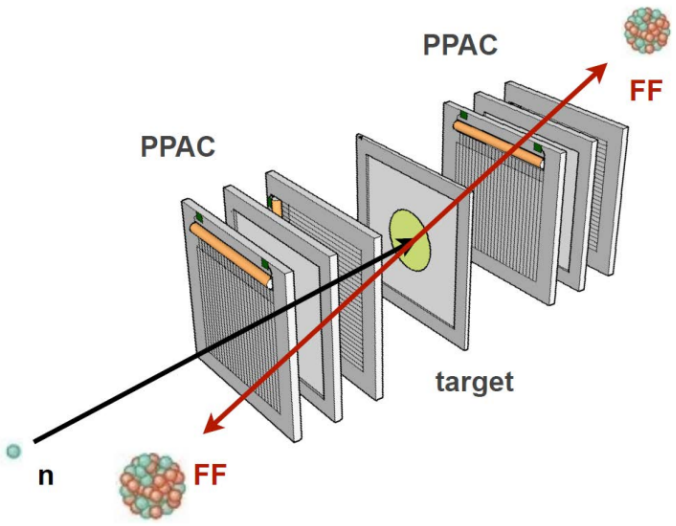

Figure 3.14: Fission detection using PPACs surrounding the target. The fission fragments emitted from the target cross the two detectors, back to back, which are closer to the sample.

ments emitted in the fission process. In such a way a high signal-to-background ratio is obtained. In order to apply the coincidence technique, a detection cell is made of a uranium sample surrounded by two PPACs, as sketched in figure 3.14. As a consequence, the backing supporting the deposited layer of the isotope being measured has to be thin enough to allow the backward-emitted fragment to be detected. The fission reaction chamber, used in the measurement of the ^{235}U(n,f) cross section, consisted of three PPACs with two ^{235}U samples in between.

The entire detector setup is confined in a reaction chamber to keep the right pressure. The enclosure consists of a cylindrical aluminum chamber. The two flanges, 90 mm of diameter, for neutrons entrance and exit of neutrons, are made of a 75 μm kapton foil, to ensure the sealing of the chamber and minimize the material in the beam.

Electronics

Two different types of preamplifiers have been used in the PPAC detectors. Those connected to the anodes are simple current amplifiers, which are used to get an enhanced signal as fast as possible. They are implemented to cut the large time tail coming from the positive ions, so that only the electron fast signal is used. The cathode signal, instead, is a charge amplifier and it is used in such a way that a circuit with only resistive impedance is obtained.

Both types of preamplifiers have been designed at the IPN d'Orsay, optimising their behaviour for the detector signal expected from the fission fragment ionization. Their

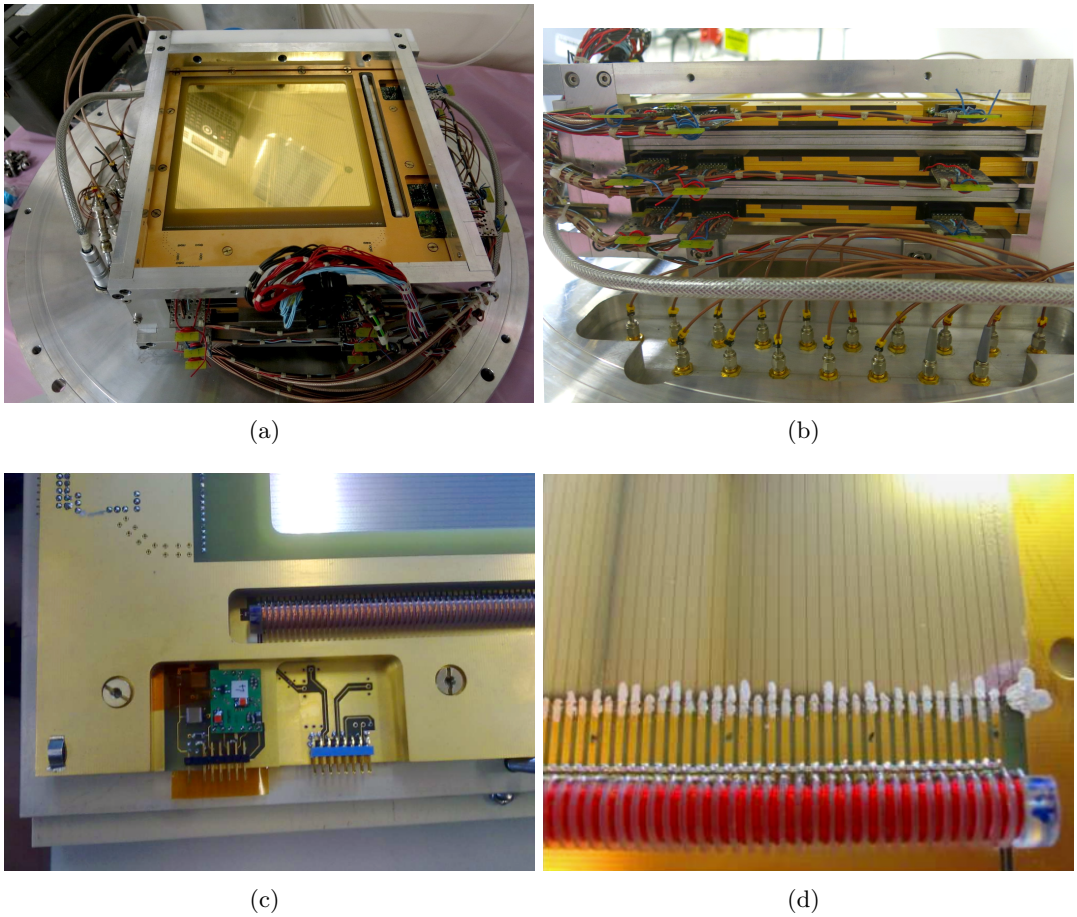

(a) (b)

(c) (d)

Figure 3.15: Photographs of a PPAC detector. Figure 3.15(a) shows the active area, 20×20 cm^2. Figure 3.15(b) shows the three PPACs with the uranium samples placed between them. A detail view of the delay line and the readout preamplifiers is shown in figure 3.15(c), while the connections to the strips are shown in photo 3.15(d).

small size is well-suited to fit inside the PPAC frame, figure 3.15(c).

Description of the targets

During the measurement campaign at n_TOF, two uranium samples, in total 27.11 mg of fissile material, were used in the PPACs detector. The targets were produced by the radiochemistry group at the IPN d'Orsay. The targets were made of a thin radioactive layer (around 0.3 mg/cm^2) deposited as an 80 mm diameter disk over aluminium foil, 2 μm thick. The aluminium foil was glued to a 1.5 mm thick epoxy frame with a 120 mm diameter centre hole in which the target had to be placed. The material was deposited by a chemical method known as molecular plating: a nitrate of the element is dissolved in isopropyl alcohol with a small amount of water. A 600 V potential is then applied for 15 minutes between a platinum foil and the aluminium foil used as backing to obtain by electrodeposition an adequate amount of each material on the aluminium support. The material is then stoved during few hours to remove the residual alcohol and water. The resulting deposits are in the form of oxides (UO_2).
An accurate knowledge of the thickness of the deposited material and its inhomo-

geneities is required for a reliable determination of the absolute cross section. From a mass spectrometry analysis the purity of the targets and the total number of nuclei was measured with an accuracy better than 1%. The ^{235}U samples have a purity of 92.699(5)%, the remaining 7.300(5)% is divided among isotopic impurities of ^{238}U (6.283(6)% in number of atoms), ^{234}U (0.7472(15)%) and ^{236}U (0.2696(5)%). The thickness of the radioactive targets is measured by counting α radioactivity at large distances with a collimated silicon detector, taking into account the presence of impurities by a selection in the energy spectrum of the α particles. In the case of ^{235}U, the recorded events came from the impurity of ^{234}U that is present. This technique has a spatial resolution of 3.5 mm (in x and y); the result for one of the samples is shown in figure 3.16(a). Furthermore, the uranium samples were exposed to a 2 MeV proton beam and the thickness was studied by exploiting the Coulomb scattering, with a step of 1.5 mm in the x and y position. The result of the analyses is reported in figure 3.16(b). The spatial distributions of the thickness of the uranium in the samples

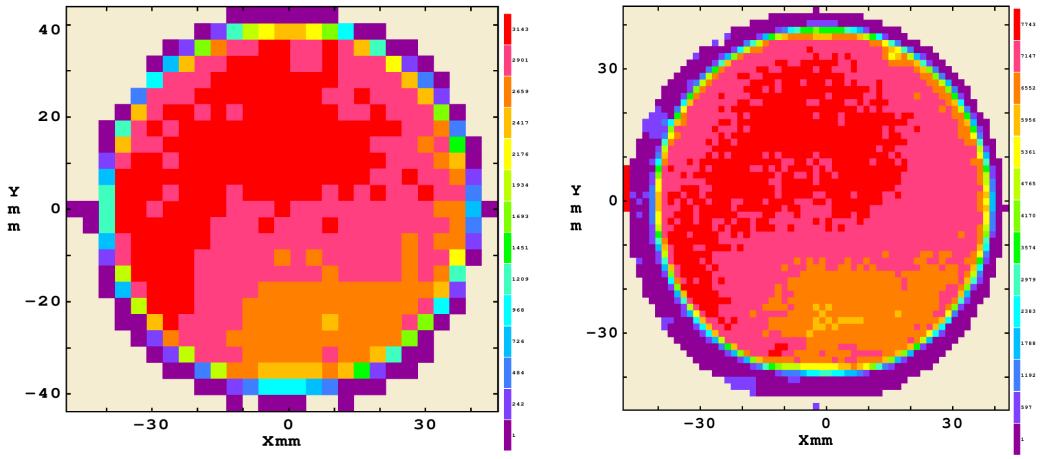

(a) (b)

Figure 3.16: Characterization of the thickness of the deposited material of one of the samples of ^{235}U used in the measurement. In figure 3.16(a) was measured the α radioactivity from ^{234}U isotope. In figure 3.16(b) was studied the sample thick through the Coulomb scattering using a 2 MeV proton beam.

extracted through the two methods are compatible within the 1% (taking into account the difference in resolution). Hence, where the ^{235}U targets are hit by the neutron beam the thickness of the sample is (1.015 $\pm$ 0.001) mg/cm^2 larger than the average, which is 0.28 mg/cm^2.

3.5 The whole experimental setup

Figure 3.17 shows the scheme and the photo of the final experimental setup including two detectors to count the fission events from the uranium targets and, at the same time, three detectors to measure the neutron fluence. Ten fissile deposits were placed in the neutron beam, for a total of 59.771 mg.
Downstream of the fission chambers two polyethylene samples, mounted along the

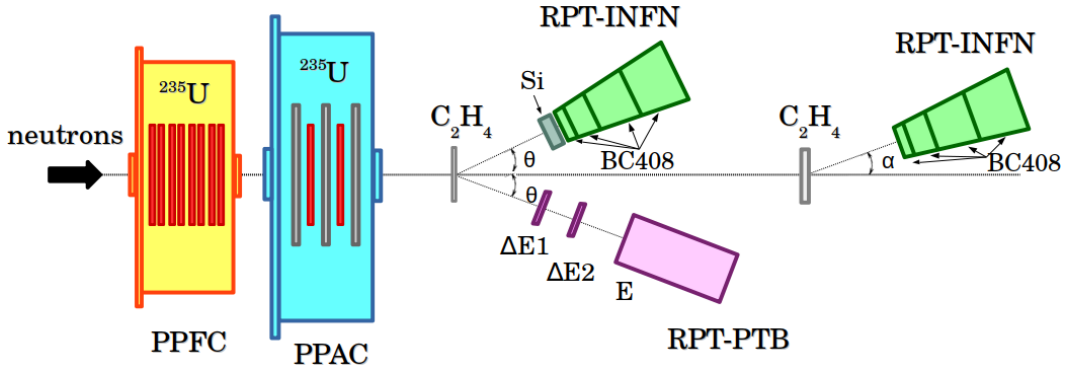

(a)

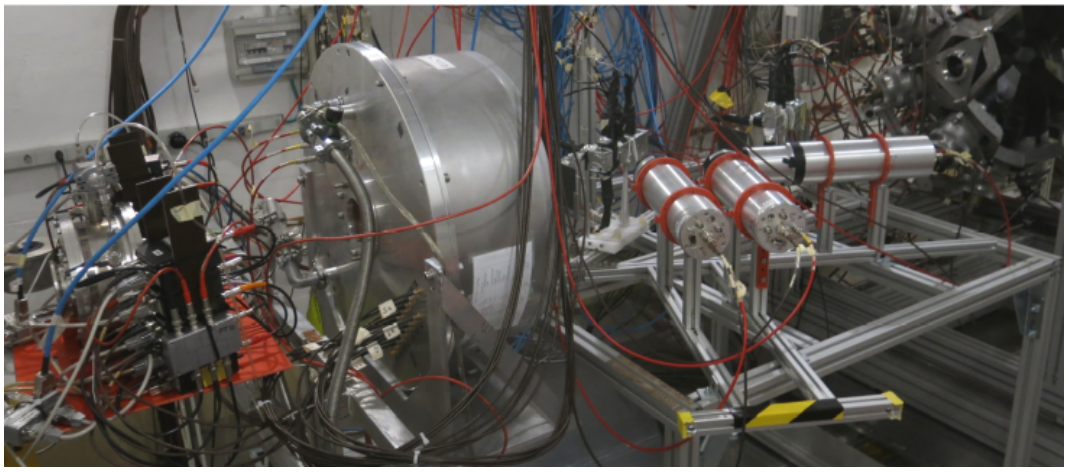

(b)

Figure 3.17: Scheme 3.17(a) and photo 3.17(b) of the setup used at n_TOF for the absolute measurement of the ^{235}U(n,f) cross section. Fission events were measured with a Parallel Plate Ionization Chamber (described in section 3.4.1) and a set of Parallel Plate Avalanche Counters (described in section 3.4.2). Recoil protons were detected and identified in three different telescopes (described in section 3.3.1 and 3.3.2), placed at a small angle outside the neutron beam.

neutron beam, act as targets for the neutron beam for triggering the proton-neutron elastic scattering reaction. Two telescopes, RPTL-INFN and RPT-PTB, were mirrored at the same angle, 25°, with respect to the beam direction, pointing to the same target of C_2H_4. The third one, RPTH-INFN, placed at a smaller angle, 20°, pointing at the other C_2H_4, was used to increase the statistics of the high energy region (from 100 MeV upwards). In fact, the telescope was coupled always with the thicker targets to increase the number of events increasing the number of areal density of the sample. The angles were chosen as a trade-off between the need of a reasonable counting statistics and while avoiding to interact with the primary neutron beam.

The use of three detectors, besides tripling the statistics of events, allow one to reduce the systematic uncertainties. This last effect is obtained as a consequence of using two detectors based on different design and analysis at the same angle, and a third one positioned at a different angle respect to the others two.

3.6 The measurement campaign

The experimental campaign for the measurement of ^{235}U(n,f) cross section took place during September 2018 and required a five-week beam-time. During this period, the proton current was monitored with the pick-up detector system based on the wall current monitor (WCM) of the CERN Proton Synchrotron.
The total accumulated statistics by the two fission detectors are shown in table 3.3 with the time dedicated, expressed as protons on target (pot) and days.

Table 3.3: Details of time allocation for the ^{235}U experiment.

Sample	PPFC		PPAC	
	# Protons (pot)	Running time	# Protons (pot)	Running time
^{235}U	3.387×10^{18}	35 days	3.83×10^{18}	40 days

In order to determine the neutron flux some auxiliary measurements to accurately characterize the background were carried out.

- In order to subtract the contribution from carbon reactions, measurements with a C sample were performed. To minimize the differences in the number of centres and the self-absorption of the sample itself and to be able to have a background subtraction as accurate as possible, for each polyethylene thickness an appropriate thickness for the carbon target was chosen.
- To correct for time-dependent background, induced by the neutron beam, measurements were carried out without samples in the beam (hereafter is referred to as Sample-Out measurements). Data were taken with the sample out and also with the first target in and the second out to measure the events coming from the first target and recorded by the telescope pointing at the second target, and vice versa with a measurement with the first sample out and the second in.
- Beam off measurements were carried out to characterize the room background and the activity of the sample and air.

In the table 3.4 the different measurements with the dedicated time, expressed as protons on target (pot) and days, summarized.

3.6.1 Alignment of the setup in the beam

A crucial point of the measurement is the alignment of the experimental setup with respect to the neutron beam. In particular this step is important for the telescopes, since these detectors count the emission of protons at a fix laboratory angle ϑ_p.

Table 3.4: Details of time allocation for the neutron flux measurement in the ^{235}U fission experiment.

Sample	RPTs at 25°		RPT at 20°	
	# Protons (pot)	Running time	# Protons (pot)	Running time
C_2H_4 - 1 mm	7.08×10^{17}	7 days	-	-
C - 0.5 mm	3.27×10^{17}	3.5 days	-	-
C_2H_4 - 2 mm	1.11×10^{18}	11 days	-	-
C - 1 mm	3.88×10^{17}	4 days	-	-
C_2H_4 - 5 mm	7.44×10^{17}	8 days	2.07×10^{18}	20 days
C - 2.5 mm	3.14×10^{17}	3.5 days	1.55×10^{18}	16 days
Sample Out	1.48×10^{17}	1.5 days	2.23×10^{17}	2.5 days
Beam Off	-	0.25 days	-	0.25 days

Therefore, for the extraction of neutron flux, the knowledge of the elastic scattering differential cross section, $d\sigma/d\Omega_p$ evaluated at the actual angle at which the detector is positioned, is necessary. In addition, the efficiency of the RPTs depends on the solid angle they subtend and therefore on their distance from the target.

For these reasons, before the start of the data-taking period, the support of CERN surveyors was commissioned to define the exact angle and the positions of the three telescopes. The survey group used the Leica Absolute Tracker AT401 [184] which is composed by a light source and a reflector. A laser beam is projected from the system to a reflector, with both the exiting, and returning beams being monitored. Moving the reflector, the return beam moves, and the wave peaks cross each other creating a superposition wave; from the laser emission wavelength is possible to calculate the exact absolute distances (in a 3D coordinate system) from the starting point (where the laser source is located).

The positions of the various elements were evaluated using the coordinates system with respect to the "real neutron beam line". The neutron beam position had been identified with a resolution of a tenth of a millimeter by a Quads Timepix detector [185, 186], produced by the CERN based Medipix2 collaboration. This kind of detector is based on a silicon sensor and works like a camera, detecting and counting each individual particle hitting the pixel. The Timepix detector consists of a pixellated silicon sensor of 256×256 pixels. Each pixel measures 55×55 μm^2 and it is individually bump bonded to a corresponding 300 μm thick silicon sensor, the Timepix Application Specific Integrated Circuit (the Timepix ASIC). The Timepix measurement was carried out before the start of the experimental campaign. The detector, placed in the neutron beam produces a cluster of pixel hits when a charged particle crosses the sensor. This cluster corresponds to the particle's track in silicon convoluted with the subsequent charge transport through the silicon sensor and signal induction on the pixel electrode.

From the measurements the surveyors obtained the position in space of the two polyethylene targets, of the detectors and the angles between the axis of the detectors and the z-axis: the angles α, β, γ reported in the sketch 3.18. The accuracy of the measure-

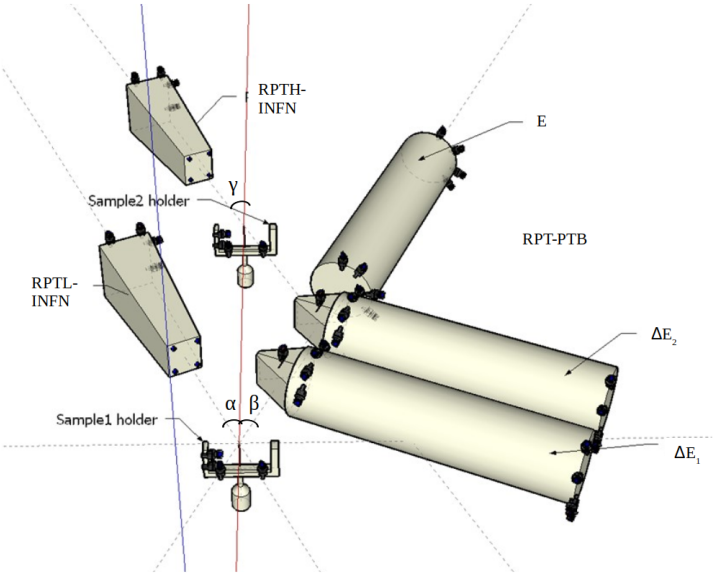

Figure 3.18: Sketch of the experimental neutron flux configuration: the two sample holders and the three RPTs pointing at the two targets with an angle of α, β and γ for the RPTL-INFN, RPT-PTB, RPTH-INFN respective. In red the z axis of the coordinate system.

ments performed is 0.15 mm (one sigma level).
The obtained results obtained are reported in the table 3.5.

Table 3.5: The geometrical calculation of the three telescopes.

Detector	Angle	Detector-target distance
RPTL-INFN	$\alpha = 25.07°$	15.74 cm
RPT-PTB	$\beta = 25.29°$	22.33 cm
RPTH-INFN	$\gamma = 20.32°$	21.6 cm

Moreover, the position of the fission chambers and the C_2H_4 samples with respect to the neutron beam were verified by the use of the GAFChromicEBT-3. The gafchromics foils, based on the thermoluminescence principle, are designed for the measurement of absorbed doses of ionizing radiation: when the active component is exposed to radiation, it reacts to form a dark polymer.
Four gafchromics foils were placed in the flange of both chambers and in the two sample holders. A gold foil was placed in front of each gafchromics in order to accelerate the process of beam impression (that results from charged particles produced by neutron interaction with Au).

The photos in figure 3.19 clearly show the image of the neutron beam after 10 hours of exposition. This procedure allows one to determine the position of the beam with an uncertainty of $\pm$ 2 mm.
The neutron beam position found with the gafchromics foils and the ones measured

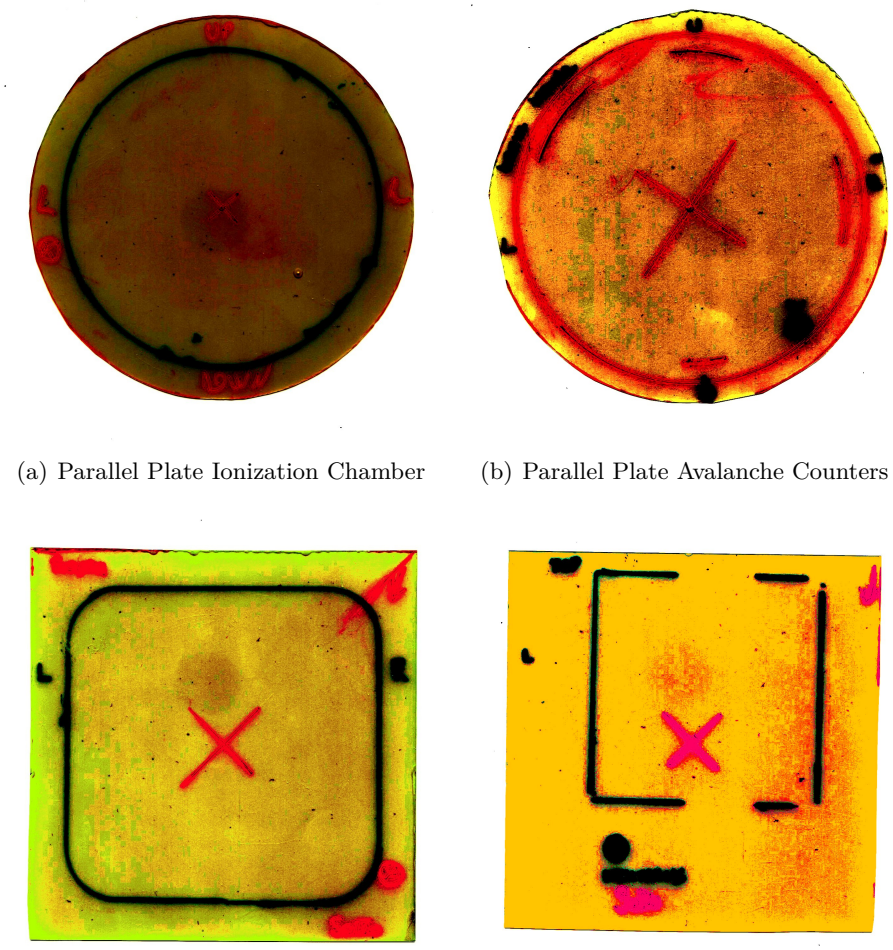

(a) Parallel Plate Ionization Chamber (b) Parallel Plate Avalanche Counters

(c) 1st polyethylene sample position (d) 2nd polyethylene sample position

Figure 3.19: Gafchromic foils were placed on the flanges of the fission chamber and in the place of the polyethylene targets for the alignment with respect to the neutron beam. The figure shows the processed images of the four gafchromics foils used before the beginning of the campaign.

with Timepix are perfectly consistent within the uncertainties.

The real point of impact of the neutrons in the uranium targets and the polyethylene targets was verified by two independent methods because, as said before, it is a fundamental ingredient for the evaluation of the efficiency of the detectors.

Chapter 4

Analysis of fission events

The description of the PPACs detector and its performances are reported in details. Every time a proton bunch is delivered to the n_TOF spallation target the Data AcQuisition system (DAQ) reads out 15 channels, limited to the PPAC detector, i.e. 5 channels per PPAC: 1 anode, 4 delay lines (top, bottom, right, left), during a few ms. The first important step is the data reduction method used to distinguish the fission fragments from the α and light particles, which constitute the main background. To this end a method based on the coincidences between the two PPACs surrounding the same uranium target was implemented. In order to obtain the fission cross sections it is necessary to know the total efficiency of the detector and its dependence on the neutron energy. Then, from the events in coincidence scaled down by absolute detection efficiency, we obtain the counts of events recognized as real fission events, attaining all the needed elements to extract the fission cross section of ^{235}U.

4.1 Signature of fission events

In order to understand the building process of fission event, it is worth reviewing briefly the operation of the PPAC detectors. A PPAC is a very thin gas detector, practically insensitive to gamma rays and neutrons but virtually 100% efficient for the detection of massive charged particles that cross it, such as fission fragments. It means that we can place the PPAC detector on the neutron beam line without affecting it significantly. The setup used for this experiment, shown in figure 4.1, included two targets interleaved in three detectors. Each target is flanked by two PPACs which are close to the target (less than 2 cm); so that the two fission fragments emitted in opposite directions hit both PPACs almost simultaneously. Therefore, two anode signals inside a time coincidence window are the signature of a fission event. This time coincidence condition makes possible to reject most of the background produced by the α emission of the radioactive targets and by spallation reactions induced by fast neutrons in the materials surrounding the samples.
With this experimental layout, different types of fission events were defined to describe the cases where two or three detectors are fired by the two complementary fission

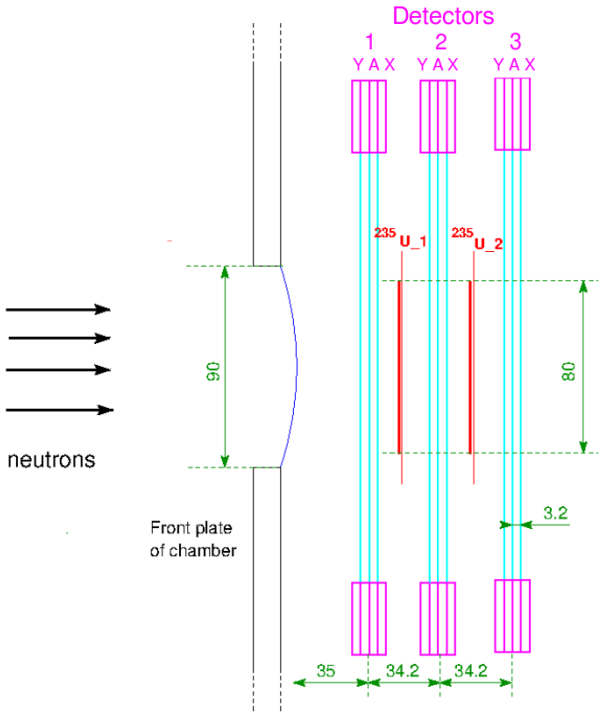

Figure 4.1: Schematic view of the experimental setup with three PPACs and two ^{235}U targets in between. All dimensions are expressed in mm.

fragments, and are named type 2, and type 3, according to the number of detectors involved. A schematic description of each type is shown in figure 4.2. The main part of the event-building process consists in identifying which signals belong to the fission fragments coming from a fission event in the target of interest and distinguishing them from signals produced by other fission products or background signals. This ambiguity can be resolved by measuring the time that the fission fragments need to reach the different detector. Hence, for the different types of fission events, the time differences (correlations) among the involved detectors are a crucial part of the analysis. In order to handle the raw data files, recorded by each detector at every neutron pulse and stored in CASTOR, the Signal Analyzed software (already illustrated in the section 2.8) is used to obtain the true signals recognition.

The PPAC data are characterized by an evident oscillation of the baseline. However, by looking at figure 4.3, the differences in frequency and rise time between the real signals and the variations of the baseline are evident. It turned out that a neat identification of the peaks is possible even if the derivative of the signal is not enough. Indeed, the derivative amplifies the high frequency component, thus increasing the noise which appears as a low level fluctuation spanning over multiple time samples. To avoid this drawback and clean up the frames, a high-frequency filter was added to the reconstruction routine before the calculation of the derivative. In this way, the oscillations of the baseline were removed. From a specific routine written for the PPAC signals, out of the signal analyser two parameters are saved for each signal: the time and the amplitude.

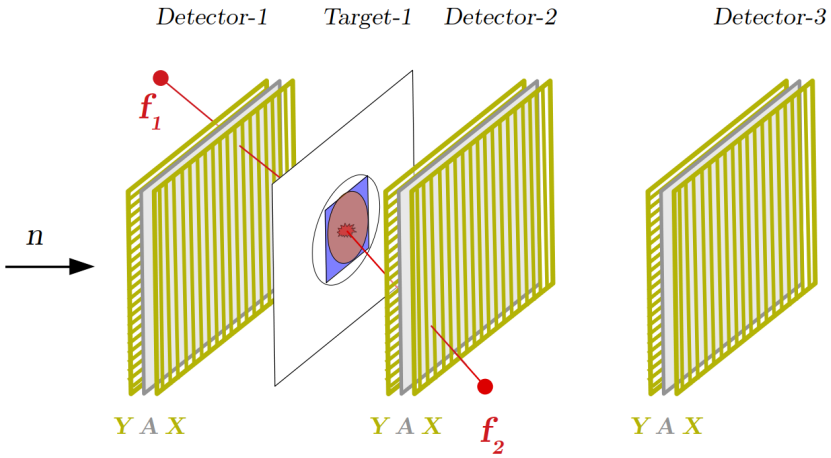

(a) Two anodes in coincidence - Type 2

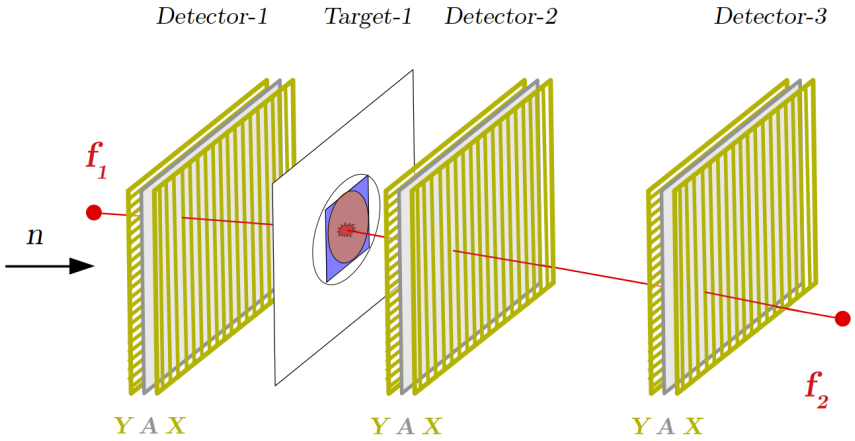

(b) Three anodes in coincidence, target allocated in-between the first anode couple - Type 3 left

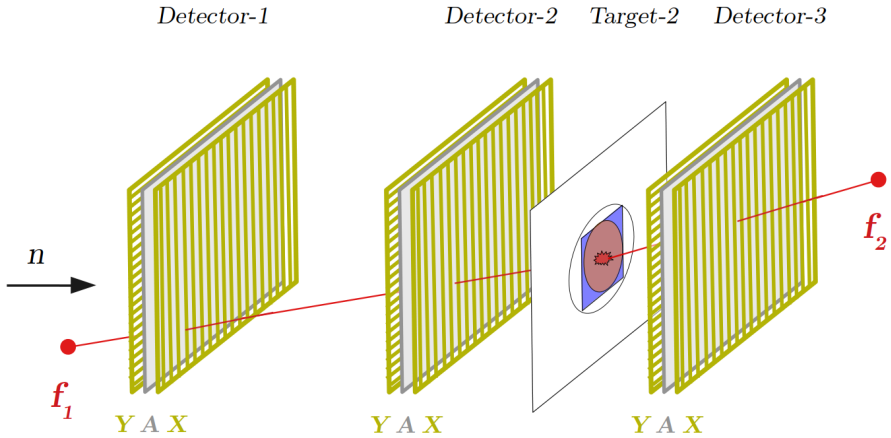

(c) Three anodes in coincidence, target allocated in-between the last anode couple - Type 3 right

Figure 4.2: Description of the possible cases for fission fragments at the PPAC setup. Only the target where fission happens is represented with the involved detectors.

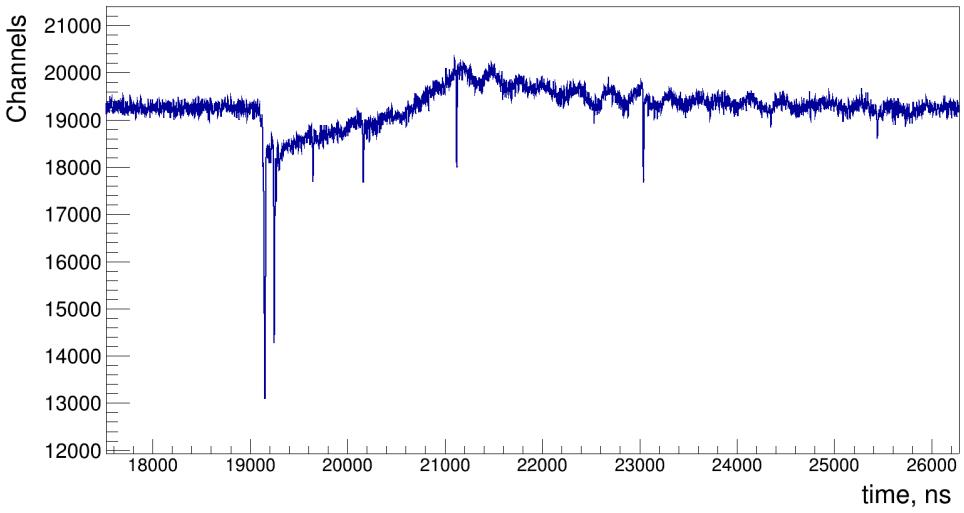

Figure 4.3: An anode raw data before the derivative filtering.

The fission identification, described later, is based on the time coincidence between adjacent detectors, hit by the two fission fragments coming from the same fission reaction (complementary fission fragments) and requires time coincidences of only a few nanoseconds accuracy. Thereby, a crucial point in the search for time coincidences between the anode signals, requires a good temporal accuracy. The precise time-calibration required to synchronize the channels is guaranteed by the common clock of all SPdevice modules.

4.1.1 Anode signal coincidences

The algorithm implemented to look for the coincidences uses a coincidence time-window between adjacent detectors of 20 ns, large enough to contain not only the signals from the complementary fission fragments, but also the signal produced by the same fragment crossing a second detector. Starting from an anode peak of one detector a time window is opened to search for coincidences in the anode of adjacent detectors. If only two adjacent detectors are in coincidence the emitting target is the one between the two detectors. This happens in most of the cases ($\sim$ 2/3 of the fission events). But, as already noticed, some fission fragments may cross more than two detectors, in this case three detectors appear to be in coincidence and there is an ambiguity on the emitting target, which has to be identified. This is the price to pay to minimize all thicknesses of detector material. The basic idea, to solve this problem, relies on the fact that when a fission takes place in the target between two detectors, the fission fragments reach each detector almost at the same time. Indeed, they have to travel the same distance between the target and the detector. This synchronization is not perfect because the velocity of the two fission fragments is not the same due to the asymmetry of mass distribution, and the length they have to cover may not be exactly the same due to the angle of the trajectory (it can be more than 2 cm, and as high as 7 cm). Instead, when a fission fragment passes through one detector and reaches the next one,

the time of the hit in the third anode is delayed by the time required to travel between the two detectors. Therefore, the observation of the time differences between adjacent detectors allowed us to disentangle the emitting target.

Figure 4.4 shows the amplitude of the events in the first anode, in coincidence between

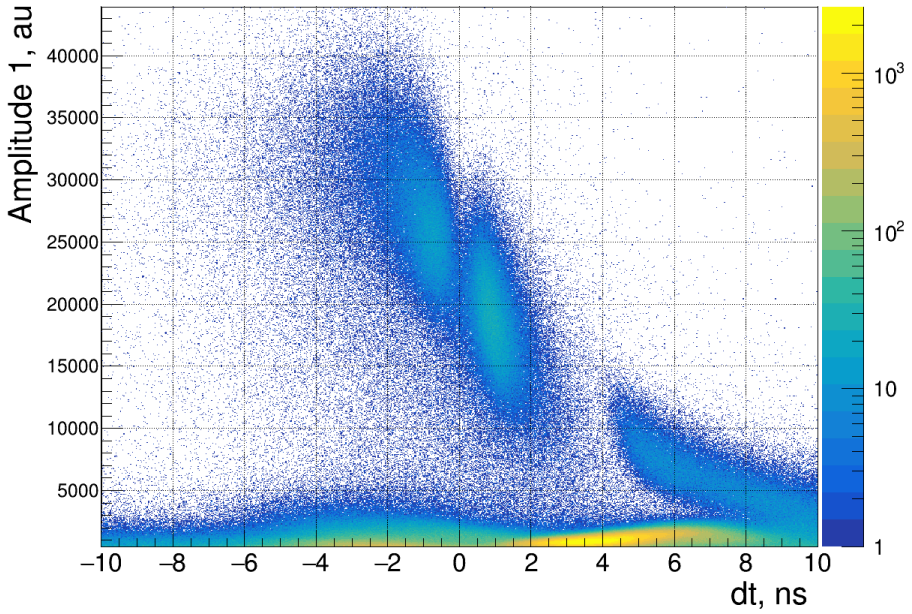

Figure 4.4: Correlation between amplitude on detector 1 with the time difference between detector 2 and 1.

the detector 1 and 2 surrounding the first target, versus the difference in time between the two detectors. The spot, at $\Delta t \sim 0$ corresponds to the fission fragments emitted by the first ^{235}U target. The two bumps indicate the asymmetric nature of the fission process: the spot at higher amplitude is due to the case where detector 1 is hit by the lightest fragment and detector 2 by the heaviest; the lowest one is for the reverse case. The relative position of the two fragments, in the figure, may seem counter-intuitive. However, this is attributable to the characteristic mean energy loss per distance travelled ($-dE/dx$) by the FFs, which is in the $\beta\gamma < 0.03$ region. Here the energy lost in the medium is proportional to the energy of the particles and the dependence with Z is reduced at the second level.

The signals at about 7 ns are due to the fragments coming from the second ^{235}U target, as indicated by *type 3 right* in figure 4.2. The amplitude is low because the fragment had to pass through an additional target and detector to reach detector 1. In the analysis a time selection of ± 4 ns allowed us to select the fragments emitted by the first target only.

In addition, figure 4.4 shows a background component at low amplitude coming from 2 different phaenomena. First, the typical α-radioactivity produces a contribution constant over the whole energy range, therefore, these events are generated by α particles crossing two or three detectors and recognized as a coincidence. Second, there can be

present low signals produced by spallation processes. In fact, this latter contribution is mainly present at small time of flights, which means at high energy, and especially above 10 MeV. More in detail, above 10 MeV reactions on low-Z elements of dead layers (C, O from mylar, Al in backings and electrode coating) take place, producing several light ejectiles and light spallation residuals as recoils. Most of them can be rejected by requiring the coincidence. Nevertheless, the counting rate due to these spallation reactions is very high and it produces coincidences between consecutive detectors. The

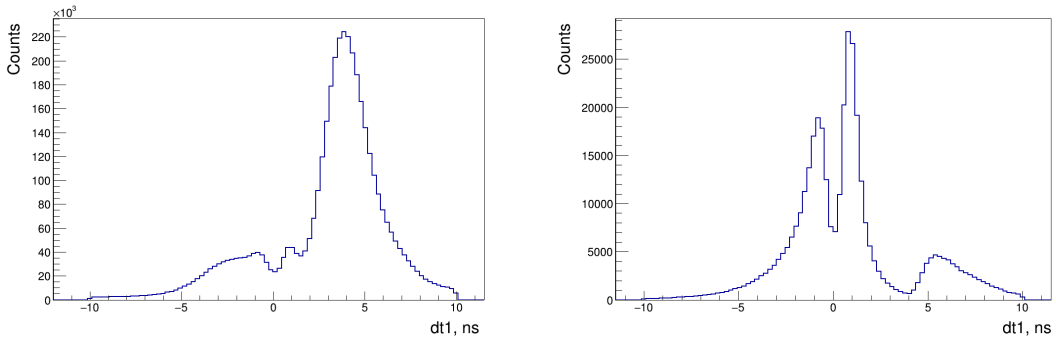

(a) (b)

Figure 4.5: On the left: the distribution of the time differences of the events in coincidence between the first and the second anodes. On the right: the counts in figure 4.5(a) filtered through the amplitude threshold condition.

time differences of the events in coincidence between the first and the second anode are displayed in figure 4.5. It is possible to appreciate how much the distribution changes adding a simple amplitude threshold, in figure 4.5(b), which allows us to remove all events generated by α and other light particles, which are, instead, dominant in figure 4.5(a). In graph 4.5(b) one clearly sees the two peaks, centered at zero, which are produced by the two fission fragments from the first target of uranium and the third lower peak, at higher times, coming from fragments from the second target.

The identification of the background events is even clearer in figure 4.6, where the sum of the amplitudes of the first and the second anode is reported as a function of time of flight. The sum of the two low-amplitude background contributions are evident as well as the higher number of low energy events in the low-time-of-flight region.

The application of a short coincidence time window allowed us to discard most of these parasitic events. However, a fraction is still remains in the data and can be removed by applying a threshold to the sum of the anode amplitudes.

By using the information of the two detectors around the emitting target, it is possible to plot the correlation between the two anode amplitudes, relation shown in figure 4.7. The two bumps of the asymmetric fission are clearly visible. The events placed in the corner distinctly correspond to low-amplitude events in both detectors. From this picture it turned out that the sum of both amplitudes allowed us to better discriminate true fission events from background.

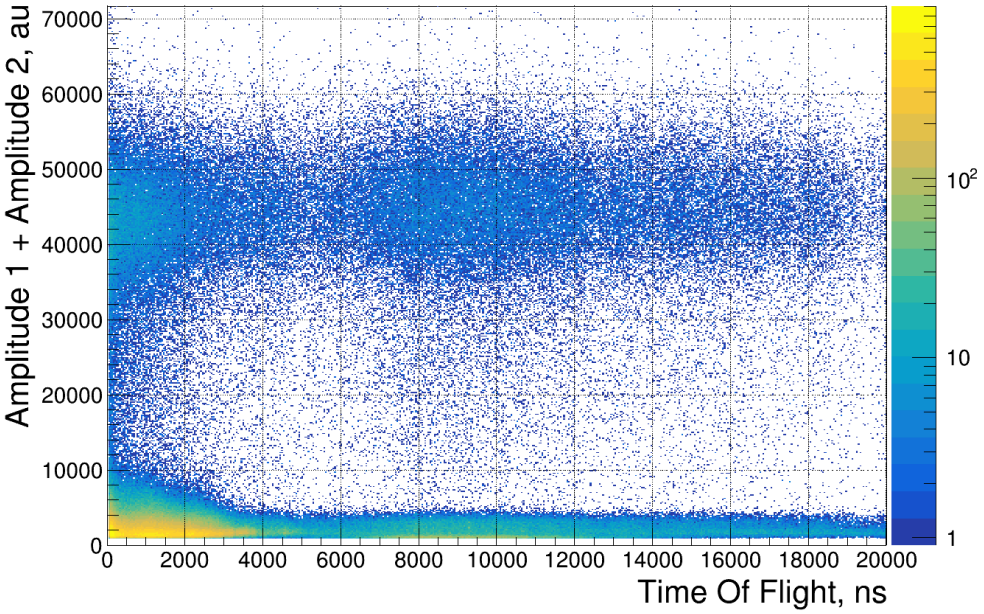

Figure 4.6: Distribution of the sum of anode amplitudes in the detector around the first ^{235}U target as a function of the neutron time of flight.

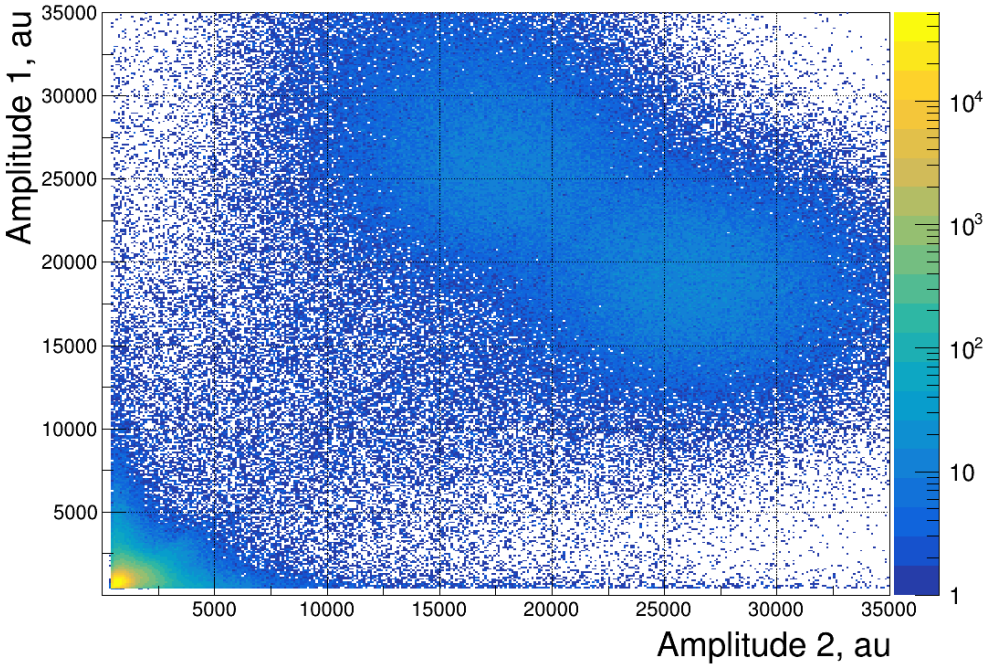

Figure 4.7: Correlation between anode amplitudes of the first and second detectors.

4.1.2 Cathode signal coincidences

As mentioned in section 3.4.2, each PPAC detector has two segmented cathodes with strips oriented in perpendicular directions. Therefore, a particle crossing the detector produces signals in both cathodes, enabling its localization. The strips are connected

to a delay line where the signals propagate in both directions, eventually reaching their corresponding preamplifiers. The combined data from both cathodes allowed us to know the detector-crossing position (x, y) of the hitting particle in the uranium target with an resolution of 1.4 mm.

Figure 4.8 shows an example of a fission event occurring in the first sample with fragments crossing detectors 1 and 2. The signals related to the three anodes are in black, red and green for the first, second and third detector, respectively. The localisation signals (cathode), of the second PPAC, are depicted in blue and purple. The cathode signals are delayed with respect to the relative one in the anode, as they travel through a delay line. It can be noticed that the peaks of the same delay line are of almost equal amplitude. This is due to the fact that they originate from the same signal (induced current on a strip) and that the attenuation of the delay line is low.

The time difference between both signals, read at the ends of the same cathode, pro-

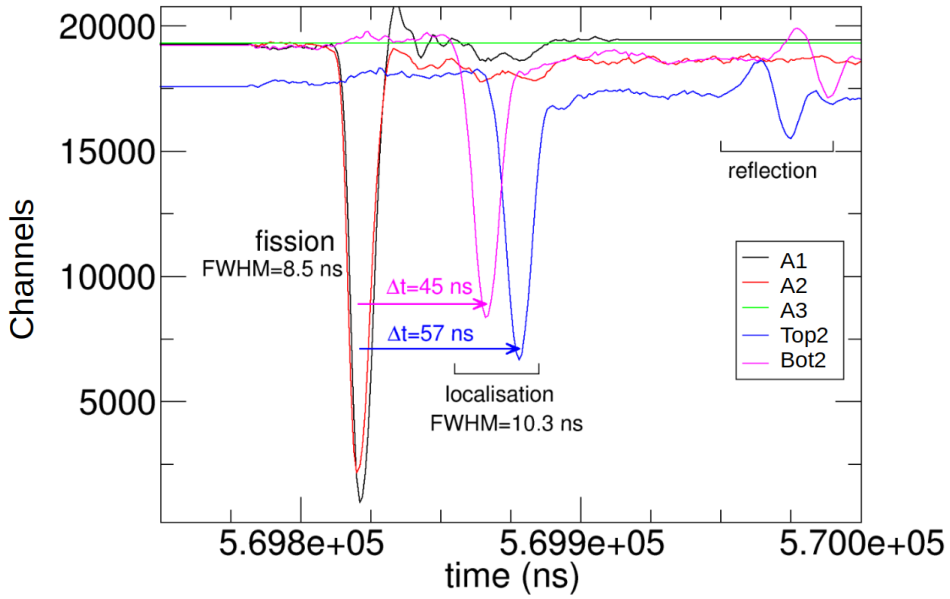

Figure 4.8: The signals from the 3 anodes of the detector and one cathode, read from both sides. In black, red and green are reported respectively the signals from the 1st, 2nd and the 3rd anode, in blue and purple are shown the localisation signals.

vides either horizontal or vertical position information.

When the PPAC signal reaches the delay line at a position x, it is propagated in

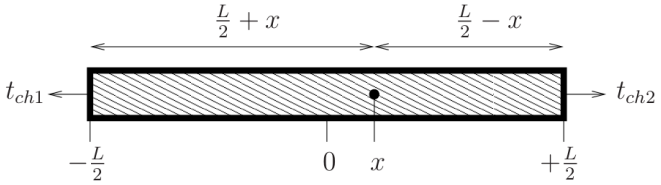

Figure 4.9: Signal propagation in a delay line of total length L.

both directions arriving at the ends in times t_{ch1} and t_{ch2} after the signal creation (see

figure 4.9). The two pieces of time information are given by:

$$t_{ch1} = t_0 + \frac{1}{v}\left(\frac{L}{2} + x\right) \qquad t_{ch2} = t_0 + \frac{1}{v}\left(\frac{L}{2} - x\right) \tag{4.1}$$

where t_0 is the reference time given by the corresponding anode signal, and v is the propagation velocity of the signal along the delay line. The position x in the delay line can be obtained as:

$$x = \frac{v}{2}\,(t_{ch1} - t_{ch2}). \tag{4.2}$$

The same logic is applied to the y-coordinate.
The propagation time is defined as the time the cathode signal takes to travel along the delay line with respect to the anode signal. $t_X = t_{ch1} - t_0$, where X is one of the 4 cathode symbols (Left, Right, Top, Bottom). The sum of the delay times, in both directions, from the anode can be written as:

$$t_{Bott} + t_{Top} = (t_{ch1} - t_0) + (t_{ch2} - t_0) = \frac{L}{v} = DLT \tag{4.3}$$

which shows that the sum of delays is independent of the position and it is related to the total propagation time in the delay length (DLT).

To find the localisation signals corresponding to a fission event, both the cathodes are treated separately using the same procedure: starting with the anode signal, the correlated cathode signals are searched for within a time window equivalent to the delay line, of length 100 ns, after t_0, and all signals occurring in this window are recorded. Then all combinations of cathode signal pairs are tested by imposing some constraints. A valid cathode event must produce two signals, one at each end of the delay line, with a sum of times equal to about the DLT value. If these conditions are fulfilled, the signals are kept for further selection.

4.1.3 Reconstruction of the fission fragment trajectory

The remaining part of the selection process is based on the cathode signal performance with the aim of reconstructing the fission fragment trajectories. Knowing the trajectory it is possible to trace the angle between the emission direction of fission fragments and the incident neutron beam, consequently to investigate the maximum detection angle of PPACs and to calculate the intrinsic detector efficiency.
It may happen that one of the four signals, that should be recorded by the two cathodes, is missing and the event is discarded. This happens when one fission fragment has to cross a large amount of material and is stopped in the anode foil of one detector, which happens for trajectories strongly tilted with respect to the perpendicular to the detectors. Therefore, the missing information about the position reduces the reconstruction efficiency to large angles.

Once fission events have been defined by unambiguously associating cathode signals with anode signals, the fission fragment trajectory can be reconstructed from the position information provided by these signals. From the calculated hit positions of the two

adjacent PPACs it is possible to reconstruct the trajectories of the fission fragments, taking into account that they are emitted from the target in opposite directions in the center-of-mass of the event. At energies comparable to the kinetic energy of the fission fragments, from around 100 MeV, the linear momentum transfer correction must be considered. The trajectory is fully determined by the position target where the fission occurs and by the emission angle with respect to the neutron axis beam, θ_m: a sketch of the geometrical arrangement is shown in figure 4.10. The coordinate origin is in

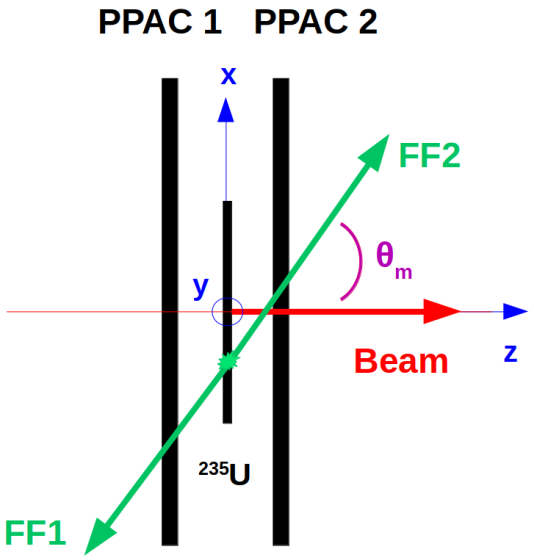

Figure 4.10: Reference frame used in the calculation of the emission angle of the two fission fragments with respect to the beam direction.

the center of the target, and the detector surfaces are parallel to the X-Y plane. The detectors and the target are placed along the Z axis. It is straightforward to determine the coordinates of the impact point in each detector using this reference system, since the X and Y coordinates are given directly by the cathode signals and the value of the Z coordinate is the distance from the target to the detector.
By using the impact points in the detectors $P_1 = (x_1, y_1, z_1)$ and $P_2 = (x_2, y_2, z_2)$ at low energy and in the laboratory frame, it is possible to identify the emission vector $\vec{V}$, connecting the two points. By construction, the direction of the neutron beam is $\vec{W} = (0, 0, 1)$, then the angle between the two vectors can be obtained from the scalar product:

$$cos\,\theta = \frac{\vec{V} \cdot \vec{W}}{|\vec{V}| \cdot |\vec{W}|}. \tag{4.4}$$

In neutron-induced reactions, part of the kinetic energy of the incident neutron is transferred to the target nucleus, so that fission does not occur at rest. This effect implies that, at large neutron energies, the nucleus acquires a linear momentum that is not negligible and the fission fragments are not emitted at 180°, contrary to was assumed in the trajectory reconstruction of fission events. In order to take into account this linear momentum transfer, the kinetic energies and the emission angles of the

fission fragments have been transformed from the center-of-mass frame to the laboratory frame. However, in such conditions, the angle θ_m is different from the emission angle in the laboratory frame $\theta_{1\,lab}$ or $\theta_{2\,lab}$, since it is not possible to know the emission point of the fission fragments, but only their final positions at the PPACs.

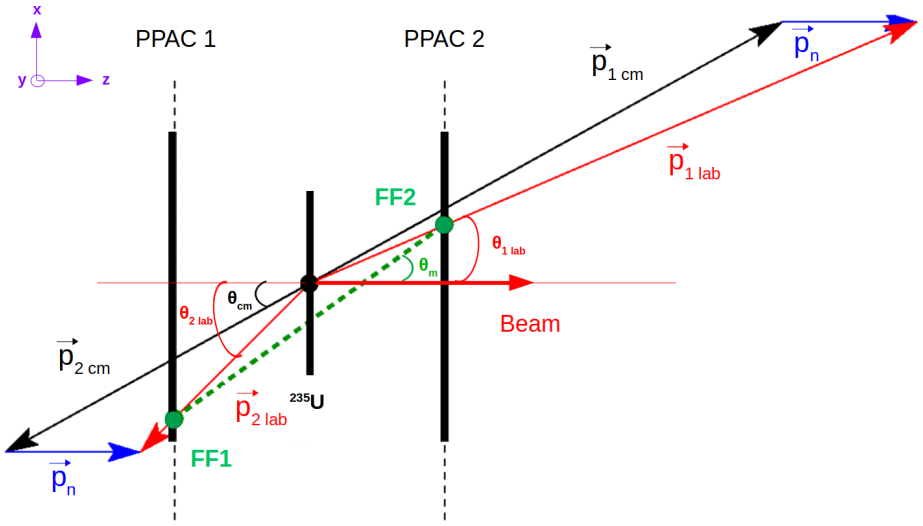

Figure 4.11: Kinematics of a fission event detected by two PPACs. The back-to-back fission velocities in the center of mass are represented by the black vectors. They add up with the recoil velocity of the fissioning nucleus (blue vector) to give the laboratory velocities (red vectors). The fragments cross the backward and forward detectors at the green points, and the analysis delivers a fission direction depicted by the green dashed line. This line is almost parallel to the original fission direction, showing that the measured angle is well representative of the fission direction.

This situation is schematically shown in figure 4.11, where two fission fragments are emitted in opposite directions in the center-of-mass frame, with momenta $p_{1\,cm}$ and $p_{2\,cm}$ at an angle θ_{cm}. The incident neutron transfers a momentum p_n to the target nucleus and, therefore, the fragments are emitted with momenta $p_{1\,lab}$ and $p_{2\,lab}$ at angles $\theta_{1\,lab}$ and $\theta_{2\,lab}$ in the laboratory frame. The angle θ_m is determined by the neutron beam direction and by the straight line between the hit points in both PPACs. It has been demonstrated, by Monte Carlo simulations, that θ_m is quite close to the angle in the center-of-mass frame θ_{cm}, even at neutron energies of 1 GeV, when the kinetic energy transferred by the incident neutron is about 350 MeV. The effect is small also thanks the angle accepted by the experimental setup (details in section 4.3), in fact at an angle greater than 60° the similarity between θ_{cm} and θ_m would no longer be true. Therefore, the error introduced by the momentum transfer in the angle measurement becomes negligible, as the difference between the cosine of the measured and the cosine of the CM angles is comparable to the angular resolution of the experimental setup [187].

The quality of the trajectory reconstruction can be checked by looking at the distribution of hit points on the target where the fission reaction takes place. Figure 4.12 shows the mapping of the emitting points when the two targets are superimposed. The impact position on the target can be used to determine the beam spatial distribution as a function of the neutron energy and some beam features. The beam spot is circular

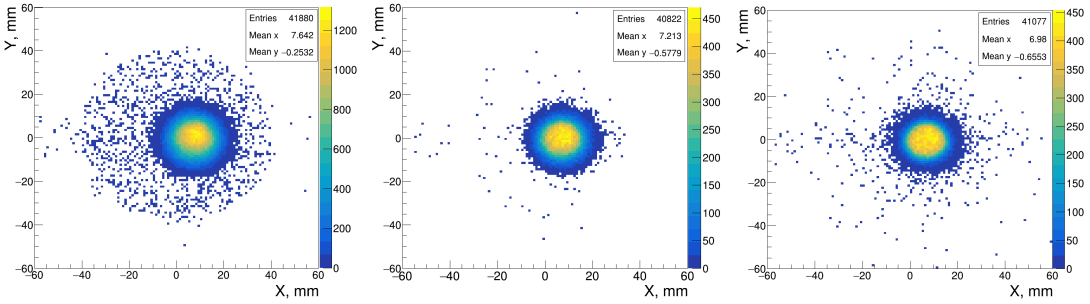

(a) E_n: 180 eV to 1 MeV (b) E_n: 1 MeV to 10 MeV (c) E_n: 10 MeV to 1 GeV

Figure 4.12: Distribution of hit points on the two uranium targets superimposed for different neutron energy intervals.

and highly populated. However, it can be observed the presence of emission points populating a wider region than the principal spot of 80 mm in diameter. These events are either produced by low-energy neutrons (figure 4.12(a)) that are much more diffuse and cover the total area of the ^{235}U deposit or they are originated by background neutrons that extend beyond the beam spot and may trigger fissions.
Figure 4.12 shows the data for three energy intervals, exhibiting a progressive transition in the shape. In particular, the root mean square of the distribution becomes smaller with increasing energy, due to the smaller emission region in the spallation target.

The uncertainty concerning the precision on the location of the fragments and the definition of the angle is reported in chapter 6 where all the systematic uncertainties of the measurement are discussed.

4.2 Time-to-energy calibration

The neutron kinetic energy is calculated from the effective length of the flight path, L, and the time of flight, t_m, using equation 2.3. Since the neutrons are produced in the spallation target, L is the sum of two terms: the geometrical one L_0 and the moderation distance λ.
A precise value of the length L_0 was calculated by comparing a number of resonances observed in the experimental fission rate of ^{235}U at low energy with the ENDF-B/VIII.0 evaluation. By using a fitting procedure a good match between the two distributions was found, as shown in figure 4.13, determining the value of L' to be (183.18 ± 0.03) m. It must be remembered that with this procedures, the fitted value L' includes L_0 and the moderation distance, λ. This latter, in the low energy region, depends weakly on the neutron energy; its value was deduced from MC simulations and resulted to be 15 cm, thus L_0 resulting from the subtraction is: $L_0 = (183.03 \pm 0.03)$ m.

The moderation distance, especially from 10^4 eV upwards, is energy-dependent as discussed in chapter 2 (figure 2.7). It is worth recalling that it is very difficult to find a global functional form, able to reproduce λ in the full range of energy because

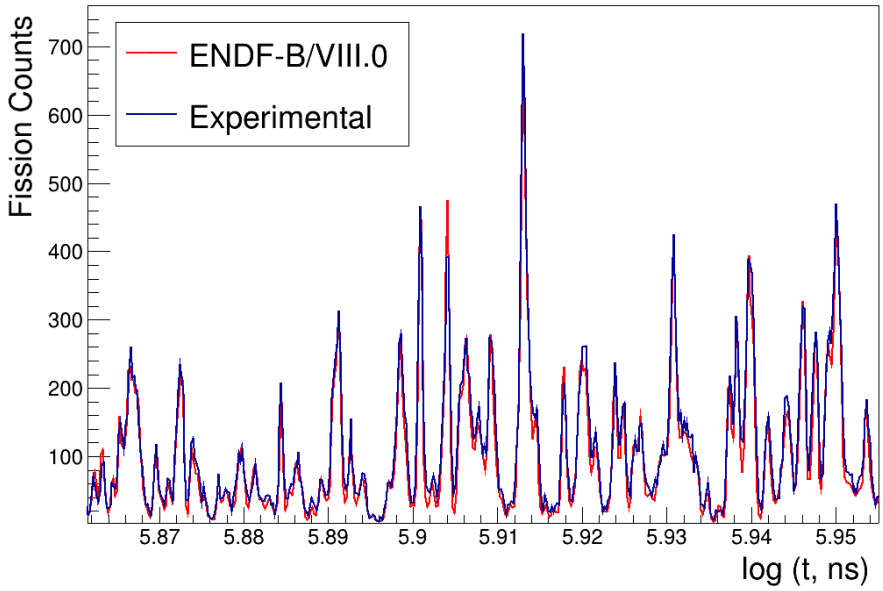

Figure 4.13: Comparison of resonance fission cross section of ^{235}U with ENDF/B-VIII.0, for a flight path of 183.18 m.

of its strong, sudden and irregular energy dependence. Therefore, a fitting procedure by small energy bins was adopted and the average value of λ was used as its best estimation. The distribution of the average λ, shown in figure 4.14, still has a strong dependence on energy, therefore the moderation distance, for each energy value, was calculated through an iterative procedure. In this approach, the first approximate value of the neutron energy E_0 is calculated, assuming λ=0. This energy, E_0, is used to calculate a moderation distance $\lambda(E_0)$, and a new value of energy, E_1, is obtained by using a flight path of $L_0 + \lambda(E_0)$. The process is repeated until the result converges, i.e. $|E_n - E_{n-1}|/E_n < 10^{-4}$, where n represent the iteration number. This precision is required in order not to affect the energy resolution that is obtained from the tof method, which is of the order of 10^{-3}-10^{-4} from about 10 MeV (details in section 2.4.1).

The missing part of the puzzle is the determination of the Time Of Flight. t_m can be expressed as:

$$t_m = T_{stop} - t_{\gamma f} + \frac{L}{c} \tag{4.5}$$

where $t_{\gamma f}$ is the time of the γ-flash and it is considered the time reference for each detector, and L/c is the time of flight of photons to cover the flight path distance. Since the γ-flash passes through all detectors within 2 ns, it can be considered instantaneous and provides a common time reference for each proton pulse. The identification of the γ-flash is obtained by software via a routine searching for anode coincidences thus identifying simultaneous hits in the detectors in correlation with the proton pulse. Contrary to other detectors, the intensity of the γ-flash in the PPACs is small and it suffers a jitter in time, the $t_{\gamma f}^{PPAC}$ is not always correctly recognized. Consequently, for

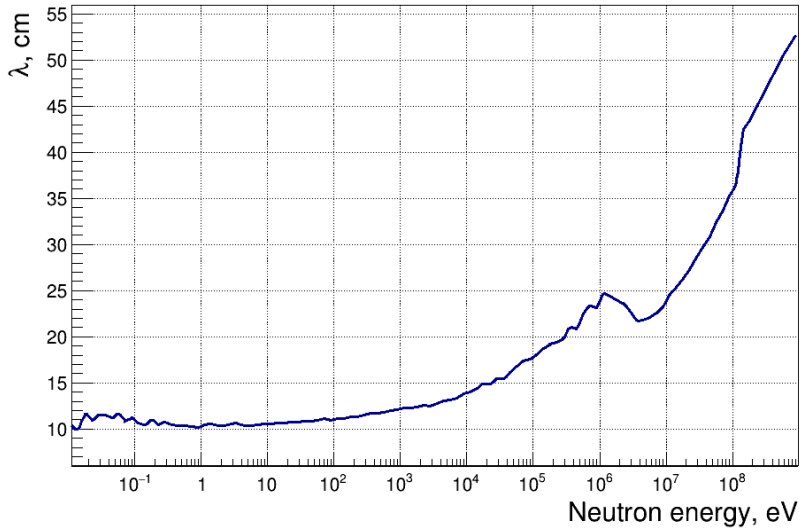

Figure 4.14: Energy dependence of the average value of the moderation distance in the n_TOF facility based on FLUKA Monte Carlo simulations.

each neutron pulse a trigger signal which represents a reliable substitute of the $t_{\gamma f}^{PPAC}$ was recorded. This trigger is provided by the proton beam passing through a resistive Wall Current Monitor placed before the spallation target, also called PKUP (already introduced in chapter 2). The difference between the time of the PKUP signal, t_{PKUP}, and the $t_{\gamma f}^{PPAC}$ is fixed for each anodes and cathodes, as it only depends on the wire length of their connection to the DAQ. Therefore, for each PPAC t_{PKUP} was calibrated

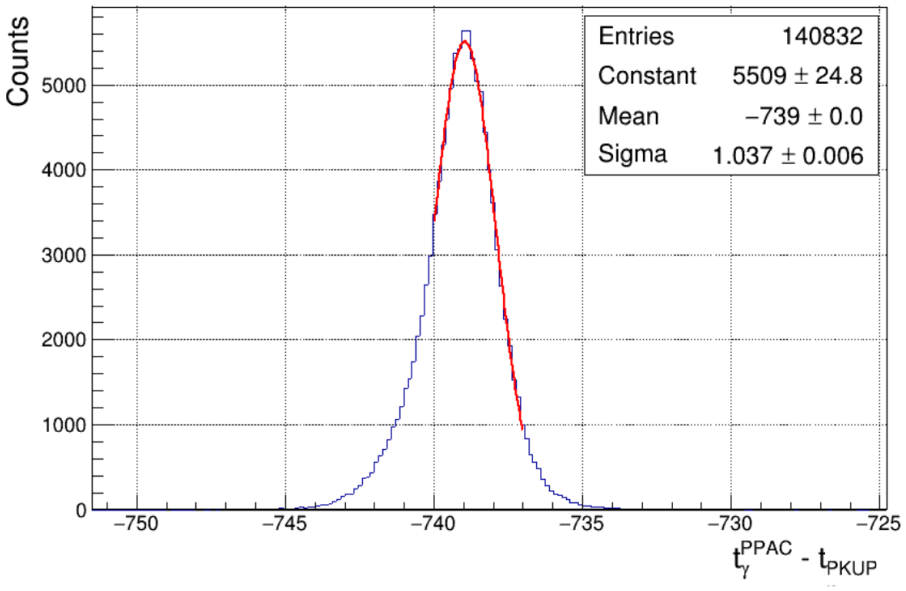

Figure 4.15: Distribution of the $t_{\gamma f}$ difference between the PKUP and a PPAC detector. The central values correspond to the constant offset assigned to PKUP's $t_{\gamma f}$ in order to reconstruct the time of the γ-flash per each event.

in time with respect to $t_{\gamma f}^{PPAC}$; an example of the time difference for one PPAC it is shown in figure 4.15. It is important to note that the width of the time distributions

was around 1 ns for all pulses.

4.3 Efficiency calculation for the PPAC setup

For a certain neutron energy, E, the number of detected fission events is given by

$$C(E,\theta) = \Phi(E)\, n_{^{235}U}\, \frac{d\sigma(E,\theta)}{d\Omega}\, \eta(\theta) \tag{4.6}$$

where the fragments are emitted at an angle θ with respect to the beam direction, $\Phi(E)$ is the neutron flux, i.e. the number of neutrons per incident proton pulse integrated over the whole spatial beam-profile impinging on the sample, $n_{^{235}U}$ is the areal density of the sample, $d\sigma(E,\theta)/d\Omega$ is the differential cross-section for emission of fission fragments at an angle θ, and $\eta(\theta)$ is the detection efficiency, which depends on the exit angle. There are two main factors that limit the PPAC detection of fission events: the energy loss of fission fragments in the different layers of PPAC and the anisotropy effect. Indeed, from of few MeV of neutron energy, the angular distribution differs significantly from isotropy and therefore must be included in the detection efficiency estimation of any experimental setup with a restricted angular acceptance. This is the case of the PPAC setup where the angular acceptance is limited to 60 degrees. This behaviour makes the global detection efficiency dependent on the anisotropy of the fission fragment angular distribution, which in turn depends on neutron energy.

Since the coincidence between the two fission fragments is required to identify a fission reaction, the efficiency has to be calculated taking into account the fact that, to recognize an event as fission, the coincidences involve both anodes and cathodes. The localisation signals are more selective about true fission events with respect to anode signals: with localisation can be distinguish the FFs against multi-fragment emission. In fact, high energy neutrons can produce many fragments and particles which, adding up their amplitudes, can mimic a fission fragment on the anode side. While on the localization side, thanks to the time-serialisation of the delay line, the signals coming from different particles can be distinguished and identified as background events.

The reduction of the efficiency due to the energy loss by the fragments in different layers greatly depends on the emission angle: the higher the angle, the longer is the path through the successive layers of matter. Consequently, the absorption probability increases and the possibility of reconstructing the fission event decreases. The situation is more critical for the forward-emitted fragment, which has to cross the aluminum sample backing of 2 μm, before reaching the PPAC active volume.
To get a qualitative idea of the effect, figure 4.16 shows the ratios of counts for validated localisation signals and anode signals. The cathode/anode ratio is almost 1 for X1 and Y2 (see figure 4.2) corresponding to the entrance gap for the FFs on each detector. It drops to lower values for the gaps Y1 and X2 because some fragments are stopped in the mylar of the anode and do not reach the second gap. In addition, above 10 MeV the ratio

starts to decrease, and the reduction is even stronger above 100 MeV. To explain this behavior it is necessary to resort to the kinematics of the reaction. In fact, remembering figure 4.11, as the energy increases, the nucleus acquires a linear momentum that is not negligible, and also the angle of the backward fragment is increased whereas it is decreased for the forward one. As a result, the detection efficiency of the backward fragment drops with the momentum transfer, explaining the steady decrease of Y1 counts in figure 4.16 (green histogram) above 1 MeV. The last point to underline from

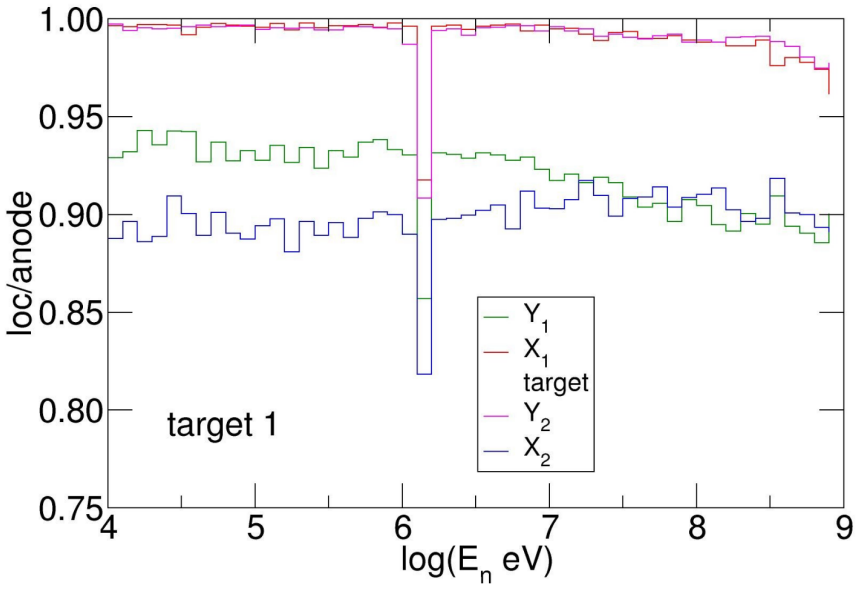

Figure 4.16: Ratio between the events recorded by the two cathodes and the anode placed in the middle as a function of the energy.

the figure is the presence of a narrow dip slightly above 1 MeV for all localisation signals; this is an artefact of the 0-suppression carried out by the second level trigger[1] This effect is, anyway, beyond the range of interest of the measurements, therefore it is not a real issue.

The angular acceptance is limited due to the stopping of fragments in dead layers to emission angles below $\sim 60°$, that means $\cos\theta \leq 0.5$. Summing up, this efficiency component is close to 1 for θ values lower than the limit angle and drops quickly to zero for larger angles.

From the fission fragment trajectory and the θ_m angle, it is possible to calculate the efficiency of PPACs as a function of $\cos\theta$. Any variation in the counting rate with $\cos\theta$ is a combined effect of angular distribution of the FFs and efficiency without any possibility of disentanglement. However, it is possible to overcome this limitation, considering the fission events triggered by low energy neutrons, for instance $E_n < 10$ keV, when the emission is isotropic. This is illustrated by figure 4.17 which shows the $\cos\theta$ spectrum obtained from the two ^{235}U targets. The main assumption here is that fission

[1]The data acquisition of the localisations event are triggered from their respective anode: the window for the cathode events acquisition is open only when a signal in the corresponding anode occurs.

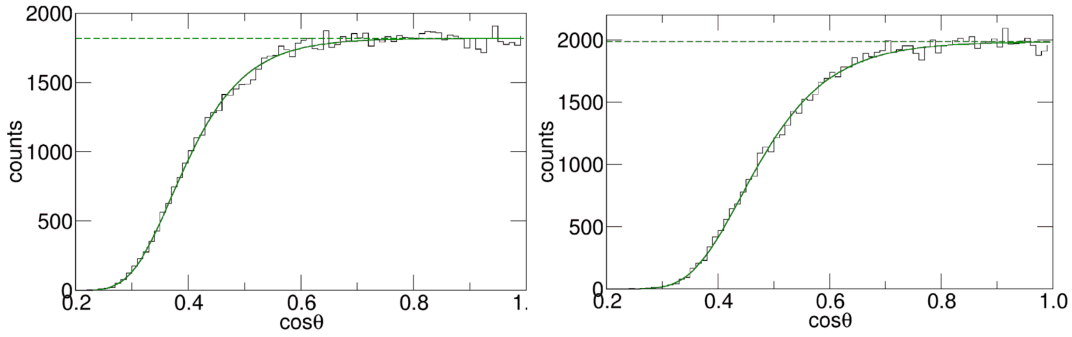

(a) Target 1 (b) Target 2

Figure 4.17: Distribution of the counts relative to $\cos\theta$, obtained by the four localisations signals, of the two uranium targets, for low neutron energy ($E_n < 10$ keV). In this energy region, the emission is isotropic, therefore, a 100% angular efficiency would lead to a constant number of counts as depicted by the horizontal green dashed line.

trajectories perpendicular to detectors and samples (parallel to the beam) are detected with an efficiency of 1 at all energies. This is corroborated by the shape of the detected angular distribution which is flat in the vicinity of $\cos\theta$=1. In figure 4.17 the green dashed line shows the angular distribution if the efficiency is 1 at all angles. The green solid curves are fits of the efficiency with the formula:

$$\varepsilon(\cos\,\theta\,|\,p_0, p_1, p_2) = \frac{1}{\left(1+\exp\left(\frac{p_0-\cos\theta}{p_1}\right)\right)^{p_2}} \tag{4.7}$$

where p_0, p_1 and p_2 are parameters. To achieve detection efficiency, it is necessary to normalize the plateau to 1 and integrate the distribution over $\cos\theta$, which is equivalent to calculating the areas under the green lines. The efficiencies obtained from the coincidences between the first and the second PPACs, surrounding the first target, and the one from the second and the third PPACs, relative the second uranium target, are different. The second target, as seen from the figures, is less efficient, due to the larger thickness of the backing and the roughness of the deposit. The estimated values are 0.589 for target 1 and 0.510 for target 2.

4.3.1 Angular distribution of the emitted fragments

The anisotropy parameter A, customarily used to characterize the dependence on neutron energy of the angular distribution, is defined as (see section 1.1.3 and formula 1.11):

$$A = \frac{W(0^\circ_{cm})}{W(90^\circ_{cm})} \tag{4.8}$$

where $W(0^\circ_{cm})$ and $W(90^\circ_{cm})$ represent the number of fission fragments emitted at 0° and at 90° with respect to the neutron beam direction. Evidently, the anisotropy parameter is useful to find at which neutron energies the angular distribution is not isotropic: an anisotropy parameter equal to one means that there is no preferential direction for the emitted fragments, and a value different from one implies an anisotropic

behaviour. Figure 4.19 shows the energy dependence of the anisotropy parameter for ^{235}U. The red curve is a recent measurement performed by the Neutron Induced Fission Fragment Tracking Experiment (NIFFTE) collaboration, using a fission time projection chamber to measure the anisotropy parameter of ^{235}U over a wide range of incident neutron energies from 180 keV to 200 MeV [36]. The blue curve is a measurement at GNEIS, the Gatchina neutron time-of-flight spectrometer [188] up to 200 MeV [189]. The behavior of the two distributions is consistent in the whole energy interval, difference consisting mainly in a smoother trend obtained by Geppert-Kleinrath et al. Because of the agreement between the two results and the greater accuracy and precision of the data published by the NIFFTE collaboration, the red curve was used to correct for the anisotropy effect. The fission process anisotropy parameter is close to 1 at

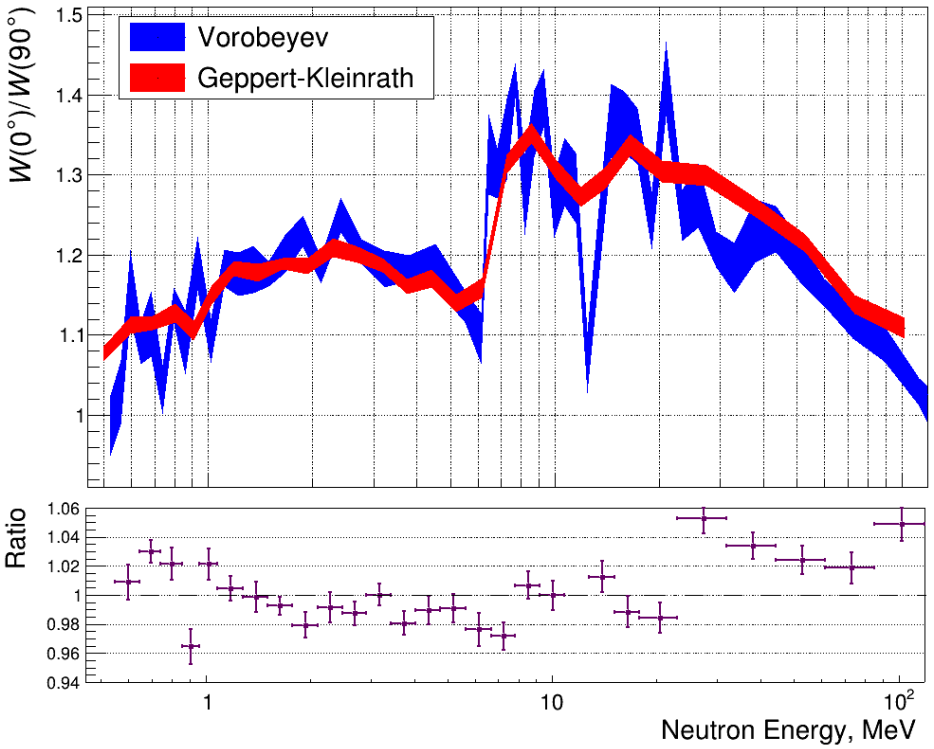

Figure 4.18: Anisotropy parameter for ^{235}U as a function of the neutron energy. In red a measurement performed by the NIFFTE collaboration using a fission time projection chamber in the energy range between 180 keV and 200 MeV [36], in blue a measurement at Gatchina up to 200 MeV, using position sensitive multiwire proportional counters [189].

low neutron energies but undergoes particularly large variations at the multiple-chance fission thresholds and decreases steadily again at intermediate energy. It is worth mentioning that in an even more recent measurement of the NIFFTE Collaboration [190] a careful determination of the linear momentum transfer from incoming neutrons to target nuclei led to a significant reduction of absolute values of the anisotropy parameter over the whole energy range under investigation, while the energy trend remains close to that of the 2019 experiment.

The next step is to derive the angular distribution from the anisotropy, which is the first-order descriptor of angular distribution. The fission fragment angular distribution can be parameterized by a sum of even Legendre polynomials $P_L(cos\theta)$ series, for each neutron energy interval. Only the even Legendre polynomials are included in the sum because of the backward–forward symmetry of the emitted fragments. The truncation in the sum over the order of the polynomial L, is defined by the total angular momentum [24]. However the mean of the angular structures brought about by the averaging over the orientations of the entrance spin ($J = 7/2$ for ^{235}U), helps reduce the number of P_L to be included. Indeed Kleinrath and collaborators showed that it is possible to stop at the second order for representing the angular distribution. In particular, they demonstrated that while including higher-order terms in the calculation of anisotropy parameter, the goodness of fit parameter χ^2_ν improves marginally, and the statistical uncertainty of the fit increases [36]. Hence, the angular distribution can be parameterized as:

$$W(cos\,\theta_{cm}) = \sum_{L=2Leven}^{L_{max}} a_L P_L(cos\,\theta_{cm}) \approx a_0 + a_2 P_2(cos\,\theta_{cm}) \tag{4.9}$$

where a_L is the energy-dependent coefficient of the L-th order Legendre polynomial obtained by fitting the experimental cosine distribution. From the condition of normalization of angular distribution:

$$\int_0^1 W(cos\,\theta_{cm}) d(cos\theta) = 1 \tag{4.10}$$

the value of the first parameter is obtained, $a_0 = 1$.
Therefore, the anisotropy parameter can be written as:

$$A = \frac{a_0 + a_2}{a_0 - a_2/2}, \tag{4.11}$$

and from this formula it is possible to calculate the value of a_2, when anisotropy is known. The last step is to combine all the ingredients and make a fit, for each energy bin, of the experimental data with:

$$C(cos\,\theta) = (1 + a_2\,P_2\,(cos\,\theta))\,\varepsilon(cos\,\theta\,|\,p_0, p_1, p_2) \cdot p_3 \tag{4.12}$$

where the parameters p_0, p_1, p_2 and p_3 are adjusted on experimental angular distributions.
Figure 4.19(a) shows the result of the procedure for the first target, in the energy range from 6.3 MeV to 10 MeV, where the anisotropy is maximal. In this energy region, the data show a slope of the plateau due to the forward-backward peaking of the physical angular distribution. The green solid line is the fit performed and the dashed line shows the trend in case of efficiency equal to 1 at each angle. Instead, the distribution corresponding to the highest neutron energies, between 630 MeV and 1 GeV in figure 4.19(b), is isotropic again. The green solid line is the result of the fit with formula 4.12, the red line, instead, is a fit using the low-energy parameterized efficiency ε, obtained by

adjusting only the p_3 parameter and corresponding to the green curve in figure 4.17(a). It is interesting to notice that the low-energy shape of the efficiency is not accurate

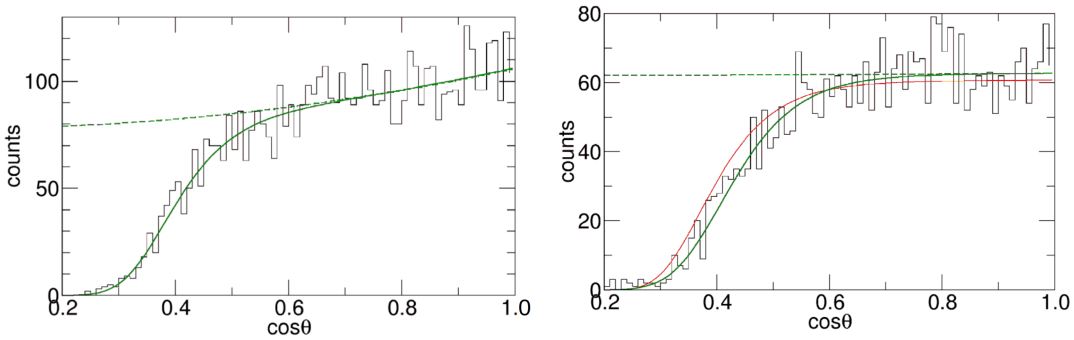

(a) Target 1 - 6.3 MeV $< E_n <$ 10 MeV (b) Target 1 - 630 MeV $< E_n <$ 1 GeV

Figure 4.19: Example of angular distribution for ^{235}U, in two different neutron energy ranges. The green solid line is a result of the fit using the formula 4.12, the red one is the fit reported in figure 4.17(a).

at all. The actual efficiency has a lower cut-off angle, due to the transferred linear momentum that tilts the angle of the fragment backwards. When the fission angle is small, the distribution is not affected by the boost, and the efficiency is equal to 1. This behavior is related to the velocity of the two fission fragments: the backward velocity is decreased and the forward one is increased. However, the backward fragment has no backing to go through, therefore the velocity reduction does not prevent its detection. Instead, when the fission angle increases, the tilting angle of the backward fragment is enhanced by the boost inducing a faster drop of the detection efficiency as a function of $\cos\theta$, as shown in figure 4.19(b).
Accordingly, the total detection efficiency η is composed of the geometric acceptance, the in-medium fission fragment absorption and the effect due to the angular distribution of the emitted fragments. For each energy interval, η can be calculated:

$$\eta = \int_0^1 (1 + P_2(cos\theta))\, \varepsilon(cos\theta \,|\, p_0, p_1, p_2)\, d(cos\theta). \tag{4.13}$$

The resulting η for the two targets are displayed in figure 4.20. The solid lines (blue and red) are constructed by taking 5 bin per decade, the dashed ones are the smoothed version, maintaining the general tendency and eliminating fluctuations due to statistics. The global trend is common to both targets and the main features are:

- constant efficiency below 100 keV; in fact, in this energy range there are no effects due to anisotropy nor to the kinematics of the reaction;
- increase of the efficiency around 10 MeV due to the physical angular distribution, and in particular the peaking at the opening of 2nd and 3rd chance fission;
- drop beyond 100 MeV due to the linear momentum transfer.

For each target an individual efficiency correction has been applied to the recorded counts. This is necessary because, although the two targets are subject to the same

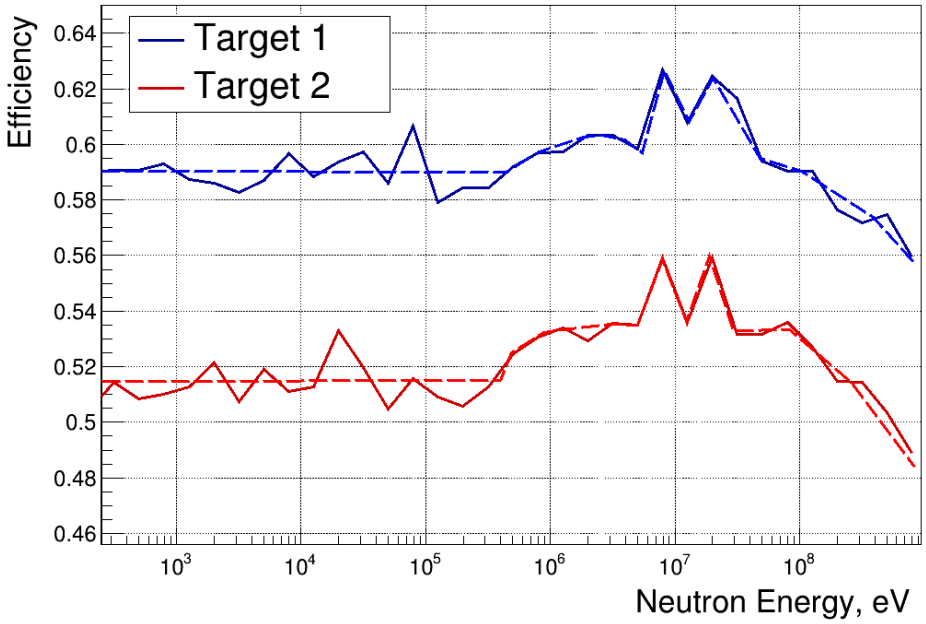

Figure 4.20: Global efficiency calculated taking into account the geometric factor, the fission fragments absorption effect and the angular distribution of the products.

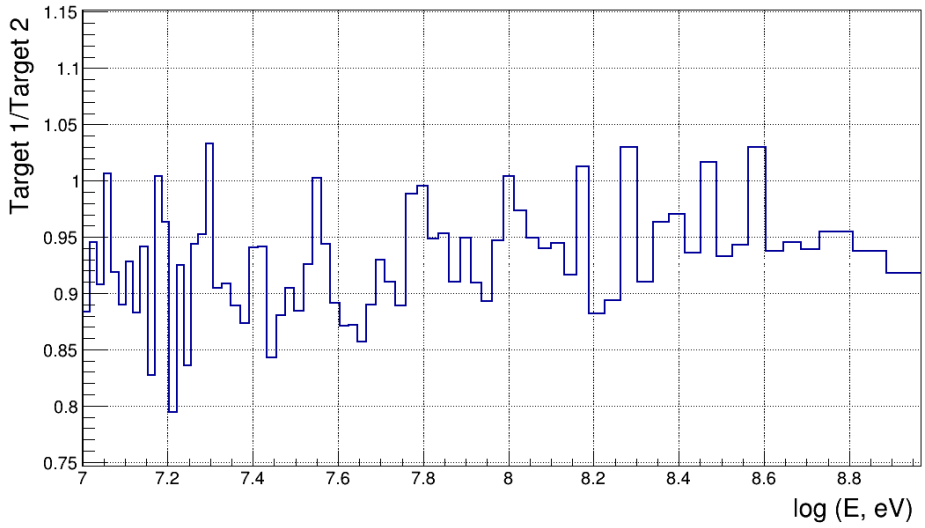

Figure 4.21: Ratio between counts recognized as fission events , in each target, and scaled up by the efficiency correction. After the corrections the ratio between the counts is almost flat.

phenomena, the weights of the various factors are not the same, therefore the total efficiency is not equal for the two targets. After the efficiency correction the ratio between the two targets is quite constant, as visible in figure 4.21.

The counts recognized as true fission events, applying the coincidence between two adjacent PPACs and the localization of the fragments, scaled for the overall efficiency of the detector, were used to extract the cross section of the reaction. Referring to formula 4.6, only two elements are missing to obtain $d\sigma(E,\theta)/d\Omega$: the areal density

of ^{235}U, $n_{^{235}U}$, and the neutron flux $\Phi(E)$. The value of $n_{^{235}U}$ calculated for the two targets are $6.99 \cdot 10^{-7}$ atoms/barn and $7.46 \cdot 10^{-7}$ atoms/barn, respectively. Recalling the composition of uranium targets described in section 3.4.2, the introduction of a factor to correct for the different isotopes, which constitute the two uranium targets, is necessary. This correction is needed to balance the contributions of the fission cross sections of the different isotopes. Up to 100 keV this factor is equal to 1 because only the fission channel of ^{235}U is open. Above this energy even for the other isotopes the fission channel is open and the correction reaches its maximum at 100 MeV, where it saturates to the value of 1.067. The many measurements in literature of the ratios between the fission cross sections of the different isotopes guarantee us a precision on this factor better than 1%.

Concluding, the last missing piece is the extraction of the neutron flux, which is obtained from the analysis of telescopes, and is the topic of the next chapter.

Chapter 5

The neutron flux analysis

An accurate determination of the ^{235}U(n,f) cross section clearly requires a similar accuracy in the determination of the neutron flux. As a consequence this aspect of the analysis is critical, primarily because the energy region of interest is very close to the γ-flash, then because, as the energy increases, the background component becomes progressively more important. Three counter telescope detectors were especially developed and realized within the collaboration expressly for this measurement campaign. In fact, since the n_TOF flux has never been measured from 10 to 500 MeV, it was decided to use a redundant apparatus, thus minimizing uncertainties and maximizing statistics, at the same time. In this chapter the analysis of the data obtained with the two INFN-telescopes will be illustrated, in particular from the signal reconstruction to the flux extraction. Particular attention was paid to the study of the detector efficiency, extensively investigated through Monte Carlo.

5.1 Telescopes configurations

It is appropriate, here, to recall the design of the two INFN-telescopes and the fundamental points on which the analysis is based (see section 3.3.2). Both detectors have a pyramidal structure, which points at a polyethylene target. The developed counter telescopes exploit the ΔE-E technique and are segmented in various stages to cope with the large dynamic range of interest. This multistage structure, consisting of silicon detectors and plastic scintillators, allowed us to work with a specific combination of detectors, depending on the energy range under analysis. For the RPTL-INFN it is possible to identify four different energy intervals in which four different combinations of detectors can be operated, depending on the energy of the neutron undergoing a reaction in the sample:

(i) events produced by neutrons with energy from 12 MeV to 30 MeV require the coincidence between the two silicon detectors;

(ii) protons generated from neutrons with energy between 37 MeV and 90 MeV stop in the second plastic scintillator, producing the coincidence between the first two plastic scintillators;

(iii) protons from neutrons with energy from 91 MeV to 145 MeV stop in the third plastic scintillator and require coincidence between the first three scintillators;

(iv) protons coming from neutrons with energy above 146 MeV involve all the plastic scintillators.

Since, the RPTH-INFN is not equipped with the two silicon detectors in front, only three energy regions can be classified.

5.2 Pulse shape analysis

For an accurate particle identification, based on the ΔE-E technique, the reconstruction of the deposited energy of the particles and the time of the event represent the fundamental observables. In fact, they enable the identifiction of events in coincidence between the different stages.
The first step of the analysis procedure is the recognition of signals using the Pulse Shape Analysis framework developed within the n_TOF collaboration. This procedure is described in section 2.8, and therefore in the present chapter only the most critical aspects for the silicon detectors and the plastic scintillators are reported.

5.2.1 Silicon detectors

The γ-flash is recognized as the first pulse in the recorded frames satisfying a certain set of conditions. It may happen that a given detector suffers the effect of the γ-flash for several hundreds of ns, giving rise to a strongly oscillating baseline. This is the case of the silicon detectors, as presented in figure 5.1, where 500 frames (i.e. bunches) showing the baseline around the γ-flash are superimposed. It is evident the presence of recurring structures with a given, frequency and decreasing amplitude with time. These oscillations could potentially lead to a shift of the temporal information of the signal and to losses of signals of small amplitudes. The main issue lies in the difficulty to properly correct for this effect: while up to about 2500 ns after the γ-flash the amplitude of the fluctuations is proportional to the amplitude of the γ-flash signal; afterwards they are independent of its intensity. This prevented us from being able to calculate an average or representative shape of the fluctuations in order to subtract it from each frame. Similarly to what was done for the analysis of the PPAC signals, for the silicon detectors a low-pass filter was applied as well via software to the derivative of the signal in order to cut off the frequency bands. The Fourier transform has been calculated to obtain the range of frequencies that compose the signal and then a high-frequency limit has been defined, corresponding to 2.5 Hz. The chosen frequency selection was a trade-off to eliminate the contribution of high frequency oscillations without affecting the rise time of the signals. Figure 5.2 shows the comparison of the same frame before the frequency selections 5.2(a) and after the Fourier transform -based correction 5.2(b). The Fuorier transform allowed us to eliminate the oscillations only in the frames produced by the

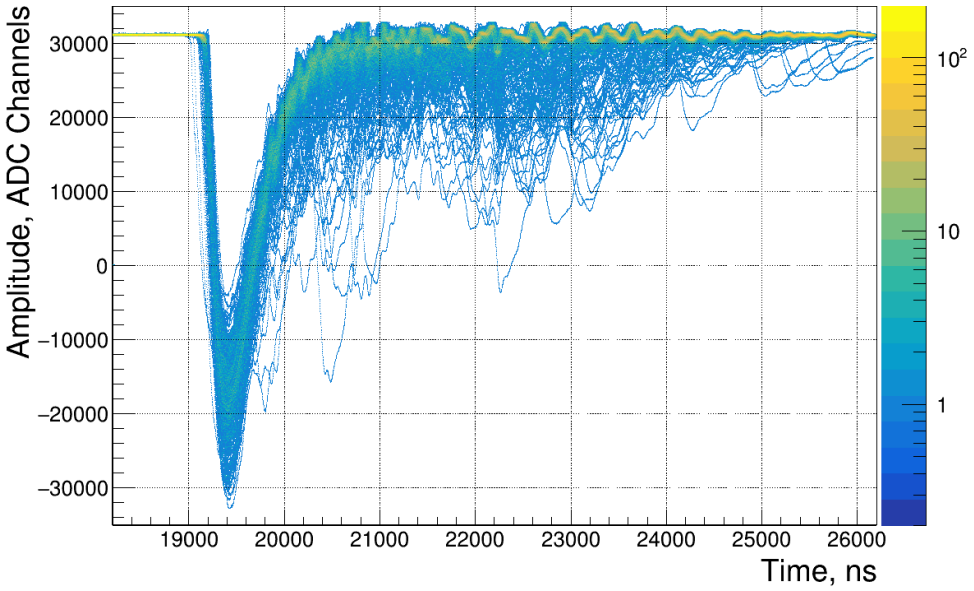

Figure 5.1: 500 frames from the γ-flash signals until the oscillation effect, due to the γ-flash, is present in the baseline for the first silicon detector in the RPTL-INFN.

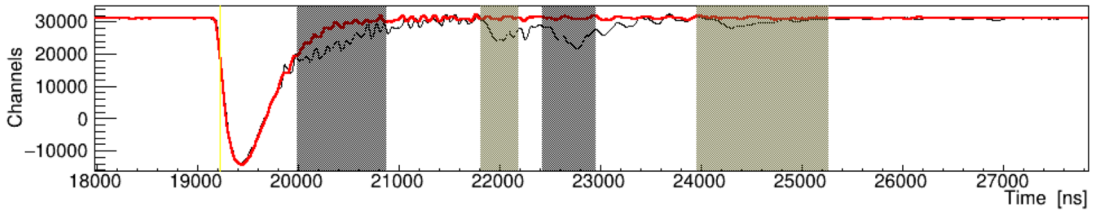

(a) Before Fourier Transform

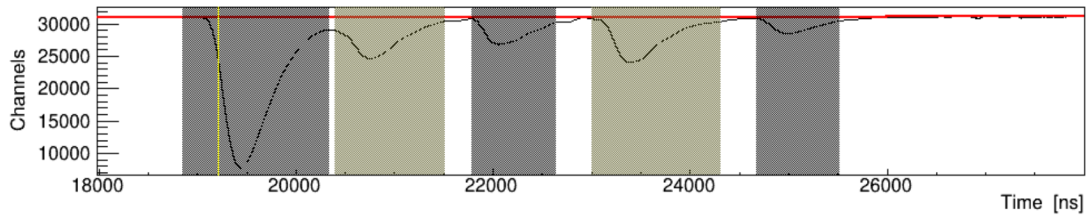

(b) After Fourier Transform

Figure 5.2: The same frame of the raw data recorded from the first silicon detector before the derivative filtering, in the top panel, and after it in the bottom panel.

events generated in parasitic mode of the PS, which is characterized by a lower intensity of the primary beam of protons (3.5×10^{12} instead of 7×10^{12}); in the dedicated mode, the effect of the γ-flash on the baseline is not completely eliminated. Therefore, in the analysis of silicon detectors, only events produced in parasitic mode were considered for the final analysis. The smoother trend after the application of the filter makes it possible to perform a clearer identification of the signals and a better reconstruction of their features.

5.2.2 Plastic scintillators

The peak and the total charge of a signal are represented respectively by the maximum amplitude and the area of a digitized signal. These two quantities are directly related to the energy deposited in the detector. Their precise reconstruction is essential when applying the ΔE-E method to perform particle identification. The Signal Analyzed framework provides the possibility of determining amplitudes of each identified signal with three different methods: a) by looking for a local maximum or b) extrapolating it from a parabolic fitting to the top of the pulse, or c) by a pulse shape fitting applying a user-definable specific pulse shape. Using the latter option the area is related to the amplitude by a fixed scale factor; otherwise, the area under the pulse is calculated by a numerical pulse integration. The pulse shape fitting with a template pulse (option c) is preferably adopted or mandatory for high counting rates, where the signals overlap frequently, since it enables the correct reconstruction of the number of original pulses, their amplitude/area as well their time. For each scintillator, a representative pulse shape was derived from real signals and they were used as input in the reconstruction routine. The procedure to extract these representative signals consists of a first signal analysis with the method (a) followed by the study of the area-amplitude correlation.
A typical example of this is shown in figure 5.3, which clearly show a non-linear trend. This behaviour is common in plastic scintillators and appears to be significant when the deposited energy in a scintillator is large. As a consequence, this effect is a more pronounced in the thickest detector of the telescope. Possible energy deposition in the first detector is between 1 and 20 MeV, the range covered by the second is from 1 to 50 MeV, and the last two (characterized by the same thickness) reach an energy of 70 MeV. This effect makes the shape of the searched signal not univocal but, rather, energy dependent. In order to study and estimate the impact of this non linearity on the pulse shape analysis, we adopted a parametric approach. In fact, the analysis of the same raw data was repeated 5 times, while changing the shape of the signal.
More in detail, the events were reconstructed in the first time using the parabolic fitting to the top of the pulse and, based on the obtained energy loss distribution (see for example figure 5.4), four different type of pulse shapes (with different area to amplitude ratio) could be sampled. For the sake of clarity, the four signals have been named *Small Signal*, *Medium Signal*, *Big Signal* and *Bigger Signal*, referring to the size of the shape with respect to the energy loss in a plastic scintillator. For instance, the amplitudes and areas of the sample signals of the 6 cm thick scintillator are shown in figure 5.4, where the black lines represent the histogram of the area and amplitude, while the colored strips define the region where the *Small*, *Medium*, *Big* and *Bigger* signals were sampled, respectively.

To cross-check the pulse shape fitting procedure, several frames were examined, firstly in a qualitative way, simply by looking at the agreement between the recorded and the fitted signal, an example of which is reported in figure 5.5. In the subsequent quantitative analysis, the spectra of the area reconstructed using pulse shape fitting,

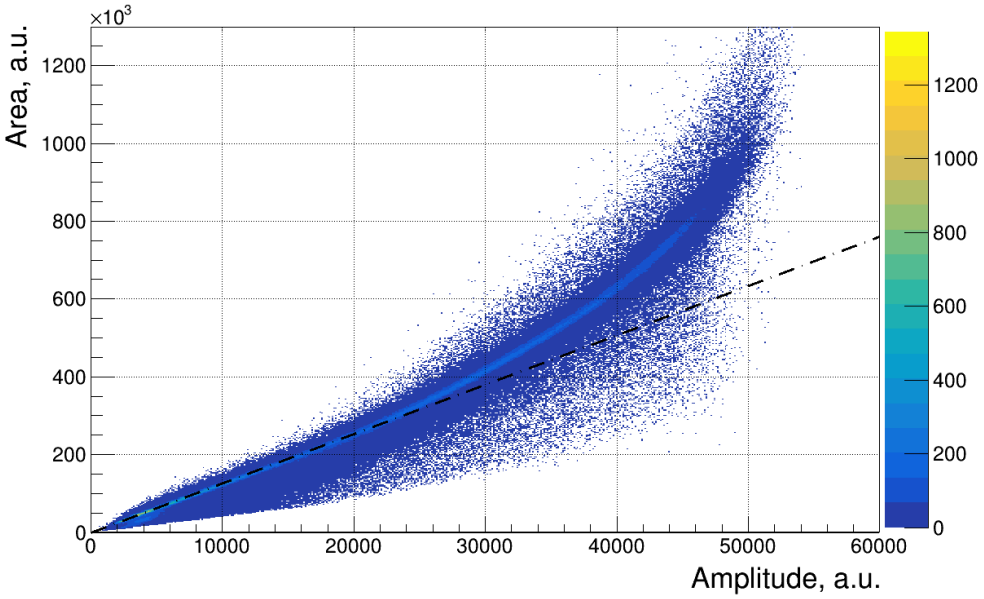

Figure 5.3: Distribution of the amplitude and area of the identified signals in the second plastic scintillator of the RPTL-INFN. It is evident that the linearity of the detector fails as the energy deposited increases.

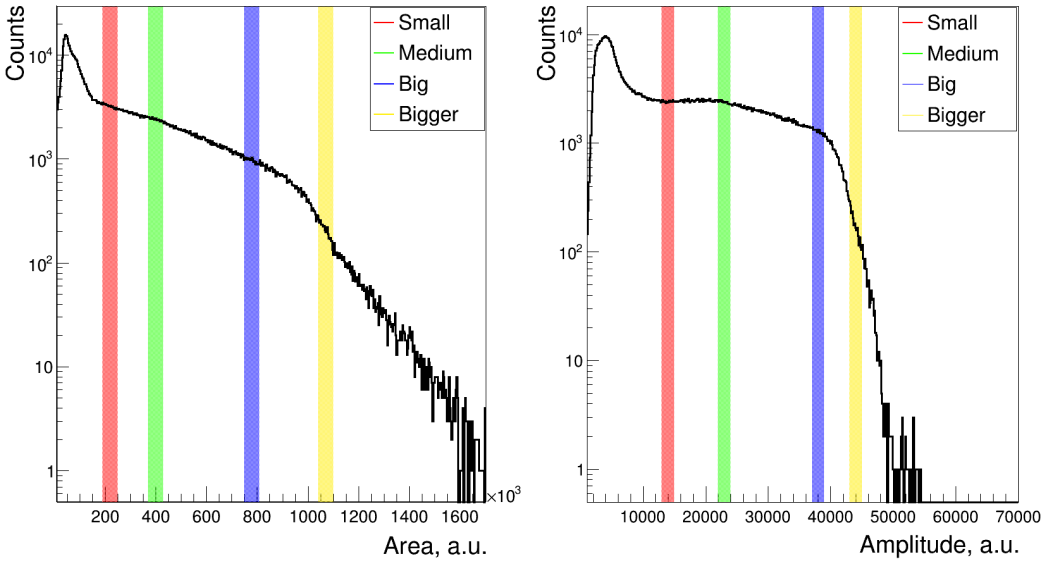

Figure 5.4: Reconstructed area (left) and amplitude (right) of the pulses in the 6-cm thick scintillator. The coloured strips limit different regions where the signals were sampled to give as input in the pulse shape analysis routine. The red one is the typical range of area and amplitude characterizing the *Small Signal*, the green corresponds to the *Medium Signal*, the blue to the *Big Signal* and, finally, in yellow to the "Bigger Signal".

were compared to the corresponding ones analyzed by the simple method (a), i.e. the amplitude is estimated by the maximum peak value. Comparing the two distributions required some care: a) a low counting rate was required in order to avoid pile-up, so that the latter amplitude reconstruction could be trusted; b) the whole energy range of interest was considered, because different shapes fit better in different TOF regions (as

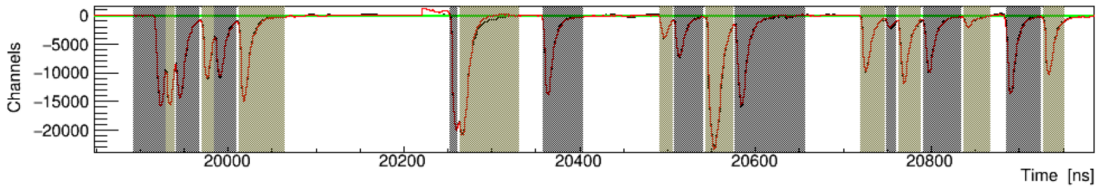

Figure 5.5: Case of a reconstruction of events in the 3-cm thick plastic scintillator. The gray and brown strips define the recognized signals, and the red curve represents their fit using the *Big Signal* shape.

energy losses depends on the primary neutron energy). Figure 5.6 shows an example of the ratios between the areas from the fitting procedure based on the four pulse shapes and those obtained by numerical integration. These ratios were studied as a function of the area of the signal, i.e. as a function of the deposited energy, with the aim of looking for the less affected one. Although a dependence on the deposited energy is identifiable in each ratio, it is possible to analyze the individual cases finding some differences:

a) the ratios for Small and Medium signals, in figure 5.6(a) and 5.6(b), increase with energy, as can also be seen in the asymmetry of the ratio distributions, reported in the histograms;

b) the ratios for the two other signals in figure 5.6(c) and 5.6(d), instead, are more stable in energy, and the two one-dimensional histograms show a narrower peak without a strong asymmetry in the tails.

The more relevant quantitative check was to count the number of "good" events, i.e.

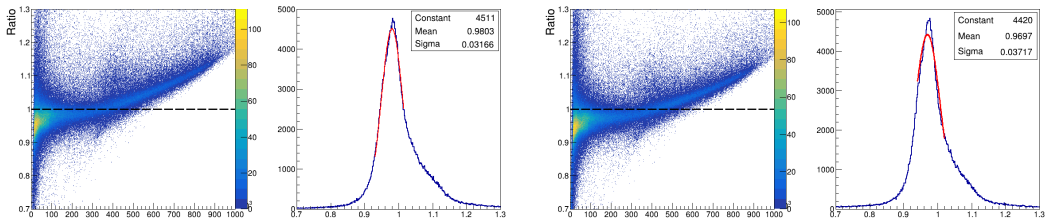

(a) Small Signal

(b) Medium Signal

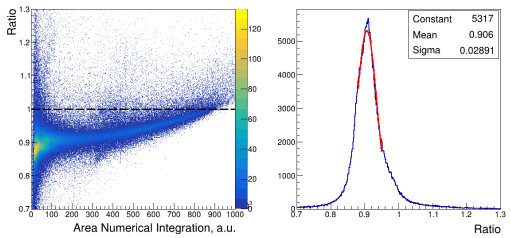

(c) Big Signal

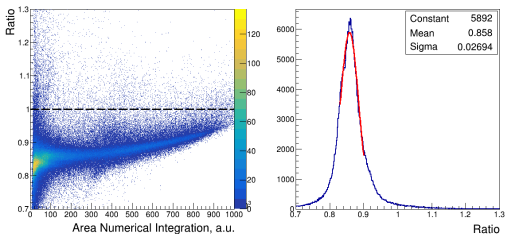

(d) Bigger Signal

Figure 5.6: Ratio of the area obtained using the numerical integration relative to the area extracted with the fit. The ratios are expressed as a function of the energy deposited in the plastic scintillator, on the left, and as a distribution, including a Gaussian fit.

the events in coincidence between adjacent scintillators. This last study, was conclusive enough to benchmark verify the goodness of the signal shape and, additionally, to quan-

tify the level of uncertainty associated to the signal reconstruction routine. Table 5.1 reports the number of the events in coincidence at some energies and for the different methods used for the signal reconstruction: at (52.5 ± 2.5) MeV the coincidence between the first two scintillators is required, while (115 ± 5) MeV requires the coincidence between the first three scintillators, and the last two energies (175 ± 5) MeV and (300 ± 10) MeV the coincidence among all the scintillators. In addition to the number of events, the ratio between the counts recorded in coincidence, obtained using a particular pulse shape and those obtained by the numerical integration, is reported.

Table 5.1: Number of events in coincidence between the first two plastic scintillators, for neutron energy from 50 to 55 MeV, among the first three, when the neutron energy ranges from 100 to 120 MeV, and among all the scintillators for the last two energies reported. The number of events is also supported by the ratio the counts of the events in coincidence using the fit with the pulse shape relative to the number obtained from the numerical integration.

	(52.5 ± 2.5) MeV		(115 ± 5) MeV		(175 ± 5) MeV		(300 ± 10) MeV	
	# events	ratio	# events	ratio	# events	ratio	# events	ratio
N.I.	12248		6988		3304		3991	
Small Signal	12209	0.9968	6943	0.9936	3250	0.9837	3939	0.9870
Medium Signal	12224	0.9980	6991	1.0004	3253	0.9846	3964	0.9932
Big Signal	12277	1.0024	6985	0.9996	3274	0.9909	3999	1.0020
Bigger Signal	12219	0.9976	6973	0.9979	3281	0.9930	3992	1.0003

Taking into account all these checks about the goodness of the fit and of the number of reconstructed events, the most appropriate signal shape to be used in the reconstruction, was provided by the *Big Signal*. It is to be noted that the uncertainty associated with the number of events reconstructed using a pulse shape as input parameter is about 1%.

5.3 Neutron flux analysis

It is important to remember that, and as mentioned above, the term flux refers to the number of neutrons of a certain energy that reach the experimental area and interact with the sample. The procedure for the extraction of the neutron flux, adopted in this analysis, can be summarized by the following formula (valid in the thin target approximation, i.e. equation 3.6):

$$\Phi(E_n) = \frac{C_{C_2H_4}(E_n) - r_C\, C_C(E_n)}{n_H\ \varepsilon(E_n)\ d\sigma_{n,p}(E_n)/d\Omega} \tag{5.1}$$

where $C_{C_2H_4}$ and C_C are the events recorded with the polyethylene and carbon sample, respectively (normalized to the number of primary protons), as a function of the neutron energy; r_C is the ratio between the number of atoms of carbon in the C_2H_4 sample and

in the carbon sample itself; n_H is the the areal density in atoms per barn of the hydrogen in the C_2H_4 target, ε is the total detection efficiency, including the solid angle subtended by the detector, and $d\sigma_{n,p}/d\Omega$ is the differential neutron-proton scattering cross section. The cross section assumed by the scientific community as a reference for the neutron-proton scattering, and used in this work, is the VL40 energy-dependent phase-shift solution, already described in detail in section 1.3.1. The number of atoms, n_H, depends on the features of the used sample used, which are summarized in table 3.2. The efficiency, ε, of the detection system has been studied with Monte Carlo simulations. Extensive simulations with neutrons impinging on a realistic setup, composed by the polyethylene or carbon sample and the counter telescopes, were performed. The same analysis approach was adopted in both experimental data and simulations, realizing the ΔE-E matrices, and applying the same analysis conditions to discriminate between background events and events produced by n-p elastic scattering.

5.3.1 Event recognition by coincidences

By selecting signals in time coincidence from different detectors, it was possible to select the events originating form the polyethylene sample only. More in detail, a specific routine was implemented to search for events that are present in a given time window in the different stages of the telescopes. Furthermore, it was necessary to study separately the various configurations in the different energy ranges where the different detectors work. More in particular, the routine searches for a signal in the first stage of the telescope (located in time after the γ-flash) and sets a time window in the second detector, where it looks for an event in coincidence. Moreover, if a signal is present also in the second detector, a window is opened in the third one, and this procedure continues in cascade up to the last scintillator that composes the telescope.
The plastic scintillators and the silicon detectors are separately analyzed, due to the rather different time features of the two detectors. Therefore, the coincidences between the two silicon detectors, those between the first two, the first three and finally, all the plastic scintillators are grouped and saved. The time windows for the two type of detectors are different: 500 ns and 10 ns for silicons and for plastic scintillators, respectively.
As done for the PPACs (for details see section 4.2), for each detector the signal provided by the PKUP was correlated to the one of the γ-flash, t_0, to perform an accurate synchronization between the different layers of the telescope and eventually a good time-to-energy calibration. Two examples of t_0 calibration are shown in figure 5.7; in both cases it is important to notice the accuracy achievable in these calibrations which is about 2.5 ns for the silicons and about 1-1.5 ns for the scintillators. Therefore, in the search for events in coincidence a precision at the level of $\sim$ns was achieved.

Finally, the length of the flight path L from the spallation target to the polyethylene sample was deduced. In particular, to the L_0 value obtained from the PPACs resonance analysis, the geometric distance between the PPAC detector and the C_2H_4 target was added. This distance, measured by mean of a laser-based device with an accuracy of a

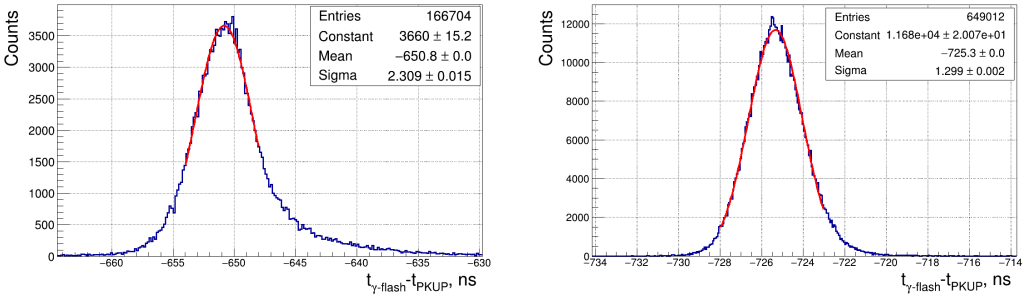

(a) silicon detector (b) Plastic Scintillator

Figure 5.7: Examples of t_0 calibration for a silicon detector and a plastic scintillator. It is important to note the sigmas of the gaussian fit, which assure us an accuracy in the order of $\approx$ns in the timing of the events.

tenth of mm, and the obtained L resulted to be (183.40 $\pm$ 0.03) m.

As already introduced, two time windows, one for the silicon detectors and one for the plastic scintillators, were used to identify the events in two consecutive detectors in coincidence. These windows are large enough to collect a signal even in case of pile up with an earlier event. Figure 5.8 shows two distributions of the time differences, dt, between events in coincidence; figure 5.8(a) reports the dt between the two silicon detectors while, figure 5.8(b) shows the coincidences between two plastic scintillators. In both distributions the peak produced by good coincidence events is easily identifiable and a sharp cut could be applied to avoid random coincidences. The narrowest selections applied in the analysis for the time differences distribution of the events, *dt*, are shown in light-blue. Random coincidences, outside the selected *dt* region, are less than 1% compared to all the events recorded in coincidence; therefore the component due to random coincidences can be considered negligible. In figure 5.9 the area of sig-

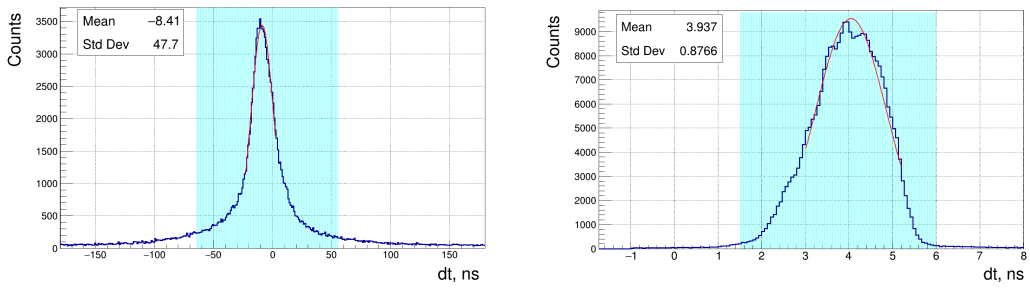

(a) silicon detector (b) Plastic Scintillator

Figure 5.8: Distributions of time differences of the recorded events in coincidence between the two silicon detectors (left panel) and two consecutive plastic scintillators (right panel). In light-blue are highlighted the narrowest regions taking into account in the final analysis. Random coincidences are less than 1% of the total recorded events.

nals, from the second (up) and the third (down) plastic scintillators, corresponding to selected events are depicted as a function of the time of flight (left) and of the neutron energy (right). It is interesting to focus on what happens in the two detectors; indeed,

since the two detectors are arranged in sequence, from a neutron energy of about 80 MeV the energy deposited in the second plastic scintillator starts to drop to the minimum, and, similarly, the energy deposited in the third stage begins to increase, as the neutron energy increases. This behaviour is explained by the energy loss described by the Bethe-Bloch formula, already discussed in section 3.3: the energy release is maximum when the particle reaches the end of its path. The main trend of the energy deposited in the two scintillators is similar and two regions can be identified: the signal area grows up to a peak and then begins to decrease. Let us consider, for example, in figure 5.9(a) the area of the signals versus the neutron energy, on the right panel:

a) protons undergoing elastic neutron scattering with energy larger than 40 MeV and less than 80 MeV have enough energy to reach the second scintillator and stop there. As the energy of the primary neutron increases, the energy deposited by the proton in the second detector increases accordingly, until it reaches a peak, which corresponds to about 80 MeV of neutron energy.

b) After the peak, protons no longer stop in the second scintillator, but arrive at the third one; then the energy deposited in the second stage starts to decrease and stabilize (from about 200 MeV it remains constant as the energy increases).

5.3.2 Monte Carlo simulations

Monte Carlo (MC) simulations were performed with two toolkits: Geant4 and MCNP. The geometry of the whole experimental setup together with the physics processes involved in the experiment were implemented in both codes. It is worth mentioning that the so-called reference physics lists (i.e. the physical models for the particle interactions with matter) in Geant4 does not correctly reproduce the differential cross section $\mathrm{d}\sigma_n p/\mathrm{d}\Omega$, therefore it was changed accordingly to the evaluation of Arndt [109, 191]. To validate and compare Geant4 and MCNP simulations a step-by-step process was followed. The first item under consideration was the response of the detector to both point-like and extended sources of monoenergetic protons, deuterons, and α particles. In particular, the energy deposited in each stage of the counter telescope and the number of recorded events resulted to be compatible within the corresponding uncertainty between the two MC simulations. Once these simplified versions were verified, a more detailed and complete simulation was performed. In particular, monoenergetic beams (with and without the n_TOF spatial profile) of neutrons were sent towards a polyethylene target, with the same characteristics as that used during the experiment. Each step was verified in the two codes and the same results are obtained within the uncertainties. This agreement allowed us to have confidence in the detection efficiency obtained from the simulations. From now on only the results obtained with the Geant4 code will be shown, owing to their compatibility with MCNP.

The efficiency of the telescope depends on several elements: the geometrical component, the multiple scattering of the particles in the sample and in the telescope itself, the effect of thresholds and cuts applied for event selection.

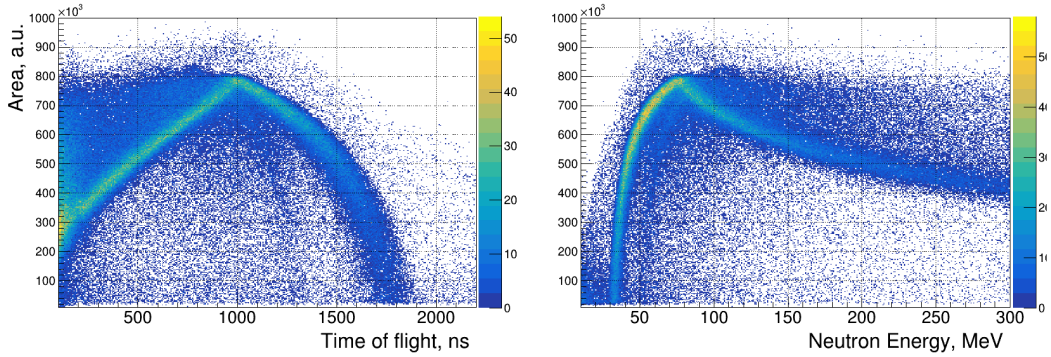

(a) Second plastic scintillator

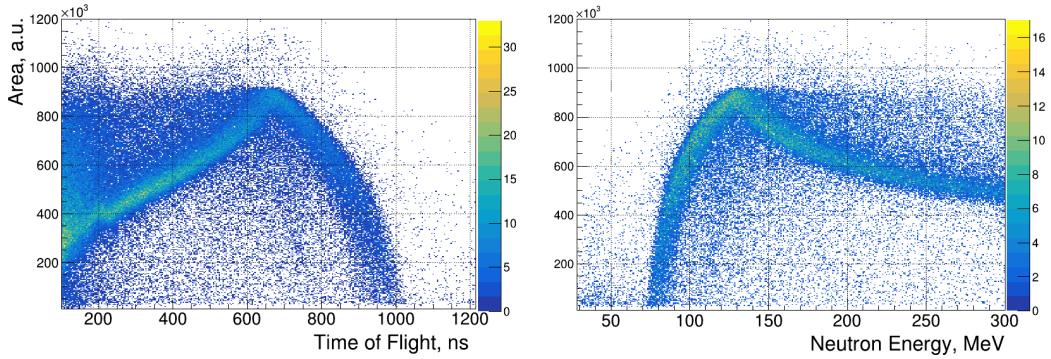

(b) Third plastic scintillator

Figure 5.9: Panels: area of the signals recorded in the second scintillator when a coincidence is present between the first and second stages of the telescope, as a function of neutron time of flight on the left, and of the corresponding neutron energy, on the right. In the bottom panels, area of the signals in the third plastic scintillator for the events in coincidence in the first three plastic scintillators, versus the neutron time of flight (left) and the neutron energy (right). Considering two sequential scintillators, it is possible to notice that from about 80 MeV the area in the second plastic scintillator starts to decrease and in the third one begins to rise.

The first component to be studied is the geometrical factor, which defines, basically, the solid angle subtended by the detector. Since the area of the two silicon detectors is the same, when the coincidence between the two is imposed, the second one defines the solid angle within which the events are accepted. On the other hand, for the trapezoid composed by the four plastic scintillators, for which the coincidence between all stages is required, the solid angle is dominated by the acceptance of the first scintillator. The results obtained by calculation were $\varepsilon = (0.0298 \pm 0.0004)$ taking into account the coincidence between the silicons and $\varepsilon = (0.0308 \pm 0.0004)$ for the plastic scintillators.
By simulating an isotropic proton source, placed in the position of the polyethylene target, it is possible to extrapolate the geometric efficiency of the telescope, taking into account the multiple scattering of protons in the scintillating material. For example, protons can lose energy in the first plastic scintillator, reach the second one and, following an interaction, escape from the telescope. In this situation, the event locates off the proton hyperbola in the ΔE-E matrix. In fact, the deposited energy in the first stage is the expected one but the proton, as it leaves the telescope, cannot deposit all

of its energy in the forward stages, only part of it being released. Although generated by n-p scattering, such event cannot be counted among the good events, therefore it is important to quantify with precision the effect of multiple scattering on the total efficiency of the detector. The left panel of figure 5.10 shows the ratio between the number of detected events relative to total number of generated protons (10^6) as a function of the proton energy. The transition among the different configurations of coincidence between detectors, at about 30, 90 and 150 MeV, are reflected in the variations in the efficiency curve.

The second step towards the final simulation of the complete experimental setup was the introduction of an hydrogen sample, 0.384 mm thick, with an areal density of 0.91 g/cm^2, thus including the neutron beam interaction with the target. The features of the neutron beam are those of the experimental beam in EAR-1 at n_TOF: a gaussian-like profile characterized by a sigma of 0.56 cm [192, 193]. As a result of this MC simulation, the right panel of figure 5.10 shows the efficiency calculated with the proton source, multiplied by the neutron-proton differential cross section. With the addition of the sample also the effects produced by the target, which are mainly the energy deposited in it and the multiple scattering, are included in the efficiency study. The consequence can be noted in the energies of the transitions between the different configurations of coincidences which are shifted by about 10 MeV and in the slope which occurs at low energies, from 10 to 15 MeV. The low detection efficiency coupled with the differential n-p scattering cross section, led to a detection rate of about 1 proton per 10^6 neutrons hitting the polyethylene target.

The geometrical efficiency obtained using a hydrogen sample needs to be adapted to

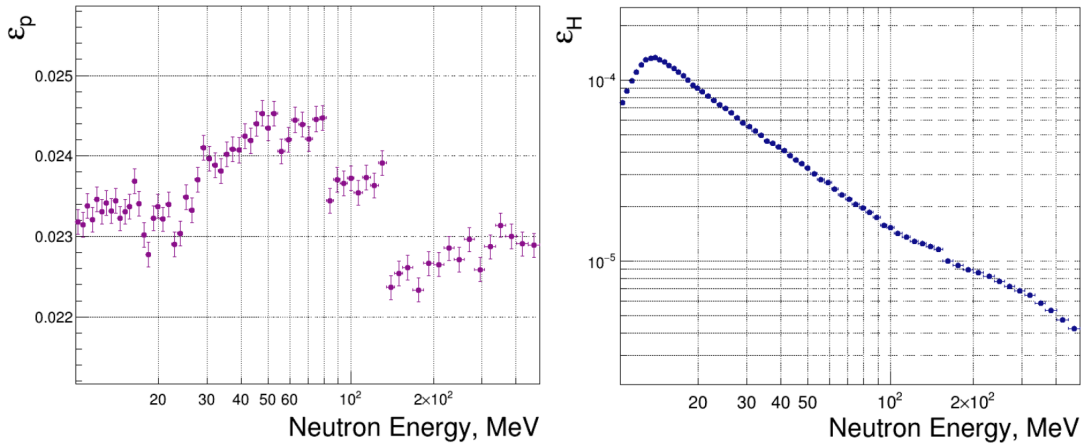

(a) (b)

Figure 5.10: In the left panel the efficiency is studied through an isotropic proton source placed in the polyethylene sample. The efficiency thus calculated incorporates the evaluation of the solid angle subtended by the telescope and the effect due to multiple scattering suffered by protons in the target and in the detector itself. In the right panel the fraction of protons detected by the telescope relative to the total number of neutron hitting an hydrogen sample with a thickness and an areal density of 0.384 mm and 0.91 g/cm^2 is shown.

the real polyethylene sample used and to the cuts applied in the analysis. Before mov-

ing on to the study of the effective efficiency, it was necessary to examine the various background components affecting the neutron flux extraction.

Background components

To complete the simulations by reproducing the final geometry similar to that used in the experimental measurement it is necessary to introduce the polyethylene target, instead of the hydrogen one. The amount of carbon present in the sample is responsible for the main component of background and manifests itself through various processes. When neutrons interact with carbon nuclei, different outgoing channels are open, thus producing neutrons, protons, deutons, tritium, α particles in the final states (the main channels are summarised in table 3.1). As already illustrated, the segmentation of the telescope ensures the suppression of the background related to particles with Z>1, which are stopped in the first stages of the detector. Typically, in the ΔE-E matrix, only the hyperbola generated by protons and deuterons remains. Therefore, a linear cut in the ΔE-E matrix is enough to select only the events containing protons. In addition, neutrons induced reactions on carbon, as well as n-p scattering in hydrogen can generate neutrons, emitted in the direction of the telescope. These neutrons entering in the telescope can cause in turn reactions and, consequently, a part of the detected protons can be generated in the detector itself. This effect becomes more important for the plastic scintillators as they contain hydrogen and carbon (C_9H_{10}). Therefore, imposing the coincidence from the first scintillator in series until the last one, this component of background is reduced considerably, surely removing all the events produced in the second, third and fourth scintillators. The number of protons produced in the last three plastic scintillators was studied through Monte Carlo simulations, and for example in the case of neutron with energy (158.3 ± 3) MeV, is about 25% of the total number of protons recorded in the last stage. However, by requiring the coincidence between scintillators it is significantly limited to less than 1%.
Finally, by choosing only protons produced in the target, a not negligible component of background is still present, because protons are generated by the interaction of neutron with carbon. Figure 5.11 shows the ΔE-E matrix produced by Monte Carlo simulations, assuming the neutron beam hitting a hydrogen target (on the left panel) and a carbon target (on the right panel). The different types of nuclear reactions involving carbon and hydrogen are clearly separated:

i) in the case of n+H, only protons are present in the ΔE-E matrix and their energy is distributed around the corresponding kinematic locus (defined by $E_p = E_n \cos^2\theta$).

ii) In the case of n+C, in addition to protons other particles are present. As the Q-value of the neutron-induced reactions on C is negative, the energy distribution of emitted particles has a lower mean value and the kinematic of the nuclear reaction does not produce a peaked distribution in energy.

In summary, all the events produced by n-p scattering are localized in a restricted region of the matrix, while those produced by the interaction with carbon are distributed throughout the whole hyperbola.

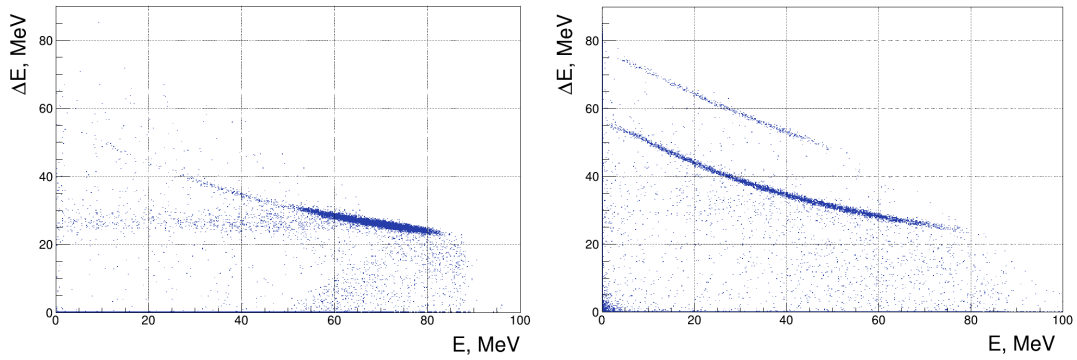

(a) Hydrogen sample (b) Carbon sample

Figure 5.11: The matrices are generated by Monte Carlo simulations with a 120 MeV neutron beam. Figure 5.11(a) shows the ΔE-E matrix when an H sample is placed on the neutron beam. The detected protons can only derive from the n-p scattering reaction, in fact all the events are positioned in a narrow region of the matrix. Figure 5.11(b) displays the ΔE-E matrix from the neutron beam hitting a carbon sample. There are two groups of events related to the families of protons and deuterons; the events are distributed throughout the hyperbola without any peak.

In spite of the different features of the involved reactions, the analysis conditions cannot be conclusive enough to achieve an unambigouos selection of the events. Therefore, in order to estimate the residual background, Monte Carlo simulation with the same number of neutrons in the same energy ranges was carried out, but with carbon targets instead of the polyethylene ones, as done in the experimental measurement. Figure 5.12 shows the ratio between the number of protons produced by nuclear reactions between neutrons and carbon and the number of total protons coming from the target. The correlation was obtained after the normalisation of carbon counts for the number of carbon atoms contained in the C_2H_4 target. In this plot, four regions are highlighted: in the red one the events in coincidence between the two silicon detectors are presented, the coincidences between the first two, the first three and all the plastic scintillators are in the orange, green and the light-blue regions, respectively. It can be noted that the general trend of this graph is repeated for each region of coincidences, the fraction of background events increases with increasing energy and exhibits an abrupt reduction at each change of detector combination. This behaviour is due to two factors; on one hand as the energy increases, more decay channels for ^{12}C are open and therefore their contribution becomes more relevant. On the other hand there is a reduction in the carbon background events due to the multi-layer structure of the telescope.

The study of the effective efficiency

Putting together all the ingredients described above: geometric acceptance of the detector and the subtraction of background; it is possible to determine the effective efficiency of the telescope for different analysis conditions. In order to have a global view of the analysis procedure, the evaluated efficiency was multiplied by the n-p cross

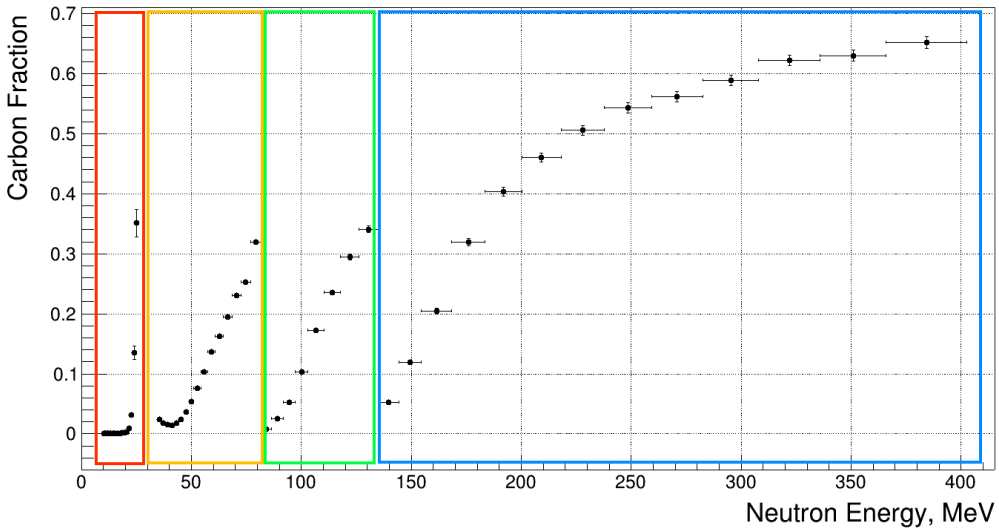

Figure 5.12: The ratio between the protons attributable to n+C reactions, normalized to the number of carbons contained in the polyethylene, relative to the total number of protons recorded when a C_2H_4 target is placed in the neutron beam. In the red strip there are the events attributable to the coincidence between the two silicon detectors, in the orange, green and light-blue strips, there are respectively the coincidences between the first two, three and all four scintillators. Each time one moves from one configuration to the next one, the number of events from the carbon sharply drops to gradually increase, within the same required coincidence, as the energy increases.

section, therefore, this procedure makes it possible to estimate the number of events recognized as protons produced by n-p scattering compared to the total number of neutrons hitting the C_2H_4 target.
A dedicated Monte Carlo simulation covering the entire energy range from 10 MeV to 500 MeV, and considering the whole experimental setup (which includes a sample placed in the neutron beam and a telescope located at 25° with respect to the beam direction) was carried out. Events from polyethylene or carbon samples with the same characteristics as those used in the measurement were simulated. All the steps and the selection of the simulated events are briefly summarised in the following list.

1. Only events that deposit energy in each layer of the detector were selected;

2. the last two detectors in which particles deposit their energy were chosen in order to perform particle identification;

3. only the hyperbola produced by protons was selected using ΔE-E matrices;

4. the protons produced by n+C reactions were subtracted, after being normalised, from the totality of protons events reconstructed in the configuration with the polyethylene target.

The events recognised, through this selection, as generated by n-p scattering and divided by the number (10^9) of incident neutrons on the target, are shown in figure 5.13. The purple, green and blue lines are, respectively, the results obtained from the thinnest

target, namely the C_2H_4 1.025 mm thick (and C 0.5 mm thick), used for the low energy part, from the 1.834 mm thick target (and C of 1.0 mm) and, from the C_2H_4 of 4.917 mm thick (and 2.5 mm for the carbon sample) particularly suited for the high-energy region, from about 70 MeV. The plots have the same sawtooth structure as in

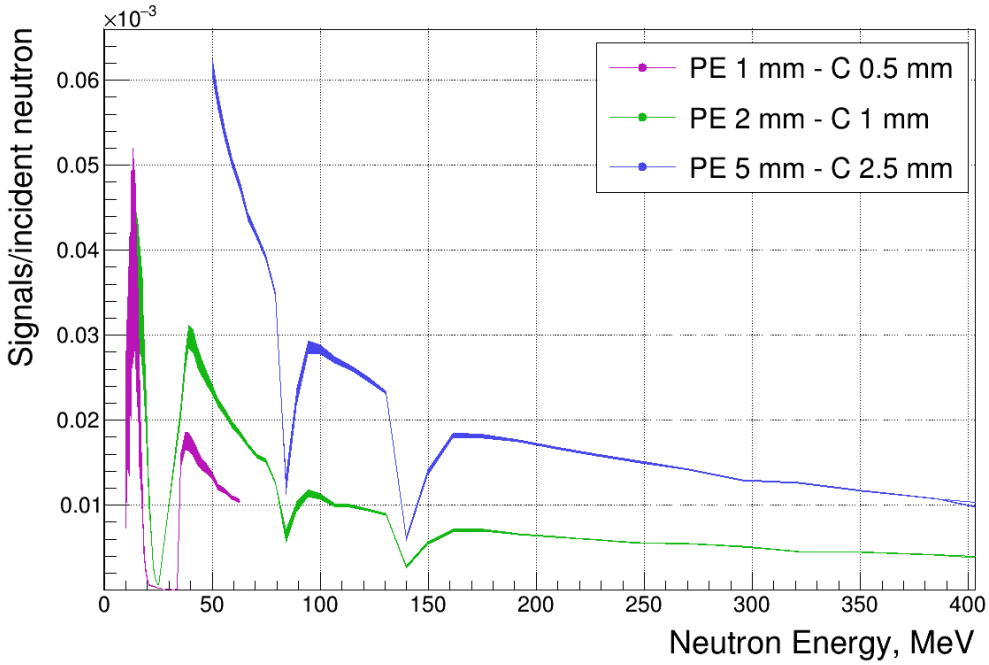

Figure 5.13: Number of protons per incident neutron produced by the neutron-proton scattering, calculated by subtracting from the number of protons from the polyethylene target, the number of protons coming from the carbon one and dividing the result by 10^9 incident neutrons in the sample. The purple line was calculated using the 1.025 mm thick C_2H_4 target, the green line using the 1.834 mm and finally the blue line using the 4.917 mm thick target, each one associated with the respective graphite targets.

figure 5.12, due to the background component generated by the n+C reactions and the design of the telescope. The low efficiency of the RPT is predominantly geometric, i.e. due to both the thickness of the polyethylene targets and the solid angle subtended by the detector; these two characteristics determine the number of produced and detected protons, respectively. As proof of this we may notice in the graph that the efficiency calculated using thicker targets is systematically higher, because, due to the greater thickness, a greater number of atoms is exposed to incident neutrons.

In addition, through Monte Carlo simulations, sensitivity studies were carried out to quantify the effect on the number of counts detected and, therefore on the final extracted flux, in case of possible misalignments between the beam and the detector. These studies are part of the estimate of the uncertainty of the final result and will be discussed in the next chapter.

5.4 Extracted neutron flux

With all the pieces of the puzzle, introduced in formula 5.1, provided the neutron flux was extracted. Figure 5.14 shows an example of ΔE-E matrices, taking into account the events produced by neutrons with energy of (74.8 ± 2.2) MeV, which stop in the second plastic scintillator. The plots 5.14(a) and 5.14(c) are based on experimental data using the C_2H_4 and the C target, respectively. The matrices 5.14(b) and 5.14(d) show the corresponding Monte Carlo simulation. The two hyperbolas from protons and deuterons are clearly identifiable and events out of the gray zone were selected and counted. At this point, the subtraction between the polyethylene and the carbon allowed us to isolate the contribution of n-p scattered protons from protons produced in the n+C reaction, obtaining the two one-dimensional histograms in figure 5.14(e) for the experimental data and 5.14(f) for the MC simulation. The discrimination between protons and deuterons in the ΔE vs E plots is quite effective up to $E_n \approx 200$ MeV neutron energy. In fact, although the protons are already beyond the punch-through energy, the deuterons are still in the upper branch of the plot where the ΔE is effective for discrimination. Above that energy the deuterons cannot be easily discriminated, but the subtraction of the data from the graphite samples basically removes all of them. An example of this scenario is in figure 5.15, where the matrices were produced by choosing neutrons with energy of (270.9 ± 11.7) MeV. In the gray exclusion zone there are no events since the signals of protons and deuterons are completely overlapping. In this case the exclusion of background events occurs only through the subtraction of the normalized events coming from carbon from all events detected with the polyethylene target. Since this technique will be used for neutrons with energies from 200 MeV upwards, it is appropriate to find a way of testing the reliability of the results obtained when the protons traverse the whole telescope without stopping inside it. Figure 5.16 aims at demonstrating the goodness of the results when the telescope works in the punch-through or with the following couple of scintillators, obtaining in both cases an equivalent extracted flux. Since this is a crucial part of the analysis, it is appropriate to examine it in detail. The top panel show the extracted flux using only polyethylene with a thickness of 1.834 mm, in different configurations: the orange points give the result obtained by imposing only the coincidence between the first two scintillators; the green points are obtained by imposing the coincidences among the first three scintillators, the blue points to the coincidence among all the plastic scintillators; among the three regions there are intentionally overlapping areas. This implies that starting from a neutron energy of about 90 MeV and imposing only the coincidence between the first two scintillators the flux can be extracted working in punch-through condition, while the coincidence among the first three scintillators is the right configuration to require. A similar scenario occurs from about 160 MeV for the coincidence among the first three plastic scintillators. The ratios shown in the bottom panel confirm that, in the overlapping zones, the flux extracted with the *right configuration* of scintillators and the one obtained with the previous couple of detectors are fully compatible. This validation allows us to work with telescopes even in the high-energy region, where

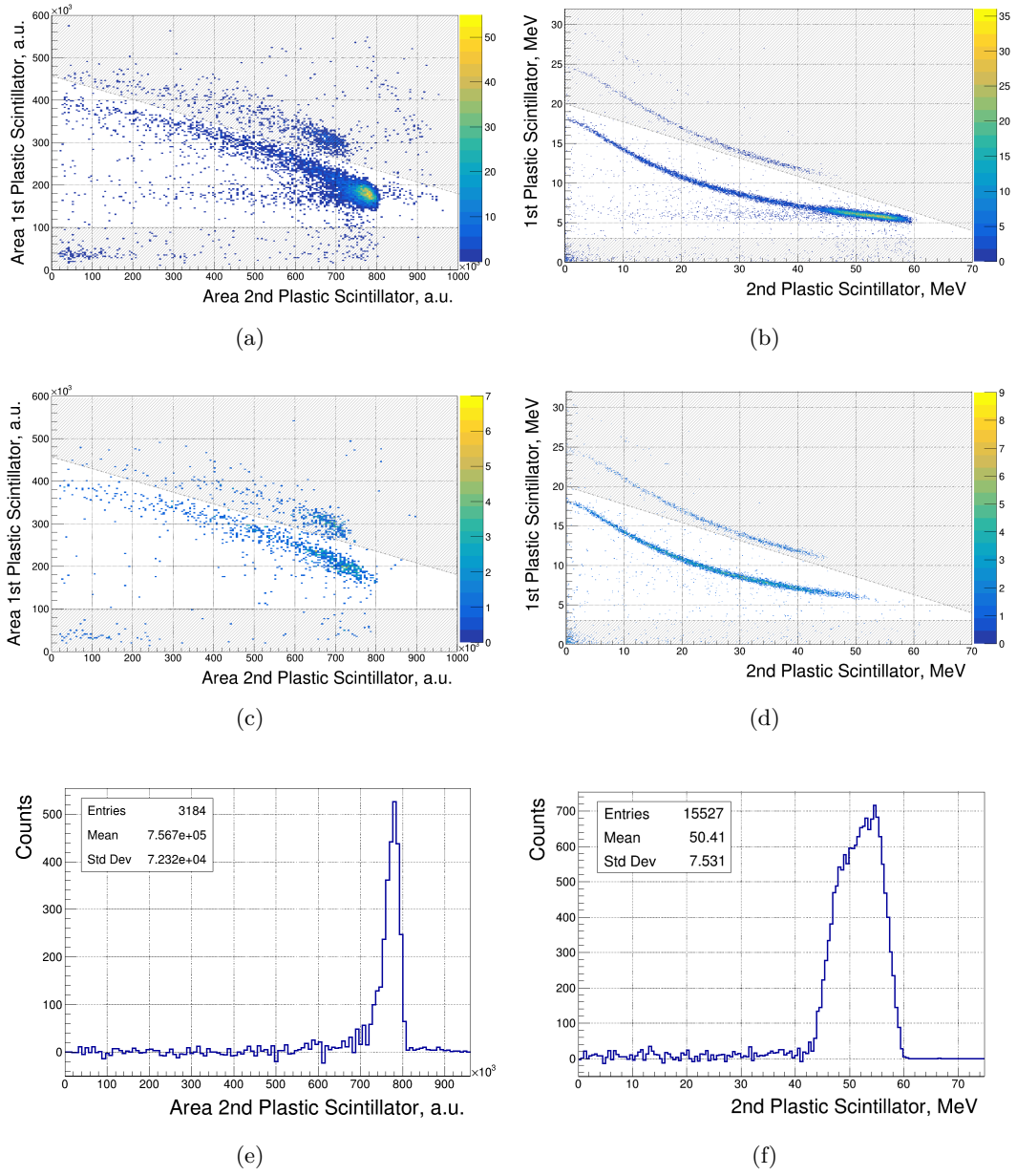

Figure 5.14: Figures 5.14(a) and 5.14(c) display the ΔE-E matrices produced by the experimental data choosing the events of neutrons with energy of (74.8 ± 2.2) MeV hitting the 1.834 mm thick C_2H_4 and the 1 mm thick C sample, respectively. Figures 5.14(b) and 5.14(d) show the same ΔE-E matrices but obtained through data from simulations. In each matrix only the proton hyperbola was selected and the subtraction between the two samples was performed. The one-dimensional histograms in the bottom panels show the result of the subtraction between the two samples for the data, the figure 5.14(e), and for the simulations in 5.14(f).

protons no further stop inside the detector.

5.4.1 Dead time correction

The counting rate determined by the n_TOF neutron beam hitting the polyethylene targets, $Counts_{C_2H_4}$, is quite high and the pileup events are fairly frequent. For this reason the correction of the reconstructed events for dead time of each stage of

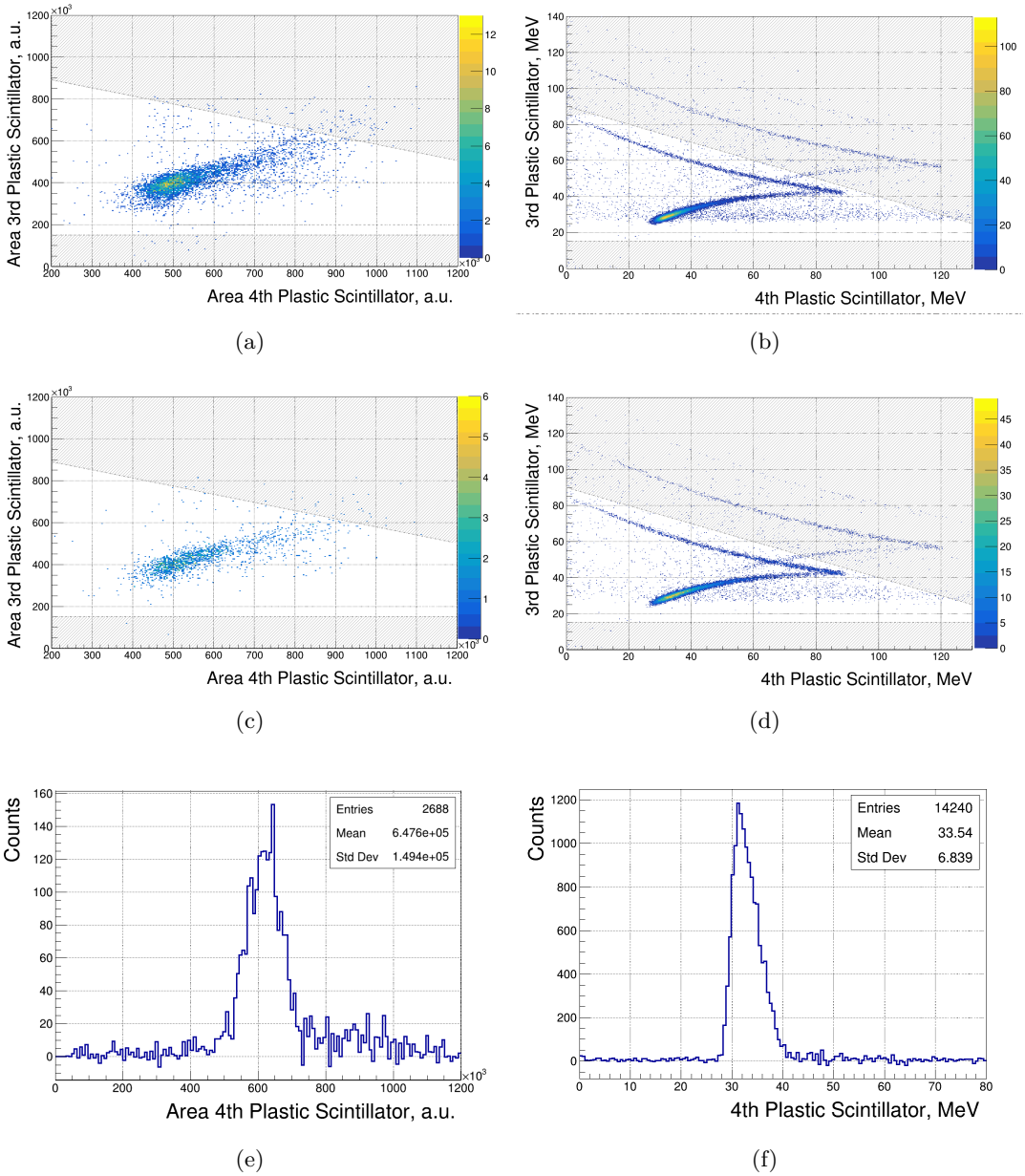

Figure 5.15: Figures 5.15(a) and 5.15(c) display the ΔE-E matrices produced by the experimental data choosing the events of neutrons with energy of (270.9 ± 11.7) MeV hitting the 1.834 mm thick C_2H_4 and the 1 mm thick C sample, respectively. Figures 5.15(b) and 5.15(d) show the same ΔE-E matrices but obtained through data from simulations. The one-dimensional histograms, in the bottom panels, show the result of the subtraction between the two samples for the data, in figure 5.15(e), and for the simulations in 5.15(f).

the telescope is necessary. In the coincidence method a non-random element is introduced that makes the calculation of the dead-time and coincidence losses somewhat more difficult. In parallel to the good events there are random events that can cause coincidence between different detectors. Although in our case the second contribution is significantly lower than the first one, it is still appropriate, for a more accurate calculation of the correction factor, to separate the two effects.

The first needed step is the evaluation of the typical dead time of each detector. The

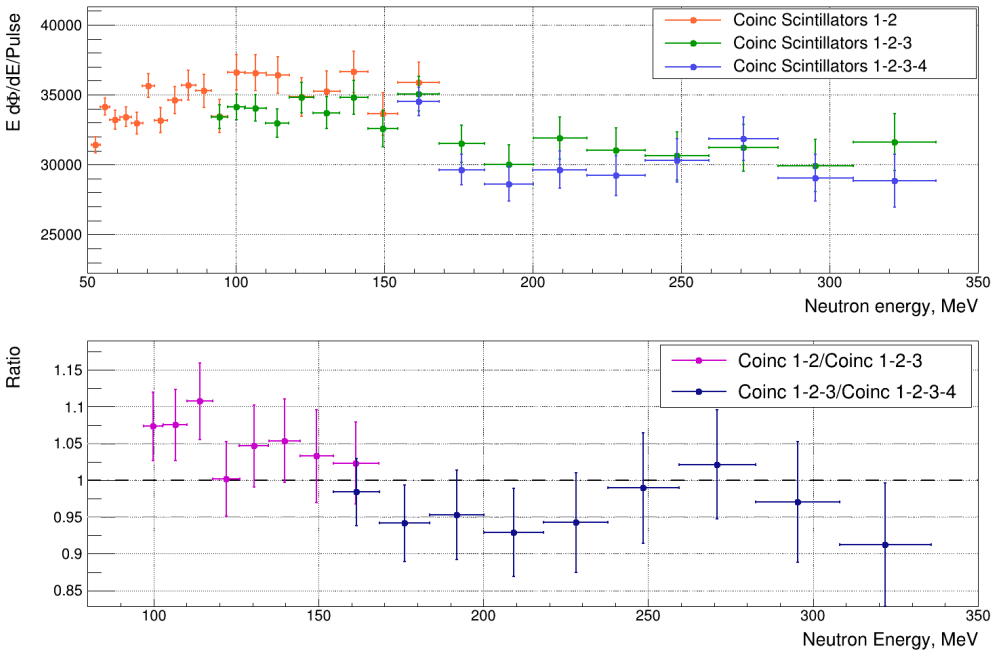

Figure 5.16: Top panel: the neutron flux extracted taking into account the coincidence between the first two plastic scintillators,in orange, the three scintillators, in green, and all the plastic scintillators in blue. In the bottom panel the ratios between the different configurations, in the energy range where they overlap, are shown. Taking into account the coincidence between only the first two scintillators, in the energy range between 100 and 160 MeV, the telescope is working in the punch-through condition in fact the protons stop in the third scintillator. The same situation is for the energy range between 160 and 330 MeV requiring the coincidence 1-2-3 instead of coincidence among all the scintillators.

time that typically elapses between two successive events in the same silicon detector or plastic scintillator had to be defined. Figures 5.17 show a distribution for the first silicon and one relative to the fourth scintillator. The value of the dead time has been

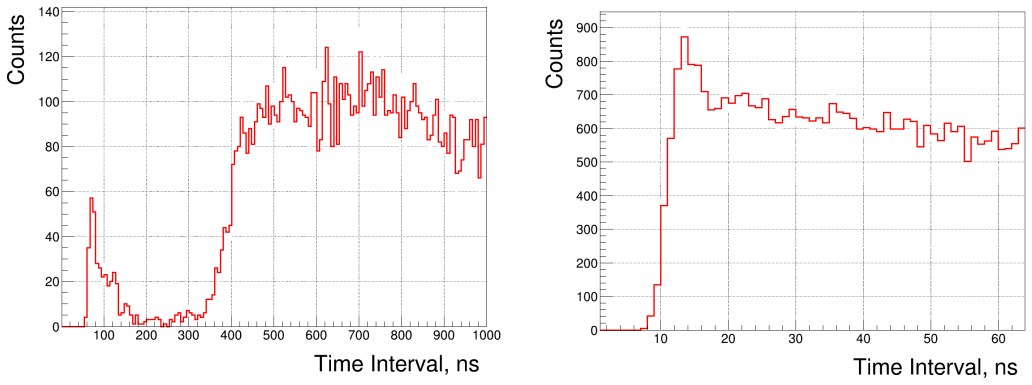

(a) (b)

Figure 5.17: Time difference between two consecutive events recorded by a silicon detector, in figure 5.17(a), and a plastic telescope scintillator, in figure 5.17(b).

established considering the point of the graph where the distributions reach the maximum and begin to decrease, therefore for example for the two histograms of the two

reported detectors the dead time is 450 ns for 5.17(a) and 13 ns for 5.17(b).
The formula used for the correction, based on the approach studied by Whitten for time of flight facilities [194], was applied separately for dedicated and parasitic pulses. The real number of coincidences $N_{t,ev}(i)$ in the $i-th$ tof bin can be expressed as:

$$N_{t,ev}(i) \;=\; \alpha(i)\, N_{t,0}(i) \tag{5.2}$$

where $\alpha(i)$ is the tof-dependent dead-time correction and $N_{t,0}(i)$ is the number of events of coincidences recorded in the $i-th$ tof bin.
In the case of n detectors, each characterized by its dead time τ_d, in coincidence with each other, the correction factor can be calculated with the formula:

$$\alpha(i) \;=\; -\frac{N_{ppb}}{N_{t,0}(i)}\, ln\left\{1 - \frac{N_{t,0}(i)/N_{ppb}}{\left(\prod_{d=1}^{n} N_d\right)\cdot N_t}\right\} \tag{5.3}$$

where N_{ppb} is the number of protons per pulse, N_d and N_t can be defined as:

$$N_d \;=\; \left(\sum_{k=i-\tau_d}^{i-1} 1 - \frac{N_d(k) - N_{t,0}(k)}{N_{ppb}}\right) \quad \text{and} \quad N_t \;=\; \left(\sum_{k=i-\tau_d}^{i-1} 1 - \frac{N_{t,0}(k)}{N_{ppb}}\right) \tag{5.4}$$

N_d is the number of events for single detector, d, integrated from the tof bin $i-\tau_d$ up to $i-1$ subtracting the total number of events in coincidence between the various detectors and N_t is the integrated number of events in coincidence. The subtraction separates the random contribution of individual detectors from the true coincident events, which are considered separately to avoid an overestimation of the final correction. The cor-

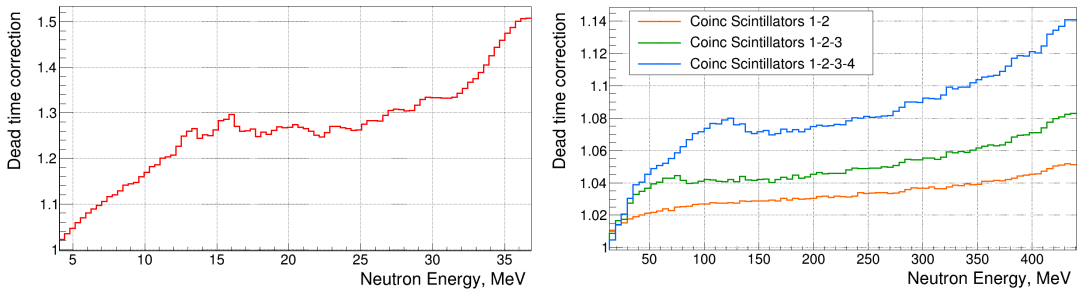

(a) (b)

Figure 5.18: Dead time correction calculated with the formula 5.3 for the coincidence between the silicon detectors (in parasitic pulse mode), in figure 5.18(a), and for the different configurations between the plastic scintillators (in dedicated pulse mode), in figure 5.18(b).

rections calculated for the various detector configurations are shown in figure 5.18: in the left panel the correction factor considering the coincidence between the two silicon, in parasitic mode, is displayed; in the right panel there are the three factors for the three coincidence configurations among the plastic scintillators, in dedicated mode. The orange line represents the correction factor for coincidences between the first two scintillators, the green line the factor for coincidences among the three scintillators

and the light-blue line the correction factor for the events in coincidence among all the scintillators.
As already mentioned, the correction for detector dead time has been implemented separately in the events recorded in dedicated and parasitic mode. This approach also allowed us to evaluate the accuracy of the correction and the uncertainty to be associated with this factor. The flux was extracted in the dedicated and parasitic pulses and the consistency of the two results revealed the validity of the applied method. In the top panel of figure 5.19 the results, from all the configurations with the plastic scintillators used, are shown; in the bottom panel there are the ratios between the flux achieved with parasitic and dedicated pulses. The consistency between the results

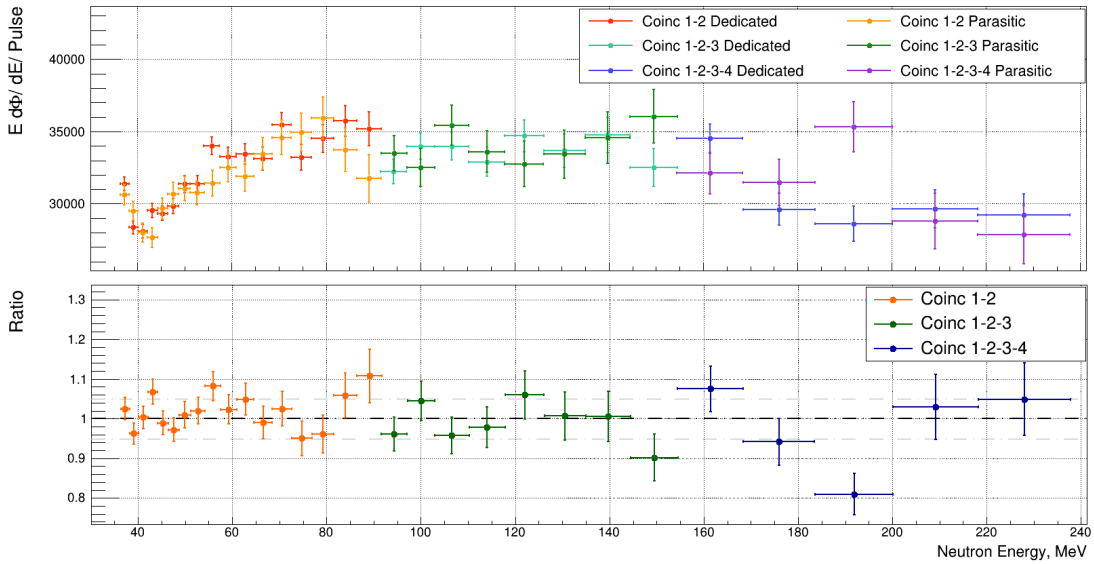

Figure 5.19: The top panel: the fluxes, in the different configurations, extracted separately for the events generated in parasite and dedicated mode, correcting them for the respective dead time factor. Bottom panel: the ratio between the fluxes extracted using the dedicated and the parasitic mode of the PS pulse.

within the experimental errors, which become more important as the energy increases, demonstrates the accuracy of the method used. The experimental uncertainties are mainly due to the reduced statistics with the parasite bunch.
In the next chapter a quantification of the uncertainty associated to the correction factor on the dead time will be illustrated, recalculating the factors with different values of dead times and evaluating the effect that these have on the final result.

At this point the final flux can be extracted by considering separately all the configurations: the dedicated and parasitic bunch and the three targets of C_2H_4 and C, with different thickness. Finally, the weighted average of all the results yields the flux reported in green in figure 5.20. The error reported is only related to the counting statistics.

Using exactly the same method composed of the above described passages, it is

possible to extract the flux from the second telescope, i.e. the one dedicated to the high-energy region. The main difference between the two detectors is the extra background source present in the RPTH-INFN. In fact, together with the particles produced in the second target to which it is pointed, it also sees some events coming from the first polyethylene target. A full simulation of the entire experimental setup including the two polyethylene targets and the two telescopes was then developed in order to estimate the mutual background contributions. Both contributions were investigated: backscattered secondary particles from the target in front of the PRTH-INFN telescope reaching the PRTL-INFN, and, on the other hand, particles from the first sample that can deposit significant energy in the second telescope [191]. From about 100 MeV of neutron energy, no significant contributions were observed for both the scenarios.
In addition, the correction due to the attenuation of the neutron beam after crossing the first polyethylene or carbon target has to be considered. This contribution was calculated considering the total cross-sections involved in the sample, calculating it for the various first samples used in the experimental campaign. The largest attenuation is obtained at about 100 MeV of neutron energy with the thick C_2H_4 target and it is about 1.2%.

The analysis of the second telescope has not yet been extended to the whole statistic. The preliminary extracted flux is in purple in figure 5.20.

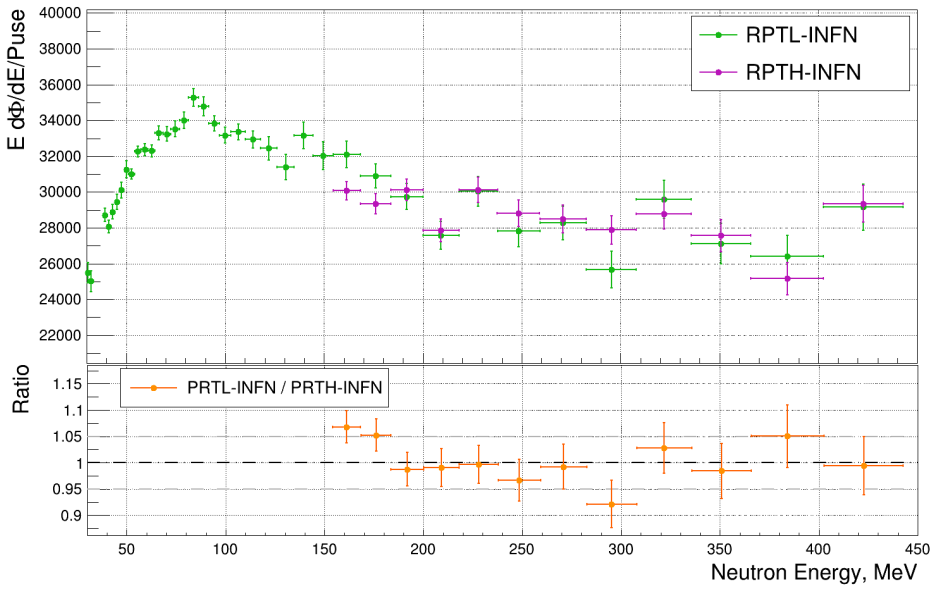

Figure 5.20: In green the extracted neutron flux combining the three polyethylene samples of different thicknesses, using the RPTL-INFN. In purple the preliminary result obtained from the RPTH-INFN. The bottom panel shows the ratio of the flux from the two telescopes in the common part of their energy ranges.

In the bottom panel of figure 5.20 it can be seen the consistency of the two fluxes extracted with the two telescopes through their ratio.

Chapter 6

Experimental results

The fission events detected by the Parallel Plate Avalanche Counters and the neutron flux measured by means of the two INFN-telescopes allowed us to extract a preliminary result for the ^{235}U fission cross section (related to the n-p scattering) in the neutron energy range between 10 and 500 MeV. A detailed assessment of the systematic uncertainties involved in the analysis was performed, and then combined to the statistical uncertainties. The resulting cross section is compared to the experimental measurements and the evaluated value present in literature. A preliminary comparison is shown between the cross section obtained in this thesis and that provided by the Parallel Plate Ionization Chamber and the RPT-PTB, both analyzed by the n_TOF colleagues from Physikalisch-Technische Bundesanstalt.

6.1 Discussion on the uncertainties

The total uncertainty in the ^{235}U(n,f) cross section is a combination of several components. The uncertainties related to neutron flux measurement and fission counts should be analyzed separately and then combined to obtain the final uncertainty of the fission cross section. Alongside the uncorrelated uncertainty due to the counting statistics, both in the results from the telescopes and the PPACs, two contributions can be highlighted: the first is related to the experimental conditions of the n_TOF facility and the experimental setup itself; the second is related to the analysis procedure.

Uncertainties related to neutron flux

To evaluate the uncertainties affecting the measurement of the neutron flux, in particular those related to the analysis of the detection procedure, it is appropriate to divide the energy range studied by the RTPL-INFN into three regions, diversified by the different detectors used or by the different working conditions:

- from 10 to 30 MeV the analysis is characterized by the coincidence between the two silicon detectors;

- from 38 to 200 MeV of neutron energy, the protons produced by scattering with neutrons stop inside the INFN-telescope;

- in events generated by neutrons with energy higher than 200 MeV, the protons exit from detectors and the telescope works in punch-through condition.

Regarding the RPTH-INFN, working in the highest energy region from about 100 MeV, the regions are reduced to two, separated at 200 MeV.

The sample-related component of the uncertainty depends on the characteristics of the samples summarized in table 3.2. Both the density and thickness of all polyethylene and carbon samples were characterised by the PTB engineering division. The density was calculated by hydrostatic weight obtaining an accuracy on the measurements at the level of 0.2%. Whereas, the thickness of each target was measured for 25 different positions, obtaining a precise knowledge of the corresponding profiles. Knowing the exact point of impact of the neutron beam on the target, it was possible to deduce the correct thickness of the samples.
The combination of density and profile measurements provided an accurate assessment of the areal density of the samples. The evaluation of the uncertainty found on this quantity was equal to 1.4% for the thinnest carbon target (0.5 mm), and well below 1% for all other samples.

As the uncertainties relating to data analysis are concerned, three main components can be identified: a) one related to the identification of the signals using the Pulse Shape Analysis framework, b) another associated to the dead time correction and c) a third for the events selection, incuding background subtraction.
a) Pulse identification. Different techniques have been used for the recognition and the reconstruction of the raw data and the complete discussion is in section 5.2. It is worth remembering what are the two most critical issues to the two types of detector: for silicon detectors the baseline oscillations present in proximity of the γ-flash, while for plastic scintillators it is the identification of overlapping events. To assess the impact of the approach chosen for the analysis and the confidence in the results obtained, the number of n-p scattering events have been extracted with all methods and compared to each other. Concerning the silicon detectors, the baseline oscillations cause an effect on the number of events which is at 2% level. While, for plastic scintillators the resolution of pile-up events using an imposed shape produces a final uncertainty smaller than 1%.
b) Dead time. The correction for the dead time of the detectors reaches up to about 40% for coincidences between the two silicon detectors and 15% when the coincidences between the 4 plastic scintillators are considered. Since in both cases it is a non-negligible correction factor, the neutron flux was calculated considering the method described in section 5.4.1 and applying different realistic fixed dead times for each single stage of RPTs. For the silicon detectors, the resulting uncertainty is slightly higher than that for the plastic scintillators, being 2% and 1%, respectively.

c) Event selection. The selection of the events was performed applying proper cuts on the ΔE-E matrices to isolate the protons coming from n-p elastic interaction, as illustrated in section 5.4. The used thresholds were properly modified, finding differences in the results smaller than 1%. The largest deviation was found when all events were considered (i.e. including both protons and deuterons). Furthermore, the carbon-generated contribution was subtracted from the ones obtained with the polyethylene target on the beam. Consequently, this subtraction eliminates all the events in the ΔE-E matrix attributable to deuterons. With this test the upper limit on the uncertainty in the number of events recognized as coming from n-p scattering was obtained, and resulted to be 5% for silicon detectors and 2% for plastic scintillators.

Other minor components of uncertainty are related to the geometry of the apparatus: d) the relative position between the detector and the target, e) the point of impact of the neutron beam in the C_2H_4 and C samples and f) its shape.

d) Distance. The distance between the target and the telescope affect the solid angle subtended by the detector, thus introducing a scale factor in the geometrical efficiency of the detector.

e) Beam position. The point of impact of the neutron beam in the polyethylene target determines the angle between detector and beam direction defining the values of the $d\sigma/d\Omega$ to be used. Small variations of the angle produce a sizable effect because of the n-p cross-section shape (figure 6.1). For instance, in this case the impact in the number of events is progressively more significant as energy increases.

f) Beam profile. The neutron beam profile used in the Monte Carlo simulations had

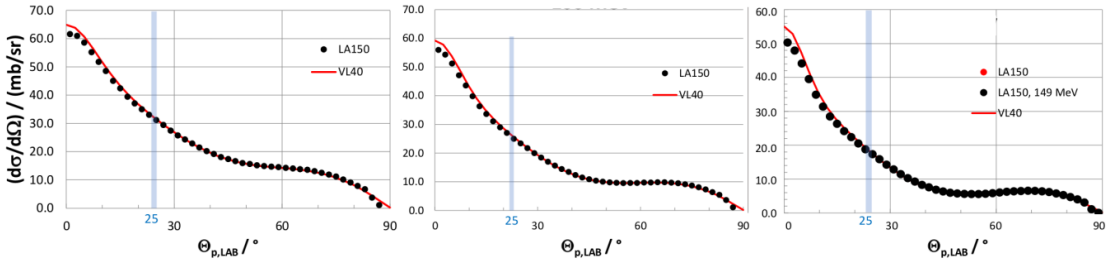

Figure 6.1: Evaluation of the neutron-proton elastic scattering cross section as a function of the angle of the scattered proton (in the laboratory reference system) at three different neutron energy: 75, 100 and 150 MeV.

a Gaussian shape to cope with the nominal value [149]. However, as mention above, it was possible to extract the beam profile at different neutron energies using the point-of-impact data provided by the PPACs. For instance, from about 30 MeV the beam profile slightly changes its spatial distribution: the peak area is wider and flattened and the tails are steeper. The following formula was found to reproduces the neutron profile shape:

$$N(r^2)\,\mathrm{d}r^2 = p_0\,\exp\left(-\frac{p_1 r^8}{(1+p_2\,r^2)^{3.9}}\right)\mathrm{d}r^2 \tag{6.1}$$

where p_0, p_1, p_2 are empirical parameters and recalling that the beam profile is sym-

metric. Clearly, this distribution modifies the area of the target that is seen by the incident neutron beam.
All these effects (listed above as d, e and f) were studied through Monte Carlo simulations slightly modifying the geometry of the experimental setup. More in detail, the effects related to the geometry and to the beam profile have an impact on the final result resulting in an uncertainty of less than 1%.

Moreover, another aspect to consider is the attenuation of the neutron beam in the uranium samples and their supports contained in the two fission chambers. This phenomenon was studied and estimated through Monte Carlo simulations. Around 1.5% of the neutrons of the beam interact inside the PPFC and can slightly change their direction, however a non-negligible fraction of these neutrons still remain in the beam. Therefore, about 0.8% of the neutrons interacting with the PPFC escape the sensitive area of the uranium samples inside the PPACs. Since the contribution of PPACs in neutron reduction is negligible for the intent of this analysis, the neutrons that reach the polyethylene target are still 99.2% of the starting beam. 0.8% has to be included in the calculation of the measurement uncertainties.

The last uncertainty to discuss is related to the neutron flux analysis. In particular, the total neutron-proton scattering cross section is completely elastic up to 350 MeV, while above the first inelastic channel opens:

$$n + p \rightarrow n + \Delta \rightarrow n + p + \pi^0, \tag{6.2}$$

which becomes sizably above 500 MeV and remains dominant up to 1 GeV. In fact, the inelastic cross section at 350 MeV neutron energy is 0.5% of the total n-p scattering cross section and at 450 MeV it reaches a few percent. From 500 MeV to 1 GeV the inelastic contribution becomes increasingly larger reaching 55% of the total neutron and proton scattering events [195]. Therefore, in the energy range for interest of this thesis, this channel is completely negligible.

In table 6.1 all the uncertainties are listed for the different energy ranges.

Uncertainties related to fission events

The constraint of coincidences between two adjacent detectors, on which the analysis of PPACs is based, ensures a an almost background-free selection of fission events. However, a few specific steps require careful evaluation of the uncertainties involved in the analysis procedure.

Most important in the evaluation of the uncertainty is the characteristics of the targets. As discussed in section 3.4.2, the composition of the targets contained in the

Table 6.1: Summary of uncertainties related to the extraction of the neutron beam flux in the ^{235}U(n,f) cross-section measurement.

Source of uncertainty	Uncertainty E_n = [10-30] MeV	Uncertainty E_n = [38-200] MeV	Uncertainty E_n > 200 MeV	Reference
C_2H_4 mass	0.4%	0.2-0.5%	0.2-0.5%	Section 3.3.2
C mass	1.4%	0.5-0.6%	0.5-0.6%	Section 3.3.2
Signal Reconstruction	1.8%	0.5%	0.7%	Section 5.2
Dead time correction	2.0%	1.0%	1.0%	Section 5.4.1
Cuts in the ΔE-E matrix	5.0%	2.0%	2.0%	Section 5.4
Telescope angle	0.6%	0.9%	1.0%	Section 3.6.1
Telescope position	0.7%	0.7%	0.7%	Section 3.6.1
Beam transmission	0.8%	0.8%	0.8%	
Beam profile	0.5%	0.5%	0.5%	
Counting statistics	1.7-3.8%	1.0-2.4%	2.8-4.5%	
Total	6.2 - 7.1%	2.9 - 3.7%	4.4 - 5.4%	

PPAC is very well known. In fact, the uncertainty, which is about 0.7%, is mainly due to the evaluation of the solid angle subtended by the detector during the sample characterization measurement, carried out by counting α particles emitted by the uranium target. Moreover, only the region illuminated by the neutron beam, rather than the full sample, is involved in the fission process. Therefore, it is necessary to know the thickness of the sample exactly where the beam-target interaction takes place. With this component the total uncertainty related to the sample masses is presently evaluated to be 1%.

The uncertainty on the efficiency is composed by three factors: g) the accuracy with which the trajectory of FFs is identified h) the combined effect of fit and the collected statistics at each angle and i) lastly the effect of correction for anisotropy.

g) FFs trajectories. The localisation of FFs is obtained from the time difference Δt between the two ends of the delay line, the method being illustrated in section 4.1.3. The propagation time along the delay line is about 100 ns, over the 100 strips (2 mm wide). The horizontal and the vertical position, respectively x and y, are obtained from $(\Delta t_{ns} - \tau)/w$, where τ and w are two calibration coefficients. The uncertainty related to the timing variable is mainly due to the uncertainty on Δt_{ns}, the time difference between signals collected by adjacent detectors which is involved in the computation of the angle. Therefore, the determination of this uncertainty is based on the shape of the position spectrum of fission fragments. These spectra, in each detector, have a Gaussian-shaped distribution, as shown in figure 6.2(a) where the y-coordinate reconstructed with the first detector is reported. In each of the three detectors, the maximum of the spectrum corresponds to the center of the beam and gives a relative reference which can be used as a common reference. Table 6.2 gives the x and y positions in ns of the peaks in the 3 detectors. The differences between the peak centers relative to the same coordinate

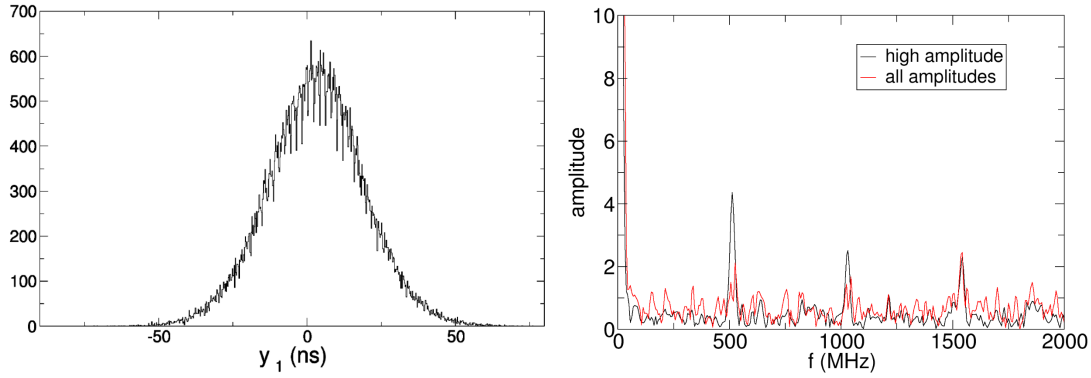

(a) (b)

Figure 6.2: In figure 6.2(a) the position spectrum of fission fragments of the y-coordinate of detector 1. In figure 6.2(b) the Fourier transform of the spectrum of figure 6.2(a).

(x or y) are within a window of 1 ns. Because there is not an absolute value of the shift, the τ given by the peak of the x and y distributions of the central detector is chosen as the common reference. Instead, the determination of w is based on the discrete structure evident from the distribution of localization signals: selecting high amplitude signals it is possible to identify the periodic structure of the strips, as shown in figure 6.2(a) for y_1. The periodic structures correspond to the strips and provide a geometrical ruler with a 2 mm pitch. A convenient way to count their spacing is to use a Fourier transform to identify the base frequency caused by the discontinuity of the strips, as shown in figure 6.2(b). The black spectrum is the result of the FT taking into account high amplitudes signals. From this spectrum it was possible to identify peaks corresponding to the periodic structures. The red spectrum was produced by considering all events and the main modulation is still present even if the background events make it less evident. In the case of y_1, for example, the main frequency was 513 MHz, hence in the original spectrum the period of the waving is 1.95 ns for a pitch of 2 mm, from which it can be inferred w: $w_{y_1} = 0.975$ ns/mm. The same process has been applied to all other coordinates and the results are summarised in table 6.2.

Table 6.2: The peak values of the fission fragment distributions and the calibration coefficient w for each x and y coordinate of each PPAC detector.

Coordinate	Peak Center (ns)	w (ns/mm)
x_1	9.0	0.97
x_2	8.6	0.97
x_3	8.1	0.97
y_1	3.1	0.97
y_2	2.5	0.98
y_3	2.2	0.98

Since the coefficient is stable within 1%, this value corresponds also to the precision

related to w. In order to obtain the uncertainty to associate to the localisation of the FFs it is opportune to recall the formula used to derive the angle:

$$cos\,\theta = \frac{d}{\sqrt{d^2 + r^2}}, \tag{6.3}$$

where d is 34 mm and is the distance between detectors and $r = \sqrt{(x_2 - x_1)^2 + (y_2 - y_1)^2}$. The derived uncertainty related to the determination of the trajectory of the fragments is well below 1%, e.g. $\Delta\cos(\theta)$ around the angle cut at $\cos\theta = 0.5$ is 0.37%.

h) Fitting angles. The second component refers mainly to the fluctuations due to low statistics. Note for example the figure 4.20, in which the smooth curves deviate at maximum with a standard deviation of about 2% with respect to the most punctual trend, obtained using 5 bins per decade.

i) Anisotropy. The method used to calculate the angular distribution is built on the anisotropy parameter (for details see section 4.1.3). The uncertainty related to the angular distribution has been evaluated by comparing the effect of three different anisotropies in the corrected FFs counts. Of the three factors used in this analysis, two are derived from experimental measurements [36, 189] and the third is a fit on different measurements contained on Experimental Nuclear Reaction Data (EXFOR) and an extrapolation at higher energy [196], above 15 MeV. The resulting uncertainty to be associated to the correction for the angular distribution of the FFs is at most 1.2%. This factor is the reason why it is appropriate to divide the energy range of the uncertainty in two parts, since the FFs emission returns to be isotropic above 200 MeV.

Table 6.3 lists all uncertainties associated with the analysis of fission counts.

Table 6.3: Summary of the uncertainties in counting FF events in the ^{235}U(n,f) cross section measurement.

Source of uncertainty	Uncertainty $E_n < 200$ MeV	Uncertainty $E_n > 200$ MeV	Reference
Sample mass	1.0%	1.0%	Section 3.4.2
Trajectories reconstruction	0.4%	0.4%	Section 4.3.1
Efficiency calculation fit	2.0%	2.0%	Section 4.3
Anisotropy correction	1.2%	-	Section 4.3.1
Counting statistics	2.5 - 4.2%	2.0 - 3.1%	
Total	3.6 - 4.9%	3.0 - 3.8%	

6.2 Extraction of the neutron flux

As mentioned above, the results obtained with RPTL-INFN are definitive, while the ones of RPTH-INFN are still preliminary, and therefore the total cross section. In

order to extract the final flux, the data obtained with the two telescopes, in the energy region where the results of the two detectors overlap, have to be combined. By using the weighted average of the two fluxes, extracted from the two independent detectors, the systematic uncertainties can be reduced. The goodness of the agreement of the two results, as observed in figure 5.20, in spite of the differences between the working conditions, i.e. the angle at which are placed relative to the neutron beam direction, the background sources and the cuts applied to the ΔE-E matrices, provides confidence on the results up to 500 MeV. Figure 6.3 shows the preliminary n_TOF neutron flux calculated by combining the results from the two INFN-telescopes. The points up to 32 MeV were extracted using the coincidence between silicon detectors (of the RTPL-INFN), while from 40 MeV upwards the coincidences between plastic scintillators were used. These different time properties of the two types of detectors explain the gap in between the two intervals: the coincidences between silicon detectors and plastic scintillators are not applicable.

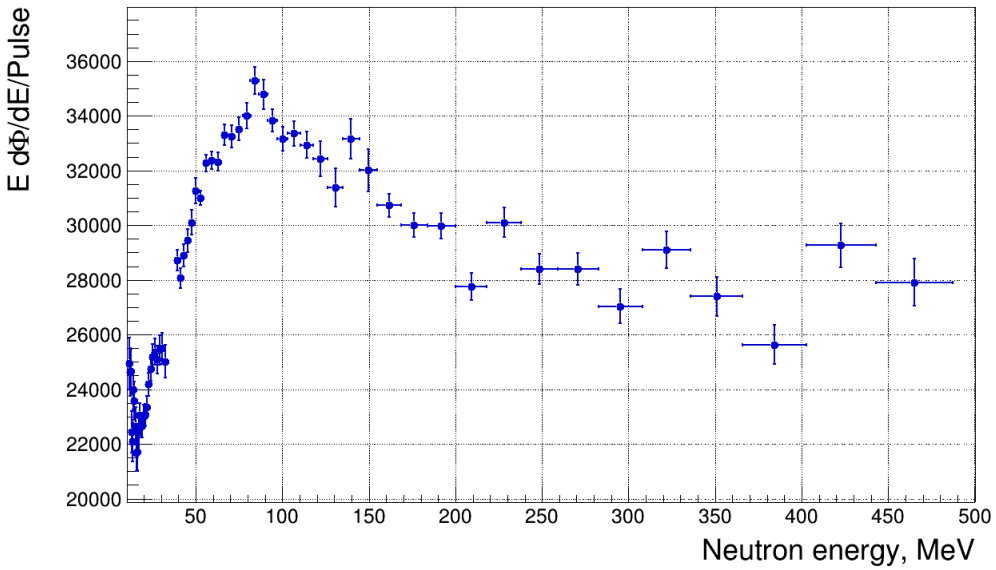

Figure 6.3: The extracted neutron flux combining the results from the two INFN-telescopes.

6.3 Comparison with PTB data

A preliminary comparison was carried out between the two independently extracted cross sections in the present measurement campaign: the PPACs and the two INFN-telescopes were compared to the data recorded by the PPFC and the flux measured with the PTB-telescope. The data from these other two detectors have been analyzed by the n_TOF colleagues from the Physikalisch-Technische Bundesanstalt institute, with whom the idea of this measurement was born, discussed and realized. The comparisons will concern the fluxes obtained through the telescopes, through the fission chambers themselves and finally the resulting fission cross section.

Figure 6.4 shows the ratio between the fluxes extracted using the two RPTs-INFN and the one obtained from the RPT-PTB analysis. The comparison always results within 5%. Since the two results were obtained using completely independent detectors and two different analysis techniques, this comparison defines the reliability and the goodness of the neutron fluxes obtained.

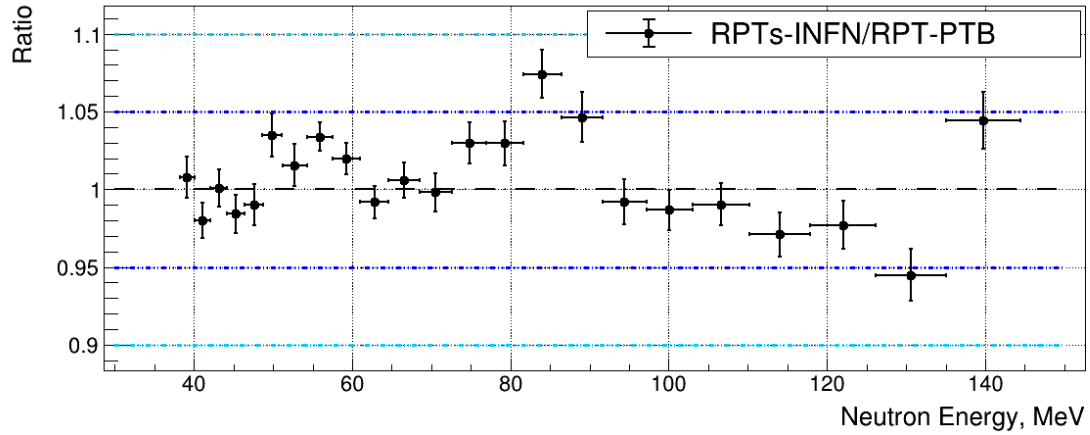

Figure 6.4: Ratio between the flux extracted using the RPTs-INFN and the ones from the RPT-PTB.

From the ^{235}U(n,f) cross section values present in literature, it is possible to extract the neutron flux incident on ^{235}U targets from the fission chamber counts (equation 3.7). Figure 6.5 shows the ratio between the flux extracted using PPACs as a beam monitor and the one obtained from the PPFC counts. Despite the in-depth and extensive studies carried out to evaluate the efficiency of the two detectors, the obtained ratio is characterized by a larger spread compared to the results obtained from the telescopes. Possibly, the best estimate of the systematic uncertainty associated with the two-chamber analysis for fission events can be defined from this ratio.

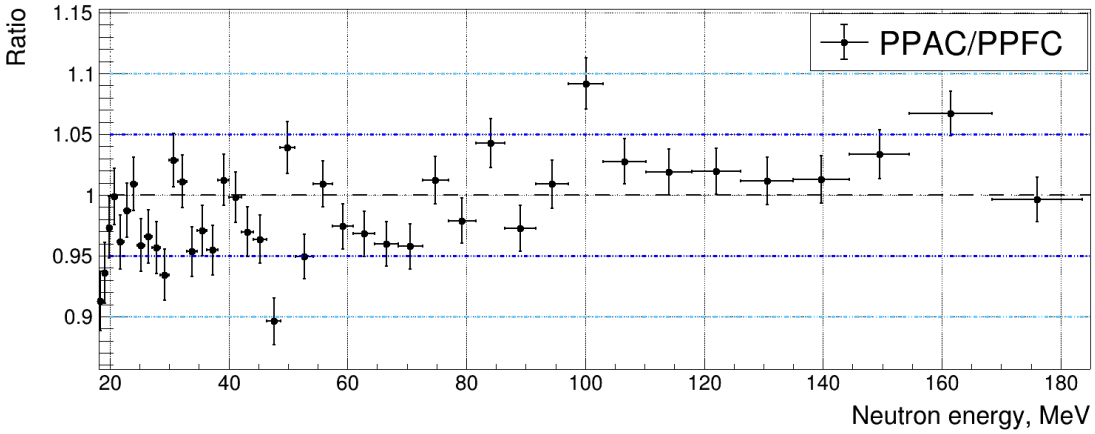

Figure 6.5: Ratio between the extracted fluxes obtained exploiting the fission chambers, PPAC and PPFC.

Figure 6.6 shows the ratio of the two extracted ^{235}U fission cross sections. Due to the characteristics of both the fission detector (PPFC) and the PTB-telescope, the

cross section extracted with these two detectors ranges from about 25 MeV up to 150 MeV of neutron energy. Although both results are preliminary, it is possible to see that they agree within 5% throughout the overlap range and that starting from 100 MeV of neutron energy the ratio is stable around 1. The agreement between the two results is fundamental to have confidence and strength also for the result obtained up to 150 MeV and to be able to give a reliable and trusted result also at higher energies.

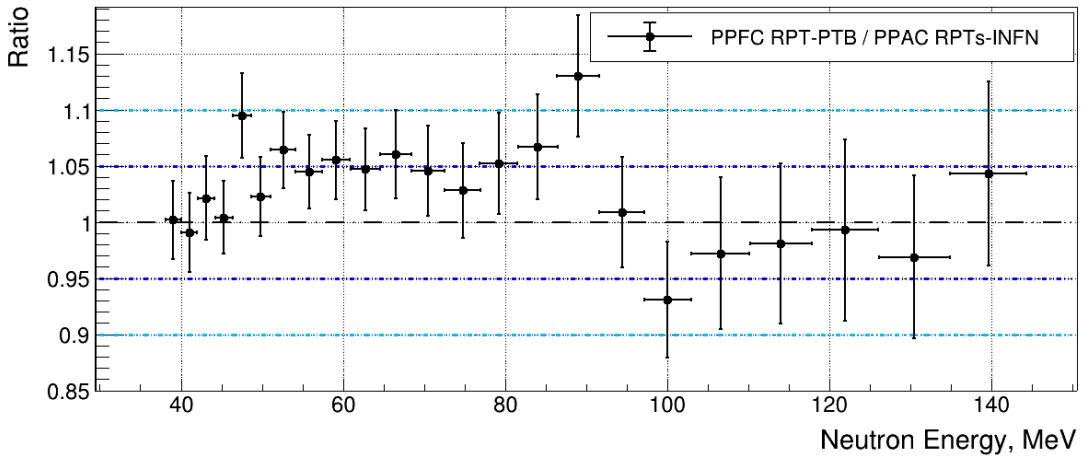

Figure 6.6: Ratio between the two cross sections measured in the experimental campaign analyzed in this work.

To conclude the analysis and extract the definitive results, the last remaining step is to extend the RPTH-INFN analysis to the whole statistics, which will allow us to reduce uncertainties and to better define the trend of the cross section at energies higher than 150 MeV. At that point, all corrections and systematics related to the five detectors used in the measurement will be fully under control, the convolution of the two cross sections, obtained on one hand from PPACs and the two INFN-telescopes and on the one hand from PPFC and RPT-PTB, will be performed. The final results will give the opportunity to deduce the theoretical implications related to this experimental measurement.

6.4 Preliminary ^{235}U(n,f) cross section

Figure 6.7 displays, with blue dots, the preliminary ^{235}U(n,f) cross section up to 200 MeV obtained dividing the events measured by the Parallel Plate Avalanche Counters by the flux extracted using the two INFN-telescopes (see formula 3.4). Uncertainties are only those related to counting statistics. Together with the result of this work, figure 6.7 shows the 1991 Lisowski data [114], in green, and the latest IAEA standard cross-section evaluation [84], the black line.
As suggested by the bottom panel where the ratios between the various data sets are reported, it is appropriate for comparison to divide this energy range in two sub-ranges, from 10 to 100 MeV and above 100 MeV. Up to 100 MeV our results confirm within

the 2% level those obtained by Lisowski and both are about 5% lower than the IAEA evaluation. Instead from 100 to 200 MeV all three cross sections are compatible within 5%. This result is in agreement with the measurement by Nolte and collaborators [113] within the experimental uncertainties. The compatibility of the n_TOF measurement of the cross section with the literature is an indication of the quality of the results and strongly supports the validity of the assessment of the cross section above 200 MeV.

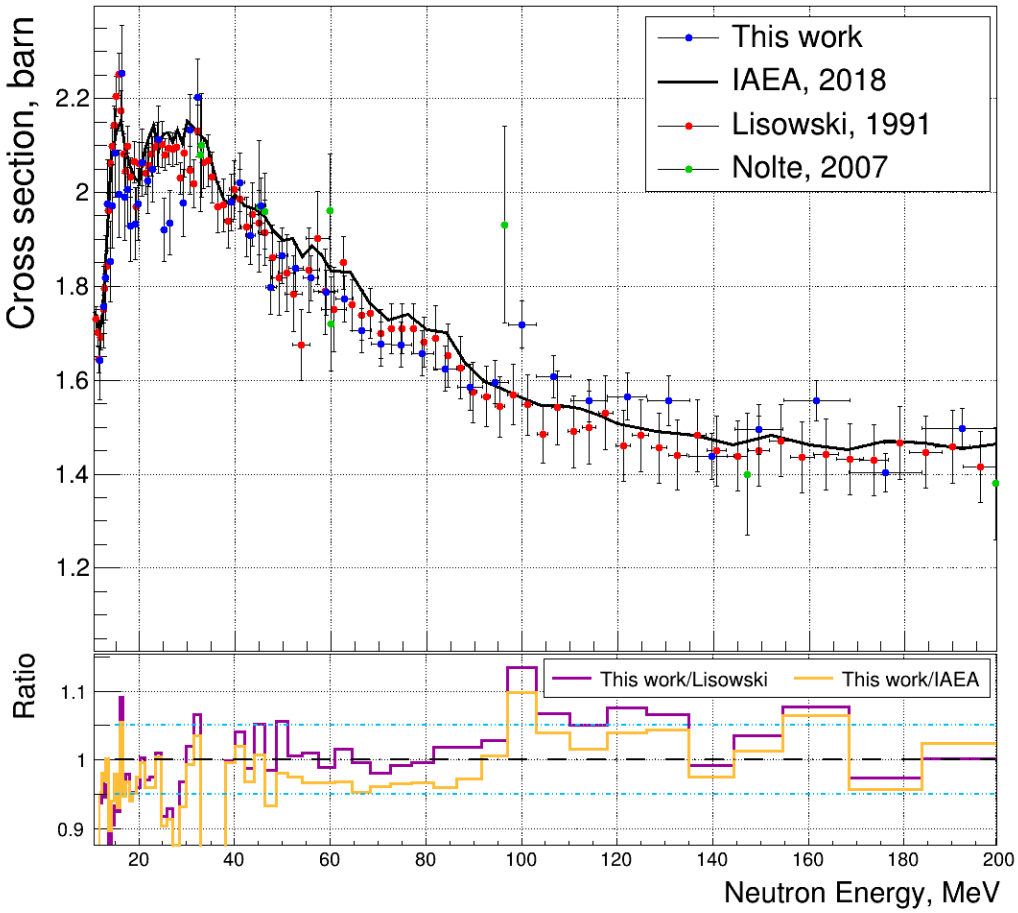

Figure 6.7: Top panel shows the ^{235}U(n,f) cross section: the blue dots are obtained in this work, the black line is the IAEA standard evaluation [84], the green dots are the experimental data obtained by Nolte [113] and the red dots are the Lisowski data set [114]. Bottom panel: ratios between the result of this work and the IAEA evaluation and Lisowski data in yellow and purple, respectively.

Moving to higher energies, it is important to underline that the fission cross section was extracted in the region where, so far, no experimental data sets exist. The result obtained is shown in the figure 6.8 with the two evaluations performed by IAEA (ADS HE) [92] and JENDL (JENDL-HE) [116]. The two evaluations were calculated using theoretical models, which reproduce the experimental trend of the proton-induced fission cross-section measurements. The measured cross section in this energy region is affected by the limited analyzed statistics of the RPTH-INFN. The resulted cross section seems to be lower than that from the theoretical models. The analysis is completed and further investigations are ongoing. In figure 6.9 are shown together with

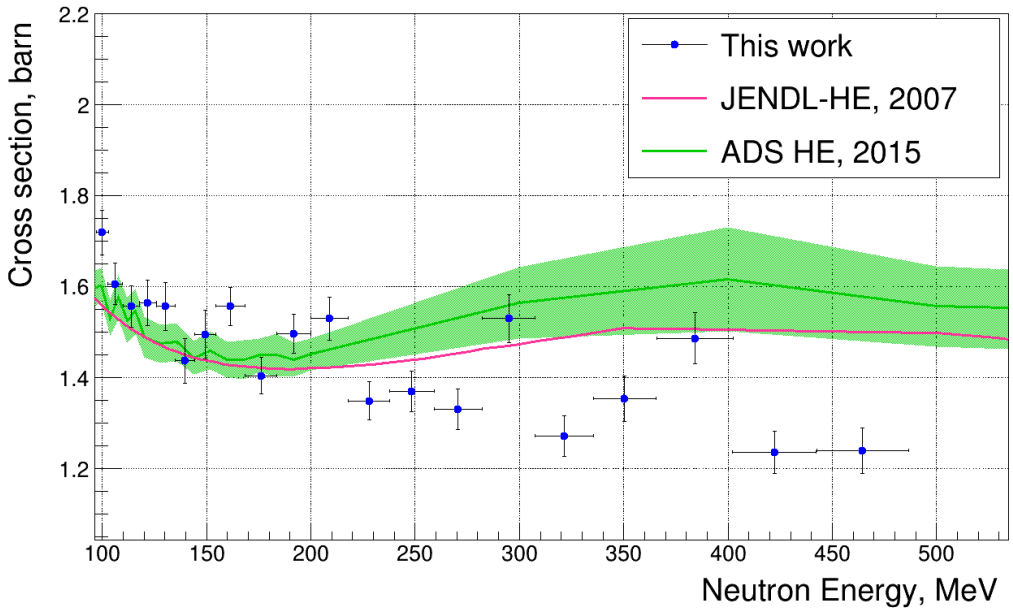

Figure 6.8: The ^{235}U fission cross section extracted in this work is reported in blue dots; the green line is the IAEA evaluation (ADS HE) [92] with the band corresponding to its uncertainty; the pink line is the JENDL-HE calculation [116].

our results the measurements of proton-induced fission cross sections currently available in literature [197, 198, 199, 200]. It is interesting to note that, with increasing

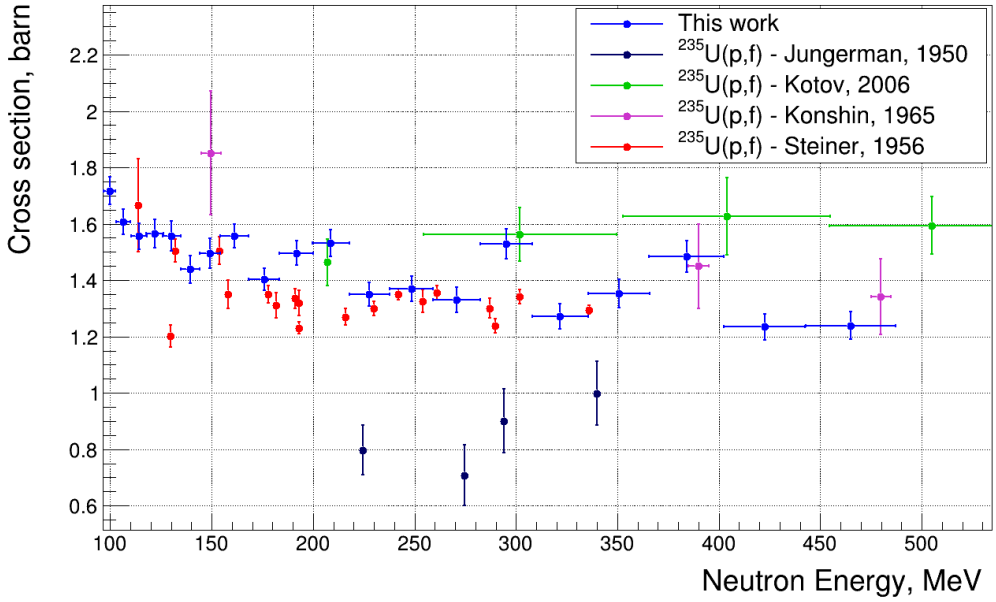

Figure 6.9: Comparison between the neutron- and the proton-induced fission cross section of ^{235}U obtained in this data analysis, and in literature, respectively. In blue this work, in dark-blue Jungerman [198], in green Kotov [200], in violet Konshin [199] and in red Steiner [197].

energy, the cross sections induced by protons and neutrons overlap. This demonstrates that, when the energy of the projectile is high enough, the effect of the isospin in the cross section becomes negligible and the ratio between σ_{nf} and σ_{pf} is approximately

1. The explanation for this phenomenon lies in the fact of that the capture probability decreases with the energy of the projectile. The system does not form a compound nucleus which would be greatly affected by the isospin. Therefore, both neutron and proton projectiles leave the ^{235}U nucleus in an excited state that can decay through fission.

So far, only the uncertainties due to counting statistics were reported. Table 6.4 resumes the total uncertainties relative, i.e. statistical combined with systematic.

Table 6.4: Summary of the uncertainties in the ^{235}U(n,f) cross section measurement.

Source of uncertainty	Uncertainty E_n = [10-30] MeV	Uncertainty E_n = [38-200] MeV	Uncertainty E_n > 200 MeV
Total RPTL-INFN + RPTH-INFN	6.2 - 7.1%	2.9 - 3.4%	3.6 - 4.9%
Total PPAC	3.6 - 4.9%	3.6 - 4.9%	3.0 - 3.8%
Total	7.2 - 8.6%	4.2 - 5.5%	4.7 - 6.3%

Conclusions

The neutron-induced fission cross-section of ^{235}U as a function of the neutron kinetic energy was measured at the neutron time-of-flight facility n_TOF at CERN. The unique features of the CERN proton synchrotron make n_TOF one of the few existing facilities for the study of nuclear reactions induced by high-energy neutrons, thus enabling the study of the ^{235}U(n,f) cross section between 20 and 500 MeV. The experiment was carried out at the 185-m long flight-path station, which provides an excellent energy resolution and where the neutron spectrum reaches the GeV region. On average, some 10^5 neutrons per bunch are produced with energies between 20 MeV and 1 GeV, corresponding to time of flights ranging from some 100 ns to 2.5 μs after the γ-flash. As a consequence, a common feature of the chosen detectors is a good timing property, so to cope with the narrow time-of-flight window of interest. In addition, a redundant measurement setup was adopted, with the aim of benchmarking the results while reducing systematic uncertainties related to the detection efficiency and the ones linked to the ^{235}U samples.

The experimental apparatus consisted of three flux and two fission detectors, thus allowing us to simultaneously record the number of neutrons impinging on the ^{235}U samples and of fission events, as a function of the neutron energy. More in detail, the experimental signature of fission reactions was obtained by detecting the fission fragments (FFs) originated from the nuclear reactions in ^{235}U. In one of the two fission detectors, i.e. the Parallel Plate Avalanche Counters (PPACs), the two fragments were recorded in coincidence, while the working principle of the Parallel Plate Ionization Chamber (PPFC) was based on the detection of one fragment only. This different detection scheme results in a different detection efficiency, which is, on average some $55 \pm 2\%$ for PPAC and near 100% for PPFC. On the other hand, because of the dissimilar gas pressure, construction properties and applied electric field, the response of the two detectors to the γ-flash makes PPFC suitable up to 150 MeV neutron energy, while PPACs can reach 1 GeV. In addition, the correction for the angular distribution of the fission fragments, which is strongly anisotropic for neutron energy from a few MeV up to 200 MeV, was taken into account. Because of the different working principle of the two detectors this correction has a different impact on the two systems. Since PPACs are limited in the angle of detection, the anisotropy correction factor for this detector can reach up to a maximum of 6%, while that of PPFC, being sensitive to FFs emitted at 4π, is as high as 1.5%. The other part of the detection setup, i.e. the

neutron flux detectors, was especially developed for this measurement (two detectors by Istituto Nazionale di Fisica Nucleare, INFN, and one by Physikalisch-Technische Bundesanstalt, PTB). The detection principle relies on the use of a counter telescope for the discrimination of the protons originating from the n-p scattering in a polyethylene sample (thus named recoil protons telescope, RPT). The measurement of the flux required an extensive background measurement and characterization to estimate the impact of the reactions induced by neutrons on the carbon, contained in the polyethylene target.

The preliminary results reported in the present PhD thesis were obtained using the data collected with the PPAC detector and the RPTs developed by INFN. The data analysis of the PPAC detector can be considered as a well-established procedure, this detector being successfully used at n_TOF in the past. On the other hand, the RPTs required a comprehensive characterization of their performances prior to the extraction of the neutron flux, and required an extensive use of Monte Carlo simulations (both Geant4 and MCNP were used for a benchmark). In particular, by simulating the detectors response to protons, deuterons, α particles and afterwards including neutrons impinging on a C_2H_4 sample, the efficiency of the RPTs was assessed. This in-depth study allowed us to introduce, in addition to the geometric factor, also the angular distribution of emitted protons from the n-p elastic scattering, as well as multiple scattering in the target and in the telescopes themselves and the absorption of the neutron beam in the C_2H_4 target.
The counter telescopes have a pyramidal multi-stage structure, providing a significant reduction of background events mainly generated by n+C reactions. This was obtained via software thanks to the selection of coincident events between two or more consecutive layers of the RPT. The coincidence technique was efficiently applied thanks to the excellent timing properties of the detectors: the distribution of time difference for the events in coincidence between the two silicon detectors resulted to be within 50 ns (FWHM), and for the plastic scintillators 1 ns (FWHM). It is well-known that the coincidences are necessary to exploit the ΔE-E technique and to perform particle identification, in particular to separate the contribution attributable to protons from that one of deuterons. The background induced by carbon reactions is not constant over different neutron energies as it increases with the incident-neutron energy, and it ranges from a few percent up to a maximum of 60% of the total proton events at 500 MeV. Above 200 MeV neutron energy, protons do not stop anymore inside the telescope and therefore it is not possible to clearly disentangle the contribution of protons from that of deuterons. As a consequence, starting from 200 MeV the contribution of the background becomes progressively more important and had to be estimated by means of Monte Carlo simulations. In the analysis procedure, among events in coincidences, protons were identified by applying suitable event selections to the ΔE-E matrices. For each energy bin, the corresponding counts were corrected for the estimated dead time of the detectors. This correction factor is significantly high for the silicon detectors, i.e. between 10 and 32 MeV neutron energy, where it reaches 40%, while for the plastic scintillators it never exceded 15%. In summary, using the developed RPTs, for the first

time the n_TOF neutron flux was measured in the energy range from 10 to 500 MeV with respect to the primary reference reaction: the n-p elastic scattering.

An extensive systematic study of the uncertainties associated with the measurement and analysis techniques and corresponding corrections was carried out. The uncertainties related to the knowledge of the number of atoms in the uranium, polyethylene and carbon samples in the region hit by the neutron beam, is 1% for the ^{235}U and below 1% for the C_2H_4 and C samples (except for the thinnest carbon sample which has an uncertainty of 1.4%). For either the PPAC detector and the two INFN-telescopes, the uncertainty associated to the efficiency and the analysis procedures, e.g., subtraction of background and event selections, is of the order of 2%. In addition, the effect of a possible misalignment between the polyethylene target and the counter telescopes was carefully evaluated via Monte Carlo simulations, resulting in differences in the number of counts within 1% with respect to the nominal detector position. Great attention was paid to detector dead time correction, to which an uncertainty of 1-2% was associated. This value was estimated using a method based on artificially increase of the detector dead time and comparison of the corresponding dead-time corrected spectra.

On average, the preliminary results agree within 5% with those obtained by the PTB group, who analyzed the data from the other counter telescope to extract the neutron flux and from FFIC to account for the fission events. As already mentioned above, the comparison between my results and that by PTB are intended firstly to increase the reliability of the experimental results and secondly to better quantify and reduce the systematic uncertainties related to the measured cross section. Moreover, the comparison with previous data is very interesting: in the energy range between 10 and 100 MeV the measured cross section is in agreement with the results obtained by Lisowski within 2% and within 5% with the IAEA evaluation. From 100 to 200 MeV neutron energy the measured cross section complies with IAEA evaluation and the Lisowski data, at 4% and 5% levels, respectively. The even more relevant output of this thesis is the first experimental determination of the ^{235}U fission cross section induced by neutrons with energy higher than 200 MeV. From this experimental result, it will be possible to constraint models on the fission process at intermediate energy, for instance the role of the isospin by comparing neutron- and proton-induced fission, the extrapolation of the fission width over other competing processes, e.g., multi-fragmentation, which provides more feedback on the the splitting time. In addition, it is worth to recall that the measurement of the cross section of fission induced by neutrons with energies higher than 200 MeV is a long standing request by the IAEA to extend the standard cross section in this region.

As a final remark, it is interesting to note that the results presented in this PhD thesis are beneficial in several research topics related to ^{235}U fission, namely basic nuclear physics, neutron standard cross sections as well as applications, for example nuclear energy production and transmutation of related nuclear wastes, radiation protection, or nuclear astrophysics. For instance, several fission reactions induced by high-energy neutrons were studied at n_TOF (e.g. on ^{nat}Pb, ^{209}Bi, ^{232}Th, ^{237}Np, ^{234}U and ^{238}U)

and the resulting cross sections were reported as the ratio with respect to ^{235}U(n,f). Using the results obtained in this PhD project, i.e. the first experimental determination of the ^{235}U(n,f) cross section above 200 MeV, it will be possible to re-analyze the reported results of the previous n_TOF fission experiments and to provide cross section values.

Bibliography

[1] E. Fermi, *Possible production of elements of atomic number higher than 92*, Nature **133** (1934).

[2] H. G. Graetzer, *Discovery of nuclear fission*, Am. J. Phys. **32** (1964), English translation of Hahn and Strassmann, Naturwissenschaften **1** (1939).

[3] L. Meitner and O.R. Frisch, *Disintegration of uranium by neutrons: a new type of nuclear reaction*, Nature **143** (1939).

[4] E. Feenberg, *On the Shape and Stability of Heavy Nuclei*, Phys. Rev. **55** (1939).

[5] J. Frenkel, *On the Splitting of Heavy Nuclei by Slow Neutrons*, Phys. Rev. **55** (1939).

[6] C.F. v. Weizsäcker, *Zum Wefelmeierschen Modell der Transurane*, Naturwiss **27** (1939).

[7] N. Bohr and J.A. Wheeler, *The Mechanism of Nuclear Fission*, Phys. Rev. **56** (1939).

[8] H.J. Krappe and K. Pomorski, *Theory of nuclear fission*, Springer (2012).

[9] K.S. Krane, *Introductory Nuclear Physics*, John Wiley & Sons Inc (1988).

[10] C.A. Bertulani and P. Danielewicz, *Introduction to Nuclear Reactions*, Routledge & Sons Inc (2004).

[11] S.M. Polikanov et al., *Production of nuclei with an anomalous spontaneous fission period in reaction involving heavy ions*, Sov. Phys.-JETP **15** (1962).

[12] V.M. Strutinsky, *Shell effects in nuclear masses and deformation energies*, Nucl. Phys. A **95** (1967).

[13] V.M. Strutinsky, *"Shells" in deformed nuclei*, Nucl. Phys. A **122** (1968).

[14] K.F. Flynn et al., *Distribution of Mass in the Spontaneous Fission of* ^{256}Fm, Phys. Rev. C **5** (1972).

[15] E.K. Hyde , I. Perlman and G.T. Seaborg, *The nuclear properties of the heavy elements: Vol 3 Fission Phenomena*, New York: Dover Publications (1971).

[16] M.C. Duijvestijn et al., *Mass distributions in nucleon-induced fission at intermediate energies*, Phys. Rev. C **64** (2001).

[17] L.E. Glendenin et al., *Mass distributions for monoenergetic-neutron-induced fission of* ^{235}U, Phys. Rev. C **24** (1981).

[18] E.J. Winhold, P.T. Demos and I. Halpern, *Minutes of the Meeting at Chicago, October 24-27, 1951*, Phys. Rev. **85** (1952).

[19] E.J. Winhold, P.T. Demos and I. Halpern, *The Angular Distribution of Fission Fragments in the Photofission of Thorium*, Phys. Rev. **87** (1952).

[20] J. E. Brolley, Jr. and W. C. Dickinson, *Angular Distribution of Fragments from Neutron-Induced Fission*, Phys. Rev. **94** (1954).

[21] J. E. Brolley, Jr., W. C. Dickinson and R. L. Henkel *Angular Dependence of the Neutron-Induced Fission Process. II*, Phys. Rev. **99** (1955).

[22] A. Bohr, *Proceedings of the International Conference on the Peaceful Uses of Atomic Energy*, Geneva, 1955, Vol **2** (1956).

[23] I. Halpern and V. Strutinski, *Proceedings of the Second International Conference on Peaceful Uses of Atomic Energy*, Geneva, 1958, Vol **15** (1958).

[24] R. Vandenbosch and J. R. Huizenga, *Nuclear Fission*, Academic Press (1973).

[25] E.P. Wigner, *Group Theory and Its Application to the Quantum Mechanics of Atomic Spectra*, Academic Press (1959).

[26] H.A.Kramers, *Brownian motion in a field of force and the diffusion model of chemical reactions*, Physica **7** (1940).

[27] D. Grange and H.A. Weidenmüller, *Fission probability and the nuclear friction constant*, Phys. Lett. B **96** (1980).

[28] M. Blann, *Preequilibrium decay*, Annu. Rev. Nucl. Sci. **25** (1975).

[29] T. Tamura, T. Udagawa and H. Lenske, *Multistep direct reaction analysis of continuum spectra in reactions induced by light ions*, Phys. Rev. C **26** (1982).

[30] H. Feshbach, A. Kerman, S. Koonin, *The statistical theory of multi-step compound and direct reactions*, Ann. Phys. (N.Y.) **125** (1980).

[31] W. Hauser and H. Feshbach, *The Inelastic Scattering of Neutrons*, Phys. Rev. **87** (1952).

[32] J.E. Simmons and R.L. Henkel, *Angular Distribution of Fragments in Fission Induced by MeV Neutrons*, Phys. Rev. **120** (1960).

[33] J. Meadows and C. Budtz-Jørgensen, *Nuclear Data for Science and Technology*, K. Böckhoff (Springer, The Netherlands) (1983).

[34] A. Vorobyev, A. Gagarski, O. Shcherbakov, L. Vaishnene and A. Barabanov, *Anisotropy of the fission fragments from neutron-induced fission in the intermediate energy range of 1–200 MeV*, , JETP Lett. **102** (2015).

[35] M.B. Chadwick et al., *ENDF/B-VII.0: Next Generation Evaluated Nuclear Data Library for Nuclear Science and Technology*, Nuclear Data Sheets **107** (2006).

[36] V. Geppert-Kleinrath et al., *Fission fragment angular anisotropy in neutron-induced fission of ^{235}U measured with a time projection chamber*, Phys. Rev. C **99** (2019).

[37] K.K. Gudima, S.G. Mashnik and V.D. Toneev, *Cascade-exciton model of nuclear reactions*, Nucl. Phys. A **401** (1983).

[38] P. Grangé, H.A. Weidenmüller, *Fission probability and the nuclear friction constant*, Phys. Lett. B **96** (1980).

[39] A. Gavron et al., *Time Scale of Fission at High Angular Momentum*, Phys. Rev. Lett. **48** (1982).

[40] P. Grangé, Li Jun-Qing, and H.A. Weidenmüller, *Induced nuclear fission viewed as a diffusion process: Transients*, Phys. Rev. C **27** (1983).

[41] P. Fröbrich, I.I. Gontchar, *Langevin description of fusion, deep-inelastic collisions and heavy-ion-induced fission*, Phys. Rep. **292** (1998).

[42] D. Jacquet, M. Morjean, *Fission times of excited nuclei: An experimental overview*, Prog. Part. Nucl. Phys. **63** (2009).

[43] D. Durand, E. Suraud and B. Tamain, *Nuclear dynamics in the nucleonic regime*, Institute of Physics Publishing (2001).

[44] V.P. Eismont, A.V. Prokofiev and A.N. Smirnov, *Cross sections of intermediate energy proton induced fission of heavy nuclei and fissility of exited nuclei*, Proc. Int. Conf. on Nuclear Data for Science and Technology, Gatlinburg, Tenessee, USA, ed. J.K. Dickens, ANS, USA, Vol **1** (1994).

[45] H. Condé, V.P. Eismont, A.N. Smirnov et at., *A comparison of proton- and neutron-induced fission cross sections of heavy nuclei at intermediate energies*, Proc. 2nd Conf. on ADTTA, Kalmar, Sweden, ed. H. Conde, Vol **2** (1997).

[46] V.P. Eismont, A.A. Rimski-Korsakov and A.N. Smirnov, *Fission cross sections of heavy nuclei at intermediate energies for hybrid nuclear technologies*, Proc. Int. Conf. on Future Nuclear Systems - GLOBAL'97, Yokohama, Japan (1998).

[47] H. Condé, V.P. Eismont, A N. Smirnov et at, *Up-to-date status and problems of the experimental nucleon-induced fission cross section data base at intermediate energies*, Proc. Int. Conf. on ADTTA, Praha, Czech Republic (1999).

[48] A.I. Obukhov, *Nuclear fission induced by intermediate-energy protons and neutrons*, Phys. Part. Nucl. **32** (2001).

[49] W.U. Schröder and J.R. Huizenga, *Heavy-ion-induced fission — experimental status*, Nucl. Phys. A **502** (1989).

[50] International Energy Agency, www.iea.org.

[51] U.S. Energy Information Administration, *World Energy Outlook 2019*, IEA, Paris https://www.iea.org/reports/world-energy-outlook-2019.

[52] United Nations, Department of Economic and Social Affairs, *World Population Prospects 2019 - Highlights*, New York, (2019).

[53] M. Collins et al., *Long-term Climate Change: Projections, Commitments and Irreversibility. In: Climate Change 2013: The Physical Science Basis. Contribution of Working Group I to the Fifth Assessment Report of the Intergovernmental Panel on Climate Change*, Cambridge University Press, Cambridge, United Kingdom and New York, NY, USA (2013).

[54] Tech. rep., International Energy Agency (IEA) (2018), webstore.iea.org/key-world-energy-statistics-2018.

[55] T. Trainer, *Can renewables etc. solve the greenhouse problem? The negative case*, Energy Policy 1textbf38 (2010).

[56] T. Trainer, *Can renewables etc. solve the greenhouse problem? The negative case*, Energy Policy **38** (2010).

[57] W.F. Laurance, M. Goosem and S.G.W. Laurance, *Impacts of roads and linear clearings on tropical forests*, Trends in Ecology and Evolution **24** (2009).

[58] P. Kyle, L. Clarke, G. Pugh, M. Wise, K. Calvin, J. Edmonds and S. Kim, *The value of advanced technology in meeting 2050 greenhouse gas emissions targets in the United States*, Energy Economics **31** (2009).

[59] F. Goldner and R. Versluis, *Transmutation capabilities of generation 4 reactors*, Tech. rep., OECD, NEA (2007).

[60] M. Salvatores, G. Palmiotti, *Radioactive waste partitioning and transmutation within advanced fuel cycles: Achievements and challenges*, Prog. Part. Nucl. Phys **66** (2011).

[61] W. Maschek et al., *Accelerator driven systems for transmutation: Fuel development, design and safety*, Prog. Nucl. Energy **463** (2001).

[62] H. Nifenecker, S. David, J.M. Loiseaux, O. Meplan, *Basics of accelerator driven subcritical reactors*, Nucl. Instr. Meth. A **50** (2008).

[63] C. Rubbia et al., *An Energy Amplifier for cleaner and inexhaustible nuclear energy production driver by a particle beam accelerator*, CERN/AT/93-47(ET) (1993).

[64] F. Venneri, C. Bowman, and R. Jameson, *Accelerator-driven Transmutation of Waste (ATW) - A new method for reducing the long-term radioactivity of commercial nuclear waste*, LA-UR-93-752, LANL (NM) (1993).

[65] The MYRRHA project, http://myrrha.sckcen.be/en.

[66] N. Colonna et al., *Advanced nuclear energy systems and the need of accurate nuclear data: the n_TOF project at CERN*, Energy Environ. Sci. **3** (2010).

[67] M. Arnould, S. Goriely, K. Takahashi, *The r-process of stellar nucleosynthesis: Astrophysics and nuclear physics achievements and mysteries*, Phys.Rept.**450** (2007).

[68] F. Käppeler, *The Origin of the Heavy Elements: The s Process*, Progress in Particle and Nuclear Physics **43** (1999).

[69] H.-T. Janka et al., *Explosion Mechanisms of Core-Collapse Supernovae*, Ann. Rev. Nuc. Part. Science **62** (2012).Lattimer

[70] J.M. Lattimer and D.N. Schramm, *Black-Hole-Neutron-Star Collisions*, Astrophys. J. **210** (1976).

[71] D. Eichler, M. Livio, T. Piran and D.N. Schramm, *Nucleosynthesis, neutrino bursts and γ-rays from coalescing neutron stars*, Nature **340** (1989).

[72] B.P. Abbott et al., *Multi-messenger Observations of a Binary Neutron Star Merger*, Astrophys. J. **848**(2) (2017).

[73] S. Goriely and G. M. Pinedo, *The production of transuranium elements by the r-process nucleosynthesis*, Nucl. Phys. A **944** (2015).

[74] M. Eichler et al., *The role of fission in neutron star mergers and its impact on the r-process peaks*, Astrophys. J. **808**(1) (2015).

[75] J. Lippuner and L.F. Roberts, *SkyNet: A Modular Nuclear Reaction Network Library*, Astrophys. J. Suppl. S. **233** (2017).

[76] N. Colonna et al., *The fission experimental programme at the CERN n_TOF facility: status and perspectives*, Eur. Phys. J. A **56** (2020).

[77] S. Goriely, *Uncertainties in the solar system r-abundance distribution*, Astron. Astrophys. **342** (1999).

[78] F.-K. Thielemann, M. Eichler, I.V. Panov, and B. Wehmeyer, *Neutron Star Mergers and Nucleosynthesis of Heavy Elements*, Annu. Rev. Nucl. Part. S. **67**(1) (2017).

[79] M. Durante and F.A. Cucinotta, *Physical basis of radiation protection in space travel*, Rev. Mod. Phys. **83** (2011).

[80] John W. Norbury et al., *Galactic cosmic ray simulation at the NASA Space Radiation Laboratory*, Life Sci. Space Res. **8** (2016).

[81] ICRP, *1990 Recommendations of the International Commission on Radiological Protection*, ICRP Publication **60** Ann. ICRP 21 (1991).

[82] ICRP, *The 2007 Recommendations of the International Commission on Radiological Protection*, ICRP Publication **103** Ann. ICRP 37 (2007).

[83] European Union, *Council Directive 96/29/EURATOM of 13 May 1996 laying down basic safety standards for the protection of the health of workers and the general public against the dangers arising from ionising radiation*, Official Journal of the European Communities L159, Vol. **39** (1996).

[84] A.D. Carlson at al., *Evaluation of the Neutron Data Standards*, Nuclear Data Sheets **148** (2018).

[85] A.D. Carlson, *The neutron cross section standards, evaluations and applications*, Metrologia **48** (2011) 328.

[86] A.J.M. Plompen, E. Bauge, O. Bersillon et al., *The joint evaluated fission and fusion nuclear data library, JEFF-3.3*, Eur. Phys. J. A **56** (2020).

[87] D.A. Brown, M.B. Chadwick, R. Capote et al., *ENDF/B-VIII.0: The 8th major release of the nuclear reaction data library with CIELO-project cross sections, new standards and thermal scattering data*, Nucl. Data Sheets **148** (2018).

[88] K. Shibata, O. Iwamoto, T. Nakagawa et al., *JENDL-4.0: A New Library for Nuclear Science and Engineering*, J. Nucl. Sci. Technol. **48** (2011).

[89] A. Blokhin, E. Gai, A. Ignatyuk, I. Koba, V. Manokhin,and V. Pronyaev, *New Version of Neutron Evaluated Data Library BROND-3*, Vopr. Atom. Nauki i Tech., Ser. Nuclear Constants Issue **2** (2016).

[90] Z.G. Ge, Z.X. Zhao, H.H. Xiaet al., *The Updated Version of Chinese Evaluated Nuclear Data Library(CENDL-3.1)*, J. of the Korean Physical Society **59** (2011).

[91] https://www.oecd-nea.org/.

[92] INDC International Nuclear Data Committee, ^{209}*Bi(n,f) and* ^{nat}*Pb(n,f) Cross Sections as a New Reference and Extension of the* ^{235}*U,* ^{238}*U and* ^{239}*Pu(n,f) Standards up to 1 GeV*, INDC(NDS)-0681 Distr. ST/J/G/NM IAEA (2015).

[93] A.D. Carlson et al., *International Evaluation of Neutron Cross Section Standards*, Nuclear Data Sheets **110** (2009).

[94] Nuclear standard reference data, *Proc. Advisory Group Meeting on Nuclear Standard Reference Data*, IAEA- TECDOG33 (1984).

[95] R. Machleidt, K. Holinde and Ch. Elster, Phys. Rep. **149** (1987) 1.

[96] M. Lacombe, 8. Loiseau, J.M. Richard, R. Vinh Mau, J. Cöte, P. Pires and R. de Tourreil, Phys. Rev. **21C** (1980) 861.

[97] J.R. Bergervoet, P.C. van Campen, W.A. van der Sanden and J.J. de Swart, Phys. Rev. **38C** (1988) 15.

[98] P. Doll, *Neutron-Proton Scattering*, Kernforschungszentrum Karlsruhe (1990).

[99] P.F. Rose, *ENDF-201 ENDF/V-VI summary documentation*, BNL-NCS–1754 1(1991).

[100] D.C. Dodder and G.M. Hale, Los Alamos National Laboratory, Los Alamos, NM, Private Communication to CSEWG (1987).

[101] H. Condé, *Nuclear Data Standards for Nuclear Measurements Nuclear Energy Agency Report*, NEANDC-311 'U', INDC(SEC)-101 (1992).

[102] R.A. Arndt et al., *Nucleon-nucleon partial-wave analysis to 1 GeV*, Phys. Rev. D **28** (1983).

[103] R.A. Arndt et al., *Nucleon-nucleon partial-wave analysis to 1100 MeV*, Phys. Rev. D **35** (1987) 128.

[104] J. Rahm et al., *np scattering measurements at 162 MeV and the ϕNN coupling constant*, Phys. Rev. C **57** (1998).

[105] W. Hürster, et al., *Neutron-Proton Charge Exchange Scattering Between 190 MeV and 590 MeV*, Phys. Lett. B **90** (1980).

[106] R.A. Arndt et al., *Updated analysis of NN elastic scattering data to 1.6 GeV*, Phys. Rev. C **50** (1994).

[107] R.A. Arndt et al., *Nucleon-nucleon elastic scattering analysis to 2.5 GeV*, Phys. Rev. C **56** (1997).

[108] http://gwdac.phys.gwu.edu.

[109] R. A. Arndt et al., *Updated analysis of NN elastic scattering to 3 GeV*, Phys. Rev. C **76** (2007).

[110] Ron L. Workman et al., *Status of JENDL High Energy Partial-wave analysis of nucleon-nucleon elastic scattering data*, Phys. Rev. C **94** (2016).

[111] K. Shibata et al., *JENDL-4.0: A New Library for Innovative Nuclear Energy Systems*, in ND2010, Int. Conf. on Nucl. Data for Sci. and Technol. (2010).

[112] Y. Watanabe et al., *Status of JENDL High Energy File*, in ND2010, Int. Conf. on Nucl. Data for Sci. and Technol. (2010).

[113] R. Nolte et al., *Cross Sections for Neutron-Induced Fission of* ^{235}U, ^{238}U, ^{209}Bi, *and* ^{nat}Pb *in the Energy Range from 33 to 200 MeV Measured Relative to n-p Scattering*, Nuclear Science and Engineering **156** (2007).

[114] P.W Lisowski et al., *Fission cross sections in the intermediate energy region*, Neutron Cross Section Standards for the Energy Region Above 20 MeV (Specialists Mtg Uppsala, 1991), Rep. NEANDC-305/U, OECD, Paris (1991).

[115] A.D. Carlson et al., in *Proceedings of the International Conference on Nuclear Data for Science and Technology*, Trieste (1997).

[116] Y. Watanabe et al., in *Status of JENDL high energy file*, Journal of the Korean Physical Society **59** (2007).

[117] S. Lo Meo al., in *Fission induced by nucleons at intermediate energies*, Nucl. Phys. A **933** (2015).

[118] A. Boudard et al., in *New potentialities of the Liège intranuclear cascade model for reactions induced by nucleons and light charged particles*, Phys. Rev. C **87** (2013).

[119] D. Mancusi al., in *Unified description of fission in fusion and spallation reactions*, Phys. Rev. C **82** (2010).

[120] G. Wallerstein et al., *Synthesis of the Elements in Stars: Forty Years of Progress*, Rev. Mod. Phys. **69** (1997) 995.

[121] S.E. Woosley et al., *Nuclear data needs for the study of nucleosynthesis in massive stars*, Nucl. Phys. A **718** (2003).

[122] F. Kappeler et al., *The s process: Nuclear physics, stellar models, and observations*, Rev. Mod. Phys. **83** (2011) 157.

[123] T. Rauscher et al., *Challenges in nucleosynthesis of trans-iron elements*, AIP Adv. **4** (2014) 041012.

[124] T. von Egidy et al., *Erratum: Systematics of nuclear level density parameters[Phys. Rev. C 72, 044311 (2005)]*, Phys. Rev. C **73** (2006) 049901.

[125] H.A. Weidenmuller et al., *Random matrices and chaos in nuclear physics: Nuclear structure*, Rev. Mod. Phys. **81** (2009) 539.

[126] S.M. Qaim, *Nuclear data for medical radionuclides*, J. Radioanal. Nucl. Chem. **305** (2015) 233.

[127] G. Aliberti et al., *Impact of Nuclear Data Uncertainties on Transmutation of Actinides in Accelerator-Driven Assemblies*, Nucl. Sci. Eng. **146** (2004) 13.

[128] A. Nuttin et al., *Potential of thorium molten salt reactors: detailed calculations and concept evolution with a view to large scale energy production*, Prog. Nucl. Energy **46** (2005) 77.

[129] A. Nuttin et al., *Comparative analysis of high conversion achievable in thorium-fueled slightly modified CANDU and PWR reactors*, Ann. Nucl. Energy **40** (2012) 171.

[130] The n_TOF Collaboration, *CERN n_TOF Facility: Performance Report*, CERN INTC-2002-037 (2003).

[131] F. Gunsing et al., *Nuclear data activities at the n_TOF facility at CERN*, Eur. Phys. J. Plus **131** (2016) 371.

[132] W. Mondelaers and P. Schillebeeckx, *GELINA, a neutron time-of-flight facility for neutron data measurements*, Notiziario **11** (2006) 19.

[133] J. Klug et al., *Development of a neutron time-of-flight source at the ELBE accelerator*, Nucl. Inst. Meth. A **577** (2007) 641-653.

[134] K.H. Böckhoff, A.D. Carlson, O.A. Wasson, J.A. Harvey and D.C. Larson, *Electron linear accelerators for fast neutron data measurements in support of fusion energy applications*, Nucl. Sci. & Eng. **106** (1990) 192.

[135] M.E. Overberg, B.E. Moretti, R.E. Slovacek and R.C. Block, *Photoneutron target development for the RPI linear accelerator*, Nucl. Instr. Meth. A **438** (1999) 253.

[136] K. Kino et al., *Measurement of energy spectra and spatial distributions of neutron beams provided by the ANNRI beam line for capture cross-section measurements at the J-PARC/MLF*, Nucl. Instr. Meth. A **626-627** (2011) 58-66.

[137] P.W. Lisowski and K.F. Schoenberg, *The Los Alamos neutron science center*, Nucl. Instr. Meth. A **562** (2006) 910.

[138] Wei Jie at al., *China Spallation Neutron Source - an overview of application prospects*, Chinese Phys. C **33** (2009) 1033.

[139] C. Weiss et al., *The new vertical neutron beam line at the CERN n_TOF facility design and outlook on the performance*, Nucl. Instrum. Meth. A **799** (2015) 90-98.

[140] Y. Kadi and J.P. Revol, *Design of an Accelerator-Driven System for the Destruction of Nuclear Waste*, Accelerator-Driven Systems for Energy Production and Waste Incineration: Physics, Design and Related Nuclear Data (2002).

[141] C. Rubbia et al., *A High Resolution Spallation Driven Facility at the CERN–PS to Measure Neutron Cross Sections in the interval from 1 eV to 250 MeV*, CERN/LHC/98-02 (EET) **131** (1998) 371.

[142] F. Gunsing et al., *The measurement programme at the neutron time-of-flight facility n_TOF at CERN*, Eur. Phys. J., Web of Conferences **146** (2017).

[143] A. Tsinganis et al., *The Fission Programme at the CERN n_TOF Facility*, Phys. Proc. **64** (2015) 130.

[144] N. Colonna et al., *The Nuclear Astrophysics program at n_TOF (CERN)*, EPJ Web of Conferences **165** (2017) 01014.

[145] J. Praena et al., *Measurement and resonance analysis of the $^{33}S(n,\alpha)$ ^{30}Si cross section at the CERN n_TOF facility in the energy region from 10 to 300 keV*, Phys. Rev. C **97** (2018) 064603.

[146] M. Barbagallo et al., *$^{7}Be(n,\alpha)$ ^{4}He reaction and the cosmological lithium problem: Measurement of the cross section in a wide energy range at n_tof at cern*, Phys. Rev. Lett **117** (2016) 152701.

[147] F. Gunsing, *Status and outlook of the neutron time-of-flight facility n_TOF at CERN*, Nucl. Instrum. Meth. B **261** (2007) 925–929.

[148] U. Abbondanno et al., *n_TOF performance report*, CERN/INTC-O-011, INTC-2002-037, (2002).

[149] C. Guerrero et al., *Performance of the neutron time-of-flight facility n_TOF at CERN*, Eur. Phys. J. A **49** (2013) 27.

[150] A. Ferrari and P.R. Sala, *Intermediate and High Energy Physics Models in FLUKA: Improvements, Benchmarks and Applications*, Proc. Int. Conf. on Nuclear Data for Science and Technology, NDST-97, ICTP (1997).

[151] J. Briesmeister, *MCNP-A General Monte Carlo N-Particlke Transport Code-Version 4c2*, LA-13709-M (2000).

[152] The n_TOF Collaboration, *n_TOF Experimental Area 2 (EAR2) preliminary feasibility study*, CERN-INTC-2011-032 / INTC-O-013 (2011).

[153] The n_TOF Collaboration, *Proposal for n_TOF Experimental Area 2 (EAR-2)*, CERN-INTC-2012-029 / INTC-O-015 (2012).

[154] M. Barbagallo et al., *High-accuracy determination of the neutron flux at n_TOF*, Eur. Phys. J. A **49** (2013) 156.

[155] M. Sabaté-Gilarte et al., *High-accuracy determination of the neutron flux in the new experimental area n_TOF-EAR2 at CERN*, Eur. Phys. J. A **53** (2017) 210.

[156] S. Agostinelli et al., *GEANT4 - a simulation toolkit*, Nucl. Instrum. Meth. A **506** (2003).

[157] J. Allison et al., *GEANT4 developments and applications*, EEE T. Nucl. Sci. **53** (2006).

[158] A. Masi et al., *The CERN n_TOF facility data acquisition system*, in Proc. 16th Int. Conf. on Accelerator and Large Experimental Control Systems (ICALEPCS'17) (2017).

[159] CERN Advanced STORage manager, castor.web.cern.ch.

[160] P. Žugec et al., *Pulse processing routines for neutron time-of-flight data*, Nucl. Instrum. Meth. A **812** (2016).

[161] D.A. Brown et al., *ENDF/B-VIII.0: The 8th Major Release of the Nuclear Reaction Data Library with CIELO-project Cross Sections, New Standards and Thermal Scattering Data*, Nuclear Data Sheets **148** (2018).

[162] C.H. Johnson, *Recoil telescope detectors Fast Neutron Physics Part I*, ed J B Marion and J L Fowler (New York: Interscience) (1960).

[163] M. Cambiaghi et al., *Fast neutron spectrometry with identification of recoil protons*, Nucl. Instr. Meth. **82** (1970).

[164] C. Cazzaniga, M. Rebai, M. Tardocchi, G. Croci, M. Nocente, S. Ansell, C.D. Frost and G. Gorini, *A telescope proton recoil spectrometer for fast neutron beam-lines*, Prog. Theor. Exp. Phys. (2015) 073H01.

[165] V. Dangendorf, R. Nolte, F. Roos, H. Schuhmacher, B.R.L. Siebert and M. Weyrauch, *Proton recoil telescopes for fluence measurement in neutron beams of 20-200 MeV energy*, Nucl. Instr. and Meth. A **469** (2001) 205.

[166] W.R. Leo, *Techniques For Nuclear And Particle Physics Experiments*, Springer Verlag (1994).

[167] https://eljentechnology.com/images/products/data_sheets/EJ-200_EJ-204_EJ-208_EJ-212.pdf.

[168] https://hallcweb.jlab.org/DocDB/0008/000809/001/PhotonisCatalog.pdf.

[169] https://www.crystals.saint-gobain.com/products/bc-408-bc-412-bc-416.

[170] https://www.hamamatsu.com/resources/pdf/etd/R1924A_TPMH1280E.pdf.

[171] C. Agodi et al., *The HADES time-of-flight wall*, Nucl. Instr. Meth. A **492** (2002) 14.

[172] L. Cosentino, P. Finocchiaro, A. Pappalardo, F. Garibaldi, *Characterization of a Scintillating Mini-Detector for Time-Of-Flight Positron Emission Tomography With Depth-Of-Interaction*, Rev. Sci. Instr. **83** (2012) 084302.

[173] http://www.micronsemiconductor.co.uk/.

[174] G. F. Knoll, *Radiation detection and measurement*, John Wiley & Sons Inc (2010).

[175] D.B. Gayther, *International Intercomparison of Fast Neutron Fluence-Rate Measurements Using Fission Chamber Transfer Instruments*, Metrologia **27** (1990).

[176] W. Parker, R. Falk, *Molecular plating: A method for the electrolytic formation of thin inorganic films*, Nucl. Instr. Meth. **16** (1962).

[177] C. Ingelbrecht, A. Moens, R. Eykens, A. Dean, *Improved electrodeposited actinide layers*, Nucl. Instr. Meth. A **397** (1997).

[178] G. Sibbens, A. Moens, D. Vanleeuw, D. Lewis, Y. Aregbe, *Nuclear targets within the project of solving CHAllenges in Nuclear Data*, EPJ Web of Conferences, submitted 2016.

[179] G. Sibbens, A. Moens, R. Eykens, *Preparation and sublimation of uranium tetrafluoride for the production of thin $^{235}UF_4$ targets*, J Radioanal Nucl Chem **305** (2015).

[180] G. Hempel, F. Hopkins, and G. Schatz, *Development of parallel plate avalanche counters for the detection of fission fragments*, Nucl. Instr. and Meth **131** (1975).

[181] J.C. Sanabria, B.L. Berman, C. Cetina, *Parallel-plate avalanche detectors with anode wire grids*, Nucl. Instr. and Meth. A **441** (2000).

[182] C. Stephan, L. Ferrant, B. Berthier, S. David, L. Tassan-Got, C.O. Bacri, F. Rejmund, and C. Moreau (n TOF Collaboration), *Neutron-Induced Fission Cross Section Measurements between 1 eV and 250 MeV*, J. Nucl. Sci. and Techn., Supp. **2** (2002) 276.

[183] A. Breskin and N. Zwang., *Timing properties of parallel plate avalanche counters with light particles*, Nucl. Instr. and Meth. **144** (1977).

[184] www.leica-geosystems.com/metrology.

[185] S.P. George, *PhD Thesis: Dosimetric applications of hybrid pixel detectors*, University of Wollongong (2015).

[186] S.P. George at al., *Very high energy calibration of silicon Timepix detectors*, JINST **13** (2018) 11014.

[187] D. Tarrío at al., *Measurement of the angular distribution of fission fragments using a PPAC assembly at CERN n_TOF*, Nucl. Instr. and Meth. A **743** (2014) 11014.

[188] N.K. Abrosimov et al., *Neutron time-of-flight spectrometer gneis at the Gatchina 1 GeV proton synchrocyclotron*, Nucl. Instr. Meth. in Phys. Res. A **242** (1985).

[189] A.S. Vorobyev et al., *Anisotropy of the fission fragments from neutron-induced fission in intermediate energy range 1-200 MeV*, Pis'ma v ZhETF **102** (2015).

[190] D. Hensle et al., *Neutron-induced fission fragment angular distributions, anisotropy, and linear momentum transfer measured with the NIFFTE fission time projection chamber*, Phys. Rev. C **102** (2020).

[191] N. Terranova et al., *Monte Carlo simulations and n-p differential scattering data measured with Proton Recoil Telescopes*, EPJ Web of Conferences **239** (2020).

[192] F. Belloni et al., *Neutron beam imaging with an XY-micromegas detector at n_TOF at CERN*, Phys. Scr. **T150** (2012).

[193] J. Pancin at al., *Measurement of the n_TOF beam profile with a micromegas detector*, Nucl. Instr. Meth. in Phys. Res. A **524** (2004).

[194] C.A. Whitten, *Correction procedures for variable intensity neutron time-of-flight measurements*, Nucl. Instr. Meth. in Phys. Res. A **309** (1991).

[195] J. Bystricky, P. La France, F. Lehar, F. Perrot, T. Siemiarczuk, P. Winternitz, *Energy dependence of nucleon-nucleon inelastic total cross-sections*, Journal de Physique **48** (1987).

[196] C. Paradela et al., *Neutron-induced fission cross section of ^{234}U and ^{237}Np measured at the CERN Neutron Time-of-Flight (n_TOF) facility*, Phys. Rev. C **82** (2010).

[197] H.M. Steiner, J.A. Jungerman, *Proton-Induced Fission Cross Sections for* ^{238}U, ^{235}U, ?232*Th,* ^{209}Bi, *and* ^{197}Au *at 100 to 340 MeV*, Phys. Rev. **101** (1956).

[198] J.A. Jungerman, *Fission Excitation Functions for Charged Particles*, Phys. Rev. **79** (1950).

[199] V.A. Konshin, E.S. Matusevitch, V.I. Regushevskii, *Cross section for the fission of* ^{181}Ta, *Re, Pt,* ^{197}Au, *Pb,* ^{209}Bi, ^{232}Th, ^{235}U *and* ^{238}U *by 150-660 MeV protons*, Yadernaya Fizika **2** (1965).

[200] A.A. Kotov et al., *Energy dependence of proton induced fission cross sections for heavy nuclei in the energy range 200-1000 MeV*, Phys. Rev. C **74** (2006).